

Characterisation of a Novel Gene-Targeted Model for PRKAG2 Disease

A Thesis Submitted for the Degree of Doctor of Philosophy

Trinity Term, 2012

Arash Yavari

Merton College

Department of Cardiovascular Medicine

University of Oxford

Supervisors: Dr Houman Ashrafian and Professor Hugh Watkins

Characterisation of a Novel Gene-Targeted Model for PRKAG2 Disease

Arash Yavari, Merton College, University of Oxford

A thesis submitted for the degree of Doctor of Philosophy, Trinity 2012

Abstract

AMP-activated protein kinase (AMPK) is an evolutionarily highly-conserved serine/threonine kinase that acts as a cellular energy sensor and integrator of metabolic signals at both the cellular and whole-body level. Interest in its cardiac role stemmed from the discovery that dominant mutations in the gene encoding its regulatory γ2 subunit (*PRKAG2*) were the cause of a cardiomyopathy characterised by left ventricular hypertrophy (LVH), ventricular pre-excitation, myocardial glycogen storage and progressive cardiac conduction disease. Several cardiac-restricted overexpressing transgenic (TG) murine models have been described which recapitulate much of this, but at the expense of markedly altered γ-isoform stoichiometry and use of an unphysiological promoter, such that overexpressing even wild-type (WT) γ2 results in glycogen accumulation and LVH. This thesis describes characterisation of the cardiac phenotype and investigation of underlying mechanisms in a novel gene-targeted, knock-in (KI) murine model of PRKAG2 disease carrying an exon 7 R299Q mutation (modelling human R302Q) that was designed to yield new mechanistic insights into the pathophysiology of the cardiomyopathy free of the confounders affecting existing TG models.

R299Q mutant transcript expression was verified in the heart, with comparable levels of γ2 protein expression to WT. Mutant γ_2 AMPK complexes demonstrated abrogated allosteric response to AMP and a trend to increased basal activity *in vitro*. Hearts from mutant mice displayed no visible glycogen excess, but a subtle increase in cardiac glycogen content was apparent in homozygous mutant mice at 12 months of age. On a mixed C57/129 genetic background, mutant mice exhibited mild LV systolic dysfunction at two months of age, but no significant LV remodelling. When backcrossed onto C57BL/6, older mutant mice manifested greater cardiac mass than WT, but in the context of a generalised increased in internal organ and body mass. Homozygous mutant mice displayed intrinsic sinus bradycardia and mild QRS prolongation, but no ventricular pre-excitation. Gene expression profiling and quantitative PCR identified downregulation of *Hcn1* and *Hcn4* expression in both heterozygous and homozygous mutant mice. These encode f-channels conducting the pacemaker 'funny' current (I_f) and are highly enriched in sinoatrial node (SAN). Isolated SAN myocytes from mutant mice exhibited reduced automaticity and I_f current density, but no evidence was found for a direct effect of mutant γ2 on f-channels. To investigate whether γ2 might play a physiological role in the regulation of heart rate, a global γ2 knock-out (KO) was also generated using Sox2cre to drive embryonic excision of R299Q mutated exon 7 of *Prkag2* in the KI. AMPK γ2 activity was markedly reduced in the hearts of γ2 KO mice. KO mice had an elevation in intrinsic heart rate and increased *Hcn1* and *Hcn4* expression. In contrast to γ1, γ2 transcript was found to be markedly enriched in the atria and SAN of WT mice. These studies indicate that mutant R299Q γ2 alters SAN automaticity and hence pacemaking via an effect on *Hcn* expression and I_f. By inference, the sinus bradycardia and chronotropic incompetence frequently present in carriers of PRKAG2 mutations are likely to reflect a direct effect of mutant γ2 to induce an f-channelopathy. By providing evidence for effects of mutant γ2 on cardiac function, electrophysiology (EP) & transcriptome independent of gross glycogen accumulation, the KI model highlights the limitations of conceptualising PRKAG2 disease purely as a glycogen storage disorder and points to the existence of direct, glycogen-independent effects of mutant γ2 in disease pathogenesis. The directionally opposite EP findings from the γ2 KO suggest a novel physiological role for γ2 in the regulation of mammalian heart rate.

Investigation of the systemic consequences of gene-targeting *Prkag2* with the R299Q mutation revealed a significant metabolic phenotype. Young mutant mice displayed increased lean mass, reduced fat mass, hyperphagia, lower fasting insulin, normal glucose tolerance and increased spontaneous exercise performance. Older mutant mice developed marked obesity – due to hyperphagia rather than reduced energy expenditure – increased somatic growth, impaired glucose tolerance, reduced *in vivo* glucose-stimulated insulin secretion and lower insulin sensitivity. *Prkag2* was seen to be expressed in the arcuate hypothalamus, with increased hypothalamic mRNA expression of the pro-orexigenic agouti-related peptide and the transcription factor BSX – both implicated in the regulation of food intake by the orexigenic hormone ghrelin. Mutant mice displayed an exaggerated food intake response to ghrelin but intact satiety response to leptin, with antagonism of the ghrelin receptor rescuing their hyperphagia. Given the activating nature of these γ2 mutations and the intense interest in AMPK activation as a therapeutic strategy for the global epidemic of obesity and diabetes, these findings have broad implication in demonstrating the potential risks of chronic AMPK activation in causing hyperphagia and obesity via a ghrelin-dependent mechanism.

Acknowledgements

I would like to express my sincere gratitude to my supervisors, Dr Houman Ashrafian and Professor Hugh Watkins, for providing me with the opportunity to undertake basic science research at Oxford and for their guidance, mentorship, encouragement, patience and inspiring academic example. I am indebted to the Wellcome Trust for funding my studies with a Research Training Fellowship and to their scientific reviewers, whose comments on the original Fellowship application proved to be remarkably prescient. I am grateful also to the staff at Merton College for their pastoral support, in particular my College supervisor Professor Kieran Clarke.

It is a pleasure to thank the very many friends and colleagues with whom I have been privileged to work with and learn science from. Foremost, I wish to acknowledge my immense debt to Dr Mohamed Bellahcene, Miss Violetta Steeples and Dr Gabor Czibik who, collectively, taught me the essentials of experimental work and the basic laboratory techniques used in this thesis, acted as a source of constant encouragement and support throughout the course of the research, as well as demonstrating remarkable patience in the face of many long discussions and hypotheses about one particular protein kinase. I am very grateful to Dr Katja Gehmlich for her expert support with cell work, Dr Katalin Pinter for her original construction of the *Prkag2* targeting vector and Dr Theo Kyriakou for advice on hypothalamic dissection and luciferase reporter assays. Special thanks must go to two outstanding medical students who are now either fully qualified or soon to become so, Dr Alexander Stockenhuber and Mr Chinh Nguyen, who both demonstrated great enthusiasm and commitment as part of their elective studies. I wish to thank other members of Professor Watkins' group, past and present, including Miss Kimberley Adams, Dr Anuj Goel, Dr Henrik Isackson, Dr Shapour Jalilzadeh, Dr Yanyan Jiang, Dr Matthew Kelly, Dr Heena Lad, Mr Adam Piers and Dr Paul Robinson. I am especially indebted to Mrs Farah Nematkhah for her kindness and in ensuring my nutritional reserves were still stocked despite many late experimental sessions and to our laboratory managers, Dr James Brown and Mr Phil Townsend, for their unfailing support with all aspects of laboratory work.

My development as a trainee scientist has been positively influenced by many others in the Department and wider University, in particular the group members of Professor Keith Channon, Professor Barabara Casadei and Professor Stefan Neubauer. Special thanks must go to: Dr Craig Lygate for his support and encouragement with animal cardiovascular phenotyping, Miss Hannah Barnes, Dr Mahon Maguire and Dr Jurgen Schneider for excellent MRI support, Dr Gillian Douglas for kind support with telemetry, Dr Merzaka Lazdam for outstanding cheerfulness during many long ELISA assays, Dr Dilair Baban, Dr Natasha Sahgal and Dr Helen Lockstone for their expertise and guidance with the microarray experiment, Dr Mike Shaw and Professor David Ferguson for support with electron microscopy, Miss Rathi Puliyadi and Dr Joe de Bono for kind assistance with running wheel experiments, Dr Laurence Brown and Dr Stuart Peirson for enthusiastic support with activity measures, Dr Jyoti Patel for assistance with printing, and Dr Peter Oliver and Dr Andrew Edwards for their expertise with neurohistology and ISH. Outside of Oxford, I am deeply indebted to the collaborators for this project who have been a key part of its success, in particular to the enthusiasm, commitment and professional expertise of Dr Claire Stocker, Mr Ed Wargent, Professor Jon Arch and Professor Mike Cawthorne at the University of Buckingham. I am also very grateful to Dr Annalisa Bucchi, Professor Mirko Baruscotti and Professor Dario DiFrancesco for their outstanding expert support with sinoatrial node phenotyping and very kind hospitality during an academic visit to Milan. I also wish to thank Dr John Gomes, Professor Andrew Tinker and Dr Craig Beall for expert experimental support.

Finally, I wish to thank my younger brother, sister and parents. Whilst my sacrifice during the course of this work was willing, theirs was not and my debt to them for their patience with an absent brother and son cannot be repaid. This work is dedicated to them, their courage and fortitude and to the shining memory of my four grandparents.

Oxford, October 2012

Declaration of own work and attribution

Except where specifically outlined below, this DPhil thesis is entirely my work. It has not been submitted, either wholly or substantially, for another degree of this University, or for a degree at any other institution.

The author gratefully acknowledges the outstanding technical expertise and contributions made by senior colleagues and fellow students within Professor Watkins' Group, the wider Department of Cardiovascular Medicine in Oxford and external collaborating laboratories. All external collaborations were sought and run by the author. For the internal and external collaborations listed below, the author generated the hypotheses, planned the experiments, genotyped and prepared all mice and was responsible for all data analysis and interpretation unless otherwise indicated.

Chapter 3: Biochemical glycogen assays were run and allelic discrimination primers designed jointly with Dr Gabor Czibik (Oxford). Cine-MRI examinations were conducted by Miss Hannah Barnes (Oxford) with the author responsible for anaesthesia, monitoring and recovery of mice. Cardiac sample harvesting and specimen preparation for transmission electron microscopy (TEM) at 2 months were undertaken by the author in the Department of Physiology under the supervision of Dr Mike Shaw (Oxford). Cardiac samples at 12 months were harvested and fixed by the author, with subsequent specimen preparation performed by Professor David Ferguson (Oxford).

Chapter 4: ECG telemetry surgery was undertaken jointly with Dr Gillian Douglas (Oxford). Invasive electrophysiology study and analysis was performed by Dr John Gomes (UCL). The microarray study was designed with advice from Dr Helen Lockstone (Oxford). Conversion of RNA to cRNA, and direct hybridisation assay were conducted by Dr Dilair Baban (Oxford). Microarray quality control, background subtraction and dataset normalisation were by Dr Natasha Sahgal (Oxford). The author analysed the microarray dataset under guidance by Dr Sahgal and Dr Lockstone. Sinoatrial cellular electrophysiology and heterologous transfection experiments were conducted in collaboration with Professor Mirko Baruscotti and Professor Dario DiFrancesco (University of Milan). Sinoatrial node patch clamping was by Dr Annalisa Bucchi, with sinoatrial node RNA extractions undertaken jointly in Milan by the author and Professor Baruscotti.

Chapter 5: Generation, validation and phenotyping of Sox2cre γ2 KO mice were undertaken jointly with Mr Chinh Nguyen (University of Melbourne Medical School) whilst the author acted as his primary supervisor for an intercalated BSc degree. Sample preparation for sequence verification of exon 7 deletion of *Prkag2* was undertaken jointly with Dr Yanyan Jiang (Oxford).

Chapters 6 and 7: Brain sectioning and Nissl staining was performed with Dr Andrew Edwards (Oxford). White adipose tissue histology was performed by Dr Alexander Stockenhuber (University of Vienna) whilst the author acted as his primary supervisor for a summer elective. *In situ* hybridisation was performed by Dr Peter Oliver (Oxford). Multiplex measurements of plasma adipocytokines using a Luminex xMAP system were undertaken jointly with Dr Merzaka Lazdam (Oxford). Voluntary wheel running experiments were designed and analysed with assistance from Dr Joe de Bono and Mrs Rathi Puliyadi (Oxford) and spontaneous activity measured by Dr Laurence Brown (Oxford). Energy expenditure and glucose handling assessment, pair-feeding and all drug challenges were planned and conducted in collaboration with Dr Claire Stocker, Professor Jon Arch and Professor Mike Cawthorne, with assistance from Mr Ed Wargent and Dr Jacqueline O'Dowd for the insulin radioimmunoassay (Clore Laboratory, University of Buckingham). Islet β-cell isolation and electrophysiology were conducted by Dr Craig Beall (University of Dundee).

Multiple chapters: The targeting vector used to design the knock-in model was constructed by Dr Katalin Pinter (Oxford), with subsequent gene-targeting performed by GenOway (Lyon). Invasive haemodynamic surgery and *ex vivo* cardiac perfusion were conducted by Dr Mohamed Bellahcene (Oxford) with support from the author for tissue harvesting. Neonatal rat cardiomyocytes were harvested by Dr Katja Gehmlich (Oxford). HL-1 and neonatal rat cardiomyocyte culture and transfection were undertaken jointly with Miss Violetta Steeples (Oxford).

Abbreviations and Acronyms

α-MHC	α-myosin heavy chain
α-MSH	α-melanocyte-stimulating hormone
Abhd1	Abhydrolase domain containing 1
Acta1	Skeletal muscle α-actin
A/D	Analogue digital converter
ACC	Acetyl-CoA carboxylase
ADP	Adenosine 5'-diphosphate
AEBSF	4-(2-Aminoethyl)benzenesulfonyl fluoride hydrochloride
AF	Atrial fibrillation
AgRP	Agouti-related peptide
AICAR	5-amino-4-imidazolecarboxamide riboside
AID	Autoinhibitory domain
AKT	Protein kinase B
AMP	Adenosine 5'-monophosphate
AMPK	AMP-activated protein kinase
ANCOVA	Analysis of covariance
ANOVA	Analysis of variance
AP	Action potential
AP1	Activator protein-1
ARC	Arcuate nucleus of the hypothalamus
ATP	Adenosine 5'-triphosphate
AUC	Area under the curve
AV	Atrioventricular
AVNERP	AV nodal effective refractory period
AVRT	Atrioventricular re-entrant tachycardia
A^y	*Agouti lethal yellow*
BAT	Brown adipose tissue
BCA	Bicinchoninic acid
BBB	Bundle branch block
BD	*Bis die* (Latin, twice a day)
BE	Branching enzyme
BSA	Bovine serum albumin
BSX	Brain-specific homeobox factor

BW	Body weight
CA	Constitutively active
CaMKKβ	Ca^{2+}/calmodulin-dependent protein kinase kinase-β
CART	Cocaine- and amphetamine-regulated transcript
CBS	Cystathionine β–synthase
CC	Corpus Callosum
CCD	Charge-coupled device
CCPA	2-chloro-N^6-cyclopentyladenosine
CCX	Cerebral cortex
cDNA	Complementary deoxyribonucleic acid
Cacna1g	Calcium channel, voltage-dependent, T type, alpha 1G subunit
CaM	Calmodulin
CNTF	Ciliary neurotrophic factor
Cntn2	Contactin-2
CO	Cardiac output
CPT1	Carnitine palmitoyltransferase 1
CREB	cAMP response element-binding protein
CSA	Cross-sectional area
cSNRT	Corrected sinus node recovery time
CSQ	Calsequestrin
CT	Crista terminalis
DBE	Debranching enzyme
DEPC	Diethyl pyrocarbonate
DEXA	Dual-energy x-ray absorptiometry
DIG	Digoxigenin
DMH	Dorsomedial nucleus of the hypothalamus
DMSO	Dimethyl sulfoxide
DN	Dominant negative
dNTPs	Deoxynucleotide triphosphates
DTA	Diphtheria toxin gene
ECL	Enhanced chemiluminescence
ECG	Electrocardiogram
EDA	End-diastolic area
EDTA	Ethylenediaminetetraacetic acid
EDV	End-diastolic volume

EE	Energy expenditure
EF	Ejection fraction
EGTA	Ethylene glycol tetraacetic acid
ELISA	Enzyme-linked immunosorbent assay
ENDO A	Endocardial area
EP	Electrophysiological
EPS	Electrophysiology study
EPSC	Excitatory post-synaptic current
EPI A	Epicardial area
ER	Endoplasmic reticulum
ES cells	Embryonic stem cells
ESA	End-systolic area
ESV	End-systolic volume
FBS	Fetal bovine serum
FC	Fold-change
FI	Food intake
f_{mEPSC}	Miniature excitatory post-synaptic current frequency
FoxO	Forkhead box subfamily O
FRT	Flp recombinase recognition target
FS	Fractional shortening
G6P	Glucose-6-phosphate
GABA	γ-aminobutyric acid
GAP	GTPase-Activating Proteins
GBD	Glycogen-binding domain
Gbe1	Glucan (1,4-α-), branching enzyme 1
gDNA	Genomic DNA
GFP	Green fluorescent protein
GHSR	Growth hormone secretagogue receptor
GLUT4	Glucose transporter 4
GP	Glycogen phosphorylase
GS	Glycogen synthase
GSD	Glycogen storage disorder
GSIS	Glucose-stimulated insulin secretion
GTP	Guanosine triphosphate
HBSS	Hank's Balanced Salt Solution

HCM	Hypertrophic cardiomyopathy
HCN	Hyperpolarisation-activated, cyclic nucleotide-gated channel proteins
H&E	Haematoxylin and eosin
HEPES	Hydroxyethyl piperazineethanesulfonic acid
HEK	Human Embryonic Kidney
HFD	High fat diet
HMG-CoA	3-hydroxy-3-methylglutaryl-CoA
HR	Heart rate
HW	Heart weight
IAS	Interatrial septum
ICV	Intracerebroventricular
IGF-1	Insulin-like growth factor 1
IL6	Interleukin 6
i.p.	Intraperitoneal
IP	Immunoprecipitation
IP3	Inositol-1,4,5-trisphosphate
IRES	Internal ribosomal entry site sequence
IRS	Insulin receptor substrate
ISH	*In situ* hybridisation
IV	Intravenous
IVC	Individually ventilated cage
KI	Knock-in
KO	Knock-out
LAMP2	Lysosome-associated membrane protein-2
LEPR	Leptin receptor
LHA	Lateral hypothalamic area
LKB1	Liver kinase B1
loxP	Locus of crossover [x] in P1
LV	Left ventricle
LVESD	LV end-systolic dimension
LVEDD	LV end-diastolic dimension
LVSP	LV systolic pressure
LVH	Left ventricular hypertrophy
MAP	Mean arterial pressure
MC-R	Melanocortin receptor

MCS	Multiple cloning site
MCD	Malonyl-CoA decarboxylase
MDP	Maximum diastolic potential
ME	Median eminence
MEF2	Myocyte enhancer factor-2
mEPSC	Miniature excitatory post-synaptic current
MIAME	Minimal Information About a Microarray Experiment
MMP	Mitochondrial membrane potential
MRI	Magnetic resonance imaging
mRNA	Messenger ribonucleic acid
MRS	Magnetic resonance spectroscopy
MT-II	Melanotan II
mTORC1	Mammalian TOR complex 1
Myh7	β-myosin heavy chain
N-terminus	Amino-terminus
NADH	Nicotinamide adenine dinucleotide
$NADP^+$	Nicotinamide adenine dinucleotide phosphate
NADPH	Reduced form of $NADP^+$
NBF	Neutral buffered formalin
NBT/BCIP	Nitro blue tetrazolium chloride/5-bromo-4-chloro-3-indolyl-phosphate
NFAT	Calcineurin-nuclear factor of activated T cells
Nppa	Natriuretic peptide A
Nppb	Natriuretic peptide B
NPY	Neuropeptide Y
NRCM	Neonatal rat cardiomyocyte
Nrf1	Nuclear respiratory factor 1
NTC	No template control
NTS	Nucleus tractus solitarius
OC	Optic Chiasm
OCT	Optimal cutting temperature compound
OGTT	Oral glucose tolerance test
PAS	Periodic acid-Schiff
PBS	Phosphate-buffered saline
PCA	Principle components analysis
PCR	Polymerase chain reaction

PEPCK	Phosphoenolpyruvate carboxykinase
PF	Pair-feeding
PGC-1α	Peroxisome proliferator-activated receptor γ co-activator 1α
PI(3)K	Phosphatidylinositol-3-OH kinase
PIR	Passive infra-red
POMC	Proopiomelanocortin
PP1	Type 1 protein phosphatase
PP2A	Protein phosphatase-2A
PPM	Permanent pacemaker
PPP	Phosphoprotein phosphatase
PVH	Paraventricular hypothalamic nucleus
qRT-PCR	Quantitative, real-time reverse-transcriptase PCR
PVH	Paraventricular nucleus of the hypothalamus
RA	Right atrium
RNA	Ribonucleic acid
RBBB	Right bundle branch block
RIPA buffer	Radioimmunoprecipitation assay buffer
RN	Rendement Napole
ROS	Reactive oxygen species
RT	Room temperature
RV	Right ventricular
SAN	Sinoatrial node
SCL	Sinus cycle length
SD	Standard deviation
SDS	Sodium dodecyl sulphate
SEM	Standard error of the mean
siRNA	Small interfering ribonucleic acid
shRNA	Short hairpin ribonucleic acid
SERCA2	Sarcoendoplasmic reticulum Ca^{2+} ATPase
SEM	Standard error of the mean
SGLT-1	Sodium-dependent glucose transporter
Slc2a4	Solute carrier family 2 (facilitated glucose transporter)
Snf1	Sucrose non-fermenting
SnRK1	Snf1-related protein kinase 1
SNRT	Sinus node recovery time

SOCS-3	Suppressor of cytokine signalling 3
Sox2	SRY (sex determining region Y)-box 2
SSC	Saline-sodium citrate
STAT3	Signal transducer and activator of transcription 3
STRAD	STE-20 related adaptor protein
SV	Stroke volume
SVC	Superior vena cava
TAK1	TGF-β-activated kinase-1
TEM	Transmission electron microscopy
TBC1D4	TBC1 domain family member 4
TBE	Tris/Borate/ Ethylenediaminetetraacetic acid buffer
TBST	Tris-Buffered Saline with Tween-20
TG	Transgenic
TL	Tibial length
T_m	Melting temperature
TNFα	Tumour necrosis factor-α
TORC2	Transducer of regulated CREB activity 2
tPAI-1	Tissue plasminogen activator inhibitor-1
TRAIL	Tumour necrosis factor related apoptosis inducing ligand
TSC2	Tuberous sclerosis protein 2
UCP	Uncoupling protein
UDPG-PPL	UDP-glucose pyrophosphorylase
VA	Ventriculoatrial
VMH	Ventromedial nucleus of the hypothalamus
VT	Ventricular tachycardia
WAT	White adipose tissue
WPW	Wolff-Parkinson White
WT	Wild-type
ZT	Zeitgeber time

Contents

ABSTRACT

Acknowledgements ..... **i**

Declaration of own work and attribution ..... **ii**

Abbreviations and Acronyms ..... **iii**

CHAPTER 1. INTRODUCTION

1.1 From adenylate charge hypothesis to AMPK **1**

1.2 AMPK's role in non-mammalian orthologues and its ancestral origins **4**

1.3 AMPK structure and subunit composition **5**

1.3.1 α subunit structure 6

1.3.2 β subunit structure 6

1.3.3 γ subunit structure 7

1.4 AMPK subunit isoforms and tissue distribution **8**

1.4.1 α subunit isoforms 8

1.4.2 β subunit isoforms 9

1.4.3 γ subunit isoforms 10

1.4.3.a PRKAG2 transcript variants *10*

1.4.3.b γ isoforms: contribution to differences in AMPK activity and distribution *12*

1.5 Regulation of mammalian AMPK **13**

1.5.1 AMPK activation by upstream kinases 14

1.5.2 Principal mechanisms of AMPK activation by adenine nucleotides 15

1.5.3 Direct allosteric activation by AMP 16

1.5.4 Protection against dephosphorylation and the emergent role of ADP 16

1.5.5 Regulation of AMPK by glycogen 19

1.5.5.a Glycogen structure and function 19

1.5.5.b Links between AMPK and glycogen metabolism 20

1.5.6 Regulation of AMPK by protein phosphatases 23

1.6 Naturally occurring mutations in the regulatory γ subunit of AMPK cause disease... 24

1.6.1 *PRKAG3* and the RN^- mutation in pig 24

1.6.2 Mutations in the γ2 subunit gene (*PRKAG2)* cause human cardiomyopathy 25

1.6.2.a Hypertrophic cardiomyopathy (HCM) and the energy deficiency hypothesis 25

1.6.2.b PRKAG2 as a causative gene for the Wolff-Parkinson-White syndrome 27

1.6.2.c Clinical features of PRKAG2 cardiomyopathy 27

1.6.3 Existing transgenic models of PRKAG2 cardiomyopathy 32

1.6.3.a Insights provided by transgenic models into pathogenesis of pre-excitation 33

1.6.3.b PRKAG2 cardiomyopathy: a novel glycogen storage disorder? 34

1.6.4 Effect of PRKAG2 mutations on AMPK activity 38

1.7 Why another model of PRKAG2 disease? 42

1.7.1 Unanswered questions 42

1.7.2 Transgenesis 43

1.7.3 Limitations of existing transgenic models of PRKAG2 cardiomyopathy 44

1.7.3.a Failure to reflect native γ2 splicing and temporal expression patterns 44

1.7.3.b Overexpression of mutant or WT γ2 disturbs normal γ isoform stoichiometry 45

1.7.3.c Consequences of overexpression of the γ subunit 45

1.7.4 Gene-targeting 47

1.7.5 Novel gene-targeted model of PRKAG2 disease: R299Q γ2 knock-in 50

1.8 Hypothesis and aims 51

1.8.1 Hypothesis 51

1.8.2 Thesis aims 52

CHAPTER 2. MATERIALS & METHODS

2.1 Animal care, genotyping and general tissue extraction 53

2.1.1 General husbandry 53

2.1.2 Mice 53

2.1.2.a R299Q γ2 knock-in (KI) mice 53

2.1.2.b C57BL/6 54

2.1.2.c Sox2cre 54

2.1.3 Genotyping 54

2.1.3.a DNA extraction 54

2.1.3.b Polymerase chain reaction (PCR) for R299Q γ2 knock-in genotyping 54

2.1.4 Tissue extraction 55

2.1.4.a Cardiac experiments 55

2.1.4.b Systemic experiments 56

2.2 RNA work 56

2.2.1.a RNA extraction 56

2.2.1.b cDNA synthesis and real-time reverse transcription PCR 57

2.2.1.c Allelic discrimination for detection of R299Q mutant Prkag2 transcript 58

2.3 Protein work 59

2.3.1.a SAMS peptide phosphorylation assay for determination of AMPK activity 59

2.3.1.b General protein extraction and quantification 62

2.3.1.c Western blotting and analysis 62

2.4 Histology and microscopy 63

2.4.1 General fixation/sectioning 63

2.4.2 Staining - H&E, PAS and Picro-Sirius red 64

2.4.3 White adipose tissue (WAT) histology and analysis 64

2.4.4 Transcardial perfusion fixation and staining with Cresyl violet for assessment of basic neuronal structure 65

2.4.5 Transmission electron microscopy (TEM) 66

2.4.5.a Cardiac TEM (at age 2 months) *66*

2.4.5.b Cardiac & skeletal muscle TEM (at age 12 months) *66*

2.5 *Ex vivo* (Langendorff) cardiac perfusion 67

2.6 Transthoracic echocardiography 69

2.7 Cardiac electrophysiology 70

2.7.1 Electrocardiography 70

2.8 Cellular work 71

2.8.1 *Prkag2* vectors 71

2.8.2 Maintenance and transfection of HL-1 cells 72

2.8.3 Isolation and maintenance of neonatal rat cardiomyocytes 73

2.8.4 Hcn4-Luciferase gene reporter assay in neonatal rat cardiomyocytes 74

2.9 Gross systemic metabolic and exercise phenotyping 75

2.10 Central mechanistic experiments 76

2.11 Data analysis and statistics 76

CHAPTER 3. VALIDATION, CARDIAC STRUCTURE & FUNCTION OF R299Q γ2 KI

3.1 Aims and objectives 77

3.2 Chapter-specific materials and methods 78

3.2.1 Biochemical quantification of glycogen 78

3.2.2 *In vivo* cine-magnetic resonance imaging (cine-MRI) 79

3.2.3 *In vivo* left ventricular haemodynamics 80

3.3 Results 81

3.3.1 Validation of the R299Q γ2 knock-in 81

3.3.1.a PCR-based genotyping 81

3.3.1.b Mutant cardiac transcript expression identified by allelic discrimination 82

3.3.1.c Relative mRNA expression levels of AMPK γ subunits in the heart 82

3.3.1.d Assessment of cardiac γ2 and γ1 protein expression by Western blotting 83

3.3.1.e Effect of the R299Q γ2 mutation on AMPK activity 84

3.3.2 Cardiac structure and function 86

3.3.2.a Cardiac histological and transmission electron microscopy appearances 86

3.3.2.b Biochemical quantification of myocardial glycogen content 91

3.3.2.c Cardiac function and dimensions by echocardiography at 2 months 92

3.3.2.d Cardiac function by cine-MRI at 2 months and 10 months 93

3.3.2.e Invasive haemodynamics and contractile reserve assessment at 12 months 96

3.3.2.f Ex vivo cardiac indices on a C57BL/6 genetic background 99

3.3.2.g Expression of cardiac stress markers 101

3.4 Discussion 102

3.4.1 Summary of principal chapter findings 102

3.4.2 Insights gained into the effect of γ2 mutations on AMPK activity 103

3.4.3 Cardiomyopathy in the absence of gross glycogen accumulation 105

3.4.4 Genetic background and modifier genes 107

CHAPTER 4. ELECTROPHYSIOLOGICAL PHENOTYPE & DISEASE MECHANISMS

4.1 Aims and objectives 110

4.2 Chapter-specific materials and methods 111

4.2.1 Intrinsic heart rate 111

4.2.2 ECG telemetry 111

4.2.3 Invasive electrophysiology study (EPS) 111

4.2.4 Microarray study and data analysis 113

4.2.5 Sino-atrial node and cardiac regional dissection for qRT-PCR 115

4.2.6 Sinus node electrophysiology and I_f recordings 115

4.2.7 Heterologous expression in HEK293 cells and I_f recordings 116

4.3 Results 118

4.3.1 R299Q γ2 knock-in electrophysiology 118

4.3.1.a Surface ECG recordings and telemetry 118

4.3.1.b Invasive electrophysiology study 120

4.3.1.c Intrinsic heart rate 122

4.3.2 Whole-genome gene expression profiling 122

4.3.2.a Approach & experimental design 122

4.3.2.b Primary dataset exploration 123

4.3.2.c Microarray results 124

4.3.2.d Validation by qRT-PCR 124

4.3.2.e Microarray data interpretation and follow-up 126

4.3.3 Sinoatrial node cellular electrophysiology 127

4.3.3.a Spontaneous rate & maximum diastolic potential 127

4.3.3.b I_f density & voltage-dependence of current activation 129

4.3.3.c Heterologous transfection experiments 129

4.3.4 Initial exploration of mechanisms underlying altered *Hcn* expression 131

4.4 Discussion 133

4.4.1 Summary of principal chapter findings 133

4.4.2 Electrophysiological disturbance – moving beyond glycogen 134

4.4.2.a Sinus bradycardia of Prkag2 cardiomyopathy – an HCN'opathy? 134

4.4.2.b Pathway linking AMPK γ2 and altered I_f 137

4.4.2.c Is the phenotype of R299Q γ2 KI mice developmental in origin? 139

4.4.2.d Other potential mechanistic players in the PRKAG2 mutant EP phenotype: CNTN2 139

4.4.3 Potential correlates for other phenotypic manifestations 140

CHAPTER 5. EXPLORING THE PHYSIOLOGICAL ROLE OF γ2 IN HEART RATE REGULATION

5.1 Aims and objectives..... 143

5.2 Chapter-specific materials and methods..... 144

5.2.1 Sox2cre mice..... 144

5.2.2 Sox2cre transgene PCR..... 144

5.2.3 gDNA sequencing for detection of *Prkag2* exon 7 deletion 145

5.2.4 PCRs for specific detection of intact or excised *Prkag2* exon 7 from gDNA..... 146

5.2.5 End-point PCR for detection of exon 7 excision from cDNA..... 146

5.3 Results 148

5.3.1 Cardiac regional expression of *Prkag2* 148

5.3.2 Generation of a Sox2cre-driven γ2 KO..... 149

5.3.3 Genotyping of Sox2cre γ2 KO 150

5.3.4 Validation of Sox2cre γ2 KO – RNA level..... 153

5.3.5 Validation of Sox2cre γ2 KO – protein level 155

5.3.6 Validation of Sox2cre γ2 KO – functional level 156

5.3.7 Baseline structure and function..... 158

5.3.8 Baseline EP phenotype..... 159

5.3.9 *Hcn* expression profile 160

5.3.10 Silencing of *Prkag* isoform gene expression in HL-1 cells..... 161

5.4 Discussion..... 163

5.4.1 Summary of principal chapter findings 163

5.4.2 *Sox2cre*-driven excision of *Prkag2* exon 7: adequate approach to KO γ2? 164

5.4.3 EP phenotype of the γ2 KO and γ2 as a novel conserver of cardiac energy 166

5.4.4 Limitations 167

5.4.5 Future cardiac work involving the Sox2cre γ2 KO model 168

CHAPTER 6. THE SYSTEMIC PHENOTYPE & UNDERLYING PERIPHERAL MECHANISMS

6.1 Aims and objectives 170

6.2 AMPK and the regulation of whole-body energy balance 171

6.2.1 AMPK as a mediator of systemic energy balance 171

6.2.2 Effects of AMPK on peripheral metabolism 172

6.2.2.a Regulation of glucose homeostasis – hepatic gluconeogenesis 172

6.2.2.b Regulation of glucose homeostasis – glucose uptake 173

6.2.2.c Role of AMPK in the hormonal regulation of peripheral metabolism 174

6.2.3 Animal models investigating the role of AMPK in energy homeostasis 176

6.3 Chapter-specific materials and methods 178

6.3.1 Body weight growth curves 178

6.3.2 Plasma chemistry 178

6.3.3 Body composition 178

6.3.3.a Quantitative magnetic resonance (MR) relaxometry 178

6.3.3.b Dual-energy x-ray absorptiometry (DEXA) 178

6.3.4 Glucose handling 179

6.3.4.a Oral glucose tolerance test (OGTT) 179

6.3.4.b Insulin sensitivity test 179

6.3.4.c Pancreatic insulin content 179

6.3.5 Spontaneous activity assessment by infra-red beam breaks 179

6.3.6 Voluntary running assessment and data analysis 180

6.3.7 Energy expenditure 181

6.3.8 Pancreatic islet β-cell isolation, culture and electrophysiology 181

6.4 Results 182

6.4.1 Appearance, body weight and food intake 182

6.4.2 Body composition 183

6.4.3 White adipose tissue (WAT) appearances and gene expression 184

6.4.4 Plasma adipocytokine profile 185

6.4.5 Glucose homeostasis 187

6.4.5.a Glucose tolerance 187

6.4.5.b Whole-body insulin sensitivity and β-cell glucose sensing 188

6.4.6 Activity assessment 189

6.4.6.a Spontaneous activity 189

6.4.6.b Spontaneous exercise performance 190

6.4.6.c Quadriceps gene expression profile 192

6.4.7 Energy expenditure 193

6.4.7.a Indirect calorimetry in young adult mice 193

6.4.7.b Thermic capacity and brown adipose tissue gene expression profile 194

6.4.7.c Energy expenditure in older mice 195

6.5 Discussion 197

6.5.1 Summary of principal chapter findings 197

6.5.2 Why investigate the systemic phenotype of the R299Q γ2 KI model? 199

6.5.3 The complex systemic phenotype of the R299Q γ2 KI 199

6.5.3.a Early phenotype 200

6.5.3.b Late phenotype 201

CHAPTER 7. THE SYSTEMIC PHENOTYPE OF THE R299Q γ2 KI: CENTRAL MECHANISMS

7.1 Aims and objectives 204

7.2 The hypothalamus and the regulation of appetite 205

7.2.1 Overview of hypothalamic regulation of appetite 205

7.2.2 The arcuate nucleus – a primary locus for hypothalamic integration of peripheral metabolic signals influencing appetite 207

7.2.3 Neuropeptide Y (NPY) and its regulation by leptin and ghrelin 208

7.2.4 Agouti-related peptide (AgRP) and the melanocortinergic system 210

7.3 Hypothalamic AMPK - an integrator of peripheral hormonal and nutrient signals of energy status 213

7.3.1 Modulation of hypothalamic AMPK activity affects food intake 213

7.3.2 Hypothalamic AMPK and the response to leptin 214

7.3.3 Modulation of hypothalamic lipid metabolism by AMPK regulates feeding 216

7.3.4 Ghrelin stimulates appetite via a mechanism involving AMPK and UCP2 217

7.3.5 AMPK-dependent regulation of synaptic plasticity onto AgRP neurons 221

7.4 Chapter-specific materials and methods 224

7.4.1 Pair-feeding (PF) 224

7.4.2 Hypothalamus dissection 224

7.4.3 *In situ* hybridisation (ISH) 224

7.4.4 Drug sensitivity challenges 225

7.4.4.a Leptin sensitivity 225

7.4.4.b Melanocortin agonist 226

7.4.4.c Ghrelin sensitivity *226*

7.4.5 Fast-refeeding 226

7.4.6 Active (acylated) ghrelin levels 226

7.4.7 Ghrelin receptor antagonism 227

7.4.7.a Acute ghrelin receptor antagonism *227*

7.4.7.b Chronic ghrelin receptor antagonism - hyperphagic rescue *227*

7.5 Results 228

7.5.1 Pair-feeding 228

7.5.2 Neuropeptide signalling profile 228

7.5.3 Gross neuroanatomy and hypothalamic γ2 expression 229

7.5.4 Leptin sensitivity 231

7.5.5 Response to melanocortinergic activation 232

7.5.6 Fast-refeeding and the response to ghrelin 233

7.5.7 Investigation of basal levels of central ghrelin signalling 236

7.5.8 Hyperphagic rescue 238

7.6 Discussion 240

7.6.1 Summary of principal chapter findings 240

7.6.2 Hyperphagia - the main driver of weight gain in R299Q γ2 homozygous mutants ... 241

7.6.3 The effect of the R299Q γ2 mutation on hypothalamic pathways regulating food intake and body weight 241

7.6.3.a Hypothalamic leptin signalling *242*

7.6.3.b Melanocortin receptor signalling *242*

7.6.3.c Hypothalamic ghrelin signalling pathway *243*

CHAPTER 8. CONCLUSIONS

8.1 Major results and significance of research 248

8.1.1 Principal cardiac findings and insights provided by the R299Q γ2 KI 248

8.1.2 Principal systemic findings and insights provided by the R299Q γ2 KI..... 251

8.2 Future directions 254

REFERENCES

APPENDICES

Chapter 1. Introduction

1.1 From adenylate charge hypothesis to AMPK

The survival of all living organisms ultimately depends on the ability to maintain an adequate supply of energy in the form of adenosine 5'-triphosphate (ATP) to drive cellular processes through hydrolysis of one or other of its phosphoanhydride bonds, yielding adenosine 5'-diphosphate (ADP) or adenosine 5'-monophosphate (AMP). Key to this is the ability of the cell to respond to highly dynamic changes in its energy status, such that the supply of energy (through catabolism of metabolic substrates) continually matches metabolic demand (by anabolic processes). Such a system is dependent upon an acute ability to sense immediate energy availability and, for more complex multicellular organisms, intermediate and longer-term nutrient stores.

Whilst the evolutionary origins of this fundamental energy sensor system are likely to be very ancient, the components of this have only been deciphered in the last 50 years. In 1966, Sir Hans Krebs highlighted the importance of adenine 5'-nucleotides in regulating the activity of phosphofructokinase and fructose-1,6-bisphosphatase, enzymes involved in the energy-yielding (glycolysis) and energy-consuming (gluconeogenesis) processes of hepatic carbohydrate metabolism, respectively, noting that: "*The concentration of AMP is a particularly apt 'signal' … because it is directly linked to the energy status of the cell, i.e. the concentration of ATP*"[1]. Daniel Atkinson broadened this concept by proposing that the balance between concentrations of adenine nucleotides regulated metabolite partitioning at key metabolic nodes into catabolic or anabolic pathways in response to the cell's changing metabolic requirements[2, 3]. His adenylate 'energy charge hypothesis' thus critically coupled the energy state of a cell to its metabolic control.

According to this hypothesis, the ratio signalling energetic surfeit or depletion could be either ADP:ATP or AMP:ATP. In his 1963 Croonian Lecture to the Royal Society[4], Krebs highlighted that the percentage change in AMP in tissues was much greater than that for ADP or ATP or ADP:ATP by virtue of the cytosolic adenylate kinase reaction (2ADP $\leftrightarrow$ ATP+AMP) which

operates at high levels in all eukaryotic cells to maintain interconversion of adenine nucleotides close to equilibrium such that:

$$\frac{[ATP][AMP]}{[ADP]^2} = K$$

Where *K* is the equilibrium constant. Rearranging this yields:

$$\frac{[AMP]}{[ATP]} \propto \left\{\frac{[ADP]}{[ATP]}\right\}^2$$

The corollary of this is that a rise in the cellular ADP:ATP ratio, indicative of cellular energetic stress, will shift the adenylate kinase reaction in favour of ATP and AMP production, which in turn causes the AMP:ATP ratio to vary as *the square* of the ADP:ATP ratio[5]. Hence, despite having basal concentrations many orders of magnitude lower than ADP and ATP, during times of energetic stress *in vivo*, the marked rise in AMP relative to ATP (Figure 1) can potentially allow the AMP:ATP ratio to serve as a highly sensitive signal of energy depletion.

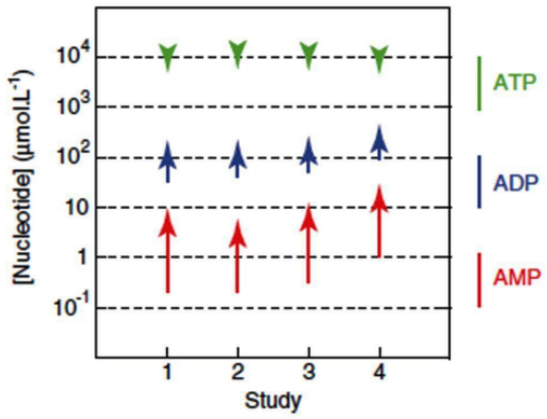


Figure 1. Estimates for changes in nucleotide levels with metabolic stress from studies investigating exercising human skeletal muscle (1-3) or isolated, perfused rat heart (4). (Note logarithmic scale).[a]

Formal recognition of the sensor arm of the adenylate energy charge system had to wait until 1987, when Carling, Zammit and Hardie[6] identified a single protein kinase activity from highly purified rat liver which: phosphorylated and inactivated the two key regulatory enzymes of fatty acid and cholesterol synthesis – acetyl-CoA carboxylase and 3-hydroxy-3-methylglutaryl-CoA reductase

[a] Reproduced from box 1 Hardie et al. *Trends Biochem Sci* 2011;36:470-7.

(ACC and HMG-CoA reductase, respectively); was stimulated by micromolar concentrations of AMP; and whose action was markedly reduced with prior treatment of the kinase preparation by protein phosphatase. Their findings unified earlier observations which had described seemingly separate AMP-stimulated/ATP-inhibited kinases for ACC[7, 8] and HMG-CoA reductase[9, 10]. It was soon realised that this kinase specifically regulated targets beyond ACC and HMG-CoA reductase, including hormone sensitive lipase and was named according to its allosteric regulator as AMP-activated protein kinase (AMPK)[11].

In fulfilment of Atkinson's remarkably prescient prediction[3] of an adenylate charge-based system that "*may directly affect nearly all metabolic processes*", AMPK is now recognised to coordinately regulate a diverse range of metabolic pathways. Thus, upon activation by energetic stress, AMPK switches on catabolic ATP-generating processes – both directly (e.g. glucose uptake and glycolysis, fatty acid uptake and β-oxidation) and indirectly, through augmenting oxidative capacity by activating mitochondrial biogenesis – whilst repressing anabolic ATP-consuming processes (e.g. lipid, glycogen, protein and ribosomal biosynthesis), ultimately functioning to restore cellular energy status and preserve cell viability (Figure 2)[12].

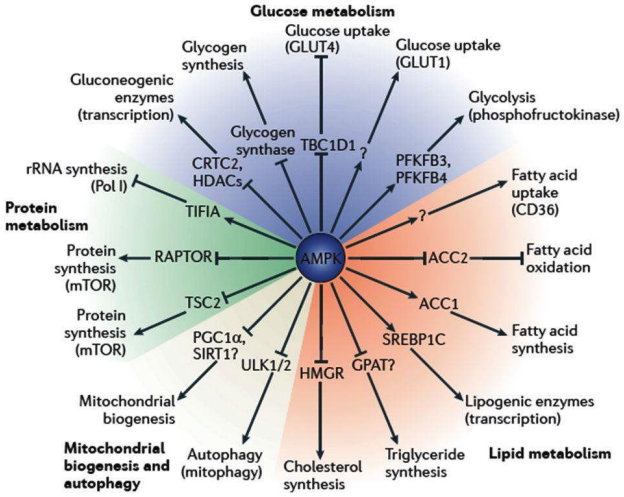


Figure 2. Mammalian AMPK is a central regulator of cellular metabolism.[b]

AMPK plays a central role in coordinating metabolism, both acutely – through direct phosphorylation of metabolic substrate enzymes – and more chronically, by modulating gene expression through phosphorylation of target transcription factors or the recently described association with chromatin and subsequent modification of histone proteins.[13]

[b] Reproduced from figure 4 Hardie et al. *Nat Rev Mol Cell Biol* 2012;13:251-62.

1.2 AMPK's role in non-mammalian orthologues and its ancestral origins

Partial purification and subsequent sequencing of AMPK from rat[14] and porcine liver[15] revealed a striking degree of identity to the catalytic domain of a serine/threonine protein kinase transcriptional regulator found in the unicellular budding yeast *Saccharomyces cerevisiae* and known as Snf1 (sucrose non-fermenting). Snf1 plays a major role in the diauxic shift of the yeast whereby, when deprived of its preferred carbon & energy substrate (glucose), the cells reduce their exponential growth rate and switch their metabolism from anaerobic fermentative (metabolism of glucose by glycolysis releasing ethanol) to aerobic (oxidative utilisation of ethanol produced during fermentation to generate ATP)[16]. The key role of Snf1 in this adaptive metabolic stress response is demonstrated by the fact that Snf1 mutants fail to grow under conditions of low/absent glucose or in the presence of non-fermentable carbon sources such as sucrose. Snf1's coordination of the response to glucose starvation appears to be largely mediated by altered gene expression, with over 400 genes of the yeast genome (out of more than 2000 genes modified in all) dependent on Snf1 for altered expression, both through regulation of transcription factors and induction of chromatic remodeling[17]. In addition to its role in the adaptation of the yeast to glucose limitation, Snf1 also affects developmental processes (e.g. meiosis, sporulation and filamentous growth) and longevity[18].

In plants, the closest homologue to mammalian AMPK and yeast Snf1 kinase is Snf1-related protein kinase 1 (SnRK1). Strikingly, loss of SnRK1 in the moss *Physcomitrella patens* leads to an inability to grow in low light or normal day-night cycles (which is partially restored by provision of exogenous carbon in the form of glucose)[19]. The plant AMPK orthologue therefore permits it to adapt to darkness, in effect a form of 'starvation' for the plant[20].

In the nematode worm *Caenorhabditis elegans*, the AMPK orthologue (AAK) couples information about energy levels to lifespan and is required for survival of dauer larvae, a dormant stage entered in response to harsh environmental conditions. Larvae deficient in AAK enter dauer normally, but fail to appropriately downregulate triglyceride hydrolysis, such that they rapidly consume their lipid energy stores and die prematurely[21].

Taken together, this data suggests a highly conserved role for eukaryotic AMPK in coordinating the response to starvation for a carbon source[20]. Orthologues of mammalian AMPK are now known to exist in virtually all eukaryotes for which genome sequences have been completed[22]. All exist as heterotrimeric complexes comprising catalytic (α) and regulatory (β and γ) subunits in a 1α:1β:1γ ratio, suggesting a common ancestral source before divergence of animals, plants and fungi over 1.5 billion years ago[17].

1.3 AMPK structure and subunit composition

Mammalian AMPK consists of three subunits and exists in crystal and solution as a monomer[23] (Figure 3). It is encoded for by seven genes, with two isoforms of α and β (α1, α2; β1, β2) and three isoforms of γ (γ1, γ2, γ3), allowing 12 different heterotrimeric combinations. In addition to varying tissue and subcellular expression, several of the genes also undergo alternative splicing, adding further complexity to the system[24]. Mammalian α and β subunit isoforms are very similar in structure, whereas the γ subunit isoforms differ significantly in their N-terminal domains. Co-expression of all three subunits is required for maximal kinase activity[25].

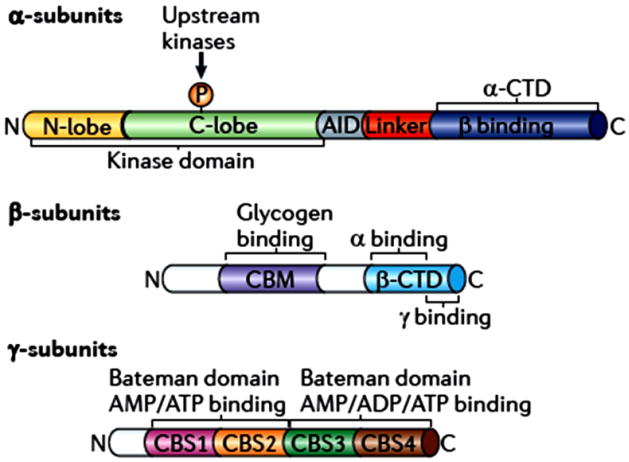


Figure 3. Domain organisation of mammalian AMPK subunits.[c]

Whilst elucidation of the full-length architecture of an AMPK αβγ heterotrimer has remained elusive, characterisation of a number of protein crystal structures from both mammalian AMPK[23, 26] and yeast homologues[27, 28] has provided significant insights into the core of the complex, with the

[c] Reproduced from figure 2 Hardie et al. *Nat Rev Mol Cell Biol* 2012;13:251-62.

most complete structure solved to date[26] – containing the AMPK regulatory core fragment (C-terminal domain of the β subunit and entire γ subunit) and N-terminally complete α subunit – shedding significant light on the nature of AMPK's regulation by adenine nucleotides[29].

1.3.1 α subunit structure

The α subunit contains a conventional serine/threonine protein kinase domain immediately followed by an autoinhibitory domain (AID) at its amino-terminus (N-terminus)[12]. Within the activation loop of the kinase domain is a highly conserved sequence containing a threonine residue (Thr172 in rat α1/α2) whose phosphorylation is an absolute requirement for AMPK activity[30]. In all species, upon phosphorylation of α-Thr172 by upstream kinases, AMPK's catalytic activity is increased over 100-fold[31]. The catalytic and carboxy-terminal (C-terminal) domains of the α subunit are connected via a long linker peptide which wraps around the γ subunit and includes a specific structure termed the 'α hook'. This is well-conserved throughout vertebrates[26, 32] and which, by interacting with a nucleotide-binding region within the γ subunit (termed site 3, section 1.3.3), has been proposed to play a key role in the protection of AMPK against dephosphorylation.

1.3.2 β subunit structure

The β subunit forms the core of the enzyme complex, acting as a scaffold to anchor the C-terminal domain of the α subunit and N-terminal region of the γ subunit together through a C-terminal αγ binding sequence[22, 29]. In addition, the β subunit also contains a mid-molecule functional glycogen-binding domain (GBD), also termed a carbohydrate-binding module, whose sequence is conserved and closely related to isoamylase domains found in glycogen and starch branching enzymes[33]. Whilst the GBD is not required to form heterotrimeric αβγ complexes[34], cell-based studies indicate its requirement for AMPK targeting to glycogen[33, 34]. Accordingly, its role *in vivo* has been suggested[22] to be in permitting close juxtaposition of AMPK to downstream targets bound to glycogen, such as glycogen synthase. Mammalian β subunits also undergo N-terminal myristoylation, a co- or post-translational modification involving the covalent addition of myristic acid (a 14 carbon lipophilic group) to an N-terminal glycine[24, 35]. These groups typically function as lipid anchors, facilitating interaction with membranes. Whilst an irreversible modification, they

permit dynamic association-disassociation with membranes via a 'myristoyl switch', whereby ligands or phosphorylation induce conformational changes in the molecule leading to exposure of a previously sequestered myristoyl group to the cytosol, or flipping of the group inside the protein to cause dissociation from the membrane[24, 35]. Speculatively, this process could permit AMPK to localise with membrane-associated substrates, such as ACC, endothelial NO synthase and HMG-CoA reductase[36]. The potential importance of this modification in the regulation of AMPK and its spatial distribution was highlighted by a recent study[36] reporting direct promotion of α-Thr172 phosphorylation by AMP – a previously controversial mechanism of AMPK-activation – but only in the presence of β subunit myristoylation. Whilst the structural basis for this is unclear, its potential physiological relevance is highlighted by the finding that metabolic stress (AMP or glucose deprivation) promotes membrane-association of myristoylated AMPK[36].

1.3.3 γ subunit structure

The γ subunit adopts a flattened ellipsoid shape[23] and contains the regulatory adenine nucleotide binding sites[37]. All γ subunits contain four conserved sequence motifs of approximately 60 amino acids each, which were first described in cystathionine β–synthase (CBS)[38]. These are numbered CBS1-4 and occur in the γ subunit and other proteins as tandem repeats known as Bateman domains. The interface between two CBS motifs forming each Bateman domain (i.e. CBS1 + 2 and CBS3 + 4) generates two potential adenyl-binding sites[37]. The significance of the CBS motifs is underlined by the finding that point mutations in their conserved residues give rise to several hereditary diseases in humans – notably including a cardiomyopathy caused by mutations in the gene (*PRKAG2)* encoding γ2 – and that that these mutations disrupt adenyl nucleotide binding[38].

Recent structural studies[23, 26] using γ1 indicate that, of the four potential nucleotide binding sites in AMPK, only three of these bind nucleotide (one molecule between CBS1 + 2 and two between CBS3 + 4). Further, nucleotide binding experiments indicate that only two of these sites readily exchange AMP/ADP/ATP, termed sites 1 and 3 according to their CBS sequence[39], whilst the remaining (site 4) contains an essentially permanently bound AMP that is non-exchangeable with ADP/ATP and may be involved in stabilising the complex[23, 37] (Figure 4).

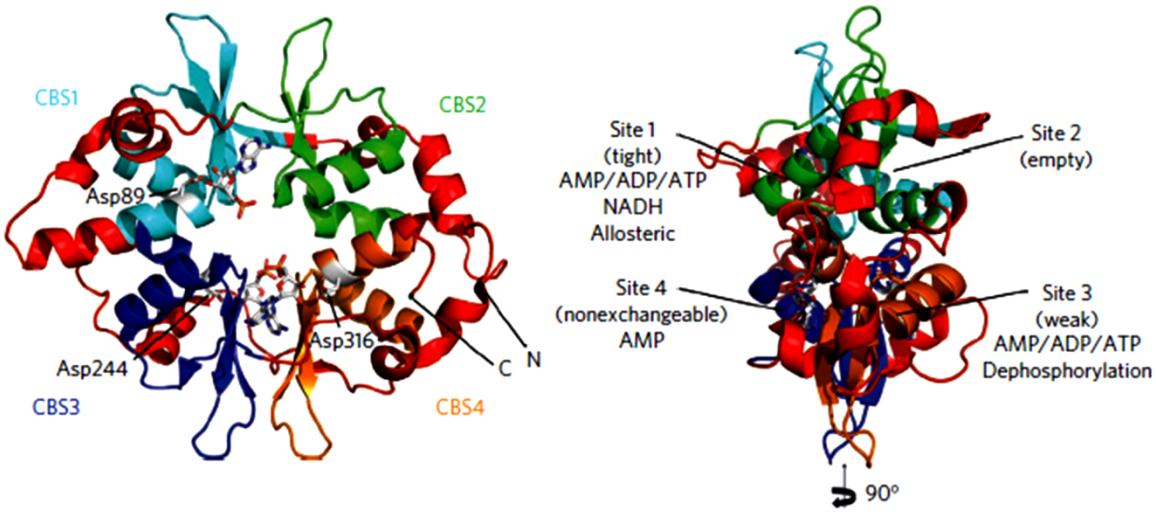


Figure 4. Ribbon representation of AMPK rat γ1 complex illustrating the adenyl binding CBS motifs (each coloured differently) in complex with AMP.[d]

The nucleotide-binding properties and function of the exchangeable binding sites differ. Site 1, or the 'tight binding' site, binds all A(X)Ps with strong affinity (AMP/ADP/ATP/Mg.ATP with dissociation constants, K_d, of 2/1.5/1.7/18 μM, respectively) as well as NADH. Binding of AMP at this region is responsible for its allosteric activation of AMPK (2-5 fold increase in activity).[26] The binding of A(X)Ps at site 3 is 30-fold weaker than site 1. Binding of AMP/ADP at this site favours a heterotrimer conformation which mediates protection against dephosphorylation of α-Thr172 through site 3's interaction with the α hook.[26] Within each site, however, the relative binding affinities of each nucleotide are comparable.

1.4 AMPK subunit isoforms and tissue distribution

In humans, the seven different isoforms of the AMPK subunits (α1, α2; β1, β2; γ1, γ2, γ3) are encoded for by distinct genes across 5 chromosomes and show differential tissue expression patterns suggesting tissue-specific function and/or regulation of the AMPK complex[24, 40, 41].

1.4.1 α subunit isoforms

The human gene loci for the α subunits are located on 5p12 (α1) and 1q31 (α2)[24]. α1 and α2 encode proteins of 548 and 552 amino acids, respectively, which are 90% identical in their N-terminal

[d] Reproduced from figure 2 Carling et al. *Nat Chem Biol* 2012;7:512-518.

catalytic core, but share only 61% identity over the C-terminal domain[42]. By Northern and Western blotting, α1 is seen to be ubiquitously expressed. In contrast, α2 shows preferential expression in skeletal muscle, heart and liver[42]. Within the heart, cardiomyocytes express predominately the α2 isoform, whilst endothelial cells are seen to exclusively express α1[43]. The α2 isoform accounts for ~70% of total cardiac AMPK activity[41]. Both α1 and α2 isoforms are activated by severe metabolic stress *in vivo*, with α2-containing complexes constituting >75% of AMPK activity during regional myocardial ischaemia induced by left coronary artery ligation in the rat[43].

In addition to differences in cell type expression, functional distinctions exist between the two catalytic isoforms in terms of AMP-dependence. Specifically, α2-containing AMPK complexes are stimulated to a significantly greater degree by AMP than α1 complexes[44]. Furthermore, the isoforms exhibit differential subcellular localisation, with both isoforms being present in the cytoplasm, but α2-containing complexes also partially localised to the nucleus[44]. Intriguingly in this regard, an acute exercise bout has been shown to increase nuclear α2 AMPK content in skeletal muscle[45], suggesting that α2-containing complexes translocate to the nucleus to regulate gene expression in response to exercise stress. Indeed, through interaction with transcriptional regulators and/or genes/chromatin directly, AMPK is now recognised to play a prominent role in the adaptive remodeling of skeletal muscle oxidative capacity in response to chronic exercise, influencing the expression/nuclear activity of such substrates as the insulin-sensitive glucose transporter GLUT4, the transcriptional co-activator PGC-1α (peroxisome proliferator-activated receptor γ co-activator 1α) and the FoxO (Forkhead box subfamily O) family of DNA-binding transcription factors[46].

1.4.2 β subunit isoforms

The human β subunit genes are located on 12q24.1 (β1) and 1q21.1 (β2)[24]. The corresponding proteins are 71% identical, with most divergence in their N-termini[47]. Whilst broadly expressed, the isoforms exhibit differential tissue expression patterns[47]. Notably, β1 protein is most highly expressed in liver, with very low-level expression in skeletal muscle, whilst β2 exhibits a reversed pattern of expression. Both isoforms are expressed in heart and brain[47].

1.4.3 γ subunit isoforms

PRKAG1, *PRKAG2* and *PRKAG3* encode the γ1, γ2 and γ3 isoforms of the nucleotide-binding subunit. The human gene loci for the γ subunits are located on 12q12-14 (γ1), 7q35-36 (γ2) and 2q35 (γ3)[24]. In common with the other AMPK subunits, the γ isoforms exhibit different tissue distribution patterns, with γ1 mRNA being ubiquitously expressed, whilst γ3 is observed to be near-specific to skeletal muscle (Figure 5)[41]. γ2 transcript is widely expressed, but particularly in heart, brain, placenta and skeletal muscle[41].

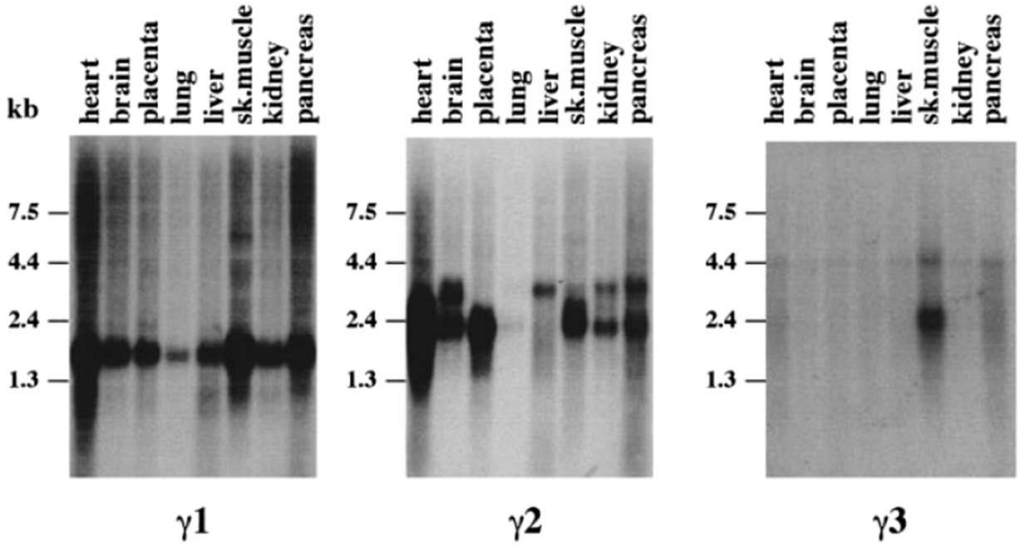


Figure 5. Tissue distribution of γ isoform transcripts identified by Northern blotting.[e]

1.4.3.a PRKAG2 transcript variants

In 2000, separate reports[41, 48] identified distinct human γ2 variants by Northern hybridisation. Originally termed γ2a (or γ2 long) and γ2b (or γ2 short), these are produced by transcription from alternative promoters, giving rise to transcripts of approximately 3.8 kb and 2.4 kb, respectively, with γ2 long composed of γ2 short in addition to a 241 residue N-terminal extension. Both reports noted that γ2 short was abundantly expressed in heart[48], whilst the γ2 long variant was the exclusively expressed transcript in liver[41]. An additional 3.0 kb message observed in one study[48] and proposed to represent another γ2 long band, was also expressed at an extremely high level in heart. Very recently a cardiac-focused investigation[49] using real-time reverse transcription polymerase chain reaction- (qRT-PCR) based analysis in human heart has extended these findings.

[e] Reproduced from figure 5 Cheung et al. *Biochem J* 2000;346:659-669.

This study suggests that γ2 long is a minority variant within the heart and, intriguingly, documents the presence of a novel, intermediate-sized γ2 transcript variant (likely corresponding to the 3.0 kb message above) relatively specific to adult and fetal heart, termed γ2-3B. Together with γ2 short, γ2-3B is proposed to account for the majority of γ2 in the heart[49]. γ2-3B is transcribed from another alternative promoter within intron 3 and possesses a unique alternative starting exon ('3B'), spliced in-frame with exon 4 and therefore identical to γ2 long in sequence beyond this. A further variant annotated in the Ensembl database (http://www.ensembl.org) and termed γ2c in a recent study[50], is expressed at very low levels in human tissues, with its mRNA expression restricted largely to brain in mice[49].

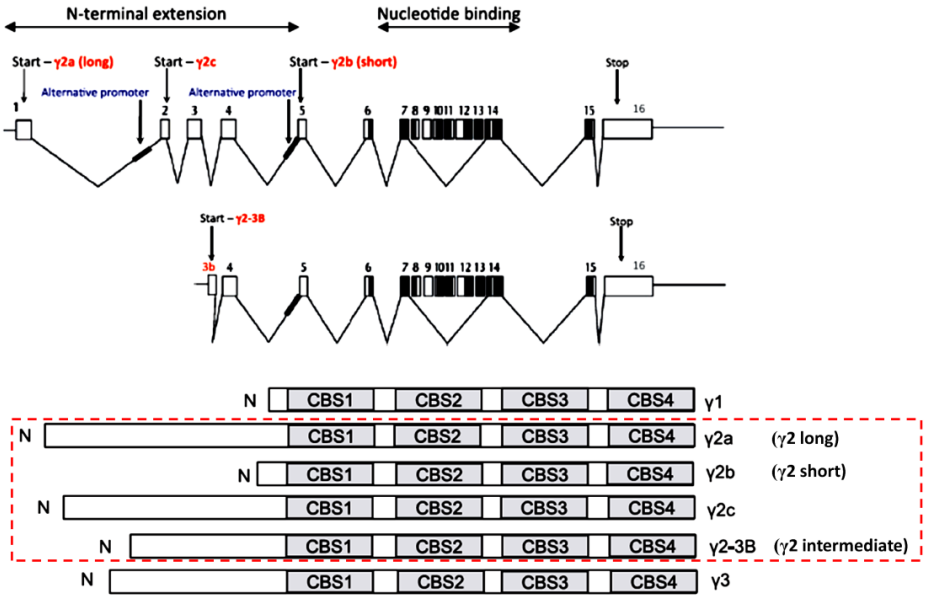


Figure 6. The *PRKAG2* locus and major described splice variants.[f]

A separate report[51] undertaking expression profiling using qRT-PCR of the γ subunits in mouse, rat and human, diverges in several respects from the aforementioned studies. The authors report the highest human γ2 mRNA expression to be in heart (5-fold higher than γ1), whereas the γ2/γ1 expression ratio was much lower in rats (1.3) and mice (1.6). Furthermore, whilst confirming a marked predominance of γ2 long transcript in rodent liver, the study suggests that γ2 long is the predominate isoform in heart[51]. The reasons underlying some of these opposing findings is

[f] Adapted from figure 6 Pinter et al. *J Mol Cell Cardiol* 2012;53:342-349 and figure 1 Kim & Tian *J Mol Cell Cardiol* 2012;53:317-319.

uncertain but, as the authors acknowledged[52], there were discrepancies between their mRNA and corresponding protein findings, with the latter in keeping with a lower abundance of γ2 compared with γ1 in the rodent heart. In total, four transcript variants for γ2 have now been described, with its regulatory complexity suggestive of distinct functional roles for the splice variants (Figure 6)[53].

1.4.3.b γ isoforms: contribution to differences in AMPK activity and distribution

The γ1 isoform polypeptide is the shortest of the three isoforms at 331 amino acids long (molecular mass, MM, 37 kDa), whereas full length γ2 is 569 amino acids (MM 63 kDa) and γ3 is 492 amino acids long (MM 55 kDa). All three γ isoforms share considerable amino acid sequence identity in their C-terminal nucleotide binding regions. γ2 and γ3 both possess long N-terminal extensions absent in γ1, but do not share obvious sequence identity in this terminus with each other[41].

In common with the α subunit, the identity of the γ isoform is also seen to affect AMP-dependence, with γ2-containing complexes exhibiting greater AMP-dependence than γ1 complexes (up to 5-fold activation in the case of α2γ2 complexes), whilst γ3 complexes are only modestly stimulated by AMP (up to 1.5-fold activation)[41]. Notably, no specific preferential association of γ subunit isoforms with the catalytic α subunits has been demonstrated[41].

Early attempts[41] at assessing γ isoform protein expression were hampered by lack of antibody specificity for γ2 and γ3 on Western blotting. Indirect delineation of tissue distribution of AMPK has been performed, however, using immunoprecipitation coupled to a peptide phosphorylation assay[54]. This assay, now regarded as the gold standard for measuring AMPK activity, measures the ability of AMPK to phosphorylate (using [γ-^{32}P]-ATP) a synthetic peptide substrate: either SAMS peptide (HMRSAMSGLHLVKRR) based on the binding sequence for AMPK at Ser79 on rat ACC[54], or the AMARA peptide (AMARAASAAALARRR) designed based on the sequence motif for mammalian AMPK[55]. Based on this, complexes containing the γ1 isoform account for the great majority of AMPK activity in most tissues (Figure 7)[41]. A notable exception to this is the brain, where there is greater parity between the three isoforms. Within the heart, γ1 complexes account for 80-90% of total activity, with γ2 complexes accounting for only 10-20% and a minimal contribution from γ3 complexes[41].

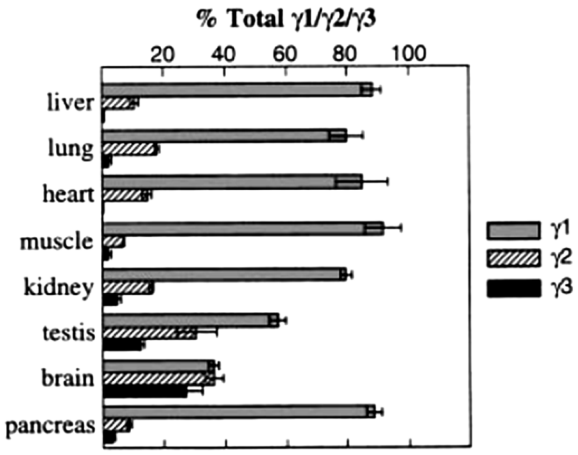


Figure 7. Proportion of total AMPK activity accounted for by γ isoforms in rat tissues.[g]

In keeping with a potential cardiac-specific role for γ2-3B, Pinter and co-workers[49] extended their observation of γ2-3B being the most abundant cardiac γ2 variant at mRNA level (accounting for 50-60% of total cardiac γ2) to identify γ2-3B protein expression as largely restricted to heart and brain. The precise biological significance of these findings is uncertain for now, but nonetheless intriguing in view of the largely cardiac-dominated phenotype of patients bearing mutations in *PRKAG2* [53]. These findings – indicative of the emerging complexity of γ2 biology – point to the need to explore potential splice-variant specific functions and subcellular localisation, as well as developing the appropriate tools to do so: well-validated, isoform variant-specific antibodies.

1.5 Regulation of mammalian AMPK

The primary mechanism of AMPK regulation involves reversible phosphorylation/ dephosphorylation of a conserved threonine residue (Thr172 in rat) within the activation loop segment of the catalytic α subunit, effectively acting as an 'on-off' switch. Upstream kinases promote attachment of phosphate, whilst cellular protein phosphatases act to remove it. Within this framework, the relative ratios of cellular adenine nucleotide levels – signifying cellular energetic status – modify AMPK activity by reversible interaction with sites 1 and 3 on the γ subunit. With the growing implication of AMPK in processes outside of its traditional metabolic role – including the regulation of autophagy, appetite, circadian rhythm, membrane excitability and the cell cycle[12]

[g] Reproduced from figure 6 Cheung et al. *Biochem J* 2000;346:659-669.

– are emerging additional levels of regulatory complexity of the kinase itself, involving modifications of the enzyme (e.g. myristoylation and acetylation) and interaction with non-nucleotide signals of energy status (e.g. glycogen) [12, 32].

1.5.1 AMPK activation by upstream kinases

AMPK is itself the downstream kinase in a kinase cascade. In mammals, two major upstream kinases have been identified which directly phosphorylate α-Thr172, namely the tumour suppressor liver kinase B1 (LKB1) and Ca^{2+}/calmodulin-dependent protein kinase kinase-β (CaMKKβ).

LKB1 exists as a heterotrimeric kinase complexed to two accessory subunits, STE-20 related adaptor protein (STRAD) and MO25, for full activity and is known to be mutated in a form of human hereditary cancer (Peutz-Jeghers syndrome), as well as somatically in several solid organ tumours[22, 56]. Stimuli increasing the AMP/ATP or ADP/ATP ratios such as phenformin, or mimicking AMP such as the nucleoside AICAR (5-aminoimidazole-4-carboxamide riboside, which is taken up by cells via adenosine transporters and converted to a monophosphorylated nucleotide, ZMP[57]) and which activate AMPK, fail to do so in cells lacking LKB1 (e.g. HeLa cells or LKB1-deficient murine embryonic fibroblasts[58]). Importantly, these effects are mediated by adenine nucleotides on the AMPK complex itself and not on LKB1 which is constitutively active and, whilst providing a high level of basal α-Thr172 phosphorylation[12], is not the primary site of regulation.[22] In most tissues, LKB1 is regarded as the predominant upstream kinase for AMPK, including α1 and α2 AMPK in liver, as well as α2 AMPK in cardiac and skeletal muscle.

Importantly, AMPK can still be phosphorylated at α-Thr172 and activated in cell lines deficient in LKB1 – notably by increased intracellular Ca^{2+} – pointing to the existence of other upstream AMPK kinases in addition to LKB1[56]. In 2005, three groups[59-61] identified CaMKKβ as responsible for this as an AMP-independent pathway for AMPK activation. Thus, activation of AMPK occurs in LKB1-deficient cells in response to oxidative and hyperosmotic stress, as well as following direct elevation of intracellular Ca^{2+} (using the ionophore ionomycin), with their effects on AMPK activity markedly attenuated by siRNA-mediated CaMKKβ downregulation or pharmacological inhibition of CaMKK with STO-609.[59] The corollary of these findings is that AMPK is likely to

play a role in Ca^{2+}-mediated signal transduction pathways – notably in the brain where CaMKK is highly expressed – to potentially prepare the cell for the increased energy consumption by ion channels and secretory processes frequently attendant on rise of cytosolic [Ca^{2+}] [56, 62]. The physiological relevance of this is highlighted by the identification of a hypothalamic CaMKK-AMPK pathway in the regulation of appetite by the gastric-secreted hormone ghrelin[63, 64].

In addition to the AMP- and Ca^{2+}-dependent pathways of AMPK activation mediated by LKB1 and CaMKKβ, respectively, TGF-β-activated kinase-1 (TAK1) – a member of the mitogen activated protein kinase kinase kinase family acting downstream of cytokine receptors – has been demonstrated to activate the yeast AMPK homologue *in vivo* and phosphorylate α-Thr172 of mammalian AMPK *in vitro*. TAK1 was identified as a potential mammalian kinase based on a genetic screen[65] for mammalian kinases that could rescue the growth failure phenotype of mutant yeast cells lacking the three native Snf1 kinase-activating upstream kinases[18] (Sak1, Tos 3 and Elm1). Its true significance *in vivo* remains unclear, but studies have implicated it in the activation of AMPK and subsequent autophagy by TRAIL[66] (tumour necrosis factor related apoptosis inducing ligand), as well as suggesting it may indirectly affect LKB1-induced AMPK activation[67].

1.5.2 Principal mechanisms of AMPK activation by adenine nucleotides

Recent crystallographic and nucleotide binding studies have shed significant light on the mechanisms underlying AMPK activation by adenyl nucleotides, in particular by highlighting the largely overlooked role of ADP[26, 68]. Through their interaction with binding sites on the γ subunit, adenyl nucleotides modulate AMPK activity via three independent mechanisms[29, 32]:

i) AMP allosterically activates AMPK once phosphorylated on α-Thr172 AMPK.

ii) AMP (and, as we now know[68], ADP) promotes α-Thr172 phosphorylation, an effect that requires β subunit N-terminal myristoylation[36].

iii) AMP and ADP protect against dephosphorylation and inactivation by phosphatases.

All of these effects are antagonized by ATP and, in the case of (i) only, by ADP also. In the absence of a native N-myristoylated β-subunit in current crystal structures for AMPK, the

mechanism whereby myristoylation alters the rate of α-Thr172 phosphorylation remains enigmatic. The mechanisms thought to underlie (i) and (iii) are discussed in the following sections.

1.5.3 Direct allosteric activation by AMP

Along with phosphorylation of α-Thr172 by upstream kinases, this represents the most intensively studied mechanism of AMPK activation[69] and is the origin of its name. Once α-Thr172 is phosphorylated (and hence AMPK activated), AMP induces further allosteric activation via its binding to site 1 of the γ-subunit. Whilst the effect of this on holoenzyme activity is modest (typically 2-5 fold elevation in activity)[32], in combination with >100-fold rise in catalytic activity upon α-Thr172 phosphorylation, it can potentially signal a rise in AMP levels to augment AMPK activity several thousand-fold[31]. This effect is specific to AMP and related analogues (e.g. the AICAR metabolite ZMP) and antagonised by ADP, ATP and NADH [37]. Interestingly, mutation of the conserved Asp residues to Ala in sites 1, 3 or 4 of the γ subunit has each been shown[68] to reduce AMP's direct allosteric effect (at least in response to 200 μM saturating AMP levels), suggesting that complex interactions between all three sites may influence this allosteric response.[29]

The structural basis for allosteric activation of AMPK by AMP binding to site 1 of the γ subunit remains unclear. Notably, there is little conformational change in the γ1 subunit between AMP- and ATP-bound forms[23], whilst sites 1 and 4 are located further away than sites 2 or 3 from the interface with the α subunit kinase domain [26]. Together these suggest a mechanism for transmission of the activation signal consequent upon AMP binding, involving changes in quaternary structure triggering a kinase domain-regulatory fragment interaction not possible when ATP is bound[37].

1.5.4 Protection against dephosphorylation and the emergent role of ADP

The highly specific ability of AMP to allosterically activate AMPK *in vitro*[70] led to its naming, but also contributed to the potential regulatory role of ADP being largely overlooked. In 2011, two groups[26, 68] reported that AMPK can bind ADP with consequent inhibition of dephosphorylation at α–Thr172 and promotion of AMPK phosphorylation by the upstream kinase CaMKKβ. Given: i) the central role played by phosphorylation in the activation of AMPK; ii) the modest stimulatory effect of allosteric activation by AMP; and iii) the significantly higher levels of free ADP in the

cell compared to AMP (with typical intracellular concentrations of free adenine nucleotides estimated as 0.5-5 μM for AMP, 50-200 μM for ADP and 3,000-8,000 μM for ATP)[26], the finding that mammalian AMPK can sense ADP has led to a significant re-appraisal of the *physiologically relevant* adenine nucleotide mediating the energy stress signal to the AMPK complex.

Site 3 (as with site 1) has similar binding affinities for AMP, ADP and free ATP[26]. Notably, however, binding of this site to ATP coordinated to Mg^{2+} (Mg.ATP) is up to 10-fold weaker. Given that the majority of ATP (~95%) in the mammalian cell is complexed with magnesium[37], the corollary is that whilst ADP can compete with higher levels of Mg.ATP and free ATP to regulate α-Thr-172 dephosphorylation, AMP is likely to play an important role at this site only under conditions of extreme physiological stress. Thus, the latest models for the regulation of AMPK by adenine nucleotides emphasise the central role played by ADP as the major transducer of stress under most physiological circumstances (Figure 8)[31, 71]. Under conditions of severe energy shortage, allosteric activation of AMPK (by AMP binding to site 1) would be expected to amplify the signals induced by ADP/AMP occupancy of site 3, leading to marked holoezyme activation. Intriguingly, yeast Snf1 is not subject to regulation by AMP (either through allosteric stimulation or by protection against dephosphorylation), but has recently been demonstrated to be regulated by ADP-mediated protection against dephosphorylation, prompting the authors to suggest that ADP, rather than AMP, may be the unifying signal of energy stress amongst all AMPK orthologues[72].

Crystallisation of an active phosphorylated form of AMPK, containing the kinase domain and two molecules of AMP bound to sites 3 and 4, has provided insights into the structural interactions likely to underlie ADP/AMP-mediated protection against dephosphorylation[26]. The activation loop containing α-Thr172 interacts extensively with the C-terminal regions of the α and β subunits, such that ready access to α-Thr172 by protein phosphatases is prevented. This process is critically dependent on the presence of the α hook region within the α subunit, which is thought to interact with site 3 in the presence of AMP/ADP to stabilise the kinase domain/regulatory interface, thus blocking access to α-Thr172 by phosphatases. Conversely, the presence of Mg.ATP at site 3 is predicted to induce a steric clash with residues from the α hook, weakening the α/β C-terminal

domain/activation loop interaction such that the catalytic domain dissociates from the regulatory interface and is exposed to permit better access to α-Thr172 by protein phosphatases (Figure 9).

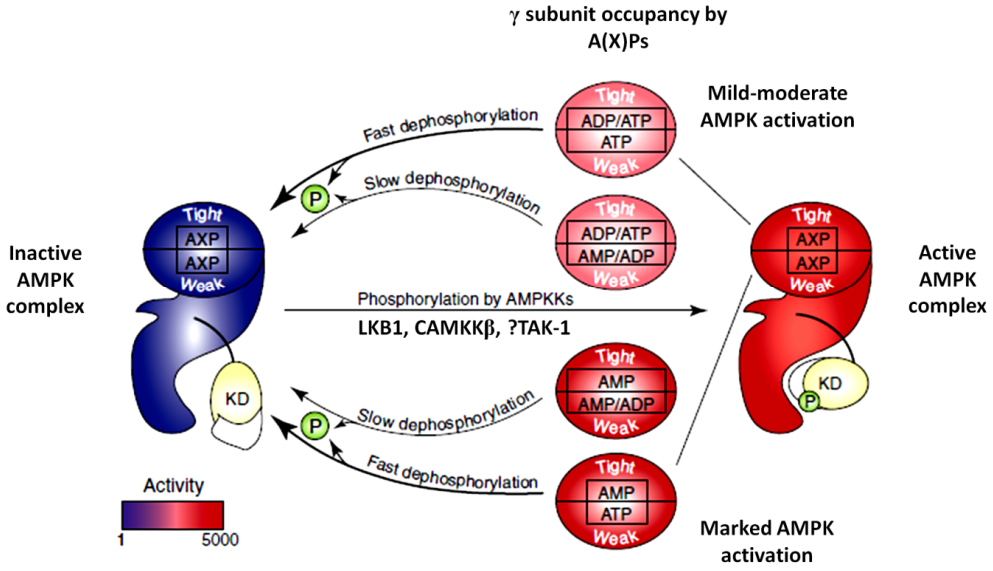


Figure 8. Model for the regulation of AMPK by adenine nucleotides.[h]

AMPK phosphorylation by upstream kinases results in activation of the enzyme complex (colour change from blue to red). This process is continually subject to reversal by phosphatases such that the proportion of active AMPK is regulated by the rate of dephosphorylation. Against this process act ADP or AMP which, by binding to the weaker affinity site 3, slow the dephosphorylation step. AMP occupancy of the tight affinity site 1 induces further allosteric stimulation of AMPK activity (signified by darker red colour). This system permits the kinase to respond to an extensive range of ADP:ATP and AMP:ATP ratios and hence operate over a very wide dynamic range[22].

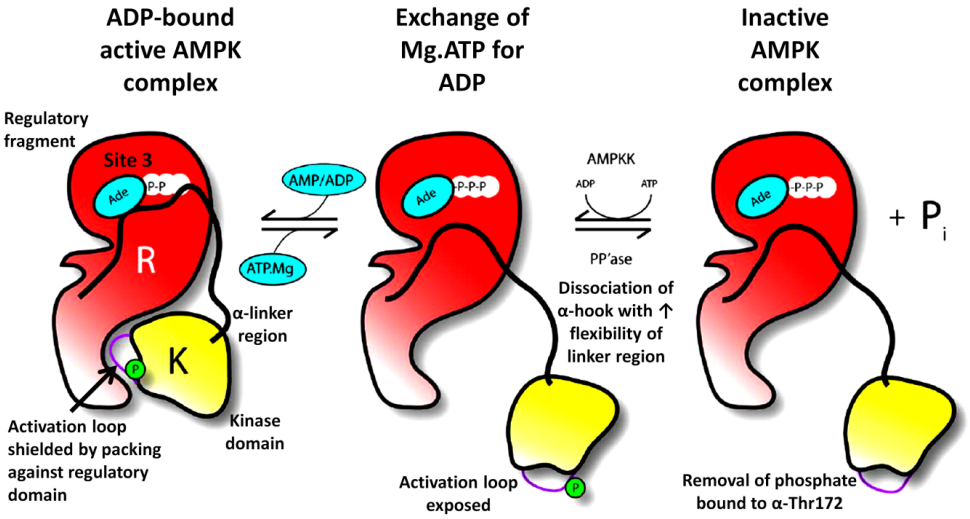


Figure 9. Model for the regulation of dephosphorylation of α-Thr172 AMPK by the interaction between adenine nucleotides and site 3 on the γ subunit.[i]

[h] Adapted from figure 2 Hardie et al. *Trends Biochem Sci* 2011;36:470-7.
[iii] Adapted from supplementary figure 1 Xiao et al. *Nature* 2011;472:230-3.

1.5.5 Regulation of AMPK by glycogen

Whilst the sensing of adenine nucleotides by AMPK allows it to act as a sensitive gauge of *immediate* cellular energy status, evidence has emerged to support the hypothesis that AMPK may also be able to sense the *intermediate* energy reserves of the cell in the form of glycogen through interaction with the glycogen-binding domain (GBD) on the β subunit.

1.5.5.a Glycogen structure and function

Glycogen is a very large, branched homopolymer of glucose that serves as an osmotically neutral means of carbohydrate storage in the cell, available for rapid utilisation[73, 74]. In mammals, the major tissue stores are in the liver and skeletal muscle, although other organs – including the heart – are also capable of glycogen synthesis[73]. Glycogen consist of primary linear chains of glucose residues coupled by α-1,4-glycosidic linkages, with further chains branching off this primary chain connected by α-1,6-glycosidic linkages (Figure 10)[73]. The chain initiation step is dependent upon a unique glycogen-binding protein called glycogenin. This self-glucosylating enzyme initiates glycogen synthesis by initially transferring glucose from UDP-glucose to a tyrosine side-chain within itself (linking to C1 of the glucose) and subsequently to form an initial α-1,4-glycosidic-linked glucose chain. Whilst still covalently attached to glycogenin, this oligosaccharide then acts as the primer for bulk glycogen synthesis by the rate-limiting enzyme for glycogen synthesis – glycogen synthase (GS) – the latter again using UDP-glucose as the nucleotide-sugar donor, with branching introduced by glycogen branching enzyme[73, 75].

Current models[73] for the macrostructure of glycogen propose an average chain length of ~13 glucose residues and two branchpoints per inner chain to form a second 'tier'[73, 75]. The primary chains making up the second tier in turn have two further branchpoints to allow formation of a third tier and so forth (Figure 10). In this way, the macromolecule is envisaged to have inner B chains containing two branchpoints and outer A chains which are unbranched, permitting access of the glycogen-degrading enzyme, glycogen phosphorylase (GP), to glucose residues on the non-reducing ends of its outer A chains. Release of glucose moieties from the outer chains by

phosphorylase continues until four glucose units remain on the branch, with further reduction by GP dependent on the intervention of glycogen debranching enzyme to cleave the α-1,6 bond.

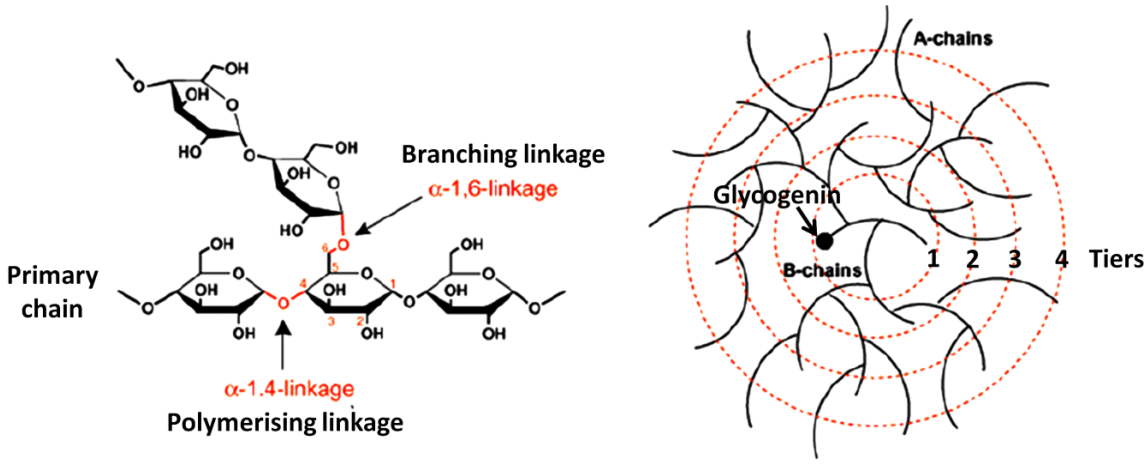


Figure 10. Glycosidic linkages involved in the formation of glycogen (left) and ensuing tiered model for glycogen macrostructure (right).[j]

A full-sized glycogen particle is postulated to have up to 12 tiers, corresponding to a single molecule containing ~55,000 glucose residues and ~44 nm in diameter[73]. Electron microscopy identifies free glycogen particles (constituting both the glycogen molecule and its associated metabolic proteins) – known as β particles – as typically possessing a diameter smaller than this, at 25 nm, corresponding to seven tiers. The stochastic nature of glycogen synthesis and its degradation likely underlie the deviation from the theoretical formulation for the macrostructure of glycogen[73]. Within the liver, larger conglomerates of glycogen particles form rosettes, known as α particles, thought to represent aggregates of β particles[73].

1.5.5.b Links between AMPK and glycogen metabolism

A number of experimental observations have associated AMPK with glycogen homeostasis in both physiology and disease states:

i) The β subunit of AMPK contains a highly conserved N-isoamylase GBD allowing targeting and binding of the AMPK complex to glycogen *in vitro*[33, 34]. N-isoamylase domains are non-catalytic

[j] Adapted from figure 1 Roach et al. *Biochem J* 2012;441:763-87.

carbohydrate-binding modules found predominately in enzymes that metabolise the α-1,6 branches found in α-1,4-linked glucans such as starch and glycogen[34].

ii) AMPK phosphorylates and thereby inactivates GS at its N-terminal site 2 (Ser-7 in human)[76], with the sequence around site 2 conforming well to the mammalian AMPK recognition motif φ[X,B]XX[Ser/Thr]XXXφ, where φ is a hydrophobic residue (Met, Val, Leu, Ile or Phe) at the P-5 and P+4 positions, B is a basic residue (Arg, Lys or His) at the P-3 or P-4 position and X is any residue[55]. Its potential relevance as a GS kinase *in vivo* is supported by the finding that perfusion of rodent muscle with the AMPK activator, AICAR, leads to site 2 phosphorylation of GS, but fails to do so in mice lacking α2 AMPK[77].

iii) AMPK has been reported to phosphorylate and thereby affect the function of other emerging components of glycogen metabolism. In particular, AMPK phosphorylates R5/PTG (protein targeting to glycogen), a glycogen-targeting protein which recruits type 1 protein phosphatase (PP1) to glycogenic substrates[78]. PP1 promotes glycogen accumulation by dephosphorylating both GS (activating the enzyme and hence glycogen synthesis) and GP (inactivating the enzyme thereby inhibiting glycogen degradation). R5/PTG glycogenic activity is modulated through ubiquitination and subsequent targeting for proteasomal degradation by the laforin-malin complex (which also ubiquitinates GS). Phosphorylation of Ser-8 of R5/PTG by AMPK accelerates its laforin-malin-dependent degradation, inhibiting the glycogenic activity of R5/PTG and thereby downregulating glycogen synthesis[78]. Recently, AMPK has also been suggested to phosphorylate laforin itself, enhancing its interaction with malin and promoting a more stable laforin-malin complex[79]. In combination with direct phosphorylation of R5/PTG and GS itself, this may potentially allow AMPK to downregulate glycogen synthesis through multiple, coordinated mechanisms.

iv) Using immunoelectron microscopy, AMPK is seen to be associated with α particles of glycogen in rat liver[74], extending previous *in vitro* findings[33, 34] of co-localisation of AMPK and glycogen/GS upon overexpressing the β subunit or AMPK holoenzyme to the *in vivo* setting. Notably, the β1 subunit was shown to preferentially associate with glycogen compared with the cytosol and, further, to be located at the periphery of the glycogen rosette[74].

v) Glycogen loading prior to exercise has been shown to suppress the activation of α2 AMPK complexes by exercise in humans, suggesting that glycogen may act to repress AMPK activity. Paradoxically, patients with McArdle's disease (glycogen storage disease type V), who have impaired glycogen breakdown due to an inherited defect in GP, exhibit *hyperactivation* of α2 AMPK complexes in response to exercise despite elevated skeletal muscle glycogen content. Together, these findings suggest that AMPK activity might not simply be responsive to the absolute levels of glycogen *per se*, but rather to structural alterations in the macromolecule, e.g. attendant on exercise or occurring with disease states interfering with normal glycogen metabolism.

vi) More recently, glycogen has been demonstrated to allosterically inhibit AMPK *in vitro*, an effect dependent on binding to the GBD[80]. This inhibitory effect varies according to the glycogen preparation used, with those with higher branching content (and hence greater number of α-1,6-linkages) exerting greater inhibition of AMPK. In keeping with the hypothesis that the branch points of glycogen are the true ligands for the GBD[75] (whose binding results in AMPK inhibition), synthetic oligosaccharides containing a single α-1,6-linkage were observed to be far more potent inhibitors of AMPK than linear oligosaccharides containing only α-1,4-linkages, although the latter did still bind the GBD[80]. Interestingly, the most potent inhibitory oligosaccharide also caused marked inhibition of α-Thr172 phosphorylation by upstream AMPK kinases. Based on these observations, the GBD has been proposed to have a role beyond mere targeting of AMPK to glycogen: through binding of and allosteric inhibition by α-1,6-branch points in glycogen, the GBD may allow AMPK to function as a glycogen sensor, regulating glycogen biosynthesis in response to its metabolism by GP and hence its branching state (Figure 11).

vii) A final important connection between glycogen and AMPK comes from the discovery of naturally occurring mutations which cause disease. Dominant mutations in the gene encoding the γ3 subunit (*PRKAG3*) have been identified[81] to cause excess glycogen accumulation in the skeletal muscle of purebred Hampshire pigs, adversely affecting meat quality (section 1.6.1). In humans, similar mutations in γ2 (encoded by *PRKAG2*) have been associated with a cardiomyopathy associated with cardiac glycogen deposition (section 1.6.2)[82].

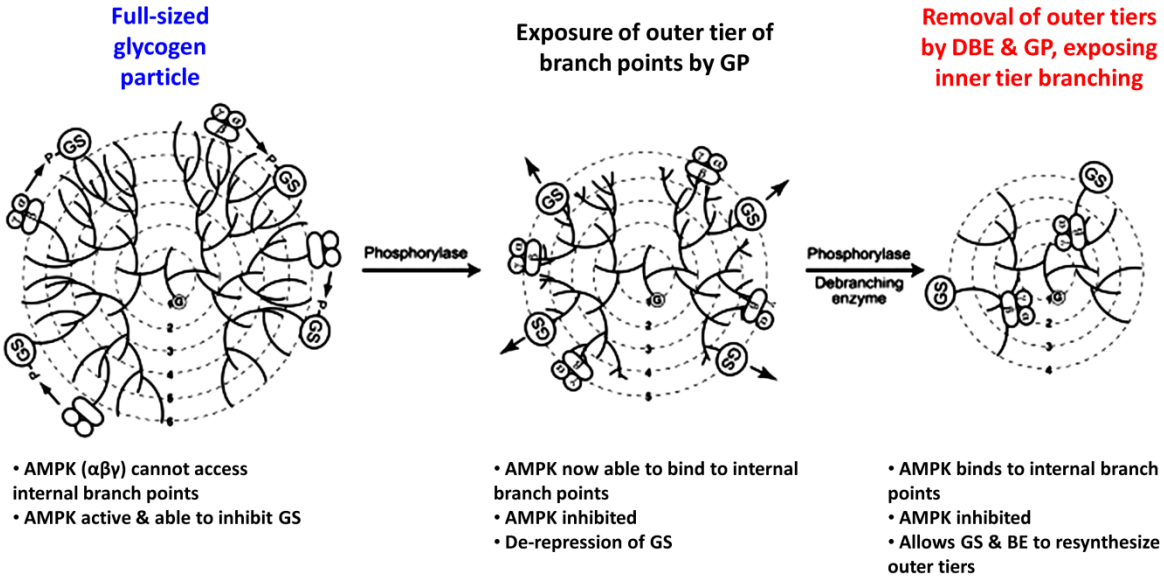


Figure 11. Model of AMPK as a sensor of glycogen structure and hence reserves.[k]

Schematic illustrating the regulation of glycogen synthesis by AMPK through the latter's dynamic sensing of branch points during glycogen particle degradation, with consequent modulation of AMPK activity via the GBD. Abbreviations: GS, glycogen synthase; GP, glycogen phosphorylase; DBE, de-branching enzyme; BE, branching enzyme.

1.5.6 Regulation of AMPK by protein phosphatases

Although much progress has been made in determining the processes that promote phosphorylation of AMPK, particularly by adenine nucleotides, this phosphorylation is dynamic and reversible through the action of protein phosphatases. Early studies[6, 70] indicated that AMPK's inhibitory effect on ACC and HMG-CoA reductase was strongly reduced by prior treatment of the kinase with protein phosphatase-2A (PP2A) or protein phosphatase 1C (PP1C), both members of the phosphoprotein phosphatase (PPP) family of serine-threonine (Ser/Thr) phosphatases. These *in vitro* observations were also extended to inhibition of AMPK activity by PP2C, the defining member of the PPM (Mg^{2+}- or Mn^{2+}-dependent) family of Ser/Thr phosphatases[83]. Use of okadaic acid – a marine toxin which potently inhibits PP1 and PP2A – in rat hepatocytes had no effect on AMPK activity, suggesting that members of the okadaic acid-insensitive PPM family (e.g. PP2C) act as the predominate AMPK phosphatases, at least in intact hepatocytes[84]. This has been supported more recently by the finding that lentiviral-mediated short hairpin (shRNA) knockdown of PPM1E (a member of the PPM family) in HEK293 cells significantly increased α-Thr172

[k] Adapted from figure 4 McBride & Hardie *Acta Physiol* 2009;196:99-113.

AMPK phosphorylation[85]. In contrast, small interfering RNA (siRNA) depletion of both of the two major PP1 cytoplasmic isoforms (PP1α and PP1β) in a mouse pancreatic β cell line (MIN6) resulted in attenuation of the normal inactivation of AMPK by switch from low to high glucose media[86]. This finding was extended to R6 – a regulatory subunit of PP1 responsible for targeting the catalytic subunit to specific substrates – whose knockdown reduced glucose-induced dephosphorylation of α-Thr172, resulting in activation of AMPK and reduction in glucose-induced insulin release[86]. These studies raise the possibility that different protein phosphatases may act to dephosphorylate AMPK in different tissues or under different physiological conditions[32].

Despite their importance as the counterparts of AMPK kinases in determining the net phosphorylation status of AMPK, the physiologically relevant protein phosphatase(s) responsible for AMPK dephosphorylation *in vivo* remain uncertain[32, 37].

1.6 Naturally occurring mutations in the regulatory γ subunit of AMPK cause disease

1.6.1 *PRKAG3* and the RN$^-$ mutation in pig

In 2000, a mutation (R200Q) in porcine *PRKAG3* was identified to account for a dominant mutation (denoted RN$^-$) previously recognised to occur in a high proportion of purebred Hampshire pigs and known as Rendement Napole[81]. Meat from RN$^-$ pigs exhibits a 70% increase in skeletal muscle glycogen content, lower ultimate pH of meat and reduced water-holding capacity, factors which negatively affect subsequent pork quality[81, 87]. The missense mutation – encoding for a change of arginine to glutamine at residue 200 (R200Q) in the first CBS domain of γ3 – was found to be associated with a reduction in total AMPK activity from muscle extracts[81], both in the presence and absence of AMP. Interestingly, the authors[81] speculated at the time that reduced activity may "*reflect feedback inhibition due to the high-energy status of the muscle*", with subsequent identification of the β subunit GBD providing a molecular substrate for this to occur[33]. However, an assessment of the equivalent mutation (R70Q) in γ1, using an *in vitro* mutant, identified a marked *increase* in basal AMPK activity of R70Q γ1-containing AMPK heterotrimers

compared to wild-type complexes, with substantial loss of AMP-dependence[88]. The authors extended these *in vitro* activity assay findings by confirming a corresponding increase in phosphorylation of the AMPK substrate, ACC, from intact cells expressing the R70Q γ1 mutant[88].

Since these reports, an R225W mutation in human *PRKAG3* has been described[89, 90], with a phenotype of elevated skeletal muscle glycogen and glucose uptake, reduced intramuscular triglyceride content, higher mitochondrial content and enhanced resistance to fatigue of R225W carriers. As with the engineered R70Q *in vitro* mutant[88], the functional effect of this mutation on AMPK was found to be an increase in basal AMPK activity from differentiated skeletal muscle cells grown in culture, although in this case mutant complexes were still largely AMP-responsive[89].

1.6.2 Mutations in the γ2 subunit gene (*PRKAG2)* cause human cardiomyopathy

Shortly after the identification of a mutation in *PRKAG3* accounting for the RN^- phenotype, mutations in human *PRKAG2* were discovered to underlie rare familial cases of autosomal dominant hypertrophic cardiomyopathy (HCM) associated with ventricular pre-excitation[91, 92].

1.6.2.a Hypertrophic cardiomyopathy (HCM) and the energy deficiency hypothesis

HCM is the commonest inherited cardiac disorder – segregating as a Mendelian autosomal dominant trait – and defined clinically by the presence of unexplained left ventricular hypertrophy (LVH), with a prevalence of 1 in 500 individuals[93, 94]. Its most feared complication is sudden cardiac death, with an annual event rate of 1-2% in children/adolescents and 0.5-1% in adults[93]. Whilst the majority of cases are recognised to be asymptomatic, it may present with shortness of breath, chest pain, palpitations, syncope (abrupt and transient loss of consciousness), exercise intolerance and heart failure. Pathologically, HCM is characterised by ventricular hypertrophy (variable in anatomical extent and severity), myocyte disarray and cardiac fibrosis[94].

The genetics of HCM are complex, with significant genetic (multiple disease gene) and allelic (multiple mutation) heterogeneity[95]. The majority of the >450 causal mutations are missense

mutations and predominately occur in sarcomeric proteins, leading to the concept of HCM as a 'disease of the sarcomere' - the fundamental contractile unit of myocytes[95].

Mutant gene products are largely stably expressed and able to incorporate into the sarcomere, suggesting that the HCM phenotype is caused by a dominant-negative action of mutant protein perturbing function of wild-type sarcomeric units[94, 96]. Mutant myofilaments generally exhibit increased activation and hypercontractility, resulting in inefficient and excessive energy utilisation by the myosin ATPase – a molecular motor that converts chemical energy from ATP hydrolysis to directed force transduction through its ATP-dependent interaction with filamentous actin[97]. Since the myosin ATPase accounts for ~70% of cardiomyocyte ATP consumption, excessive ATP consumption by mutant sarcomeres has the potential to compromise cardiomyocyte energetics, adversely affecting the function of other key ATP-consuming processes, such as the removal and re-uptake of Ca^{2+} by the sarcoendoplasmic reticulum Ca^{2+} ATPase (SERCA2) pump[94, 98]. Reduced calcium uptake during ventricular diastole (the end of the cardiac cycle when the ventricles undergo relaxation and filling for subsequent contraction) can elevate cytosolic calcium concentrations, promoting calcium-dependent hypertrophic signalling (e.g. via activation of calcineurin-nuclear factor of activated T cells [NFAT] signalling) and susceptibility to arrhythmia[94]. Support for this 'energy deficiency hypothesis' as the pathophysiological basis for HCM has emerged from: findings from functional analysis of isolated mutant myofibrils indicating increased energetic cost of tension generation[94]; evidence of altered energetics in the $\alpha MHC^{403/+}$ mouse model of HCM[99]; clinical ^{31}P-MRS (magnetic resonance spectroscopy) data indicating energetic compromise (utilising the cardiac phosphocreatine to ATP ratio[100]) in HCM hearts irrespective of the degree of LVH[101]; and clinical observation of a number of inherited non-sarcomeric phenocopies (i.e. apparently similar disorders with different aetiologies) of HCM that involve mutations in genes encoding important components of myocardial energy production or transport, e.g. mitochondrial tRNA mutations or defects in fatty acid uptake (CD36)[94, 98].

1.6.2.b PRKAG2 as a causative gene for the Wolff-Parkinson-White syndrome

Use of comprehensive genetic screening identifies sarcomeric mutations in only up to two thirds of patients with HCM, suggesting additional non-sarcomeric genetic aetiologies[93, 94]. Intriguing in this regard was the recognition of families with evidence of a HCM phenotype combined with an electrophysiological disturbance, termed ventricular pre-excitation and often manifesting as the Wolff-Parkinson White (WPW) syndrome (Figure 12). A disease locus for dominantly-inherited HCM and WPW had been mapped[102] to chromosome 7 band q3 (7q3) in 1995. The subsequent mapping[48] of the human gene encoding the energy-sensing regulatory γ2 subunit of AMPK (*PRKAG2*) to the same locus (7q36) in 2000 – in conjunction with evidence supporting energetic compromise as a common unifying mechanistic basis for HCM – made *PRKAG2* a highly attractive non-sarcomeric candidate gene for HCM. Accordingly, in 2001, Hugh Watkins' group[91] identified two mutations – a missense mutation substituting arginine for histidine at residue 142 (H142R) in CBS2 and an in-frame codon insertion between CBS 1 and 2 (exon5:insLeu) – in *PRKAG2* in two separate families with HCM, some of whom also manifested pre-excitation. In parallel, Robert Roberts' group[103] utilised a genetic linkage approach to identify a missense mutation resulting in substitution of glutamine for arginine (R302Q) in CBS1 of *PRKAG2* as the cause of ventricular pre-excitation with associated hypertrophy in two separate families with WPW (Figure 12).

1.6.2.c Clinical features of PRKAG2 cardiomyopathy

Both initial reports[91, 103] of the disease indicated a broader cardiac phenotype that went beyond cardiac hypertrophy and ventricular pre-excitation. Blair et al.'s initial description[91] highlighted the malignant phenotype of patients carrying the exon5:InsLeu *PRKAG2* mutation, with high incidence of early sudden death, prominent left ventricular dysfunction with early cardiac dilatation (in marked contrast to the majority of patients with typical 'sarcomeric' HCM) and consequent need for cardiac transplantation. Also present were additional electrophysiological (EP) manifestations, including atrial fibrillation (AF) and bundle branch block (BBB, a surface ECG pattern observed with interruption of normal electrical activity in the His-Purkinje system). Gollob et al.'s clinical evaluation[103] identified high penetrance (i.e. high proportion of mutation carriers with a clinically

detectable phenotype[94]) of the R302Q disease allele, with all 24 subjects for whom baseline ECGs were available demonstrating pre-excitation, but found variable expressivity. A significant proportion (~40%) of R302Q carriers manifested AF or atrial flutter, whilst three quarters of affected patients over the age of 30 years had undergone implantation of a permanent pacemaker for either high-grade sinoatrial or atrioventricular block[103]. More subtle conducting system disease was also observed, notably resting sinus bradycardia and inadequate exertional heart rate (chronotropic) response. Cardiac hypertrophy was identified in only 8 out of 31 affected subjects (26%), with a single member progressing to severe ventricular dysfunction and transplantation[103].

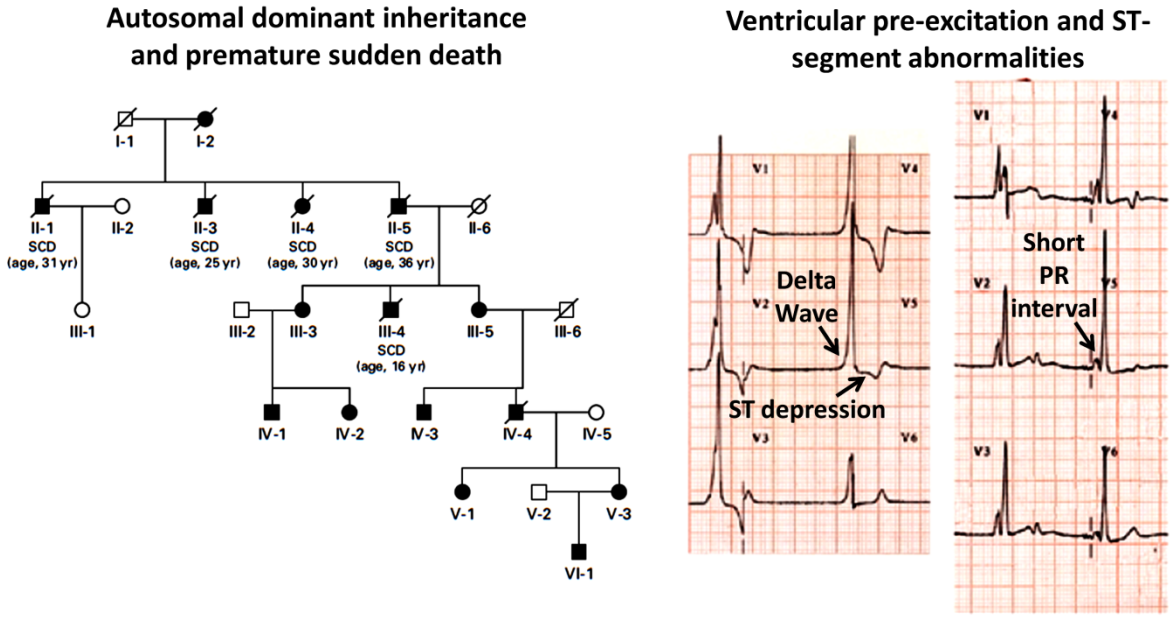


Figure 12. Pedigree of family bearing the R302Q *PRKAG2* mutation (left) and typical surface electrocardiogram (ECG) findings of ventricular pre-excitation (right).[1]

Symbols in pedigree: filled denote affected individuals; squares denote males; circles denote females; slash overlying symbol denotes deceased.

The surface ECG illustrates two classical features of ventricular pre-excitation: a (very) short PR interval caused by premature activation of the ventricles by an accessory atrioventricular connection outwith (and therefore bypassing) normal atrioventricular (AV) nodal/His-Purkinje conduction; and a slurred, broad initial upstroke to the QRS complex. The latter appearance, termed a delta wave, reflects the fusion of the initial aberrant slow ventricular conduction via the accessory pathway with the termination of activation through the native conducting system. Together, these are known as Wolff-Parkinson-White *pattern*. The WPW *syndrome* requires association of WPW pattern on the ECG with evidence of tachycardias – either re-entrant tachycardia or atrial fibrillation or flutter[104]. Also illustrated are evidence of ventricular repolarisation abnormalities, often secondary changes associated with ventricular pre-excitation but also observed in significant LVH[105].

[1] Adapted from figure 1 Gollob et al. *N Engl J Med* 2001;344:1823-1831 and figure 4 Blair et al. *Hum Mol Genet* 2001;10:1215-1220.

In 2002 the Seidman laboratory[82] identified two further γ2 mutations (asparagine substituted for threonine at residue 400, T400N and isoleucine substituted for asparagine at residue 488, N488I). Their study highlighted the presence of unique cardiac histopathological features associated with these mutations (Figure 13). Unlike traditional sarcomeric HCM, *PRKAG2* mutations were not associated with significant cardiac fibrosis or myofibre disarray, but exhibited unusual cytosolic vacuolation for a PAS-positive[m] substance that was largely diastase-resistant[n], with ultrastructural features which the authors described[82] as characteristic of amylopectin or polyglucan (suggestive of an abnormal glycogen structure that may be relatively inert to physiological turnover[106]).

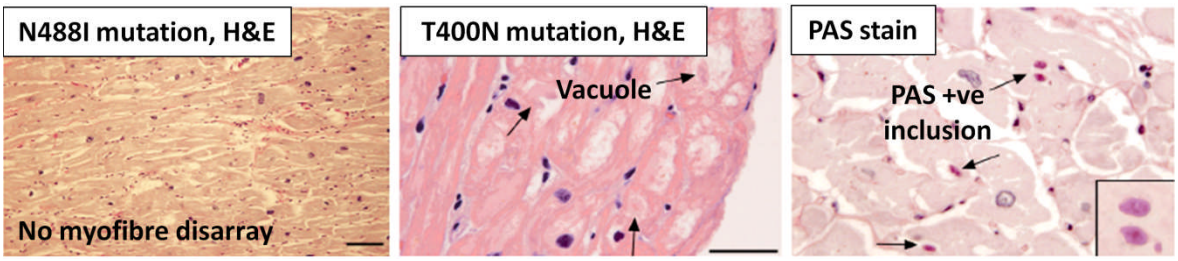


Figure 13. Characteristic histopathological features of PRKAG2 cardiomyopathy.[o] Scale bar 100 µm.

Left panel – cardiac biopsy stained with haematoxylin and eosin (H&E) from a 26-year-old individual with the N488I *PRKAG2* mutation who experienced sudden death.

Centre panel – Prominent cardiomyocyte vacuolisation from a 39-year-old individual carrying a T400N *PRKAG2* mutation.

Right panel – Vacuoles contain PAS-positive but largely diastase-resistant inclusions.

Murphy et al.[107] presented longitudinal follow-up data on a series of 45 patients, the majority of whom carried an N488I *PRKAG2* mutation. They confirmed earlier reports' findings of generally young age at onset (mean 24 years, range 9-55 years) and a clinical presentation reminiscent of sarcomeric HCM, including: syncope, palpitations, exertional breathlessness and chest pain. Notably, their report described extra-cardiac disease manifestations, with 15% of patients exhibiting myalgia (in one patient associated with reduced muscle power and requiring a wheelchair by 46 years of age) and four patients experiencing poorly-controlled, generalised tonic-clonic seizures[107]. Further assessment of patients with myalgia identified: clinically apparent

[m] Periodic acid-Schiff - a stain used to detect polysaccharides.
[n] Diastase - an enzyme used to digest glycogen by cleaving α-1,4-glycosidic linkages.
[o] Adapted from figure 2 Arad et al. *J Clin Invest* 2002;109:357-362.

muscle weakness (proximal myopathy); normal muscle fibre size on biopsy; mild excess of glycogen on semi-thin sections; an appearance of 'ragged red fibres'[p] on histology[108]; and a visual appearance (albeit not quantified) of 'excess mitochondria' on electron microscopy. In their cohort[107], 78% of patients exhibited LVH and 60% had pre-excitation. Requirement for pacemaker implantation was also high (38% by 38 years), with the indication in the majority being symptomatic sinus bradycardia or chronotropic incompetence. Of the four disease-related deaths, three were due to thromboembolic stroke resulting from AF (age range 55-62 years), whilst the other was sudden cardiac death in the context of massive LVH at 27 years.

These and subsequent clinical reports helped to delineate the key features of a complex and heterogeneous phenotype distinct to sarcomeric HCM, that has been termed the 'PRKAG2 cardiac syndrome'[109]. These are: LVH (varying from absent-massive); ventricular pre-excitation (via a variety of frequently multiple atrioventricular, atriofascicular, nodoventricular[110] or fasciculoventricular[111] accessory pathways); cardiac glycogen accumulation (ranging from absent-to-profound); sinus node dysfunction and progressive cardiac conduction system disease (including atrioventricular and bundle branch blocks, BBB); and high risk of premature sudden cardiac death (~10%) due to brady-asystolic rhythm or pre-excited supraventricular rhythms degenerating into terminal ventricular tachyarrhythmia[109].

Although dominated by cardiac pathology, the documented existence of extra-cardiac features, on a background of known widespread tissue expression of γ2, may suggest that 'PRKAG2 disease'[112] is a more accurate term for the disorder. The pathogenesis of these extra-cardiac disease manifestations – which includes seizures, hypertension and skeletal myopathy – remains unclear.

[p] Refers to abnormal subsarcolemmal accumulation of mitochondria visualised as bright red against blue background with Gomori trichrome staining and regarded as a hallmark of mitochondrial disease.

Table 1. Reported human *PRKAG2* mutations with associated phenotype.[q]

Mutation	Age of onset	Key features	Extra-cardiac /other features	Refer-ence
Arg302Gln	Late adoles-cence to middle age	Prominent EP phenotype: pre-excitation, AF/atrial flutter, sinus bradycardia (in up to 90%), AV block, chronotropic incompetence. Common requirement for permanent pacemaker (PPM) implantation Familial variant also described manifesting as high incidence of atrial tachyarrhythmia, right bundle branch block (RBBB), sinus bradycardia & short PR interval, late-onset complete heart block but no pre-excitation or LVH Highly variable LVH ranging from absent to severe. Frequency reported as 10-74%. Absence of glycogen accumulation despite LVH also reported Rare reports of sudden cardiac death. Severe LV dysfunction and requirement for transplantation rare	Commonest described *PRKAG2* mutation	Gollob et al., 2001[92] Arad et al., 2002[82] Sternick et al., 2006[113] Tan et al., 2008[110]
Leu351Ins	Adult	High incidence of sudden death & requirement for cardiac transplantation. WPW, broad QRS, AF. Massive LVH	Single family of 5	Blair et al., 2001[91]
His383Arg	Paediatric	Pre-excitation, broad & bizarre QRS, LVH	Single family of 3	Blair et al., 2001[91]
Arg384Thr	Neonatal	Fetal bradycardia, massive biventricular hypertrophy, atrial wall thickening, elevated cardiac and skeletal muscle glycogen on PAS, short PR interval. Death at 5 months age	Single patient Likely *de novo* mutation.	Akman et al., 2007[114]
Thr400Asn	Adult	Pre-excitation, moderate LVH, sinus bradycardia	Single patient	Arad et al., 2002[82]
Tyr487His	Paediatric	Modest LVH, short PR, sudden cardiac death	Family of three	Arad et al., 2005[115]
Asn488Ile	Paediatric -adult	Pre-excitation (23 - 58%), moderate LVH (70%) with progression, AF/SVT (30%). Lower reported requirement for PPM implantation than for Arg302Gln mutation. Sudden cardiac death uncommon, but several deaths due to thromboembolic stroke (AF) described Mild excess of glycogen on semithin sections of skeletal muscle, confirmed on EM	Second commonest described *PRKAG2* mutation Myalgia (18%) & proximal myopathy	Arad et al., 2002[82] Murphy et al., 2005[107]
Glu506Gln	Infancy	Biventricular hypertrophy, subaortic outflow tract obstruction. Short PR & ventricular pre-excitation. Normal glycogen content & absence of glycogen deposits on histology and EM of endomyocardial biopsy	Single family of 3	Kelly et al., 2009[116]
Glu506Lys	Adult	Severe LVH, high incidence of RVH, LV outflow tract obstruction and pre-excitation reported	Family of eight	Bayrak et al., 2006[117]
Arg531Gly	Paediatric	Absence of LVH. Pre-excitation. High incidence of AF & atrial flutter. High-grade conduction disease	Early-onset, persistent hypertension	Gollob et al., 2001[92]
Arg531Gln	Neonatal	Massive biventricular hypertrophy, bradycardia *in utero*, 2-10-fold increase in cardiac glycogen, short PR/wide QRS interval Additional multisystem features	Enlarged dysmorphic kidneys, macro-glossia,	Burwinkel et al., 2005[106]
Ser548Pro	Adult	Prominent muscle stiffness, family history of SCD, severe sinus bradycardia, BBB, mild-moderate LVH, normal LV EF, subsarcolemmal vacuoles on skeletal muscle biopsy	Single patient	Laforet et al., 2006[118]

[q] Adapted and updated from table 2 Arad et al. *Circ Res* 2007;100:474-488.

1.6.3 Existing transgenic models of PRKAG2 cardiomyopathy

In order to define the mechanisms underlying the cardiomyopathy phenotype associated with *PRKAG2* mutations, transgenic (TG) mice modelling four separate mutations[119-122] have been developed and characterised (Table 2). All share a similar approach in their design in overexpressing either wild-type (WT) or mutant full-length human γ2 cDNA sequence under the action of a strong tissue-specific promoter cassette – the α-myosin heavy chain (α-MHC) promoter – allowing directed transgene expression in (primarily fetal) atria & postnatal ventricle[123].

Table 2. Mouse models of PRKAG2 cardiomyopathy

Mutation	Principal model findings	Effect on AMPK activity[r]	Reference
Arg302Gln	LVH with TG^{R302Q} heart weight 2 x TG^{WT} and 3 x non-TG WT. Ventricular dilatation/impaired systolic function on echo at two months accompanied by two-fold increase in natriuretic peptide B (but not A, atrial) expression by northern blotting in TG^{R302Q} Prolonged sinus cycle lengths, preserved sinus node recovery times and evidence for accessory pathways on invasive EP study Abundant glycogen accumulation. Muscle bundles extending from atrium to ventricle in region of fibrous body in TG^{R302Q} only	TG^{R302Q} myocardial AMPK enzyme activity was 22% of TG^{WT} mice and <4% that of non-TG WT mice No significant increase in AMPK activity of TG^{R302Q} heterotrimers with AMP stimulation	Sidhu et al., 2005[120] Folmes et al., 2009[124]
Thr400Asn	Glycogen excess, early LVH and remodelling characterised by dilatation and impaired contractility at 8-12 weeks in TG^{T400N} Markedly short PR and wide QRS consistent with pre-excitation Partial normalisation of phenotype by crossbreeding TG^{T400N} with mice carrying dominant negative AMPK α2 catalytic subunit	Initial increase in AMPK activity from two days to two weeks followed by decrease below TG^{WT} levels	Banerjee et al., 2007[122]
Asn488Ile	20-fold greater cardiac *PRKAG2* RNA expression than non-TG LVH by 8 weeks with massive glycogen accumulation Thinning and disruption of the annulus fibrosus in hypertrophied TG^{N488I} hearts with multiple vacuolated, glycogen-loaded myocytes Short PR/delta wave in 50% of TG^{N488I} mice. Bradycardia & pre-excitation in 2 independent TG^{N488I} lines confirmed by invasive EP. Spontaneous & stress-induced mortality (20-40 weeks) in TG^{N488I}	Significantly increased basal α1- and α2-subunit-associated AMPK activity in cardiac extracts from TG^{N488I} hearts compared to TG^{WT} and non-TG WT hearts	Arad et al., 2003[125] Patel et al., 2003[125]
Arg531Gly	LVH, LV dilatation & poor contractile function by 4 weeks with massive glycogen accumulation in TG^{R531G}. Milder LVH in TG^{WT} Surface ECG recordings compatible with ventricular pre-excitation. Increased spontaneous mortality in TG^{R531G} (greater in males)	Total & γ2-associated AMPK activity of TG^{R531G} immune complexes near-undetectable by 4 weeks but normal at 1 week	Davies et al., 2006[121]

Whilst employing a relatively blunt genetic experimental approach, overexpression of human

[r] Effect on AMPK activity discussed further in section 1.6.4.

mutant γ2 in adult mouse heart uniformly induces a highly malignant phenotype (Figure 14), recapitulating key aspects of the human cardiomyopathy, namely: severe LVH, profound glycogen accumulation, ventricular pre-excitation and premature death.

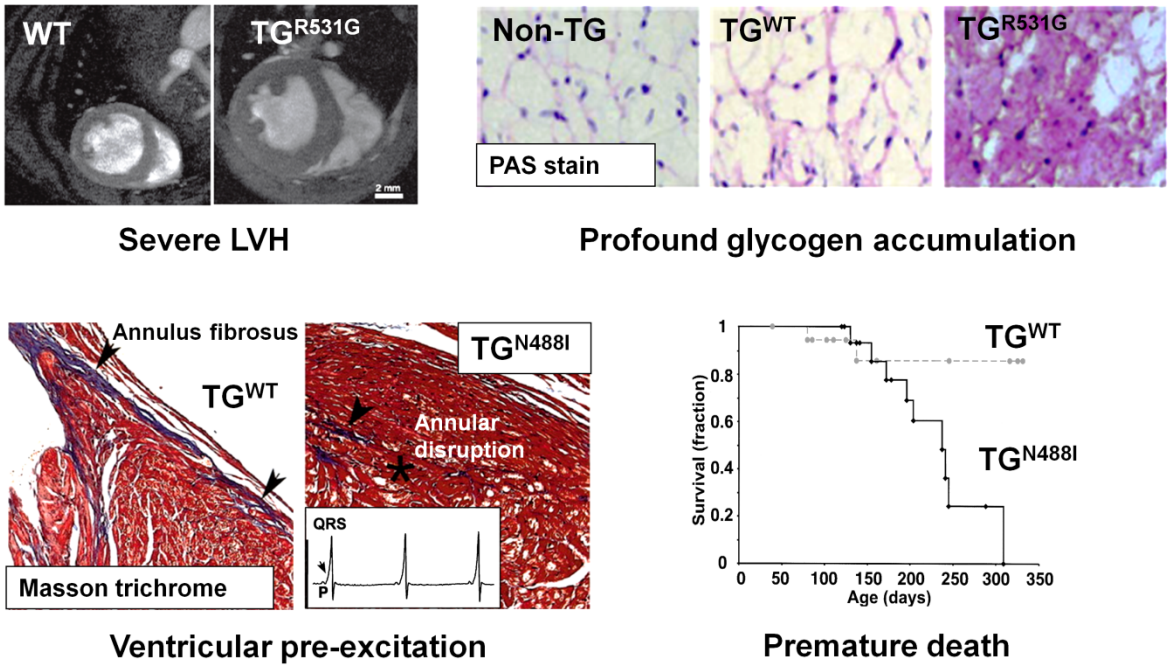


Figure 14. Phenotypic features of transgenic mouse models expressing mutant human γ2 in the heart.[s]

Upper left – mid-ventricular, end-diastolic cine MRI images in the short-axis orientation demonstrating marked LVH in mice carrying the TG^{R531G}. Upper right – PAS staining of control and TG^{R531G} hearts. Lower left – Disruption of the annulus fibrosus (arrow heads) in TG^{N488I} mice (indicated by *), with corresponding ventricular pre-excitation on the surface ECG. Lower right – Kaplan-Meier plot demonstrating poor survival in TG^{N488I} mice compared with TG^{WT}.

1.6.3.a Insights provided by transgenic models into pathogenesis of pre-excitation

Careful electrophysiological and histopathological assessment of the N488I transgenic mutant mouse (TG^{N488I}) model[119, 125] has provided significant insights into the likely aetiology for ventricular pre-excitation in *PRKAG2* cardiomyopathy. Approximately 50% of TG^{N488I} mice were observed to display sinus bradycardia and features suggestive of pre-excitation on the surface ECG, which became apparent in the first few weeks of life (consistent with the temporal expression profile of the α-MHC promoter[123]). Invasive *in vivo* electrophysiological studies, in conjunction

[s] Adapted from figures 2 & 4 Davies et al. *Am J Physiol Heart Circ Physiol* 2006;290:H1942-H1951 and figures 4-6 Arad et al. *Circulation* 2003;107:2850-2856.

with pharmacological challenge, confirmed the presence of atrioventricular connections outwith the normal atrioventricular (AV) node-His pathway that were: sensitive to procainamide (a class Ia antiarrhythmic agent which depresses conduction relatively selectively in accessory pathways over the AV node[105]), resulting in prolongation of the abnormally short PR interval and QRS interval narrowing; resistant to adenosine (an AV nodal blocking agent), which caused AV block in all WT transgenic (TG^{WT}) but no TG^{N488I} mice with apparent pre-excitation on the surface ECG[125]. Serial AV node sectioning revealed post-natal disruption of the annulus fibrosus (a ring of dense connective tissue that normally electrically insulates the ventricles from inappropriate excitation by the atria) by vacuolated, glycogen-engorged myocytes in TG^{N488I} but not TG^{WT} mice, providing an anatomical substrate (i.e. accessory AV connection) for the observed pre-excitation[119, 125].

1.6.3.b PRKAG2 cardiomyopathy: a novel glycogen storage disorder?

On the basis of the body of data provided by these transgenic models, PRKAG2 cardiomyopathy has been defined as distinct to sarcomeric HCM and styled mechanistically as a metabolic glycogen storage disorder, with virtually all of its clinical manifestations envisioned as secondary to bulk accumulation of glycogen rather than any primary effect of AMPK *per se*[109, 126-128]. In addition to the murine data outlined earlier, several lines of argument support this hypothesis[126]:

i) Several of the clinical features of PRKAG2 cardiomyopathy – particularly LVH and ventricular pre-excitation – closely resemble those seen in classical glycogen storage disorders. These include: infantile Pompe's disease[129] caused by recessive mutations in the gene encoding α-1,4-glucosidase which mediates glycogen degradation; as well as Danon's disease[130], an X-linked dominant condition due to lysosome-associated membrane protein-2 (LAMP2) gene mutations.

ii) Increased glycogen content is observed in the skeletal muscles of pigs harbouring a γ3 variant homologous to the human R302Q γ2 mutation[81] (section 1.6.1).

iii) A series of experiments[112] investigated the preventability and reversibility of PRKAG2 cardiomyopathy in an inducible N488I mutant mouse model using a tetracycline-controlled binary α-MHC-driven system of N488I transgene expression. In this system, oral administration of

tetracycline (or its analogue doxycyline) suppresses mutant protein expression through binding to a tetracycline-controlled transactivator protein, thereby preventing its binding to a tet-responsive promoter (minimal CMV promoter coupled to 7 tandem *tet operator* sequences)[131]. The authors demonstrated that transgene suppression - if instituted prenatally - prevented the development of pre-excitation and partly ameliorated the cardiomyopathy, in association with reduced cardiac glycogen levels[112]. Transgene suppression after 8 weeks of age failed to suppress pre-excitation on the surface ECG or alter electrophysiological properties of accessory pathways, consistent with the notion that a direct or indirect (i.e. glycogen-mediated) effect of AMPK in the perinatal period was critical for *de novo* development or persistence of existing bypass tracts (the latter present prenatally and thought to normally resolve during maturation)[112]. The partial rescue of the mutant phenotype led the authors[112] to propose that modulation of cardiac tissue glycogen content could be used as a clinical therapeutic strategy in PRKAG2 cardiomyopathy.

iv) Extensive evidence links AMPK with glycogen metabolism (section 1.5.5.b). Moreover AMPK influences glucose transport (see chapter 6), with chronic activation of AMPK promoting glucose uptake. Formal confirmation of this as a mechanism to explain the excess cardiac glycogen observed in PRKAG2 mutant hearts came from Rong Tian's group[127], who identified elevated glucose uptake in isolated TG^{N488I} hearts, together with reduced glycolytic flux from exogenous glucose and redirecting of exogenous glucose moieties towards glycogen synthesis. Complementing these changes were a remodelling of glycogen metabolism, with a finding of elevated expression and activity of UDP-glucose pyrophosphorylase (the enzyme catalysing the formation of UDP-glucose from glucose-1-phosphate and UTP) in γ2 mutant mouse hearts[127] (Figure 15). The finding of elevated glucose uptake has also been confirmed in the TG^{T400N} model, in association with elevated expression of a novel sodium-dependent glucose transporter (SGLT-1)[132]. Taken together, both these reports describing enhanced glucose uptake would suggest that the predominate effect of γ2 mutations is to activate AMPK complexes. However, activation of AMPK also phosphorylates glycogen synthase (GS), inhibiting its activity (section 1.5.5.b). A recent study[133] has addressed this apparent paradox by identifying allosteric activation of GS by glucose-6-phosphate (G-6-P) as critical to the promotion of muscle glycogen storage in response to AMPK

activation. Notably, elevated cardiac G-6-P content has been identified in mutant TG^{N488I} hearts[127]. Accordingly, current models[127, 133] for muscle glycogen accumulation in the setting of chronic AMPK activation propose that the effect of enhanced glucose-transport to increase the allosteric activator of GS, G-6-P, outweighs the inhibitory effect of AMPK on GS activity (Figure 15).

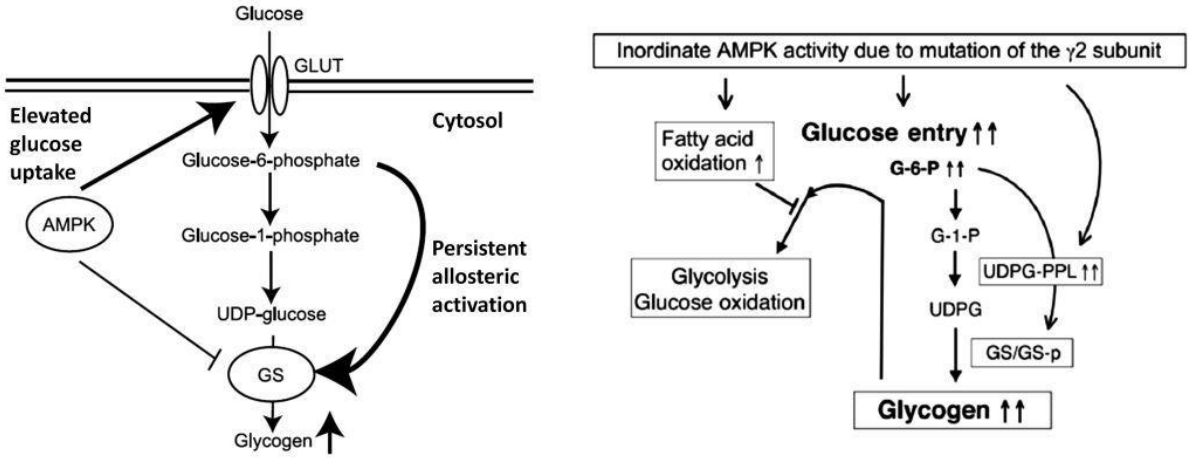


Figure 15. Models for mechanisms underlying muscle glycogen accumulation in association with increased AMPK activity.[t]

Left – Importance of increased G-6-P as an allosteric stimulator of GS activity to promote glycogen formation in the absence of increased glucose utilisation and counteracting the inhibitory effect of AMPK on site 2 of GS.

Right – Remodelling of the intracellular metabolic network in favour of glycogen retention with: inhibition of glucose utilisation (via oxidation and glycolysis) by products of fatty acid oxidation (intramitochondrial pyruvate dehydrogenase inhibition by acetyl-CoA and NADH accumulation, together with phosphofructokinase inhibition by cytosolic citrate[134]); and channelling of intracellular glucose to UDP-glucose synthesis via elevated UDPG-PPL expression[127]. Both models critically rely on enhanced glucose uptake, with chronic antagonism of one glucose transporter (SGLT-1 by phlorizin) leading to a 25% reduction in cardiac glycogen content in TG^{T400N} hearts[135]. Somewhat surprisingly, the only human study[136] investigating glucose uptake in adult patients with the R302Q *PRKAG2* mutation identified *reduced* myocardial glucose uptake compared to controls. This may reflect the dynamic interplay between glycogen accumulation and AMPK activity (mediated via the GBD on the β subunit) to modulate glucose uptake variably, dependent on the stage of the disease (i.e. early with minimal cardiac glycogen effect on AMPK activity versus established disease with marked glycogen accumulation and inhibition of AMPK heterotrimers).

Notwithstanding the evidence linking γ2 mutations to glycogen, the conceptualisation of PRKAG2 cardiomyopathy as purely a novel form of glycogen storage disease[109, 119, 126] (akin to Pompe's

[t] Adapted from figure 8 Hunter et al. *Diabetes* 2011;60:766-774 and figure 6 Luptak et al. *J Clin Invest* 2007;117:1432-1439.

disease) has a number of limitations, suggesting that a more nuanced view of the pathogenic mechanisms underlying the phenotype is appropriate[137]:

i) Emerging clinical reports now recognise the existence of symptomatic, genotype-positive patients with PRKAG2 cardiomyopathy without *any* demonstrable glycogen excess[110, 116], serving to highlight the diversity of clinical disease expression and pointing to the necessity for glycogen-independent disease mechanisms.

ii) Whilst mutant γ2 transgenic mouse models exhibit a marked increase in cardiac glycogen levels (70-fold higher than non-TG in the case of the TG^{R531G} model[121]), in absolute terms this reaches ~30-50 μg/mg wet heart weight for mutant TG hearts that have increased in size by nearly threefold to ~300 mg[119, 121]. This makes passive enlargement of cardiomyocytes by glycogen insufficient to account for all, or even the majority, of increase in cardiac mass observed[94, 121]. Indeed, it has been pointed out that the same is likely to be true of 'traditional' glycogen storage disorders[137]. Furthermore, the finding of increased cardiac expression of several hypertrophy-associated genes (e.g. natriuretic peptide B and β-myosin heavy chain)[121], in addition to early activation of hypertrophic signalling pathways[138] in TG mice overexpressing mutant γ2, argues in favour of true cardiomyocyte hypertrophy (i.e. increase in protein content) in addition to glycogen retention.

iii) Whilst early suppression of an inducible model of N488I transgene expression is able to prevent or reverse ventricular pre-excitation in association with reduction in cardiac glycogen content, it served to delay but not prevent development of the cardiomyopathy[112]. In addition, transgene suppression and modulation of glycogen content had limited efficacy on development of cardiac conduction system disease with, notably, little effect on the bradycardia of mutant mice[112].

iv) Increasing evidence implicates AMPK as a regulator of ion channels through both direct and indirect effects, thereby coupling the high energetic demands of membrane ion transport to cellular energy availability[139, 140]. With regard to cardiac ion channels, adenoviral transduction of rat

ventricular cardiomyocytes with a constitutively active mutant form of AMPK-α1 (CA-AMPK-α1) has been shown to prolong action potential duration[141]. Furthermore, use of a mammalian heterologous expression system to co-express recombinant human heart sodium channel ($Na_v1.5$) and CA-AMPK-α1 resulted in altered biophysical properties of $Na_v1.5$, with slowing of channel inactivation and a hyperpolarizing shift in the voltage activation curve[141]. Delayed inactivation of sodium channels, with consequent prolonged sodium current influx and action potential prolongation, can predispose to arrhythmia[142]. Furthermore, ZMP (the AMP-mimetic metabolite of the AMPK activator AICAR) has been shown to activate rat ventricular K_{ATP} channels, an effect lost in the presence of the AMPK inhibitor, compound C[143].

Clinical reports have now identified mutation carriers who exhibit striking combinations of conduction block in one cardiac structure (e.g. right bundle branch block), with accelerated conduction in another (e.g. in the AV node giving rise to a short PR interval but no evidence of pre-excitation on invasive testing)[113]. Thus, whilst the development of pre-excitation would appear to be critically related to excess cardiac glycogen[112], the full range of electrophysiological disturbances observed in PRKAG2 cardiomyopathy (including sinus bradycardia, atrial fibrillation, atrial flutter or other supraventricular tachycardia, advanced atrioventricular block and bundle branch block), are likely to reflect both direct (modification of ion channel function and/or expression) and indirect (e.g. a putative glycogen-mediated reduction in cellular pH with subsequent alteration of channel kinetics[128]) effects of mutant γ2-containing AMPK complexes.

1.6.4 Effect of PRKAG2 mutations on AMPK activity

The majority of the identified PRKAG2 disease-causing mutations occur within or in close proximity to the CBS domains, suggesting that they may disrupt the energy sensor function of AMPK by interfering with its ability to bind AMP, ADP and/or ATP (Figure 16).

The description of the crystal structure of the regulatory fragment of mammalian AMPK (comprising the C-terminal domains of the α1 and β2 subunits and full length γ1 subunit in complexes with AMP and ATP) provided structural support for the hypothesis that γ2 mutations directly interfere with adenine nucleotide binding by AMPK[23]. Mapping of the corresponding

residues onto γ1 revealed that nearly all mutations involve amino acids with side chains in close proximity to the adenyl binding site, with several directly involved in co-ordination of the nucleotide phosphate groups (Figure 17). The importance of these residues is further suggested by the fact that many (e.g. R302, H383, R384 and R531, numbered according to human γ2) are conserved in all known vertebrate and invertebrate γ sequences[144]. Furthermore, the location of several of the γ2 point mutations occurs in structurally equivalent positions in other hereditary diseases involving human CBS proteins, for example R302Q in γ2 aligns with the D444N mutation in cystathionine-β-synthase that causes homocystinuria[145].

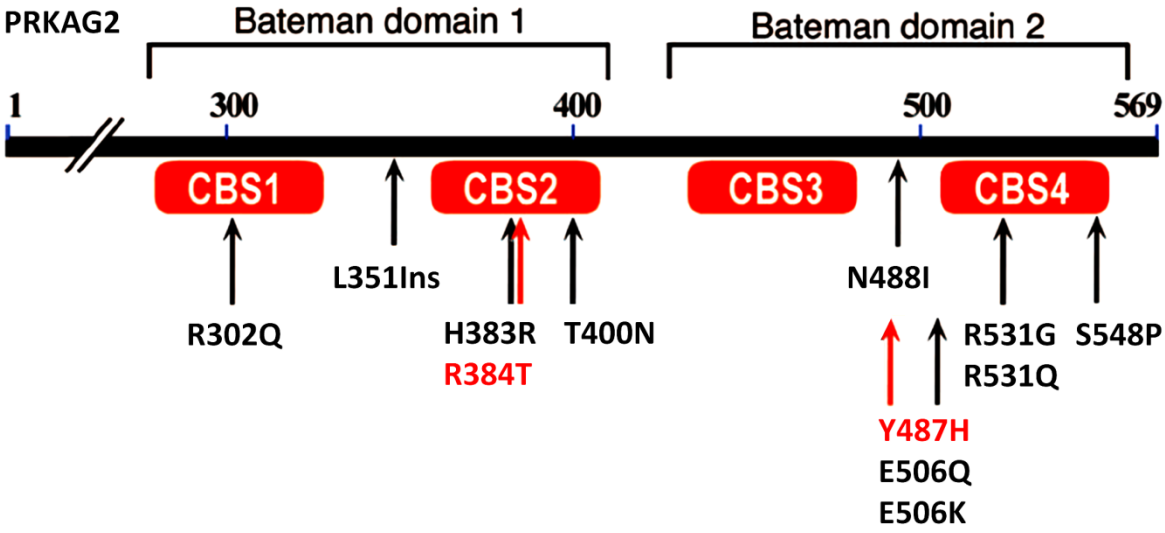


Figure 16. Location of human mutations identified to cause PRKAG2 cardiomyopathy.[u]

A significant number of pathogenic PRKAG2 mutations occur in equivalent positions in CBS domains. For example, the R302Q, H383R and R531G mutations occur in three separate CBS domains, but all align with each other and with a naturally occurring mutation in CBS1 of porcine PRKAG3 (R200Q) [38]. Further support for the functional significance of these residues comes from the first described mutation in the human γ3 isoform – R225W – causing an analogous phenotype to the porcine RN⁻ mutation and homologous in location to the R302Q mutation in γ2 [89].

Given the varying effects of adenyl nucleotides on AMPK activity (i.e. promotion of activation by AMP/ADP and inhibition by ATP, section 1.5.2), the net effect of mutations interfering with their binding on γ2-specific or total AMPK activity to cause gain- or loss-of-function is not simple to predict. However, γ2's status as a minority isoform within the heart[41] would suggest that loss-of-function of one γ2 allele (i.e. haploinsufficiency) is inadequate to cause a dominant Mendelian

[u] Adapted from: figure 4 Akman et al. *Pediatr Res* 2007;62:499-504 and figure 3 Kim et al. *Acta Physiol* 2009;196:37-53.

disorder. In conjunction with the view of AMPK as being largely quiescent in the unstressed state[146], this would in principle suggest that γ2 mutations result in an abnormal gain-of-function.

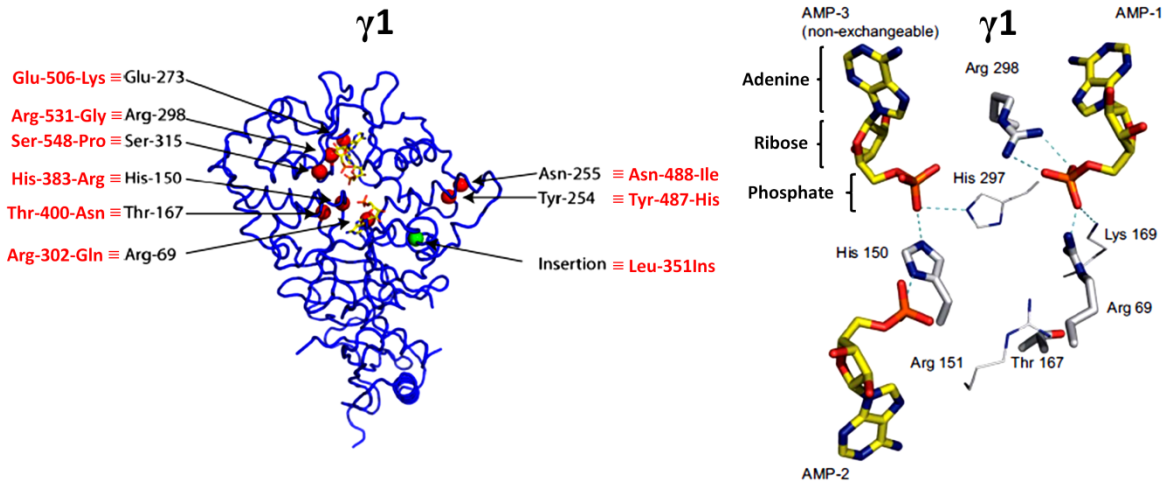


Figure 17. Mapping of human γ2 mutations onto the crystal structure of mammalian γ1.[v]

Left – Worms representation of the γ subunit of AMPK complexed with AMP, with superimposed γ2 mutations (red) depicted as equivalent residues in γ1 (black).

Right – Ball-and-stick representation of the interactions between the primarily basic residues from the γ subunit with the phosphate groups of bound AMP molecules. Interacting residues that have been implicated in causing PRKAG2 cardiomyopathy are indicated with thicker bonds.

Several groups have sought to address the functional consequences of these mutations on AMPK activity *in vitro*[38, 147]. Consistent with an interruption of adenyl binding sites, early studies identified the majority of mutations assessed as causing defective activation by AMP *in vitro*[38, 147]. Using a human cell line (CCL13, regarded as a HeLa cell variant), no significant differences were found in total AMPK activity of rapidly-lysed cells transfected with mutant γ2 compared with WT γ2, arguing against a basal gain-of-function[38]. However, use of a slower lysis procedure – which is associated with a marked stress-induced activation of WT γ2 complexes – was found to cause less AMPK activation in cells transfected with mutant γ2, suggesting that the major biochemical consequence of the mutations was *loss* of AMPK activation in response to stress[38]. These results contrasted with findings from two indirect approaches to assess mutation impact on holoenzyme activity: one study[88] utilised a mutation in γ1 (R70Q) equivalent to that causing excess muscle

[v] Adapted from figure 4 and figure accompanying supplementary table 2 Xiao et al. *Nature* 2007;449:496-500.

glycogen storage in Hampshire pig (R200Q); whilst the other[82] introduced mutations (T400N and N488I) into the yeast γ subunit homologue (Snf4) and analysed interaction with Snf1 (the α subunit homologue). Both studies provided support for *increased* basal AMPK activity. Burwinkel et al.[106] shed light on these conflicting results in their report of a novel sporadic PRKAG2 mutation presenting with a florid cardiac phenotype in three neonates and resulting in death in all by three months of age. The causal heterozygous R531Q missense mutation in PRKAG2 was characterised biochemically and identified to induce a striking >100-fold reduction in binding affinities for both AMP and ATP (the most severe described). Furthermore, it was observed to induce a 3.5-fold increase in basal AMPK activity when expressed in HEK293 cells, the latter correlating with elevated phosphorylation of AMPK α-Thr172 and ACC [106]. Critically, the authors[106] utilised a mammalian cell line which expresses the major upstream AMPK kinase, LKB1. Both studies[38, 147] which did not identify evidence of increased basal AMPK activity consequent to γ2 mutations utilised CCL13 cells which are now recognised to not express LKB1. Overall, these data are consistent with the concept that, in the presence of adequate upstream LKB1, the described PRKAG2 mutations cause increased basal activity of AMPK (due to impaired binding of ATP), but also significantly blunt or abolish stimulation by AMP[146].

Activity assays of AMPK complexes derived from cardiac tissue of transgenic mice overexpressing mutant γ2 have also been undertaken in an attempt to define the effects of these mutations on AMPK activity in the heart. In common with findings from studies utilising transient expression of γ2-containing complexes in mammalian cells, these too have yielded somewhat conflicting results. Thus, α1 and α2 subunit-associated basal AMPK activity was found to be elevated in the TG^{N488I} model[119], whilst total and γ2-specific AMPK activity were found to be markedly reduced compared to non-transgenic controls in the TG^{R302Q} model[120] and similarly in the TG^{R531G} model[121] (the latter with no difference at 1 week however). These differences might be reconciled by inferring that different γ2 mutations exert divergent influences on AMPK, but how these converge to produce a strikingly similar murine phenotype is difficult to envisage.

The observation that age influences the observed AMPK activity in these TG models was critical to potentially explaining these discrepant findings[121]. The dynamic nature of this over time[122] (with AMPK activity peaking by 2 weeks but falling below WT controls by 4 weeks), coupled with the finding that the activity of γ1-containing complexes was also markedly reduced in older mice[121], pointed to a non-intrinsic factor influencing the activity readings. The most obvious candidate for this was the steady accumulation of glycogen with age and this has been shown to inversely correlate with AMPK activity in the TG^{T400N} model[122]. Examining the R302Q mutation, a recent study utilising both transgenic mice and acute adenoviral transduction experiments involving neonatal rat cardiomyocytes[124] has delineated the acute (i.e. primary) effects of a γ2 mutation versus chronic effects (i.e. potentially influenced by compensatory changes) on AMPK activity. Adenoviral-mediated overexpression of R302Q mutant γ2 in isolated cardiomyocytes resulted in increased total AMPK activity, whilst activity was seen to be clearly reduced from AMPK complexes isolated from hearts of adult TG^{R302Q} mice[124].

Further strong support for the notion that inappropriate basal γ2-associated complex *activation* is the prime driver of the cardiomyopathy associated with PRKAG2 mutations comes from the study of compound heterozygous mice overexpressing both mutant N488I γ2 (TG^{N488I}) and a dominant negative α2 ($TG\alpha2^{DN}$) in the heart (the latter overexpressing an inactive form of α2 resulting in a selective reduction in α2 subunit activity)[148]. Compared to TG^{N488I} mice, compound TG^{N488I}/ $TG\alpha2^{DN}$ mice have a marked reduction in LVH and cardiac glycogen content, together with increased (i.e. improved) PR interval and normalised cardiac function[148].

1.7 Why another model of PRKAG2 disease?

1.7.1 Unanswered questions

Despite the undoubted success of the existing overexpressing TG models in recapitulating much of the gross phenotype (section 1.6.3), key questions relating to the human disease remain unanswered, including: whether PRKAG2 cardiomyopathy represents a form of primary LVH (akin to sarcomeric HCM) or a glycogen storage disease; what aspects of the human phenotype, if

any, are due to *primary* effects of the mutation rather than secondary manifestations of excessive glycogen accumulation; what are the mechanisms underlying the widespread conduction system disturbances (sinus bradycardia, AV block, bundle branch block) which, whilst having attracted far less scientific attention than pre-excitation, are still a major source of morbidity and mortality associated with the disorder; whether PRKAG2 mutations activate[148], inactivate[120, 121] or impose a more complex effect[149] on AMPK either in humans or using non-over expressant models which more faithfully reflect the disease at a molecular level. From a physiological viewpoint, the potential role(s) of the γ2 subunit have received very little attention beyond the heart. In other words, 'does γ2 play a wider role outside the myocardium'? This question cannot be explored using existing overexpressing transgenic platforms due to their cardiac-restricted expression however.

1.7.2 Transgenesis

First described in 1980, transgenesis involves injection of linearised foreign DNA into one or both pronuclei of zygote-stage embryos[150-152]. A basic transgenic construct consists of the critical elements required for gene expression: a promoter (determining the temporal and spatial pattern of transgene expression) in the 5'-flanking region fused to the protein-coding sequence (usually full-length cDNA derived from the RNA of interest and including a Kozak consensus sequence to direct the ribosome to the start codon, thereby permitting efficient translation of mRNA; ATG translational start codon; and a terminal stop codon), followed by a 3'-end transcriptional stop sequence (e.g. from human growth hormone including a polyadenylation signal)[153].

Upon injection, the transgenic construct can randomly integrate into the host genome, typically as tandem head-to-tail concatemers early in development – often at a single locus – and usually present in all cells of the subsequent mouse[153]. Several surviving injected embryos are then surgically implanted into the oviducts of a pseudopregnant recipient female (generated by mating a fertile female with a vasectomised male) and allowed to progress to term. The resulting offspring are then tested for the presence of the transgene to identify founder mice (F0), with each founder possessing variable copy number and unique insertional site(s). These F0 founders are then crossed with WT mice to generate (assuming non-mosaicism and germ-line carriage of the transgene by the

founder) F1 offspring inheriting the transgene in half of cases[153]. Given the potential for insertional mutagenesis (due to random transgene integration) and variable transgene copy number, analysis of multiple independent F1 lines is required to ensure that the observed phenotype is due to the introduced coding sequence rather than disruption of a native gene and, ideally, to identify lines with lower copy number (minimising risk of an artefactual phenotype consequent upon abnormally high protein expression)[154]. Importantly, the endogenous gene is unaffected by introduction of the transgene, therefore the generation of a phenotype is dependent on the transgene protein product exerting a dominant effect over native protein[151].

1.7.3 Limitations of existing transgenic models of PRKAG2 cardiomyopathy

The interpretation of findings from the published mouse models of PRKAG2 cardiomyopathy is complicated by a number of factors inherent to the transgenic approach and, in particular, the use of the α–MHC promoter.

1.7.3.a Failure to reflect native γ2 splicing and temporal expression patterns

Interpretation of the phenotype of the transgenic models is confounded by use of the α-MHC promoter to drive transgene expression. The α-MHC promoter undergoes transient activation in the early heart tube, followed by atrial expression throughout development but minimal ventricular expression until very shortly before birth, whereupon its expression markedly increases[123].

Several γ2 isoform splice variants are recognised, with their expression profiles recently assessed in the heart[49]. The precise role(s) of these alternative γ2 transcripts is currently unknown but, given the key regulatory role of alternative splicing in influencing proteome diversity, they may function to allow the generation of multiple, non-redundant γ2 isoforms with potentially different substrate specificity, subcellular localisation, or ability to engage in protein-protein and protein-DNA interaction[155]. Therefore, altering endogenous splicing patterns has the ability to modify the cell's protein repertoire and, ultimately, its function[131]. Bearing in mind that γ2 subunits are expressed during cardiac development, use of the α-MHC promoter, which is powerfully active only after birth[123], will also result in aberrant temporal expression of γ2 (Figure 18). Indeed, current murine transgenic models for PRKAG2 cardiomyopathy overexpress full-length (i.e. γ2 long form)

PRKAG2 postnatally at high levels, a scenario which contrasts with its identification as a minority splice variant in normal adult human heart[49].

1.7.3.b Overexpression of mutant or WT γ2 disturbs normal γ isoform stoichiometry

On the basis of contribution to total AMPK activity, γ2 is a minority isoform in the heart[41]. The use of the α–MHC promoter results in dramatic over-representation of exogenous γ2 subunits causing a reversal of physiological γ1:γ2 cardiac stoichiometry (Figure 18).

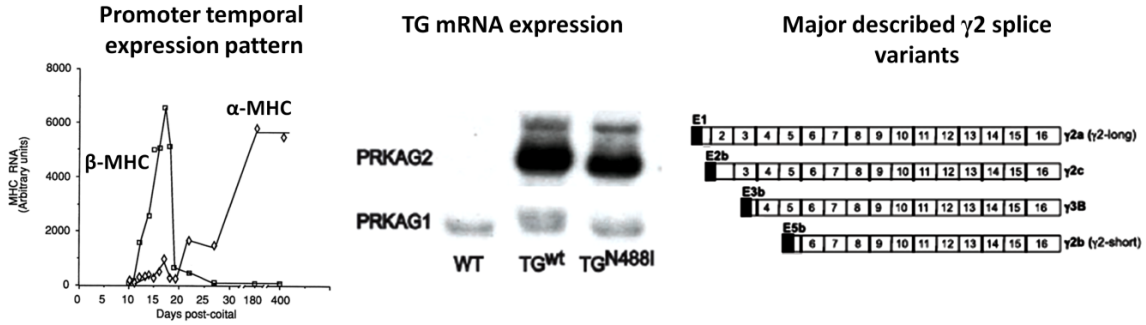


Figure 18. Current overexpressing mouse models for PRKAG2 cardiomyopathy have limitations inherent to their transgenic design and use of the α-MHC promoter.[w]

Left – Relative levels of α-MHC and β-MHC mRNA in the developing mouse heart illustrating predominately postnatal expression of α-MHC.

Middle – Northern blot analyses using *PRKAG1* and *PRKAG2* cRNA probes to assess cardiac γ isoform expression in the TG^{N488I} mouse model and its controls, illustrating the reversal of normal γ1:γ2 stoichiometry.

Right – Schematic representation of γ2 splice variants described in mammalian heart.

1.7.3.c Consequences of overexpression of the γ subunit

Whilst cardiac-specific transgenesis remains the basis for the majority of murine models of cardiovascular pathology, transgene expression at very high levels can result in unphysiological consequences and does not accurately reflect levels of expression observed in disease states[151]. As a corollary of this, exacerbated by the random site and copy number integration of transgenes, overexpressing even WT γ2 in the mouse induces LVH, upregulation of associated hypertrophy markers, significant glycogen retention and dynamic changes in AMPK activity (Figure 19)[124, 125].

The magnitude of the increase in glycogen content as a result of overexpression of γ2 in TG^{WT}

[w] Adapted from figure 2 Ng et al. *Circ Res* 1991;68:1742-50, figure 1 Arad et al. *Circulation* 2003;107:2850-6 and figure 7 Pinter et al. *J Mol Cell Cardiol* 2012;53:342-9.

hearts – although significantly lower than mutant TG hearts – is still not trivial, accounting for a 10-fold increase over non-TG WT hearts[124]. Of potential significance in this regard is the consistent finding of increased expression of β2 in both TG^{WT} and TG mutant hearts[121, 124], prompting the suggestion that overexpression of γ2 may exert specific effects on β2 expression or stability[124] and potentially bring about changes that promote AMPK-glycogen complex aggregation[34].

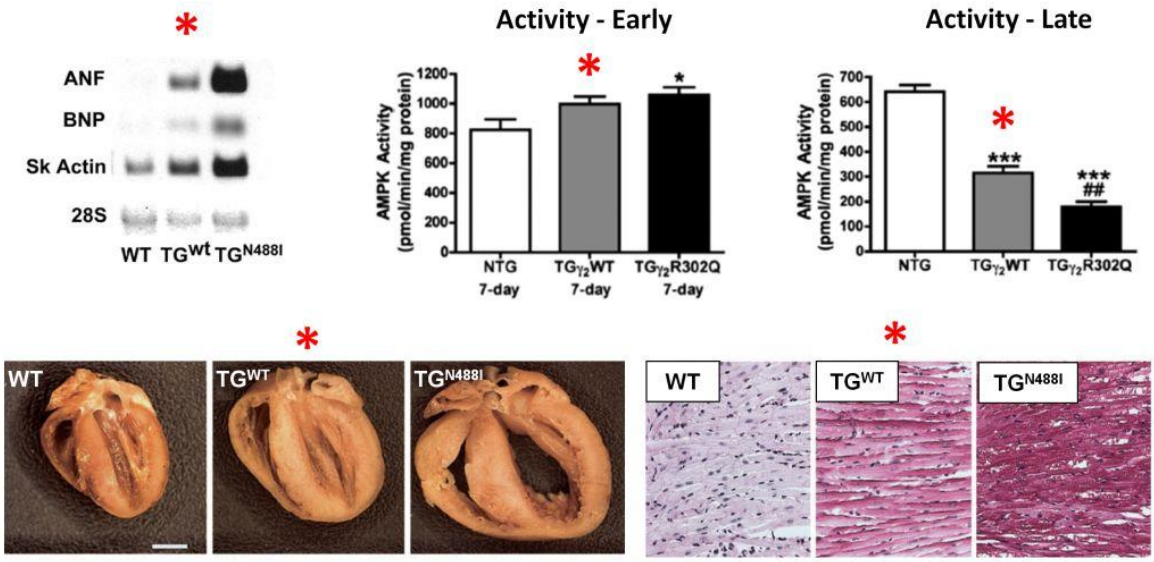


Figure 19. Cardiac overexpression of WT γ2 (TG^{WT}, *) induces an abnormal phenotype.[x]

Upper panel: left – Transcript expression of hypertrophy-associated genes in TG^{N488I} hearts and their TG and non-TG WT controls; middle/right – early and late total AMPK activity of TG^{R302Q} and control mice.

Lower panel: left – gross visual appearances of TG^{N488I} and control hearts; right – corresponding PAS stain appearances.

Why simple overexpression of WT γ2-subunit complexes should induce significant glycogen accumulation is unclear, but a study has demonstrated that co-expression of α and γ with full-length β (but not truncated β-subunits lacking the glycogen-binding domain) causes the accumulation of striking inclusions co-staining for the β-subunit and for glycogen or glycogen synthase[34].

Notably, whilst there are clear confounding factors associated with simple overexpression of γ2 in the interpretation of current mutant γ2 transgenic models, the degree of increase in glycogen content, altered AMPK activity and hypertrophy are insufficient to induce ventricular pre-excitation. This would suggest that mutant γ2-containing AMPK complexes themselves have

[x] Adapted from figures 2 and 3 Arad et al. *Circulation* 2003;107:2850-2856 and figure 1 Folmes et al. *Circ Cardiovasc Genet* 2009;2:457-66.

either: a specific effect on inducing the development or failure of normal embryonic resorption of accessory pathways (e.g. through influencing cardiac transcription factors regulating AV septation or conduction system patterning)[91, 103]; and/or that extreme levels of glycogen accumulation (not reached in the TG^{WT} model) are required to induce pre-excitation[124] through anatomical disruption of the AV node[119, 125], potentially in concert with perturbed cardiomyocyte conduction characteristics. The murine transgenic data[119, 125] provide support for the concept that pre-excitation is mediated via structural disruption of the annulus fibrosus by glycogen-laden myocytes, rather than true muscular accessory bypass tracts; furthermore, that this must occur during embryonic development or the early neonatal period[112]. In contrast, a clinical report[110] has identified the existence of multiple, genuine nodoventricular (Mahaim type) accessory pathways in an R302Q mutation carrier with antecedent invasive electrophysiological evidence of pre-excitation, but no increased cardiac glycogen over control hearts. Taken together, this data is suggestive of multiple (non-mutually exclusive) direct and indirect mechanisms whereby mutant *PRKAG2* promotes accessory pathway formation and/or persistence during or shortly after development.

1.7.4 Gene-targeting

An alternative to using random insertional transgenesis to model disease is the use of gene-targeting, the technology development of which was awarded the 2007 Nobel Prize in Physiology or Medicine. This utilises homologous recombination in embryonic stem cells (ES cells) to allow precise manipulation of genes within their endogenous chromosomal context[152]. Homologous recombination refers to the exchange of genomic sequences between homologous allelic sequences and is responsible for repair of harmful double-strand DNA breaks, as well as contributing to genetic diversity during meiosis. Murine ES cells are derived from the inner cell mass of normal blastocyst embryos and have the capacity to divide in culture and remain pluripotent, i.e. they can differentiate into any cell type[156]. Use of homologous recombination to introduce a new genetic sequence with a precise genetic alteration (e.g. a pathogenic mutation) into a specific genetic locus is utilised to generate a 'knock-in' mouse[152]. More commonly, though, gene-targeting has been used to generate 'knock-out' mice which have a defined non-functional allele; either by replacing

and thereby disrupting coding sequences of a gene with irrelevant DNA (e.g. a drug-selection marker), or by the use of targeted deletion to remove a critical region of the gene[152].

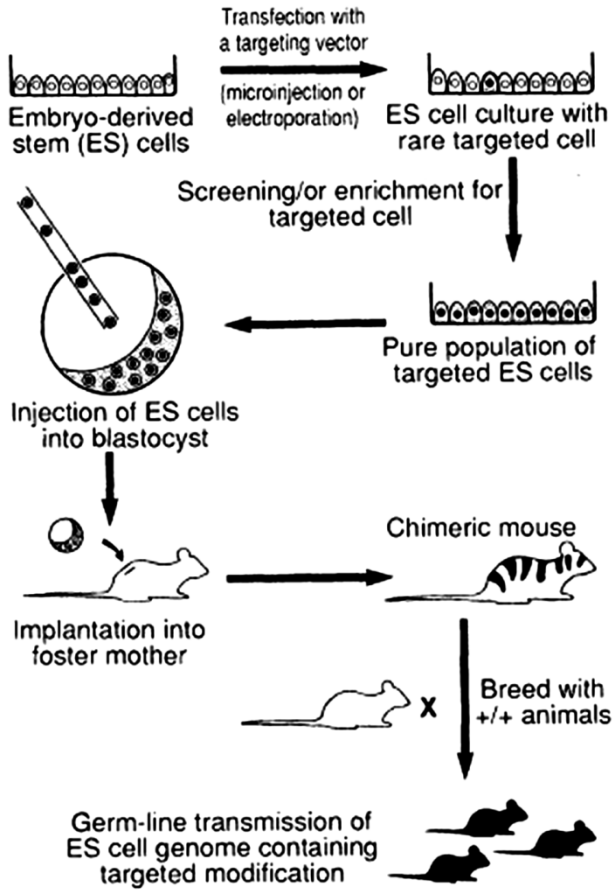


Figure 20. Generation of gene-targeted knock-in or knock-out mice.[y]

Gene-targeting to generate a knock-in (KI) or knock-out (KO) mouse involves the introduction of a DNA targeting construct, containing regions of homology (or identity) to the gene or locus of interest into murine pluripotent ES cells, traditionally from the 129 inbred strain and usually by electroporation[152, 156]. The regions of homology both flank a central region which contains the desired sequence to be introduced, together with a positive selection marker such as the neomycin resistance gene. Positioned outside of the flanking regions of genetic homology is a toxic negative selection marker, such as the diphtheria toxin gene (DTA), which will remain intact (and therefore express lethally in the host cell) if incorporated into the host genome by random non-homologous integration, but is spliced out (and therefore absent) when homologous recombination occurs[156].

[y] Adapted from figure 1 Capecchi *Science* 1989;244:1288-92.

Given that homologous recombination is an extremely rare event in mammalian cells – with the great majority of transfected ES cells undergoing scattered non-homologous recombination events – this strategy permits the identification of correctly targeted ES cells in culture, based on concomitant positive (e.g. expression of the neomycin drug resistance cassette conferring ability to survive in the presence of G418) and negative (e.g. lack of DTA expression) selection strategies.

Correctly recombined ES cells are then microinjected into a 3.5 day old blastocyst (10-15 ES cells/host embryo), typically from the C57BL/6 mouse strain, with subsequent transfer to a pseudopregnant female to complete gestation (Figure 20). The resulting animal is chimeric, being composed of cells from both the donor ES cells and the original host blastocyst. If the original ES cells were 129 strain-derived (with the agouti coat colouration) and the blastocyst from a C57BL/6 strain (which possesses black coat colouration), the resulting chimeras will have patches of lighter agouti and darker C57BL/6-derived fur, the ratio of which can give an indication of the degree of chimerism. Subsequently, male founder chimeras (those judged to have high amounts of chimerism based on coat colour) are out-bred to female mice to confirm germline transmission[152, 156].

1.7.5 Novel gene-targeted model of PRKAG2 disease: R299Q γ2 knock-in

In order to circumvent the disadvantages inherent to a transgenic strategy for *in vivo* modelling of PRKAG2 cardiomyopathy and to more precisely reflect the human genetic alteration, the R302Q mutation was introduced (through gene targeting) into the equivalent position (R299Q) of the orthologous murine *Prkag2* (Figure 21). Whilst having the potential to mimic the human disease in a more subtle manner than existing overexpressing transgenic models, the R299Q γ2 KI was designed to be more faithful genetically in retaining physiological levels of expression by the native promoter and undergoing regulation by endogenous control mechanisms.

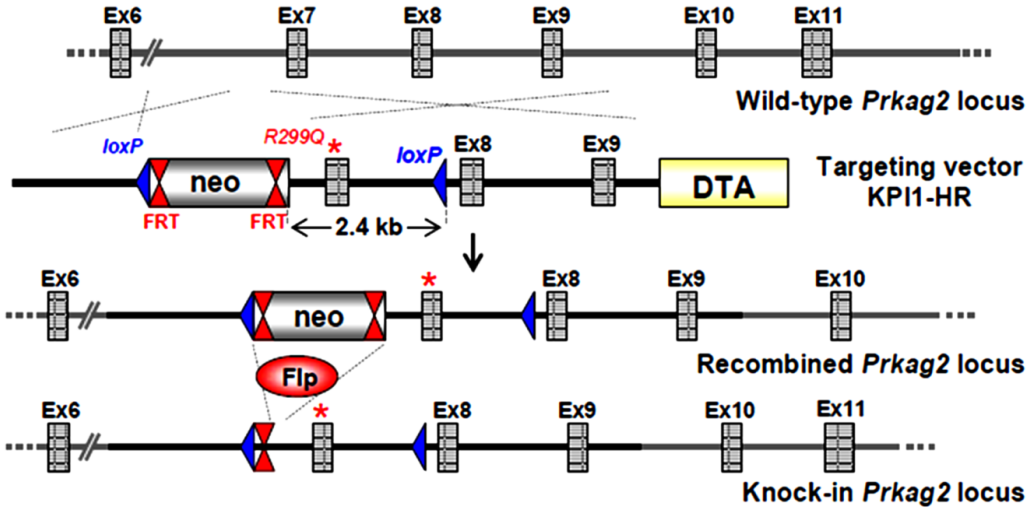


Figure 21. Gene-targeting strategy used to introduce the R299Q point mutation (denoted by *, equivalent to the human R302Q mutation) into exon 7 of murine *Prkag2*. The targeting strategy included insertion of a *loxP* site together with a *FRT* flanked neomycin selection cassette (*neo*) within intron 6 upstream of the R299Q mutated exon 7 and a single distal *loxP* (locus of crossover [x] in P1) within intron 7 downstream of the mutation. Founder lines were bred with constitutively expressing Flp recombinase[z] deleter mice to remove *neo* and generate R299Q heterozygote floxed mice. The KI targeting vector, KPI1-HR, was constructed by Dr Katalin Pinter (Oxford) with recommendations from GenOway (Lyon, France). Subsequent homologous recombination steps in 129/Ola ES cells, blastocyst injection, chimera generation and breeding to the F1 generation were conducted by GenOway.

As an additional feature, the targeting strategy permitted generation of a γ2 KO model by crossing KI mice with mice expressing Cre recombinase (the latter recognising and binding to *loxP* sites, inducing recombination to remove the intervening segment[157]).

[z] As with Cre, Flp is a site-specific recombinase that is able to recombine specific DNA sequences, termed *FRT* (Flp recombinase recognition target) with high fidelity. As with *loxP*, *FRT* sites consist of two inverted repeat (palindromic) sequences, with an intervening 8 bp asymmetric 'spacer'.

1.8 Hypothesis and aims

1.8.1 Hypothesis

Existing transgenic mouse models for PRKAG2 cardiomyopathy recapitulate many aspects of the human cardiac phenotype. However, their lack of genetic precision results in an extremely florid cardiac phenotype, whose interpretation is confounded by unphysiological levels of γ2 overexpression, altered γ isoform stoichiometry and a disregard for the endogenous gene regulatory mechanisms (section 1.7.3). Beyond a clear role for glycogen in some aspects of the disease phenotype (notably ventricular pre-excitation), underlying disease mechanisms, or potential primary molecular changes directly consequent to the γ2 mutation and independent of glycogen, have not been clearly delineated. Moreover, the use of a cardiac-specific promoter limits the ability of these models to provide any insights into the described extra-cardiac features of PRKAG2 disease or to probe the wider biological role of γ2 beyond the heart, an area of scientific enquiry that remains poorly annotated.

By reflecting more precisely the genetic alteration present in the human disorder than currently available transgenic models, the specific hypotheses of this thesis are that the R299Q γ2 knock-in mouse model of the human R302Q γ2 mutation will:

i) model the human disease in a more subtle manner;

ii) provide an *in vivo* platform with which to dissect the primary effects of the mutation on AMPK activity and phenotype from those consequent to excess glycogen[aa];

iii) enhance our understanding of the mechanisms underlying PRKAG2 disease;

iv) provide novel insights into the potential extra-cardiac role(s) of γ2 and the consequences of chronic modulation of (γ2-specific) AMPK activity *in vivo*.

[aa] Largely based on hypothesis (i) that precise gene-targeting of *Prkag2* with a point mutation would engender a significantly more subtle phenotype than marked overexpression of mutant γ2 using the α-MHC promoter.

1.8.2 Thesis aims

Based on the aforementioned hypotheses, this thesis seeks to characterise the cardiac phenotype and delineate the underlying mechanisms in the newly-generated R299Q γ2 KI mouse model of PRKAG2 cardiomyopathy, in addition to evaluating the systemic consequences of the gene-targeting experiment.

Accordingly, the specific aims of this thesis (with relevant chapter numbers in parentheses) are:

Aim 1 - To validate the novel R299Q γ2 KI model with respect to confirming tissue expression and ascertaining effect on AMPK activity (chapter 3).

Aim 2 - To characterise the baseline cardiac phenotype of R299Q γ2 KI heterozygote (Het) and homozygous (Homo) mutant mice in comparison to WT littermate controls with respect to cardiac morphology, contractile function and electrophysiology (chapters 3 and 4).

Aim 3 - To follow-up cardiac phenotypic lead(s) to define novel underlying cellular/molecular pathomechanisms (chapter 4).

Aim 4 - To begin to explore the physiological role(s) of γ2 in the heart by generating the first-described γ2 KO mouse model (chapter 5).

Aim 5 - To undertake an assessment of the systemic effects of gene-targeting *Prkag2* with the R299Q mutation by assessing the systemic metabolic phenotype and, if present, delineate the underlying mechanisms involved (chapters 6 and 7).

Chapter 2. Materials & Methods

For completeness, all of the techniques used in this thesis are listed here, together with details of those general methods and techniques used in more than one data chapter.

Chapter-specific methods are listed here only and detailed further within the relevant chapter. All chemicals were obtained from Sigma-Aldrich unless stated otherwise.

2.1 Animal care, genotyping and general tissue extraction

2.1.1 General husbandry

Mice were bred and maintained in a specific pathogen-free facility in individually ventilated cages (IVCs, Techniplast, Milan, Italy) with controlled temperature (20-22°C), humidity and exposure to a 12-hour light-dark cycle. All animals were maintained on a standard rodent chow diet (Teklad Global Diet: 16% protein, 4% fat; Harlan Laboratories, UK), except where indicated for short-term fasting for experiments. Water was provided *ad libitum*. Animal procedures were carried out in accordance with the 1986 British Home Office Animals Scientific Procedures Act (UK), or conformed to the European directive (86/609/CEE) on care and use of laboratory animals (Milan, Italy) and in both cases were approved by the local university ethics review committee.

2.1.2 Mice

2.1.2.a R299Q γ2 knock-in (KI) mice

Mice heterozygous for the R299Q γ2 KI mutation were generated by GenOway (Lyon, France), with several heterozygous mutant mice on a mixed C57BL/6/129/Ola genetic background subsequently transferred to Oxford for generation of a colony. Mice heterozygous (Het) or homozygous (Homo) for the R299Q γ2 KI mutation were used for all experiments. Age- and sex-matched WT littermates obtained from heterozygous crossings were used as controls for all experiments. Initial cardiac experiments (echocardiography, invasive haemodynamics and MRI) were performed on a mixed C57BL/6/129/Ola genetic background, with subsequent experiments performed on mice backcrossed for 7 generations to C57BL/6.

2.1.2.b C57BL/6

Inbred C57BL/6 mice were obtained from Harlan laboratories and used for backcrossing genetically-modified mice onto an inbred background and dose-range finding studies for central mechanistic work.

2.1.2.c Sox2cre

Sox2cre mice and the generation of Sox2cre γ2 knock-out mice are described in chapter 5.

2.1.3 Genotyping

Ear-notching was used to identify individual mice and obtain tissue for genetic identification.

2.1.3.a DNA extraction

Ear-notch tissue was incubated at 50°C overnight in 500 µL of lysis buffer (50 mM Tris-HCl, 100 mM ethylenediaminetetraacetic acid [EDTA], 100 mM NaCl, 1% sodium dodecyl sulphate [SDS]) containing 0.2 mg/mL proteinase K (Bioline). DNA was precipitated by addition of 500 µL ice-cold isopropanol, gentle inversion of the microfuge tube and placement on ice for 20 minutes. The DNA was pelleted by centrifugation at 13,000 x g for 15 minutes. The supernatant was carefully removed and the pellet washed with 70% ethanol. After repeating the centrifugation step and discarding the supernatant, the pellet was allowed to air dry, facilitated by use of a heat block (60°C for 10 minutes). Pellets were then resuspended in Tris-EDTA buffer (50 µL/pellet), aided by use of a heat block followed by gentle shaking at room temperature (RT) for 1 hour. DNA was then quantified by spectrophotometry (Nanodrop ND-1000, Wilmington, DE) and genotyping subsequently performed by polymerase chain reaction (PCR) amplification and agarose gel electrophoresis separation and visualisation of products.

2.1.3.b Polymerase chain reaction (PCR) for R299Q γ2 knock-in genotyping

PCR was performed using a forward primer hybridising upstream of the *loxP-FRT* sequence in intron 6 of *Prkag2* and a reverse primer hybridising downstream of the *loxP-FRT* sequence, with both primers upstream of the R299Q mutated exon 7 (illustrated in chapter 3). By virtue of the

loxP-FRT sequence, mutant and WT PCR products were distinguishable using agarose gel electrophoresis (475 and 352 base pairs, bp, respectively). Genotyping primer sequences were:

Forward primer (KPI1-H1) 5'-CACCTGAAGTTGCCGTGTGACCTCC-3'

Reverse primer (KPI1-H2) 5'-GAGGCATTTCCTCAAGGGAGGCTCC-3'

The original PCR protocol utilised by GenOway was optimised and reactions were set-up on ice and run on a thermal cycler (DNA Engine Tetrad 2 Peltier thermal cycler, Bio-Rad) (Table 3). PCR products were resolved on a 1% agarose gel (1 X TBE, Tris/Borate/EDTA buffer) and visualised with ethidium bromide. PCR set-up, amplification and analysis were conducted in separate areas of the laboratory to minimise risk of contamination.

Table 3. Reaction mix and PCR reaction conditions for genotyping R299Q γ2 KI mice

R299Q γ2 KI PCR Reaction Mix			**Reaction conditions**			
			Step	**Temp.**	**Time**	**Cycles**
Genomic mouse DNA	100.0	ng	Initial step	95°C	600s	1x
Primers	0.3	µmol				
dNTPs	0.20	mM	Denaturing	95°C	30s	
Immolase Reaction Buffer	0.1	Vol	Annealing	73°C	45s	12x
$MgCl_2$	1.5	mM	Extension	72°C	60s	-1°C/cycle
Taq Polymerase (Immolase)	1.0	U				
			Denaturing	95°C	30s	
Reaction Volume	12.5	µL	Annealing	61°C	45s	20x
			Extension	72°C	60s	
			Completion	72°C	420s	1x
			Hold	4°C	-	

2.1.4 Tissue extraction

2.1.4.a Cardiac experiments

Hearts were rapidly removed from the thorax after euthanasia by cervical dislocation. Whole hearts or regions thereof (left/right atria or ventricles) intended for RNA or protein extraction were subsequently rinsed and agitated gently in ice-cold phosphate-buffered saline (PBS) to remove blood, then blotted dry and immediately snap-frozen in liquid nitrogen prior to storage at -80°C until further analysis. In certain cases, the hearts were weighed prior to snap-freezing using an analytical fine balance. Murine sinus node isolation is described in chapter 4.

2.1.4.b Systemic experiments

Tissue harvesting was carried out rapidly after cervical dislocation. Organs were removed, rinsed in ice cold PBS, blotted dry and weighed before snap-freezing in liquid nitrogen and storage at -80°C until analysis. For white adipose tissue removal, fat pads associated with the gonads (gonadal), retroperitoneal fat adherent to the kidneys (perirenal) and subcutaneous fat located at the base of the lower limbs (inguinal) were removed. Bilobular interscapular brown adipose tissue was also removed and carefully separated from any associated white adipose tissue as described[158]. Histological or molecular analysis of samples was consistently from lobes/organs of the same side. Murine hypothalamus dissection is described in chapter 7.

2.2 RNA work

The cardiac microarray experiment (including design, execution and statistical analysis) is described in chapter 4.

2.2.1.a RNA extraction

Tissues for RNA extraction were snap-frozen in liquid nitrogen immediately after harvesting and subsequently stored at -80°C. Surfaces and instruments were cleaned with RNaseZap (Invitrogen) and RNase-free water. All subsequent steps were performed with RNase-free gloves and sterile, RNase-free pipette tips, with close attention paid to not allowing samples to thaw prior to disruption in Qiagen's lysis/RNase-inactivating buffer (Buffer RLT).

For fibrous samples (including whole heart) and adipose-rich samples, tissue was ground under liquid nitrogen or pulverized on dry ice, then aliquoted for immediate use or storage at -80°C. Buffer RLT (Qiagen) was added and samples immediately mechanically disrupted on ice with a homogeniser (Ultra-Turrax, VWR). Whole hypothalami underwent direct mechanical disruption in Qiagen Buffer RLT. Sinus node samples were pooled (three per sample), Buffer RLT added and disruption instituted by 20 strokes in a loose-fitting Dounce homogeniser.

Total RNA was then extracted with an RNeasy Fibrous Tissue Mini Kit (Qiagen, including proteinase K digestion step) according to the manufacturer's instructions, including on-column

DNase treatment for all samples. In the case of lipid-rich white/brown adipose tissue and hypothalamus, phenol/guanidine-based lysis (QIAzol) and spin-column based isolation/silica membrane purification of RNA were carried out using an RNeasy Lipid Tissue Mini Kit (Qiagen). RNA yield and quality of selected samples was checked by measuring absorbance at 260 and 280 nm using a spectrophotometer (Nanodrop ND-1000) and integrity checked on an agarose gel.

2.2.1.b cDNA synthesis and real-time reverse transcription PCR

Equal amounts of total RNA (up to 1 μg, diluted in RNase-free water) were used to synthesise single-stranded cDNA using a high-capacity cDNA reverse transcription kit (Applied Biosystems) in the presence of random hexamer primers using a reaction size of 20 μL, according to the manufacturer's instructions.

cDNA was then added to TaqMan Fast Universal PCR Master Mix in the presence of an inventoried TaqMan Gene Expression Assay probe/primer set (both Applied Biosystems) specific for the gene of interest and multiplexed with a probe/primer set for an internal housekeeping gene (β-actin/GAPDH for cardiac and brown-adipose tissue, β-actin/cyclophilin for hypothalamus) as the endogenous control (Table 4). Proprietary TaqMan PCR primers were selected, where possible, to produce the shortest amplicons to maximise PCR efficiency and to span at least one exon-exon junction in the target mRNA to minimise risk of genomic DNA (gDNA) amplification. TaqMan gene expression assays used are listed in Appendix 1.

Quantitative, real-time reverse-transcription PCR (qRT-PCR) was run on a StepOne Real-Time PCR system (96-well format) or ABI Prism 7000 (384-well format) sequence detection system (Applied Biosystems). All samples were analysed in duplicate (triplicate for hypothalamus) and relative expression calculated using the $2^{-\Delta\Delta Ct}$ method[159] (where ΔCt is the difference in cycle threshold value between the target transcript and the endogenous control), with Ct values measured in the exponential phase of the PCR reaction using Applied Biosystems' StepOne Software (version 2.0) or RQ manager software (version 1.2). Samples minus reverse transcriptase enzyme and samples minus cDNA template were used as negative controls (to exclude gDNA

contamination or reagent cross-contamination, respectively) and checked to ensure failure to reach threshold by 40 cycles.

Table 4. Reaction mix and PCR reaction conditions used for TaqMan-based real-time PCR

General Real-Time PCR Reaction Mix			Reaction conditions			
			Step	**Temp.**	**Time**	**Cycles**
Diluted cDNA template	1	µL	Initial step	95°C	20s	1x
TaqMan Fast Master Mix (2X)	5	µL				
Gene expression assay (20X)	0.5	µL	Denaturing	95°C	1s	
Endogenous control (20X)	0.5	µL	Annealing	60°C	20s	40x
RNase-free water	3	µL	Extension	60°C		
Reaction Volume	10.0	µL	Hold	4°C	-	

2.2.1.c Allelic discrimination for detection of R299Q mutant Prkag2 transcript

For specific detection of mutant transcript, common primers and two TaqMan MGB fluorogenic probes specific for the mRNA sequence of murine *Prkag2* and the mutant/WT alleles, respectively, were designed with Primer Express 3.0 software using published sequence for *Prkag2* cDNA (Ensembl) and custom-synthesised by Applied Biosystems[160]. The common primers (with complete homology for both alleles) were chosen to span exon-exon boundaries (exons 6-7 and exons 7-8 boundaries) in the *Prkag2* mRNA sequence to prevent gDNA amplification, whilst TaqMan oligonucleotide probes specific for either WT or R299Q mutant allele were labeled with different reporter dyes (FAM & VIC). In accordance with manufacturer guidance primers were designed to be positioned as close as possible to the probe without overlapping, with a T_m of 58-60°C (Primer Express v1.5 and TaqMan MGB Probes for Allelic Discrimination: User Bulletin, Applied Biosystems). TaqMan oligonucleotide probes were designed to be as short as possible (but >13 nucleotides) and positioned such that the mutation site was in the middle third of the probe, with an estimated melting temperature (T_m) of 65-67°C. The nucleotide sequences used were:

Forward primer	5'-CTTCTTTGCCTTGGTAGCCAAC-3'
Reverse primer	5'-CATTCCTACAAAGCTCTGCTTTTTACTT-3'
WT γ2 probe	5'-FAM-AGTCCGTGCAGCGC-MGB-3'
Mutant γ2 probe	5'-VIC-AGTCCAAGCAGCGC-MGB-3'

On-column DNA digestion with DNase (Qiagen) was utilised for all RNA extractions prior to cDNA synthesis. cDNA was prepared from whole-tissue RNA extracts as outlined (section 2.2.1.b). The end-point assay was performed under competitive conditions with primers, multiplexed probes and TaqMan Universal PCR Master Mix in a 96-well format with reaction conditions as per Applied Biosystems guidelines[160] on a StepOne Real-Time PCR system (Table 5). Data were analysed and depicted with StepOne Software (version 2.0, Applied Biosystems).

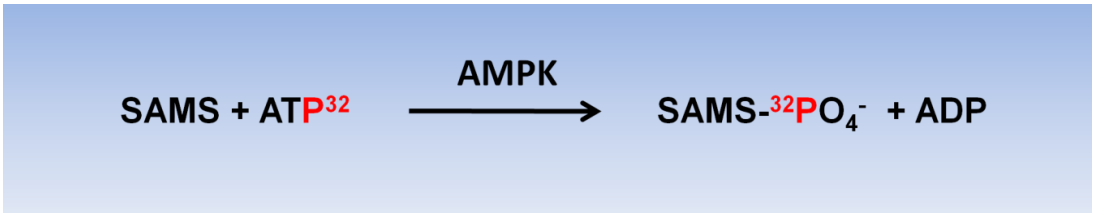
Table 5. Reaction mix and PCR reaction conditions used for allelic discrimination assay

Allelic Discrimination PCR Reaction Mix			**Reaction conditions**			
			Step	**Temp.**	**Time**	**Cycles**
Diluted cDNA template	1	µL	Initial steps	60°C	30s	1x
TaqMan Universal M/Mix (2X)	10	µL		95°C	600s	1x
Forward primer	1.8	µL	Denaturing	95°C	15s	40x
Reverse primer	1.8	µL	Annealing	60°C	60s	
WT probe	0.8	µL	Extension	60°C		
Mutant probe	0.8	µL				
RNase-free water	3.8	µL	Final step	60°C	30s	
Reaction Volume	20.0	µL				

2.3 Protein work

2.3.1.a SAMS peptide phosphorylation assay for determination of AMPK activity

This peptide kinase assay measures the incorporation of radiolabeled phosphate from [γ-^{32}P]-ATP into a synthetic peptide substrate, SAMS (HMRSAMSGLHLVKRR) by AMPK as follows[54, 161]:



Samples (heart/liver/hypothalami) were harvested as indicated (section 2.1.4). Aliquoted samples were kept on dry ice and weighed with an analytical balance. Samples were then rapidly minced with fine scissors and briefly mechanically homogenised (Ultra-Turrax, VWR) on ice following the

addition of ice-cold modified SAMS kinase homogenisation buffer[121]: 50 mM Tris-HCl, 250 mM mannitol, 50 mM NaF, 5 mM sodium pyrophosphate, 1 mM dithiothreitol (DTT), 1 mM benzamidine, 0.1 mM phenylmethylsulphonyl fluoride (PMSF), supplemented with a protease inhibitor cocktail tablet (Roche), 1% triton, pH to 7.4 at RT. The volume of SAMS kinase homogenisation buffer added was so as to uniformly dilute all samples (typically 3-5X) based on the pre-determined sample weight. Extracts were then centrifuged at 13,000 x g for 10 minutes at 4°C. Protein concentration was determined from a diluted aliquot of the soluble fraction using a bicinchoninic acid (BCA) assay kit (Pierce, Thermo Scientific) and bovine serum albumin (BSA) as standard, according to manufacturer instructions, with readout of absorbance at 562 nm on a microplate reader (VMax kinetic, Molecular Devices).

AMPK rabbit γ2 subunit-specific antibody recognising the C-terminus (kind gift of Professor David Carling, MRC Clinical Sciences Centre, Imperial College London, UK) was pre-bound to a 50% protein G-sepharose bead slurry (30 µL protein G-sepharose slurry; 5 µL γ2-specific antibody, 215 µL ice cold phosphate buffered saline [PBS]) on an orbital shaker (IKA Vibrax VXR) at 4°C for 2 hours. These were then gently pelleted and washed in ice-cold PBS/1% triton, followed by a further wash in ice-cold PBS. Tissue lysate (equivalent to 250 µg protein/sample) was then added to the pre-bound protein G-antibody mix in ice-cold 1% triton/HBA buffer (latter is: 50 mM 4-(2-hydroxyethyl)piperazine-1-ethanesulphonic acid [HEPES], 50 mM NaF, 5 mM sodium pyrophosphate, 1 mM EDTA, 10% glycerol [v/v], 1 mM DTT, 1 mM benzamidine, 0.1 mM PMSF, supplemented with a protease inhibitor cocktail tablet [Roche], pH to 7.4 at RT). Immunoprecipitation (IP) was performed on an orbital shaker at 4°C for 2-3 hours (each IP consisted of 30 µL protein G-Sepharose/antibody slurry and 250 µg of sample lysate, made up to 500 µL in HBA/1% triton with fresh protease inhibitors). Alternatively, for measurement of total (rather than γ2-specific) AMPK activity, IP was carried out by directly adding a rabbit antibody (sip2, kind gift of Professor David Carling) that recognises both beta subunits, without pre-binding, to the IP mix. The immune complexes were then subject to several ice-cold washes (HBA/1% triton, then HBA alone, followed by PBS). All reaction runs included an IP reaction control with no antibody, to allow correction for non-specific background activity.

SAMS reaction assay mix was prepared by adding 200 µL each of: 1 mM SAMS peptide synthetic substrate; 1 mM AMP; and HGE/1% triton buffer (HGE buffer is: 50 mM HEPES, 1 mM EDTA, 10% glycerol [v/v], 1 mM DTT, 1 mM benzamidine and 0.1 mM PMSF). For determination of γ1 or γ2-specific activity, duplicate reactions were set up either in the presence of 0.2 mM AMP, or with AMP absent, to measure the degree of allosteric stimulation of AMPK by AMP. For measurements of total AMPK activity, SAMS reactions were conducted in the presence of 0.2 mM AMP alone. The SAMS reaction was initiated by adding a final volume of 25 µL to the washed immune complexes, constituting: SAMS assay mix (15 µL), HBA/1% triton (5 µL) and [γ-^{32}P]-ATP/$MgCl_2$ solution (5 µL). [γ-^{32}P]-ATP/$MgCl_2$ solution consisted of 10 µL of [γ-^{32}P]-ATP (370 MBq≡10 mCi/mL stock, Hartmann Analytic), 10 µL of 100 mM ATP and 25 µL of 1 M $MgCl_2$ made up to 1 mL with distilled water. The reaction mixture was briefly centrifuged and transferred to an orbital shaker placed in a 37°C incubator for 30 minutes. Samples were briefly centrifuged again and a 20 µL aliquot removed and spotted onto a small prelabelled square of phosphocellulose paper (P81 from Whatman) to capture the phosphorylated peptide. Papers were then immediately immersed and washed in at least three changes of orthophosphoric acid (1% v/v) of 500 mL each. Papers were then allowed to air dry and counted by immersion in scintillation fluid (Ecoscint, National Diagnostics) on a scintillation counter (Tri-carb 2800TR, Packard). The specific radioactivity (SR) of stock [γ-^{32}P]-ATP was measured from 1 µL of stock 1 mM [γ-^{32}P]-ATP solution in triplicate (typically yielding 1 x 10^5 - 1 x 10^6 counts per minute, c.p.m), to then determine the specific activity (SA) of the assay (expressed as pmol of phosphate incorporated into the substrate peptide per min/mg total protein) as follows[bb]:

$$SA = \frac{(Assay\ c.p.m) - (Blank\ c.p.m.)}{SR\ of\ ATP} \times \frac{1}{time\ (min)} \times \frac{reaction\ volume}{correction} \times \frac{concentration}{correction}$$

All radioisotope experiments were planned and conducted in accordance with Departmental and University of Oxford safety policy on work with ionising radiation. Personal protection equipment was used at all times and solutions containing ^{32}P-ATP handled behind plexiglass (Perspex)

[bb] SR of ATP measured in terms of c.p.m. per nmol ATP; reaction volume correction is instituted due to the fact that only a proportion of the assay reaction volume is spotted onto P81 paper (typically 20 µL out of a total of 25 µL); concentration correction refers to adjustment of units from µg protein loaded to mg readout.

shielding with attention to minimising exposure time and proximity of distance to radioisotope and regular monitoring for contamination.

2.3.1.b General protein extraction and quantification

Samples were harvested and homogenised using largely similar methods to those described in section 2.3.1.a. Aliquots of powdered tissue samples (typically weighing 10-30 mg) were homogenised on ice in a 300-400 µL volume of either RIPA buffer (50 mM Tris-HCl, pH 8.0, 150 mM NaCl, 1% Igepal CA-630, 0.5% sodium deoxycholate, 0.1% SDS) or modified SAMS kinase homogenisation buffer, supplemented with fresh 1 mM DTT, 1 mM benzamidine, 0.1 mM PMSF and a protease inhibitor cocktail tablet (Roche). Extracts for phosphoproteins were additionally supplemented with sodium orthovanadate (1 mM) and a phosphatase inhibitor cocktail tablet (PhosSTOP, Roche). Extracts underwent centrifugation at 13,000 x g for 10 minutes at 4°C and protein concentration determined from diluted aliquots of the soluble fraction with a BCA assay. The original extracts were then diluted in the initial lysis buffer used to yield equal protein concentrations for Western blotting.

2.3.1.c Western blotting and analysis

Protein lysates were mixed with lithium dodecyl sulphate sample buffer with 50 mM DTT (both NuPAGE, Invitrogen) and boiled at 95°C for 5 minutes, prior to separation by SDS-polyacrylamide gel electrophoresis. Equal amounts of protein (typically 20-50 µg) were loaded onto pre-cast polyacrylamide gels (Nupage 4-12% Bis Tris gel, Novex, Invitrogen) and electrophoresed at 120-150 V for 2 hours. Protein molecular weight marker (Amersham full-range rainbow marker, GE Healthcare) was also loaded to enable determination of molecular size post-transfer. Proteins were then transferred onto a polyvinylidene difluoride (PVDF) membrane (Immun-Blot, Bio-Rad) using an electrophoretic transfer cell (Mini Trans-Blot, Bio-Rad) in pre-cooled transfer buffer (48 mM Tris Base, 390 mM glycine, 0.1% SDS, 20% methanol) at 200 mA for 2-3 hours at 4°C.

Membranes were blocked in 5% low-fat dry milk powder (w/v) in TBST (Tris-Buffered Saline with Tween-20: 15 mM Tris-HCl, 137 mM NaCl, 0.1% Tween-20, pH 7.6) at 4°C overnight.

Blocked membranes were incubated with the desired primary antibody diluted (typically 1:1000) in 5% milk/TBST for 2-3 hours at RT. For some antibodies, blocking for 2 hours at RT followed by overnight incubation in primary antibody at 4°C gave a clearer final signal and was used in preference. This was followed 5 x 5 minute washes in TBST and immunodetection by membrane incubation with an appropriate secondary horseradish peroxidase-conjugated antibody diluted 1:4000 in 5% milk/TBST for 45 minutes at RT, followed by further 5 x 5 minute washes in TBST. Visualisation was with enhanced chemiluminescence (ECL) reagents (GE Healthcare) using manual photographic film (Hyperfilm ECL, GE Healthcare) development. Probing of membranes with rabbit polyclonal β-tubulin antibody or rabbit polyclonal anti-α actinin antibody (for heart only) served as loading control (both from Abcam). All antibodies used are listed in Appendix 2.

In some experiments the membrane was subsequently stripped of antibodies and reprobed with a new antibody (e.g. to determine total protein levels after initial probing for a phospho-residue). For this, membranes were briefly washed free of ECL reagents in TBST and then incubated in stripping buffer solution (2% SDS, 62.5 mM Tris-HCl, pH 6.8 and 100 mM 2-mercaptoethanol) with rotation at 50°C for 30 minutes, followed by 3 x 10 minute washes in TBST and re-blocking.

For analysis, bands were quantified by scanning densitometry. Films were scanned using a flatbed scanner and digital images imported into ImageJ (NIH)[162] for analysis and quantification of signals as outlined (http://www.lukemiller.org/journal/2007/08/quantifying-western-blots-without.html).

2.4 Histology and microscopy

Hypothalamic *in situ* hybridisation is described in chapter 7.

2.4.1 General fixation/sectioning

Freshly removed tissues were rinsed in ice-cold PBS and immerse-fixed in 10% neutral buffered formalin (VWR) for at least 24 hours (≥ 10:1 ratio of fixative to tissue), followed by transfer to 70% ethanol. Samples were then processed (dehydration with ascending ethanol series, 'clearing' to remove dehydrant, replacing it with Histo-Clear and paraffin infiltration) in an automatic tissue

processor (Bavimed Histomaster, Germany) overnight. Processed tissue was subsequently manually aligned and embedded in blocks using hot paraffin wax. Cross-sections of 5-7μm thickness were obtained on a rotary microtome (Leica RM 2155), floated on a warm water bath and spread on polysine covered glass slides (VWR) prior to drying. For all tissues, care was taken to ensure adequate sections were obtained and visualised throughout the block to provide representative images of overall tissue morphology.

2.4.2 Staining - H&E, PAS and Picro-Sirius red

Prior to staining, slides were deparaffinised in Histo-Clear (Fisher Scientific) and rehydrated in a graded ethanol series to ionised water to permit penetration by water-soluble dyes. For haematoxylin & eosin (H&E) staining, slides were immersed in Harris' haematoxylin for 10 minutes, washed in running tap water for 3 minutes and then counterstained with eosin for up to 1 minute. For periodic acid-Schiff (PAS) reagent staining for glycogen, slides were immersed in 0.5% periodic acid for 5 minutes at RT, washed in 3 changes of distilled water and then incubated in Schiff's reagent for 15 minutes at RT. Slides were then washed in running tap water prior to counterstaining with haematoxylin solution and a further rinse. Picro-Sirius red staining for visualisation of collagen was performed using a kit (Polysciences) according to the manufacturer's instructions, with incubation for one hour in 0.1% picro-Sirius red followed by 2 x 30 second washes in acidified water (0.5% v/v glacial acetic acid). Post-staining, slides were dehydrated in an ethanol series and cleared in two changes of Histo-Clear (National Diagnostics). Slides were cover-slipped with Neo-Mount (Merck) mounting medium. and images acquired with a light microscope (Leica DMRBE or Nikon Eclipse TE2000U) coupled to a digital camera (Media Cybernetics coolSNAP-Pro or Nikon Digital Sight DS-5M colour CCD, respectively).

2.4.3 White adipose tissue (WAT) histology and analysis

Right-sided gonadal (epididymal) white adipose tissue harvested from single-housed, male R299Q γ2 knock-in (KI) mice (N=5/genotype) aged 38-40 weeks underwent fixation, processing and paraffin embedding as described in section 2.4.1. Sections 7 μm in thickness were taken at 100 μm intervals. Non-overlapping sections (at least 300 μm apart) were stained with H&E, viewed with a

10X objective (Leica DMRBE) and three images acquired from each level with a digital camera (Media Cybernetics coolSNAP-Pro). At least 250 WAT cells in each mouse were evaluated blind to genotype for adipocyte area (quantified in pixels) using ImageJ software.

2.4.4 Transcardial perfusion fixation and staining with Cresyl violet for assessment of basic neuronal structure

Following administration of intraperitoneal (i.p.) sodium pentobarbital (100 mg/kg) and ensuring that pedal reflexes were abolished, a thoracotomy was made to expose the heart. An incision was made in the right atrium to allow for exsanguination. The left ventricle (LV) was punctured with a butterfly needle and 10 mL of 0.9% saline injected to purge blood present within the vasculature. Subsequently, ~20 mL of fixative (4% paraformaldehyde in 0.9% NaCl) was administered slowly over ~3 minutes. Care was taken to ensure adequate perfusion efficacy using the criteria of prompt discolouration of the liver (< 1 minute), stiffening of the tail and hardening of the abdominal organs[163]. The skull was opened with fine dissecting scissors and the brain removed and post-fixed by placement in a falcon tube containing 10 mL of perfusion fixative for 16 hours at 4°C. Brains were prepared for cryoprotection by placing them in 10 mL of 30% sucrose in PBS until they reached osmotic equilibrium and sank (~24 hours). Brains were then mounted on a freezing microtome using OCT compound (VWR) and sectioned coronally at a thickness of 40 µm (Leica Leitz 1400, Germany). Harvested sections were placed in 96-well plates containing antifreeze (25% glycerol, 25% ethylene glycol in PBS) for storage. Every 8th section was then mounted from a Petri dish containing 1 X PBS onto electrostatic slides (VWR) and air dried. Slides were then dehydrated in ascending concentrations of ethanol (distilled water, 50% ethanol, 75% ethanol, 95% ethanol, 100% ethanol), stained with 0.1% cresyl violet (Nissl) for 1-2 minutes and defatted for 10 minutes in Histoclear (Raymond Lamb). Slides were then mounted in DPX (Sigma) and coverslipped.

2.4.5 Transmission electron microscopy (TEM)

2.4.5.a Cardiac TEM (at age 2 months)

Two month old female R299Q γ2 KI mice and WT littermate controls (N=2/genotype) of mixed 129/C57BL/6 genetic background underwent euthanasia by cervical dislocation, then thoracotomy to remove the heart. Hearts were promptly placed in a Petri dish containing fixative (2.5% glutaraldehyde in 100 mM phosphate buffer). Left ventricular myocardium was then cut finely into small (<1 mm^3) blocks using a fresh scalpel and immersed into fixative. After 15-30 minutes, the fixative was refreshed and samples subject to primary fixation at 4°C for 16-24 hours. Samples were then washed briefly in cacodylate buffer (200 mM, pH 7.3), prior to post-fixation at 4°C in 1% osmium tetroxide in 100 mM cacodylate buffer. Samples were then liberally washed with distilled water and stained *en bloc* in 0.5% aqueous uranyl acetate for 16 hours at 4°C in the dark. Following this, samples were dehydrated in a graded series of ethanols followed by two times in propylene oxide and embedded in epoxy resin (Agar 100, Agar Scientific). The embedding schedule consisted of infiltration with a graded mixture of propylene oxide/resin to 100% resin, then embedding with fresh resin in embedding capsules and polymerisation for 24 hours at 60°C. Blocks were then sectioned on an ultramicrotome (Reichert Ultracut E, Germany). In preparation for sectioning, blocks were initially trimmed by hand to trapezoid shape in the ultramicrotome specimen holder using a fresh razor blade and the aid of a microscope. Semi-thin sections (~1 μm) were then cut using a dry glass knife to select the appropriate tissue area, followed by ultra-thin sectioning (50-70 nm). Sections were floated onto filtered distilled water and then collected on to a copper grid. Grids were allowed to dry on filter paper before further brief staining with 2% aqueous uranyl acetate and lead citrate. Sections were examined with a Philips Technai 12 electron microscope and digital images acquired with a lens-coupled CCD camera.

2.4.5.b Cardiac & skeletal muscle TEM (at age 12 months)

The above procedure was repeated with minor modifications on R299Q γ2 mice aged 12 months on a C57BL/6 genetic background. Small pieces of heart or soleus skeletal muscle were harvested and fixed overnight in 4% glutaraldehyde in 100 mM phosphate buffer. Post-fixation was in 2%

osmium tetroxide in 100 mM phosphate buffer. Subsequent *en bloc* treatment with uranyl acetate, dehydration in ethanol and transfer to propylene oxide steps were as above, prior to embedding in Spurr's epoxy resin. Ultra-thin sections were cut and stained with uranyl acetate and lead citrate prior to being examined in a JEOL 1200EX electron microscope.

2.5 *Ex vivo* (Langendorff) cardiac perfusion

Mice were deeply anaesthetised with i.p. pentobarbitone (140 mg/kg body weight) and given i.p. heparin (150 IU). Hearts were then rapidly excised, cannulated on a 20-gauge cannula and retrogradely perfused in Langendorff mode at a constant perfusion pressure of 80 mmHg with a modified Krebs-Henseleit buffer containing (in mM): 118.5 NaCl, 25.0 $NaHCO_3$, 4.75 KCl, 1.18 KH_2PO_4, 1.19 $MgSO_4$, 1.41 $CaCl_2$, 11.0 D-glucose and 5.0 pyruvate, at pH 7.4, saturated with 95% O_2 and 5% CO_2, as described[164]. Cardiac temperature was monitored through a K-type thermocouple passed into the right ventricle retrogradely via the pulmonary valve. Hearts were maintained at 37°C throughout the experiment by immersion in a jacketed bath of Krebs-Henseleit perfusate kept at 37°C and aortas perfused with the same warmed buffer. A small fluid-filled, polyvinylchloride film balloon was introduced into the left ventricle via an atrial appendage incision (with diastolic pressure maintained between 5-10 mmHg). This was connected via fluid-filled tubing to a pressure transducer (ADInstruments, Oxford) and converted to a digital readout of pressure using an 8-channel PowerLab A/D converter. Quality inclusion criteria used for hearts[164] were: time interval between thoracotomy and aortic cannulation <3 minutes; a coronary flow measurement 1.5-4.5 mL/min; and absence of persistent arrhythmias during the stabilisation phase. Applying these criteria, there were no significant differences between genotypes in the proportions of mice excluded from analysis.

AMPK activity measures from perfused hearts

For measurement of AMPK activity in the context of preserved cellular energetic status, hearts were freeze-clamped after a 25 minute stabilisation period of perfusion as described[149].

Ex vivo intrinsic heart rate

Hearts were isolated and prepared as above, then perfused with an identical Krebs-Henseleit buffer except in the absence of supplemental pyruvate. The pressure reading was digitally processed to provide a ventricular pressure recording from which heart rate was derived. Intrinsic heart rate was recorded as the average measured rate over 30 seconds, 5 minutes after cannulation.

2.6 Transthoracic echocardiography

After induction of general anaesthesia with 3-4% isoflurane, mice were positioned supine on a heating pad and the chest wall shaved to allow application of pre-warmed ultrasound coupling gel. Anaesthesia was maintained with 1-1.5% of isoflurane in 100% oxygen administered via nosecone and carefully titrated to ensure heart rate (HR) remained stably above 420-450 beats/min during image acquisition. Transthoracic echocardiography was performed using a 6-15 MHz linear array transducer (Agilent Sonos 5500). Care was taken to ensure the thoracic cage was not distorted during the procedure to minimise risk of reflex bradycardia or artefactual alteration in intrathoracic geometry. Parasternal short- and long-axis images were taken and mice were then recovered in a heat incubator prior to transfer to their home cage. All dimensions were measured off-line from leading edge to leading edge according to American Society of Echocardiography guidelines[165] and taken as the average of at least three consecutive cardiac cycles. The evaluation included[cc]: *systolic function* measures, including LVESD, LV FS (%FS = [(LVEDD – LVESD)/LVEDD] x 100), LV ESA at mid-papillary level in short-axis, fractional change in LV CSA ([ED cavity area – ES cavity area]/ED cavity area); markers of *ventricular dilatation*, including LV EDD and LV EDA; and *hypertrophy parameters*, including estimated LV mass using the 2D area-length method[166], where LV mass = 1.05 x ([5/6 x EPI A x (L + t)] – [5/6 x ENDO A x (L)]), as well as measuring LV CSA at mid-papillary level in short-axis. Images were acquired and analysed blind to genotype.

Scanning of the Sox2cre γ2 line was performed in a similar manner to the above but using a Vevo 2100 Imaging System (VisualSonics, Toronto, Canada) with a 30 MHz linear array transducer on a bench-mounted adjustable heating platform[164]. Teicholz ejection fraction (EF)[167] was calculated by:

$$LV\ ESV = \frac{7LVESD^3}{2.4+LVESD}\ ,\ LV\ EDV = \frac{7LVEDD^3}{2.4+LVEDD}\ ,\ LV\ EF = \left(\frac{LV\ EDV - LV\ ESV}{LV\ EDV}\right) \times 100$$

Peak radial systolic velocity of the inferior wall was obtained using tissue Doppler[168].

[cc] Abbreviations: LV, left ventricle; LV ESD, LV end-systolic dimension; FS, fractional shortening; LV EDD, LV end-diastolic dimension; ESA, end-systolic area; CSA, cross-sectional area at level of papillary muscles in short-axis; EDA, end-diastolic area; EPI A, epicardial area; ENDO A, endocardial area; L, LV length in parasternal long-axis; t, LV wall thickness in diastole.

2.7 Cardiac electrophysiology

ECG telemetry and invasive electrophysiology study are described in chapter 4.

2.7.1 Electrocardiography

Electrocardiograms (ECGs) were recorded from conscious, unrestrained mice using the AnonyMOUSE ECG screening tool (Mouse Specifics). Mice were placed on a platform which was embedded with paw-sized gel-electrodes connected to an amplifier. ECG data was obtained when 3 single electrodes made contact with 3 paws. ECGs were obtained within a heated surgical hood under dim lighting to maintain rodent body temperature and minimise stress. Mice were allowed to acclimatise for 5 minutes after being handled before recording of data. ECG signal data was processed and analysed off-line blind to genotype using e-MOUSE software (Mouse Specifics), with all traces analysed manually for arrhythmia and correct recognition of R wave peaks.

Anaesthetised ECGs were obtained under light isoflurane (1.25%) inhaled anaesthesia via nosecone. Four fine needle electrodes were positioned subcutaneously and a lead II configuration ECG recorded with filtering and amplification of signals using a BioAmplifier (ADInstruments). Animals were allowed to equilibrate after induction of anaesthesia for 5 minutes before starting a 10 minute recording. Subsequent off-line analysis by signal-averaging of ECG waveforms was performed using PowerLab software (ADInstruments) blind to genotype. All signal-averaged ECG waveforms were manually inspected and adjusted to ensure accurate detection of intervals.

In the absence of a defined gold standard for mice, a uniform approach to ECG analysis was adopted based largely on conventional clinical ECG analysis with adaptations to minimise subjectivity in defining murine ECG intervals: the duration of the QRS complex was measured as starting from the onset of the Q wave and finishing at the intersection of the S wave with the ECG baseline; if the S wave did not intersect with the isoelectric baseline, then no QRS interval was calculated; the end of the T wave was taken as the end of the positive component of the T wave; if the T wave did not appear to overlap with the isoelectric baseline, then no QT interval was calculated for that set of traces.

2.8 Cellular work

Sinus node electrophysiology and heterologous transfection experiments are discussed in chapter 4.

2.8.1 *Prkag2* vectors

Mammalian pIRES-hrGFP II expression vectors (Agilent Technologies) containing WT and R299Q mutant *Prkag2* were a kind gift of Miss Violetta Steeples (University of Oxford, UK). Full length *Prkag2* cDNA, with a 5' Kozak sequence to initiate translation, had been generated by PCR from the R299Q γ2 mouse line, cloned into the vector's multiple cloning site (MCS) between BamHI and NotI restriction sites and sequence verified. The pIRES-hrGFP II vector contains a bicistronic expression cassette whereby the MCS is followed by an internal ribosomal entry site sequence (IRES) linked to the hrGFP II coding sequence. This allowed expression of mutant (R299Q) or WT murine *Prkag2* to be monitored at the single-cell level (using GFP fluorescence) due to translation of separate hrGFP II and *Prkag2* products from a single bicistronic mRNA. A single 5' FLAG tag had also been fused to *Prkag2*, whilst a stop codon had been introduced before the three contiguous copies of the FLAG epitope provided by the vector, preventing the latter's fusion with *Prkag2*. Empty pIRES-hrGFP II vector without *Prkag2* insert was used as a negative control for all experiments.

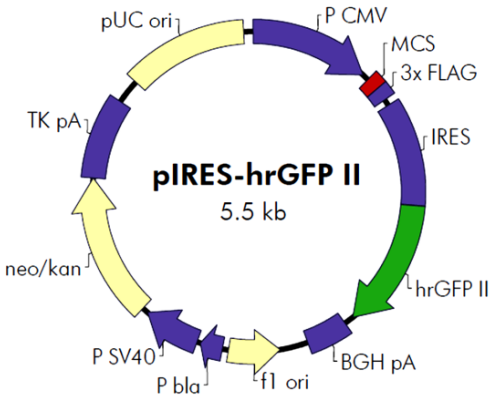


Figure 22. Vector map of pIRES hrGFP II used to overexpress WT or R299Q *Prkag2*.[dd]

[dd] Reproduced from Vitality hrGFP II Mammalian Expression Vectors Instruction Manual, Agilent Technologies.

2.8.2 Maintenance and transfection of HL-1 cells

Origins

HL-1 cells, derived from AT-1 cells, are an immortal cell line unique amongst cardiac cell lines in their ability to continuously divide, exhibit spontaneous contractions when confluent and maintain a differentiated adult cardiomyocyte-like phenotype in culture through repeated passages[169]. AT-1 cells are atrial cardiomyocytes derived from a transgenic mouse line expressing the SV40 large T cell antigen under the direction of the atrial natriuretic peptide A promoter[170]. HL-1 cells were kindly provided by Dr Katja Gehmlich (University of Oxford) and obtained from Professor Claycomb's laboratory (Louisiana State University School of Medicine, New Orleans, USA).

Culture conditions & passaging

HL-1 cells were cultured in Claycomb media (SAFC Biosciences) supplemented with 10% fetal bovine serum (FBS), 100 U/mL penicillin/100 µg/mL streptomycin (Life Technologies), 0.1 mM norepinephrine and 2 mM L-glutamine (Life Technologies). Cells were grown in T75 flasks pre-coated with a 0.02% gelatin/25 µg/mL fibronectin solution (2 mL/25 cm^2 surface area) and incubated at 37°C with 95% air/5% CO_2 at 95% relative humidity. Fully confluent cells were split on average every 3 days at a 1:3 ratio by washing flasks with sterile PBS, then adding warmed 0.05% trypsin/EDTA (3 mL/T75 flask) for 3 minutes at 37°C. Trypsin was inactivated by adding growth media supplemented with FBS and cells pelleted by centrifugation at 175 x g for 5 minutes. Pellets were resuspended in fresh supplemented Claycomb media pre-warmed to 37°C and transferred to new pre-coated flasks.

Harvesting and siRNA knockdown

HL-1 cells were seeded at 7 x 10^5 cells/well in fibronectin/gelatin pre-coated 6-well culture plates (CellStar, Greiner Bio-One) in Claycomb media supplemented as above but in the absence of antibiotics or noradrenaline. Cells were transfected at full confluency overnight with a pre-designed ON-TARGETplus smartpool (Dharmacon ThermoScientific, Lafayette, CO, USA) of four targeting siRNA oligonucleotides against the gene of interest (*Prkag1*, *Prkag2*, *Prkag3*) or control siRNA using Dharmafect 1 (Dharmacon) diluted in reduced-serum (Opti-MEM, Life Technologies) media according to the manufacturer's instructions. In brief, separate siRNA/Opti-MEM and

Dharmafect/Opti-MEM mixes were made and incubated for 5 minutes at RT. siRNA complexes for each gene of interest were prepared by adding equal volumes of the two mixes and incubating for 20 minutes at RT. Antibiotic-free, supplemented Claycomb media was added to each mix to yield a transfection medium with final siRNA concentration of 25 nM. Culture media was aspirated from pre-plated cells and the appropriate transfection media added to each well (2 mL total volume per well of 6-well plate). Media were changed to fresh media the following morning and RNA harvested at 48 hours post-siRNA transfection for qRT-PCR-based detection of gene silencing. Six replicates were used for all treatment and control groups. Controls used in pilot and formal RNA knockdown experiments included: a negative control designed to not target any known cellular gene (ON-TARGETplus non-targeting siRNA, Dharmacon), thus allowing distinction of non-specific from sequence-specific silencing effects; a positive control targeting a constitutively expressed housekeeping gene (smartpool targeting cyclophilin B, Dharmacon) to allow optimisation of siRNA delivery conditions and monitoring of transfection efficiency; and untreated controls to determine basal gene expression.

2.8.3 Isolation and maintenance of neonatal rat cardiomyocytes

Harvesting and culture

Primary neonatal rat cardiomyocyte (NRCM) cultures were prepared from ventricles of 1-2 day-old Sprague-Dawley rat pups. Newborn pups were euthanized by cervical dislocation, followed by immediate removal of hearts into a pre-cooled Petri dish containing ice-cold dissociation buffer (106 mM NaCl, 20 mM HEPES, 0.8 mM NaH_2PO_4, 5.3 mM KCl, 0.4 mM $MgSO_4$, 5 mM glucose, pH 7.4). Ventricles were rapidly dissected free of atria and aorta, placed into a second Petri dish containing ice-cold dissociation buffer and minced into ~1 mm^3 pieces. These were transferred to a sterile Falcon tube containing 9 mL dissociation buffer to which collagenase (Roche) and pancreatin were added (22.5 mg and 62.5 mg, respectively, per 50 mL dissociation buffer) and incubated at 37°C for 5 minutes. After discarding the supernatant, the digestion procedure with collagenase-pancreatin was repeated at 37°C for 20 minutes, the pellet (A) kept and the supernatant (containing cells) collected and FBS added. The supernatant was then centrifuged at 100 x g for 5 minutes to pellet the cells. This was then resuspended in 2 mL of FBS incubated at 37°C. The

original pellet (A) then underwent serial collagenase-pancreatin digestion/pelleting steps at 37°C until all tissue was digested. Digested cell suspensions in FBS were then pooled, pelleted down by centrifugation (100 x g for 5 minutes) and resuspended in M1 medium (Dulbecco's Modified Eagle Medium-25 mM HEPES, 17.5% medium M199, 10% horse serum, 5% FBS, 2 mM glutamine and 100 U/mL penicillin/100 µg/mL streptomycin [Life Technologies]). This was then pre-plated onto a 10 cm culture dish (1 dish/5 hearts) at 37°C for 2 hours, which left the myocytes in suspension. The supernatant (containing the myocyte-enriched fraction) was removed and pelleted down by centrifugation at 100 x g for 5 minutes. This pellet was then resuspended in M1 media, before being seeded at 150,000 cells/well of a fibronectin/gelatin-coated 24-well plate.

2.8.4 Hcn4-Luciferase gene reporter assay in neonatal rat cardiomyocytes

Plasmid transfection

Initial pilot experiments were run with several different transfection reagents at multiple ratios of DNA:transfection reagent, including Lipofectamine 2000, Lipofectamine LTX (both Life Technologies), FuGENE 6, FuGENE HD (both Promega) and X-tremeGENE HP (Roche Applied Science) according to the manufacturer's instructions. Relative transfection efficiency – assessed by GFP fluorescence – and cell viability were determined visually. Using this approach, transfection with Lipofectamine 2000 at a ratio of 1:2.5 (total DNA in µg:Lipofectamine in µL) resulted in the best efficiency and lowest toxicity of the transfection reagents and conditions tested.

NRCMs were seeded at a density of 150,000 cells/well in 24-well culture plates. After being cultured overnight at 37°C with 5% CO_2 and 95% relative humidity, NRCM cells were washed with warmed PBS the following morning and incubated in NRCM transfection medium (20% medium M199, 75% DBSSK [116 mM NaCl, 1 mM NaH_2PO_4, 0.8 mM $MgSO_4$, 5.5 mM glucose, 32.1 mM $NaHCO_3$, and 1.8 mM $CaCl_2$, pH 7.2], 4% horse serum [Life Technologies], and 4 mM glutamine) for 2 hours prior to transfection. Transient transfection was performed with Lipofectamine 2000 at a ratio of 1:2.5 according to the manufacturer's instructions with: 0.4 µg of the pIRES-hrGFP II mammalian expression vector (Agilent) containing full length WT or R299Q mutant murine *Prkag2* cDNA or 'empty' vector alone; 0.4 µg of HCN4-luciferase reporter

construct constituting either the CNS13 enhancer fragment and HCN4 promoter fused to firefly (*Photinus pyralis*) luciferase coding sequence, or HCN4 promoter fused to firefly luciferase alone (kind gift of Professor Makoto Takano, Kurume University, Japan); and 0.1 μg of pGL4.74[*hRluc/TK*] vector which expresses sea pansy *Renilla* luciferase under the control of the herpes simplex virus thymidine kinase promoter (pGL4 luciferase reporter vectors, technical sheet, Promega), acting as an internal reporter to control for variations in cell viability and transfection efficiency. Each individual transfection was performed in at least quadruplicate. Media was changed to fresh transfection media the following morning and live cells imaged briefly at 24 hours post-transfection for visualisation of GFP fluorescence. 48 hours after transfection, cell lysates were harvested for determination of luciferase activity.

Firefly and renilla luciferase assay on transiently transfected NRCMs

After removal of growth media and a single wash in 1 X PBS, cell lysis was undertaken directly in multi-well plates by adding Dual-Luciferase Reporter (DLR) Passive Lysis Buffer reagent (Promega). Cell lysates were centrifuged and the supernatant transferred to fresh tubes prior to sequential measurement of luciferase activities of firefly (Fluc) and renilla (Rluc) luciferase in the same sample by measurement of luminescent signals (POLARstar Omega reader, BMG Labtech, Germany) using the DLR Assay System according to the manufacturer's instructions. Fluc readings were normalised to Rluc activity for each sample and quadruplicate samples then averaged for each test group. Transfections and assays were repeated on 3 occasions for the final analysis.

2.9 Gross systemic metabolic and exercise phenotyping

Systemic metabolic phenotyping methods including plasma chemistry, non-invasive body composition assessment, glucose handling, spontaneous activity assessment (infra-red beam breaks and voluntary wheel running), energy expenditure and pancreatic islet β-cell electrophysiology are described in chapter 6.

2.10 Central mechanistic experiments

Pair-feeding, drug sensitivity challenges (with leptin, melanotan-II and ghrelin), fast-refeed and hyperphagic rescue methods are described in chapter 7.

2.11 Data analysis and statistics

Data were acquired and analysed blind to genotype or treatment. Statistical comparisons between two groups were made using an unpaired, two-tailed Student's *t*-test, or – if three or more groups – by one-way analysis of variance (ANOVA) followed by correction for multiple comparisons by Tukey's method or the Newman-Keuls test. Non-parametric data were analysed by the Mann-Whitney U test (two unpaired groups) or Kruskal-Wallis test (three or more unmatched groups) followed by Dunn's post-hoc multiple comparison. Comparisons between genotypes in a single cohort over time were made with two-way repeated measures ANOVA and application of Bonferroni's correction for multiple testing. Statistical analysis and graphical representation were performed using Prism Software (v6.0 for Windows, GraphPad Software, La Jolla California).

Data are expressed as mean ± standard error of the mean (SEM) throughout unless otherwise stated. $P<0.05$ was considered statistically significant. Annotation used to record significance: *$P<0.05$; **$P<0.01$; ***$P<0.001$ unless stated otherwise.

Chapter 3. Validation, cardiac structure and function of R299Q γ2 knock-in

3.1 Aims and objectives

Beginning with mice heterozygous for the R299Q γ2 knock-in (KI) mutation on a mixed 129/ C57BL/6 genetic background, the focus of the work presented in this chapter was to validate the newly generated model and interrogate the cardiac phenotype with respect to structure (gross and histological) and function.

Accordingly, the specific objectives of the experiments presented here were to:

i) Verify the expression of R299Q *Prkag2* mutant transcript in the heart.

ii) Assess cardiac levels of γ2 protein of KI mice in comparison to WT littermates.

iii) Investigate the mutation's effect on the expression of the other AMPK γ subunits.

iv) Define the mutation's effect on AMPK activity by SAMS peptide phosphorylation assay.

v) Determine the effect of the mutation on cardiac histology and glycogen content.

vi) Assess the cardiac structure, mass and function of KI mice with non-invasive imaging.

vii) Examine the contractile reserve of KI mice by assessing their response to IV dobutamine.

3.2 Chapter-specific materials and methods

3.2.1 Biochemical quantification of glycogen

Cardiac glycogen was quantified in R299Q γ2 mutant and WT mice aged 12 months as described with minor modifications[121]. Snap-frozen hearts were ground under liquid nitrogen. Tissue (~80 mg) was extracted in 300 µL of glycogen homogenisation buffer (50 mM Tris, 0.25 M mannitol, 1 mM DTT, 0.1 mM PMSF, supplemented with a Roche protease inhibitor and PhosSTOP tablet, pH 7.4). After brief vortexing, lysates were sonicated for 2 x 30 seconds and passed through a 23 G needle six times. 50 µL of homogenate was then mixed with 50 µL of 2 M KOH and incubated at 70°C for 20 minutes to solubilise glycogen. Samples were centrifuged for 7 minutes at 16,000 x *g*. From the supernatant, 40 µL of each sample was digested with 200 µL of acetate buffer (0.3 M sodium acetate, pH 4.8, 0.5% amyloglucosidase, 2.5% glacial acetic acid) to release glucose. Blanks were set up for each sample using acetate buffer in the absence of amyloglucosidase. Samples were then vortexed and incubated overnight at RT.

Glucose content was then determined based on measurement of NADPH using a coupled assay. Glucose-6-phosphate (G-6-P), produced by the action of hexokinase, was oxidised by glucose-6-phosphate dehydrogenase with concomitant reduction of the co-enzyme $NADP^+$ (nicotinamide adenine dinucleotide phosphate) to NADPH (reduced form of $NADP^+$), such that the amount of NADPH formed was stoichiometric with the original amount of glucose:

$$Glucose + ATP \xrightarrow{Hexokinase} G-6-P + ADP$$

$$G-6-P + NADP^+ \xrightarrow{G6P\ dehydrogenase} 6-phosphogluconate + NADPH$$

For this, 20 µL of sample was added to 200 µL of assay cocktail (0.3 M triethanolamine, 3 mM ATP, 0.56 mM $NADP^+$, 3 mM $MgSO_4$, 1% v/v hexokinase/glucose-6-phosphate dehydrogenase mix [Roche]) and incubated for 30 minutes at RT. NADPH production was then measured at 340 nm using a spectrophotometer.

3.2.2 *In vivo* cine-magnetic resonance imaging (cine-MRI)

High-resolution *in vivo* cine-MRI was performed on a cohort of R299Q γ2 KI mice and WT littermate controls of mixed 129/C57BL/6 genetic background at 2 and 10 months of age, to accurately assess left ventricular volumes, function and mass with high spatial resolution.

Anaesthesia was induced with 3-4% isoflurane and maintained with 1.5-2.5% isoflurane in 100% oxygen. Electrodes were positioned subcutaneously and the animal placed in a custom-built, heated cradle (containing a respiration sensor) and positioned in the isocentre of the radiofrequency coils. Eyes were protected with a petroleum-based ophthalmic ointment. Cine-MRI experiments were carried out using a horizontal 210 mm bore 9.4 T magnet with VNMRS Direct Drive console and 1000 mT/m actively shielded gradient system (Agilent Technologies, USA). A 33 mm internal diameter quadrature birdcage resonator (Rapid Biomedical, Germany) optimised for mice was used for transmission and reception. After initial tuning and matching of the coil, shimming and scout imaging was performed, followed by acquisition of 7-10 contiguous, multi-frame slices 1 mm in thickness orthogonal to the long-axis of the left ventricle (LV). This gave a stack of short-axis images from apex to base, with 18-32 frames per cardiac cycle. Images were acquired subject to physiological gating with respiratory gating to minimise motion artefacts and cardiac-triggering to synchronise images to the cardiac cycle[171]. Cradle temperature, ECG and respiration signals were monitored throughout the experiment and anaesthesia/oxygen flow rate adjusted accordingly.

Images were reconstructed off-line as TIFF files using custom written software. End-diastolic and end-systolic frames were selected for each slice according to maximal and minimal ventricular cavity size and manual image segmentation performed by a single operator using AMIRA software (Visage Imaging, versions 4.1.2 or 5) blind to genotype as described[172, 173]. LV measurements derived included: end-systolic and end-diastolic volumes (ESV and EDV); stroke volume (SV = EDV-ESV); cardiac output (CO = SV x heart rate); ejection fraction (EF = SV/EDV); and LV mass. A multi-slice volumetric approach[174] was used to calculate LV volumes, whereby all slice volumes were summated to yield total volume. Papillary muscles were included in myocardial mass measurements, with LV mass defined as the LV cavity volume subtracted from the volume

contained within the LV epicardial border multiplied by a myocardial specific gravity constant of 1.05 g/cm^3, as described[174]. Pearson correlation and linear regression analyses were used to compare LV mass estimates from MRI with measured *ex vivo* cardiac mass.

3.2.3 *In vivo* left ventricular haemodynamics

Terminal invasive haemodynamic recordings were obtained under isoflurane general anaesthesia in a cohort of AMPK γ2 KI mice of mixed genetic background aged 12 months. After anaesthetic induction, mice were placed on a homeothermic mat and commenced on maintenance 2% isoflurane. The anterior neck region was surgically prepared and the right carotid artery and jugular vein dissected. The carotid artery was then cannulated with an ultra-miniature 1.4F pressure catheter (SPR-671 Millar Mikro-tip, ADInstruments, UK), which was advanced to the aortic root for a 30 second baseline aortic pressure recording. The pressure catheter was then passed retrogradely into the LV cavity under pressure recording guidance. The jugular vein was cannulated with polyethylene tubing for subsequent intravenous infusion of dobutamine. Anaesthetic was reduced to 1.5% isoflurane and LV pressures were allowed to equilibrate for 15 minutes, at the end of which baseline LV pressure was noted. Baseline aortic root pressures, continual heart rate, LV systolic (LVSP) and end-diastolic (LVEDP) pressures and derived dP/dt (change in LV pressure as a function of time) were obtained using a PowerLab 4SP data acquisition system (ADInstruments). After a further 15 minutes of baseline recording, contractile reserve was assessed by infusion of low-dose dobutamine (4 ng/g body weight/min) for 5 minutes, followed by high-dose dobutamine (16 ng/g body weight/min) for 5 minutes. At the close of the procedure, animals were euthanized by cervical dislocation. Organs were subsequently harvested, washed in 1 X PBS and weighed. Pressure tracings were analysed off-line, blind to genotype using LabChart Pro software (version 7, ADInstruments).

3.3 Results

3.3.1 Validation of the R299Q γ2 knock-in

3.3.1.a PCR-based genotyping

R299Q γ2 KI mutant heterozygote (Het), homozygote (Homo) and WT mice were viable (up to the time point studied of 12 months) and fertile with normal breeding behaviour. Genotyping of mice was performed with PCR, using the presence of a residual *FRT* sequence and *loxP* site within intron 6 upstream of the mutated exon 7 to distinguish WT *Prkag2* locus from the recombined, Flp-excised *Prkag2* allele of mutant mice. PCR of genomic DNA (gDNA) extracted from ear-notch tissue revealed amplification products of expected size for WT and Flp-excised alleles (Figure 23).

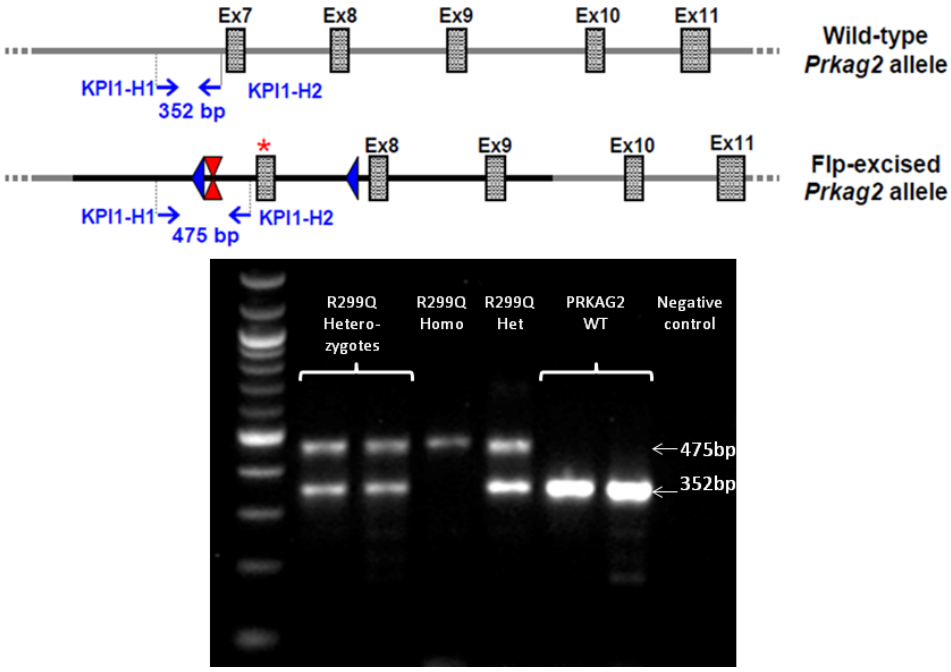


Figure 23. R299Q γ2 KI PCR-based genotyping strategy and typical results from a heterozygous intercross.

Upper panel – Depiction of the *Prkag2* WT locus and allele resulting from homologous recombination of exon 7 post-Flp excision. The positions of the PCR genotyping primers are indicated (blue arrows). The primer combination used (KPI1-H1/KPI1-H2) allowed distinction between WT and mutant KI alleles (amplification products of 352 and 475 bp, respectively).

Lower panel – PCR products from ear-notch gDNA run on a 1% agarose gel. From left-to-right: lane 1, 100 bp DNA ladder (Bioline); lanes 2 and 3, R299Q γ2 heterozygotes; lane 4, R299Q γ2 homozygote; lane 5, R299Q γ2 heterozygote; lanes 6 and 7, γ2 WT; lane 8, negative control (no input DNA).

3.3.1.b Mutant cardiac transcript expression identified by allelic discrimination

A TaqMan competitive, multiplex PCR assay on cardiac cDNA confirmed expression of R299Q mutant transcript in both heterozygous and homozygous mutant, but not WT mice (Figure 24).

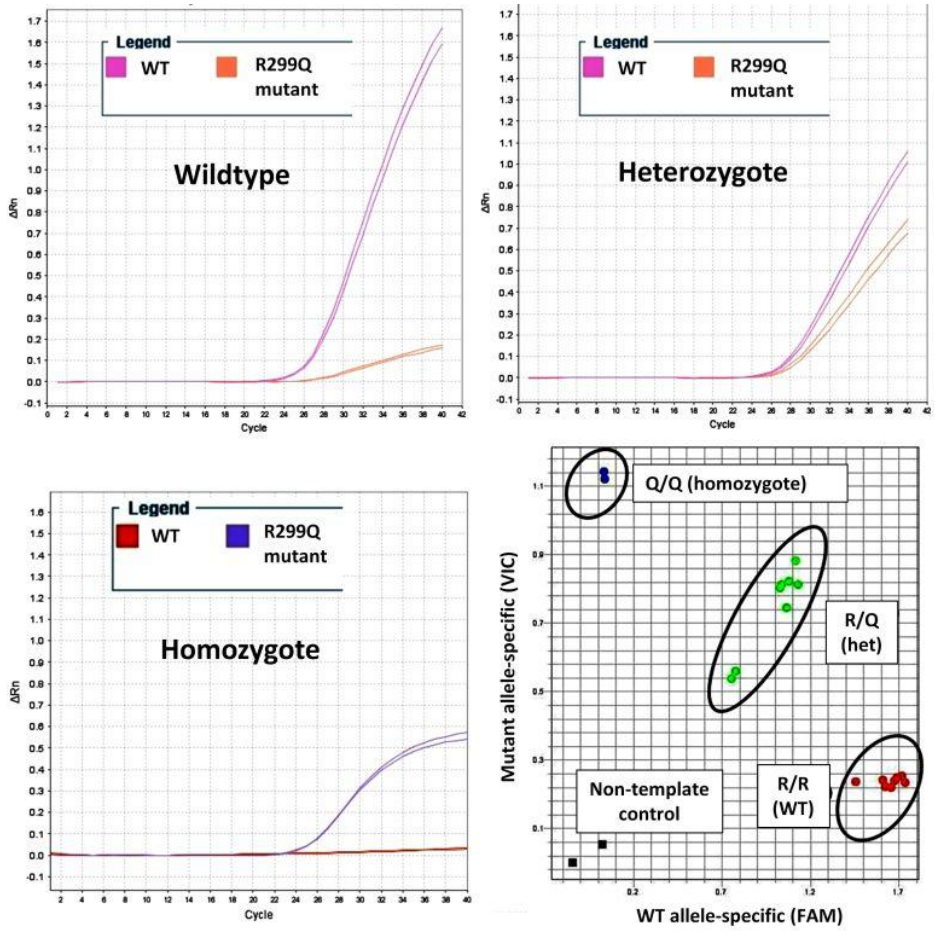


Figure 24. Allelic discrimination on cardiac cDNA using 5'-exonuclease assay.

Upper row and lower left panels – Representative amplification plots: fluorescent signals from each probe were distinguished by labelling with different reporter dyes (VIC & FAM). A slight reaction of the mutant probe with the WT allele template was observed (upper left).

Lower right panel – Allelic discrimination plot: there was clear and distinct clustering of fluorescent signals for each of the three genotypes, in full agreement with PCR-based genotyping from ear-notch derived gDNA. A substantial increase in fluorescence of both reporters (central green cluster) indicated heterozygosity.

3.3.1.c Relative mRNA expression levels of AMPK γ subunits in the heart

Relative mRNA expression levels of the different γ subunit isoforms were compared in the heart between genotypes using qRT-PCR (Figure 25). Whilst no evidence was identified for altered *Prkag1* isoform expression, a significant signal for downregulation of *Prkag3* was identified in

R299Q γ2 homozygous mutant mice, albeit with very low cardiac expression levels of this isoform in comparison to *Prkag1* and *Prkag2* (mean Ct difference ~10 cycles, suggesting a >1000-fold lower cardiac abundance of *Prkag3* transcript).

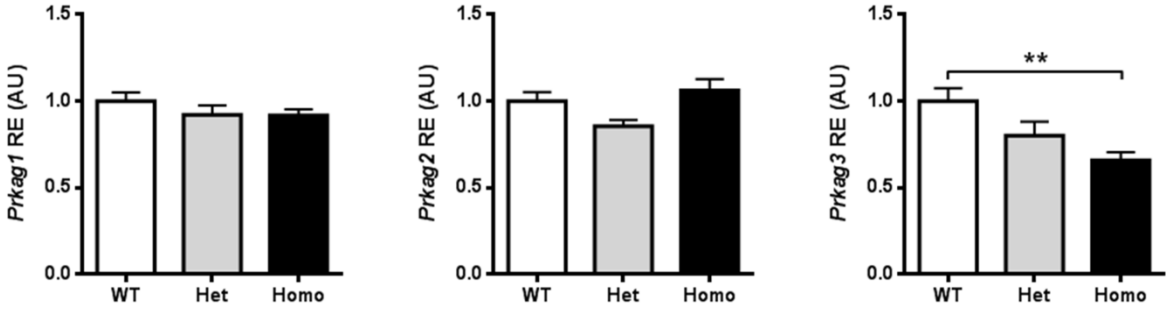


Figure 25. Cardiac *Prkag* isoform transcript expression (N=8/genotype). **$P<0.01$

3.3.1.d Assessment of cardiac γ2 and γ1 protein expression by Western blotting

Overall expression levels of γ2 protein were assessed from hearts by Western blotting using an N-terminal antibody. This revealed comparable levels of expression in both mutant and WT mice. γ1 protein expression was observed to be unaffected by mutant R299Q γ2 expression (Figure 26).

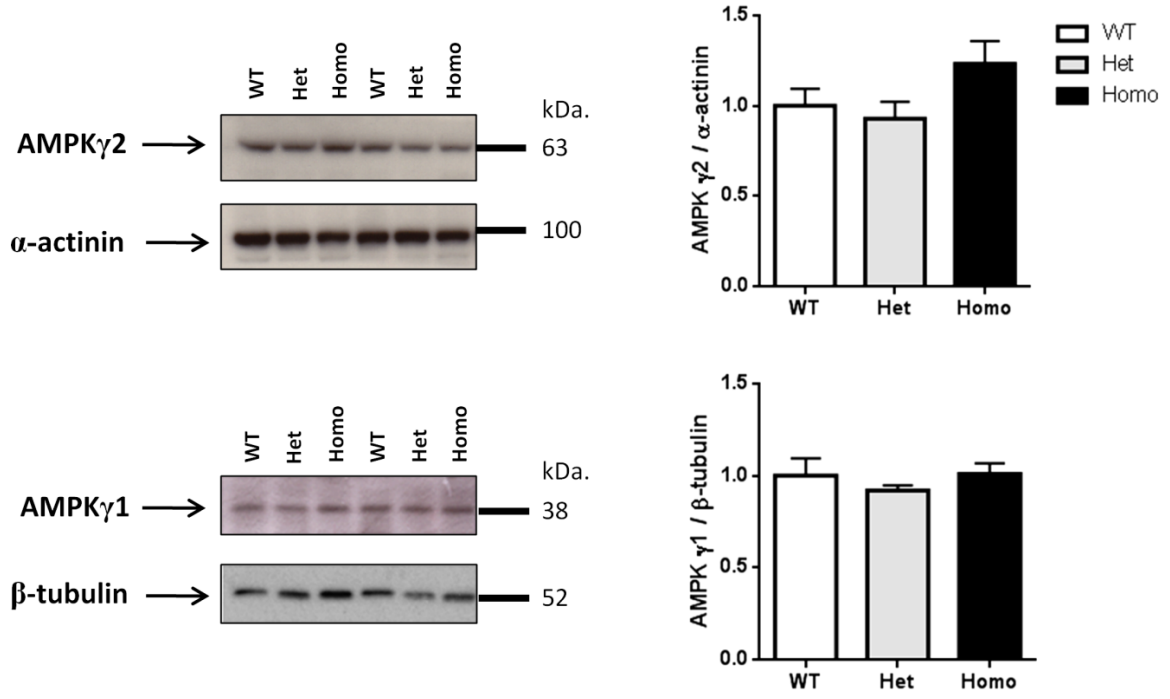


Figure 26. Western blotting and densitometry for γ2 and γ1 from whole heart protein extracts from R299Q γ2 mutant mice and their WT controls aged 2 months (N=4-5/genotype).

3.3.1.e Effect of the R299Q γ2 mutation on AMPK activity

The functional impact of R299Q γ2 mutant protein on AMPK activity was determined *in vitro* using the SAMS peptide phosphorylation assay. Hearts were rapidly harvested from 2 month old mice and immediately snap-frozen. γ2-specific AMPK activity was determined after immunoprecipitation of γ2-containing heterotrimers with a C-terminal antibody. Mice homozygous for the R299Q γ2 mutation exhibited clear loss of allosteric stimulation by AMP, although heterozygotes still appeared AMP-responsive (Figure 27). Surprisingly, both mutant genotypes also demonstrated lower levels of γ2-specific AMPK activity compared to WT, both basally and in response to AMP.

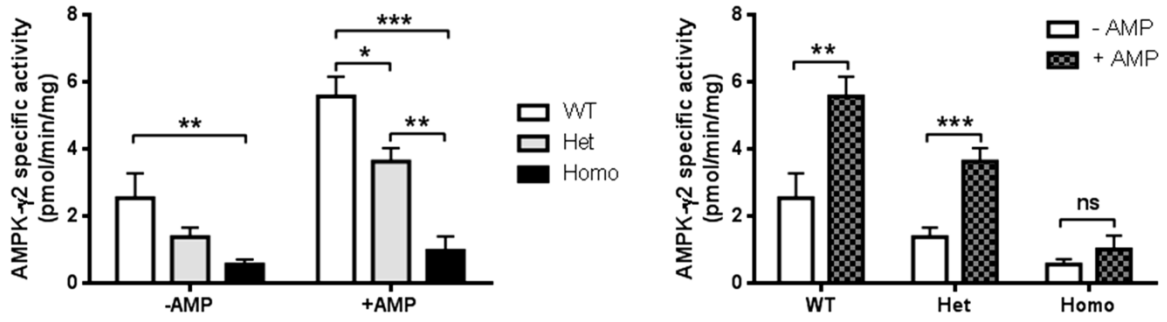


Figure 27. Cardiac γ2-specific AMPK activity in R299Q mice and controls aged 2 months (N=6-8/genotype). Note - The right panel has exactly the same genotype groups and data as the left panel, but arranged to better illustrate the response to AMP. ****P*<0.05, *****P*<0.01, ******P*<0.001

To explore the possibility that extraction of a more accessible organ with robust glycogen reserves may (at least partially) offset the activation of AMPK complexes inherent to tissue harvesting, γ2-specific AMPK activity was also measured from rapidly-isolated liver tissue of 2 month old mice. Whilst this recapitulated the same clear signal of loss of AMP-dependence in R299Q γ2 mutant mice (this time including the heterozygotes), strikingly it suggested no significant difference between genotypes in γ2-specific basal activity (i.e. in the absence of AMP) (Figure 28).

In light of this finding and in order to obtain a more faithful reading of *in situ* AMPK activity than was possible with routine post-mortem tissue collection, γ2- specific AMPK activity was measured in perfused, beating hearts that had been freeze-clamped. In this experiment, hearts were harvested

rapidly from the animal as usual, but then underwent aortic cannulation and a period of *ex vivo* perfusion to stabilise cellular energetic state, followed by immediate freeze-clamping. Using this approach, a trend (*P*=0.07) to significant elevation in basal γ2-specific AMPK activity was observed in R299Q γ2 homozygous mice, although the allosteric response to AMP from the freeze-clamped hearts was not found to be significant for any genotype (Figure 29).

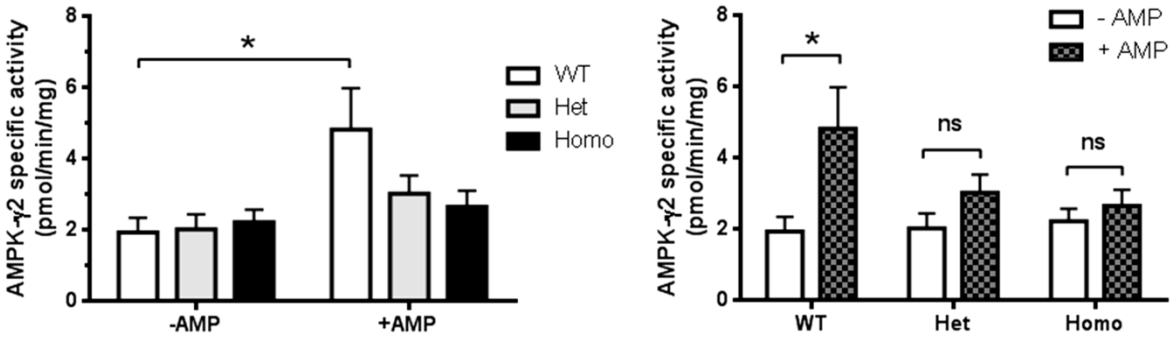


Figure 28. Hepatic γ2-specific activity of R299Q mutant and control mice aged 2 months (N=7-8/genotype). Note - The right panel has exactly the same genotype groups as the left panel, but arranged to better illustrate the response to AMP. ****P*<0.05

Quantification of *total* AMPK activity by immunoprecipitating tissue samples with an antibody that recognizes both β subunits (sip2) revealed *lower* total AMPK activity from rapidly harvested, non-perfused hearts, consistent in direction with the findings from γ2-specific AMPK activity (Figure 30). Once again, this signal of apparent loss-of-γ2 function in mutant mice was not clearly observed from perfused hearts, although the signal-to-noise ratio was significantly lower compared to non-perfused hearts (Figure 30).

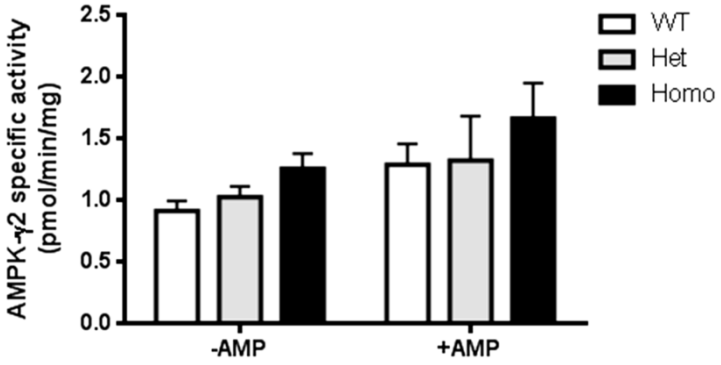


Figure 29. γ2-specific AMPK activity from isolated, perfused hearts (N=6-7/genotype).

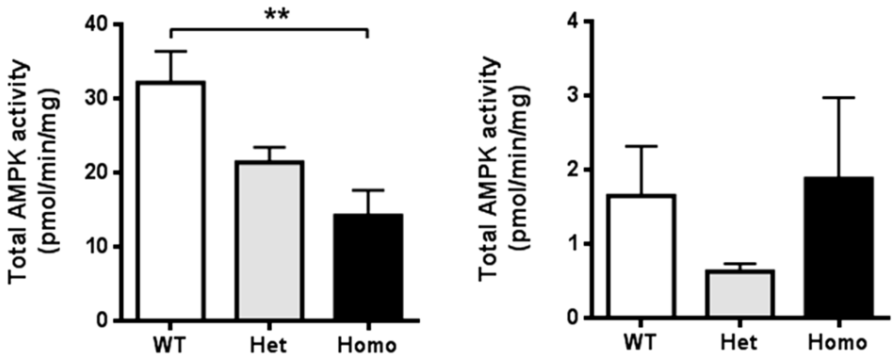


Figure 30. Total AMPK activity from rapidly extracted/non-perfused (left, N=8-9/genotype) or perfused, freeze-clamped (right, N=5-7/genotype) hearts. *****P*<0.01

Taken together, the findings from both liver tissue and perfused hearts strongly suggest that the extraction process itself has significant and genotype-divergent effects on γ2-specific (and total) AMPK activity. Furthermore, data from perfused, freeze-clamped hearts is *suggestive* of a potentially small increase in basal γ2-specific AMPK activity in homozygous mutant mice. Interpretation of the mutation's effect on total AMPK activity is complicated by the much greater contribution of unperturbed γ1 complexes however[41]. Notwithstanding this, the data from rapidly extracted (and therefore energetically stressed) hearts may suggest that γ2 contributes more significantly to total AMPK activity under conditions of significant ATP depletion.

3.3.2 Cardiac structure and function

3.3.2.a Cardiac histological and transmission electron microscopy appearances

Cardiac tissues from 12 month old R299Q γ2 mutant mice fixed in 10% neutral buffered formalin (NBF) and stained with haematoxylin and eosin showed histological appearances comparable to age-matched WT littermates (Figure 31). In particular, no cardiomyocyte vacuolation was seen. Sirius red staining for detection of myocardial fibrosis revealed a normal pattern of collagen fibre distribution, being predominately perivascular, with no evidence of significant interstitial fibrosis.

Consistent with the lack of distinct vacuole formation on cardiac H&E staining, use of the periodic acid-Schiff (PAS) stain for the detection of glycogen did not reveal any significant glycogen deposits in R299Q γ2 mutant mouse hearts at 12 months of age (Figure 32). The selection of this

age for PAS assessment was – in common with the preceding histological stains – based on the finding of normal histological appearances at younger time points, coupled with the assumption that any abnormalities, including excess glycogen deposition, were likely to progress with age.

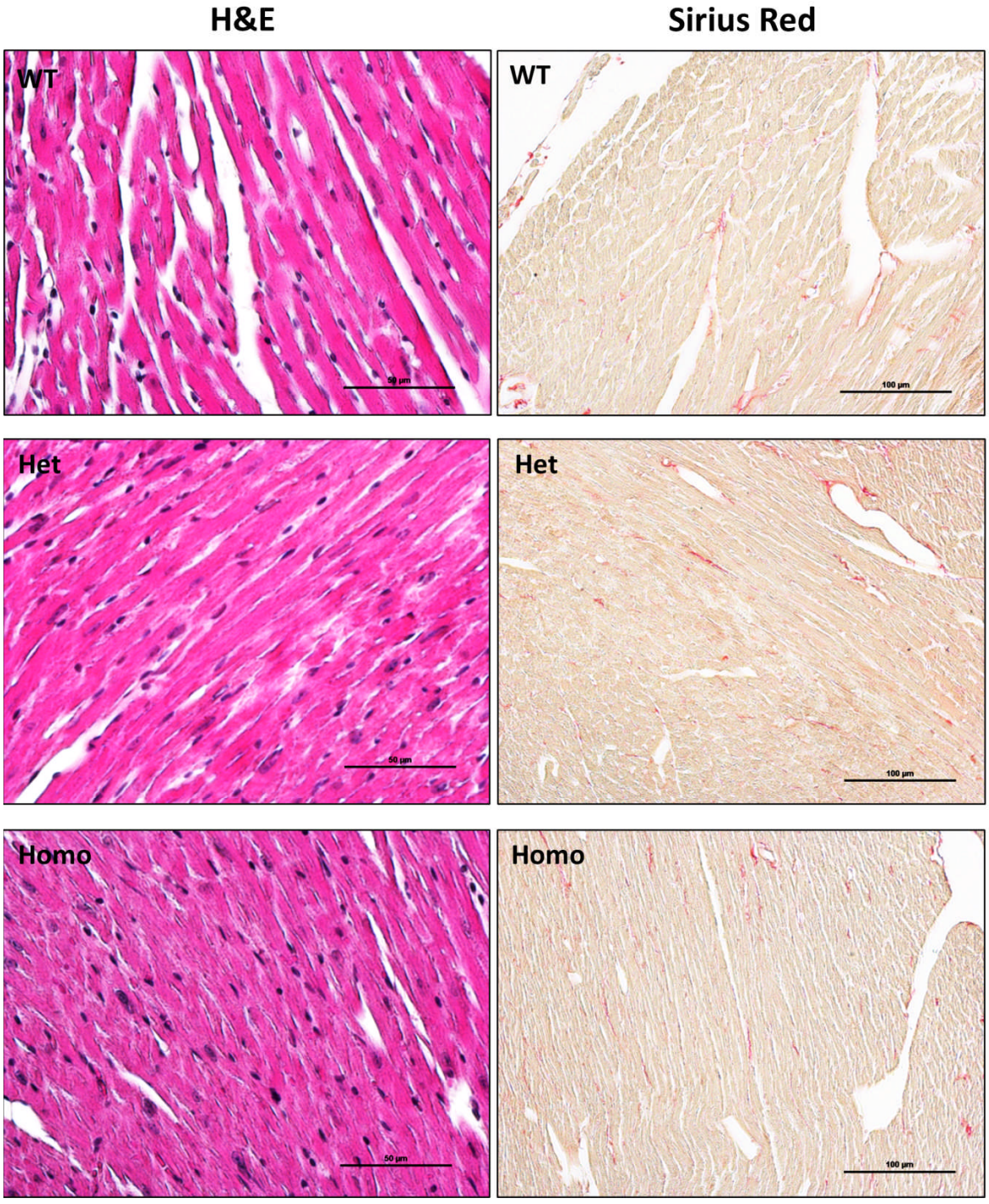


Figure 31. Cardiac histological appearances of R299Q γ2 mutant and WT mice at 12 months.
Left hand side panels – Haematoxylin and eosin (H&E) staining. Scale bar 50 µm.
Right hand side panels – Sirius red staining. Scale bar 100 µm.

Traditional paraffin embedding processing is recognised to sometimes lead to poor preservation and loss of glycogen. Use of a modified fixation protocol[175], involving 48 hours primary fixation with 10% NBF, followed by 48 hours post-fixation in 1% periodic acid/10% NBF led to a modest improvement in glycogen retention at best (seen as a mild increase in the normal PAS positivity around blood vessels), but still did not provide evidence to support the presence of significant glycogen accumulation in the hearts of R299Q γ2 mutant mice.

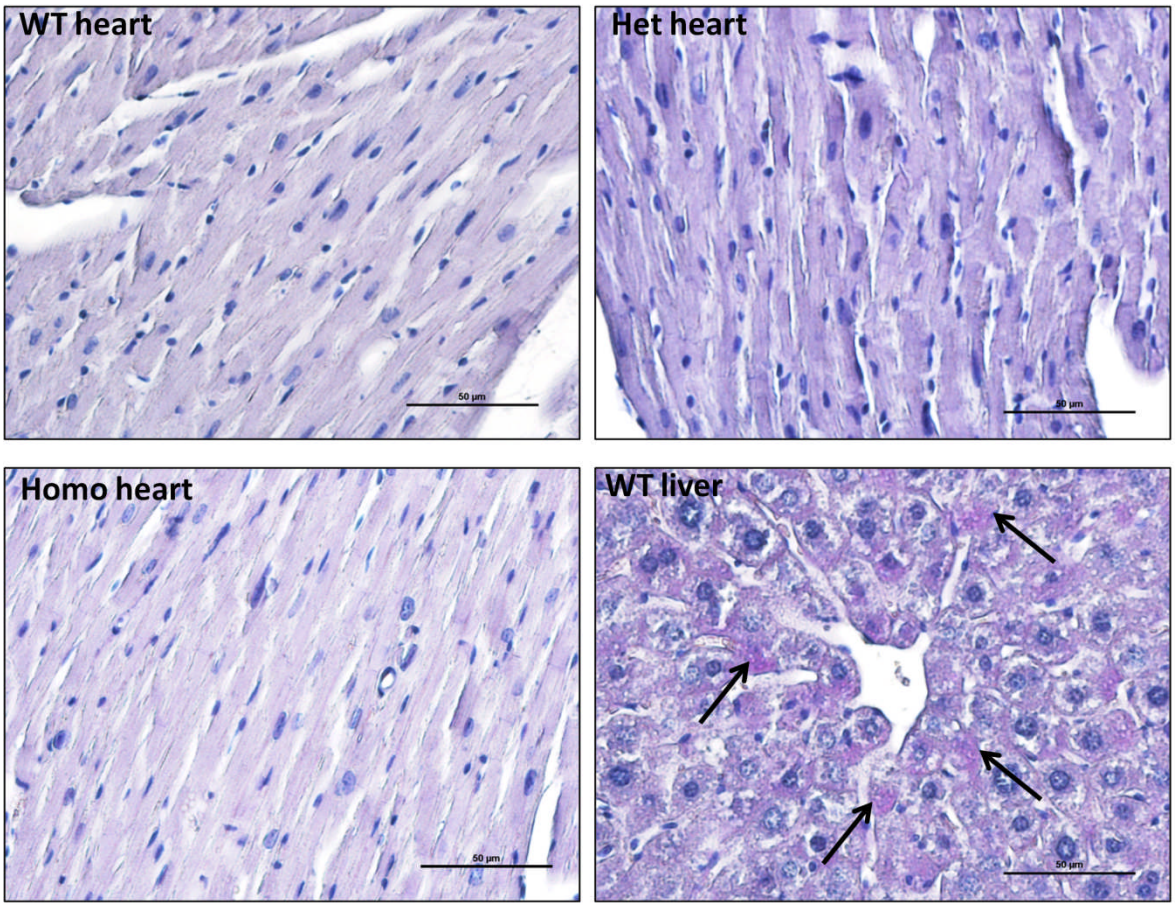


Figure 32. Upper row and lower left panel – PAS staining of hearts from R299Q γ2 mutant and WT mice aged 12 months.

Lower right panel – PAS staining of paraffin-embedded liver sections, stained concurrently, were used as a positive control. Visible deposits of magenta stained glycogen are indicated (arrows). Scale bar 50 µm.

In order to assess detailed myocardial ultrastructure, as well as utilise a separate modality to evaluate for excess glycogen accumulation, transmission electron microscopy (TEM) was employed (N=2/genotype). In addition to an assessment for glycogen (including abundance, type & location), sarcomeric integrity and stigmata consonant with energy dysregulation (e.g. abnormal

mitochondrial morphology) were specifically examined for. Using TEM, sarcomeric appearances were observed to be normal, with no vacuolation or abnormal glycogen deposits detected in the hearts of mutant mice both at 2 and 12 months of age (latter illustrated in Figure 33). However, TEM of concurrently prepared (uranyl acetate/lead citrate stained) ultrathin sections of skeletal muscle (soleus) did reveal clear but scattered glycogen deposits as free β particles, largely in the intermyofibrillar space of heterozygote (Figure 33) and homozygote R299Q γ2 mutant, but not WT, mice. Given the otherwise preserved skeletal muscle architecture across genotypes, the significance of this finding in isolation is uncertain. However, it does serve to illustrate that the specimen preparation and staining technique used was able to detect glycogen in striated muscle.

Taken together, the structural appearances of the hearts from R299Q γ2 KI mutant mice were normal up to 12 months of age, with a notable absence of either cardiomyocyte vacuolation or excess glycogen deposition compared to existing transgenic models for PRKAG2 cardiomyopathy.

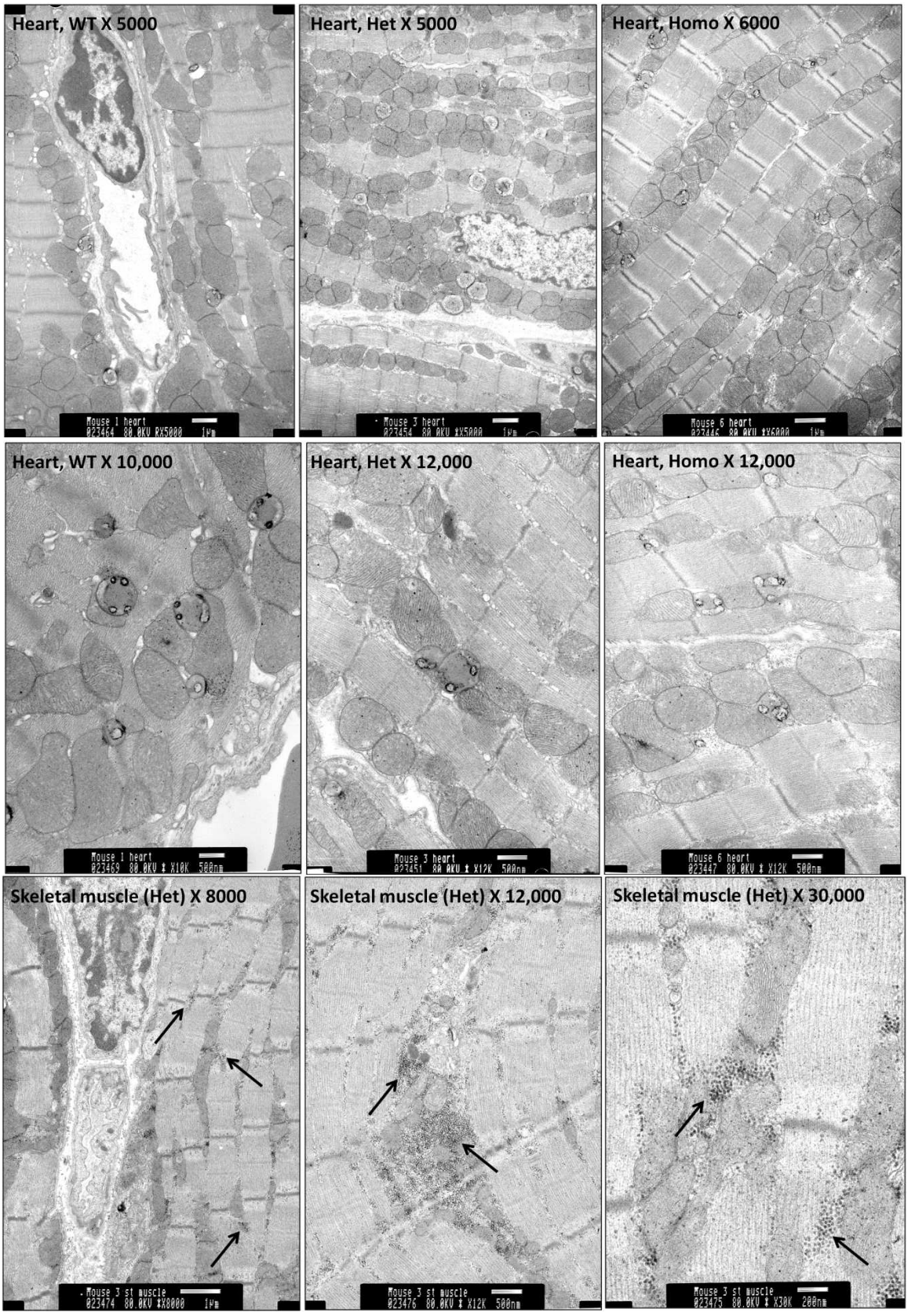


Figure 33. Transmission electron microscopy appearances of cardiac muscle at 12 months (upper and middle two rows) revealing normal ultrastructure and absence of significant glycogen excess in R299Q γ2 mutant hearts. Lower row – Glycogen granules visible (arrows) in soleus muscle from a heterozygote mouse, illustrated at several levels of magnification.

3.3.2.b Biochemical quantification of myocardial glycogen content

Given the largely qualitative nature of the information provided by PAS staining and TEM regarding glycogen accumulation and based on the assumption that the R299Q γ2 mutation may well exert a subtle effect to promote glycogen content that is not readily observable using histological assessment modalities, cardiac glycogen content was measured biochemically in a cohort of 12 month old mice (Figure 34). This revealed a small but significant elevation in tissue glycogen content in homozygous R299Q γ2 mutant mice.

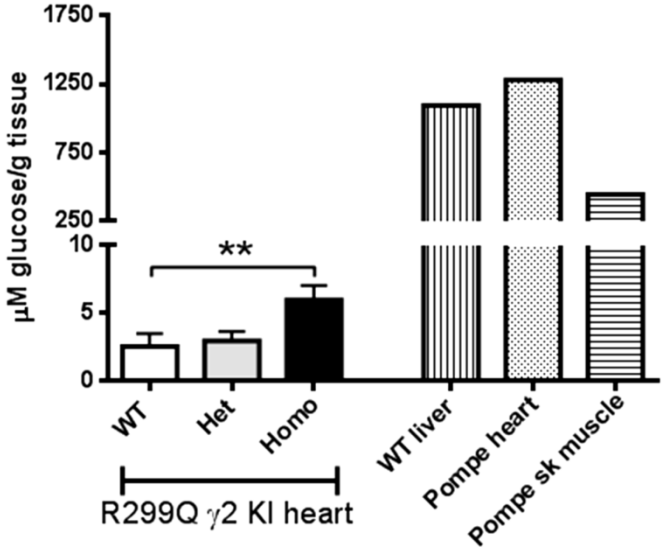


Figure 34. Cardiac glycogen content measured from 12 month old R299Q γ2 mutant hearts and WT mice and expressed as µM glucose yield per g of tissue (N=12-14/genotype). *****P*<0.01 **As positive controls, glycogen was also extracted and quantified from a WT liver and from the heart and skeletal muscle ('sk muscle') of a knock-out mouse model[176] characterised by grossly elevated levels of striated muscle glycogen retention. The latter model is homozygous for targeted disruption of exon 6 of the *Gaa* gene (encoding lysosomal acid α–glucosidase) by *neo* cassette insertion and models human glycogen storage disease type II (Pompe disease).

Following this, the relative mRNA expression of genes involved in glycogen metabolism and glucose transport was investigated with qRT-PCR in mice aged 2 months. In contrast to mouse models overexpressing the N488I and T400N mutant *PRKAG2* transgenes in the heart (TG^{T400N} and TG^{N488I})[127, 135], no significant differences in expression were identified for the genes assayed, except a marginal but statistically significant upregulation in the gene (*Slc2a4*) encoding GLUT4. The expression of SGLT1 (encoded by *Slc5a1*) was also examined given a report[135] of its upregulation

and role in mediating glucose uptake in the TG^{T400N} model, but its cardiac expression was found to be very low across all genotypes, with unreliable amplification (Ct value > 36).

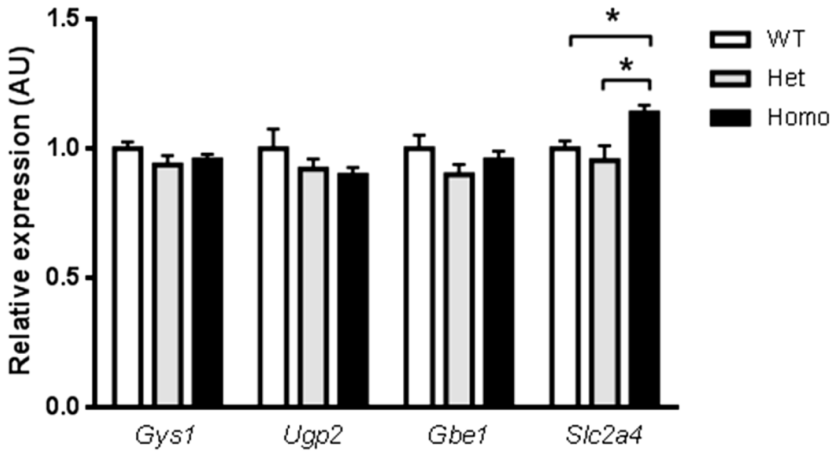


Figure 35. Cardiac glycogen metabolism-related gene expression in R299Q γ2 mutant mice and WT littermate controls aged 2 months (N=7-8/genotype). *P<0.05

Genes: *Gys1*, Glycogen synthase 1, muscle; *Ugp2*, UDP-glucose pyrophosphorylase 2; *Gbe1*, Glucan (1,4-α-), branching enzyme 1; *Slc2a4*, Solute carrier family 2 (facilitated glucose transporter), membrane 4.

3.3.2.c Cardiac function and dimensions by echocardiography at 2 months

Initial non-invasive assessment of cardiac contractile function, left ventricular (LV) dimensions and LV wall thickness was undertaken using transthoracic echocardiography in R299Q γ2 heterozygous mutant and WT mice on a mixed 129/C57BL/6 genetic background at 2 months of age[ee] (Figure 36). This identified some signals suggestive of mild LV systolic dysfunction in R299Q γ2 heterozygous mutant mice, but revealed no evidence of significant structural remodelling in terms of either LV dilatation or LV hypertrophy (LVH).

[ee]Owing to the very small number of homozygote mutant mice available at the time of this study, the initial assessment of cardiac function by echocardiography was confined to the heterozgote versus WT comparison.

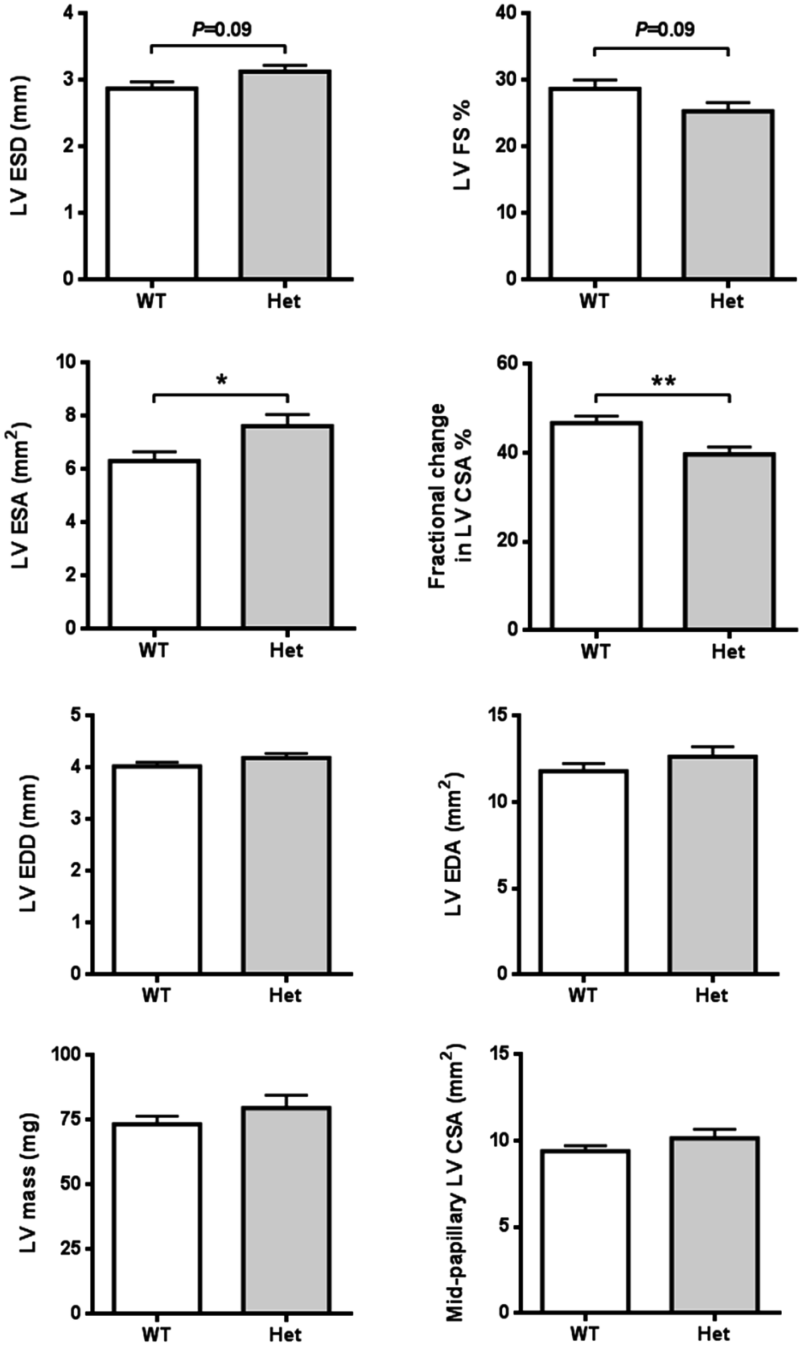


Figure 36. Echocardiography indices in mice aged 2 months on a mixed genetic background (N=10-13/genotype). Abbreviations: LV ESD, LV end-systolic dimension; FS, fractional shortening; ESA, end-systolic area; CSA, cross-sectional area at level of papillary muscles in short-axis; LV EDD, LV end-diastolic dimension; EDA, end-diastolic area. *P<0.05, **P<0.01

3.3.2.d Cardiac function by cine-MRI at 2 months and 10 months

Given the subtle degree of LV dysfunction apparent in R299Q γ2 heterozygous mutant mice, a decision was made to utilise cardiac MRI (Figure 37), with its high spatial and temporal resolution, and freedom from geometric assumptions[171], to accurately determine LV mass, volumes and

function longitudinally in all three genotypes, again on a mixed 129/C57BL/6 background.

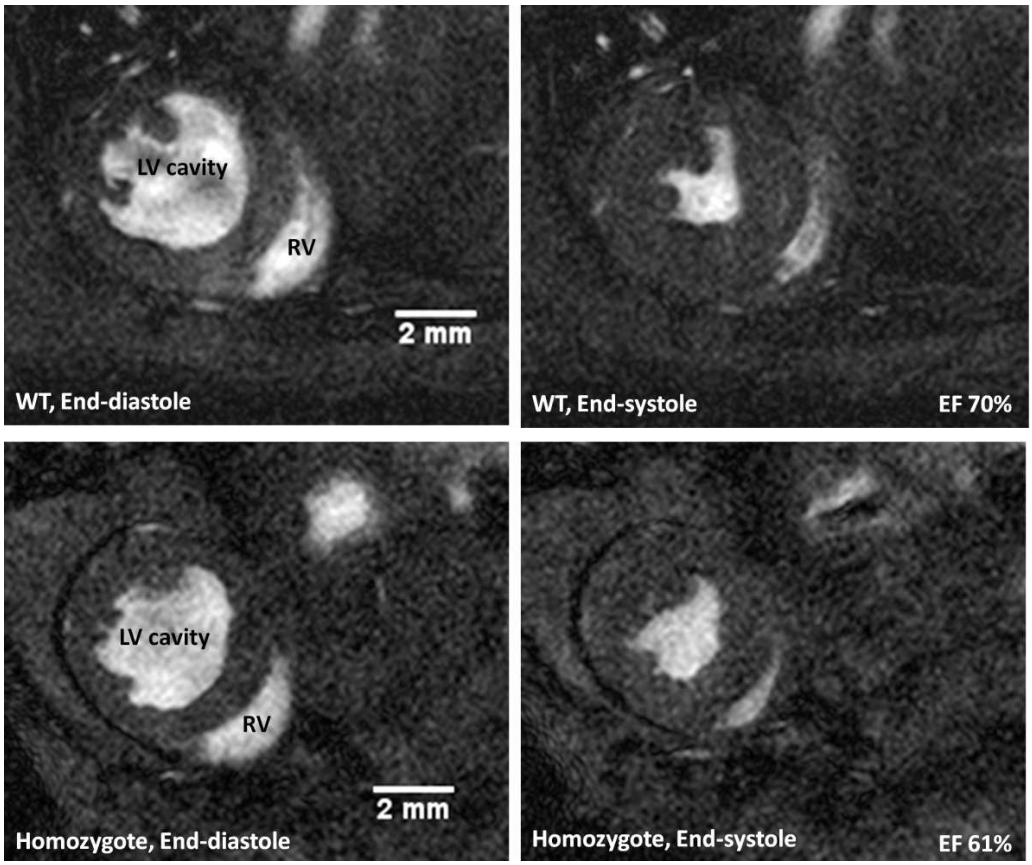


Figure 37. Representative mid-ventricular, end-diastolic/end-systolic short-axis cine-MRI images obtained from a WT (upper row) and an R299Q γ2 homozygous mutant mouse (lower row), both at age 10 months.

Abbreviations: RV, right ventricular cavity; EF, calculated ejection fraction.

As with echocardiography, cine-MRI confirmed signals consistent with mild LV systolic dysfunction in R299Q γ2 mutant mice at 2 months, including in homozygotes (Figure 38). No evidence was found of progression in LV systolic dysfunction with age, however. Differences in cardiac output (CO) and cardiac index (CI) did not reach significance at either time point.

Despite the signal for impairment in contractility, no significant LV dilatation was identified in this cohort up to 10 months of age, although there was a trend towards statistical significance (P=0.06) for the effect of genotype on LV end-diastolic volume index (LV EDVI) by two-way ANOVA (Figure 39). Similarly, assessment of LV mass revealed no evidence for LVH, including when indexed to body weight at either time point (Figure 39), or when indexed to tibial length for the 10 month time point (data not shown).

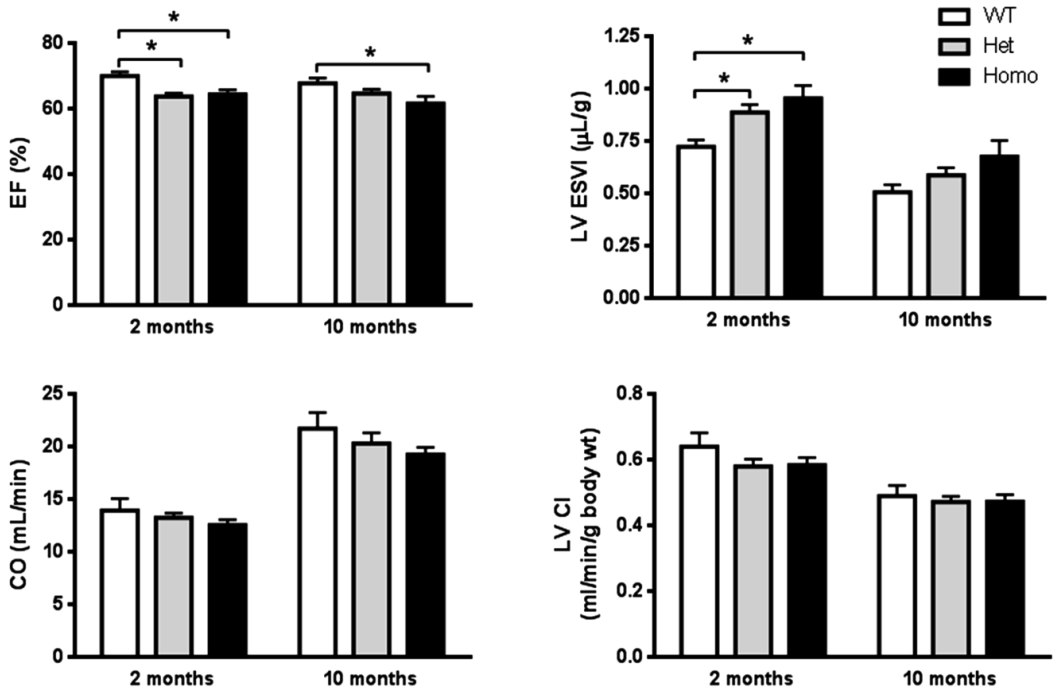


Figure 38. Cine-MRI of R299Q γ2 mutant mice on a mixed genetic background reveals mild LV systolic impairment, but preserved cardiac output (N=7-19/genotype). *P<0.05

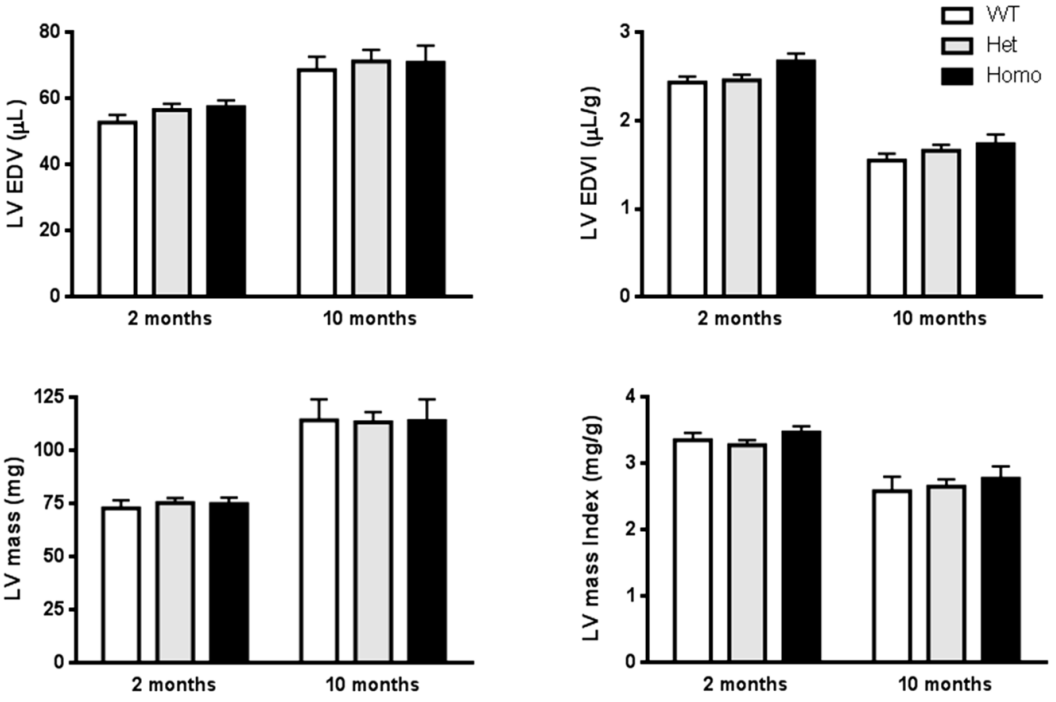


Figure 39. R299Q γ2 mutant mice on a mixed 129/C57BL/6 genetic background do not manifest significant LV dilatation or LVH in the unstressed cardiac state (N=7-19/genotype).

Ex vivo cardiac mass correlated well with *in vivo* measurements of LV mass by cine-MRI. A Bland-Altman plot of difference in mass measurements against their mean (Figure 40) indicated consistently lower estimates for LV mass by MRI, in line with the fact that the *ex vivo* post-mortem

measurement was of *total* wet cardiac weight, inclusive of the right ventricle.

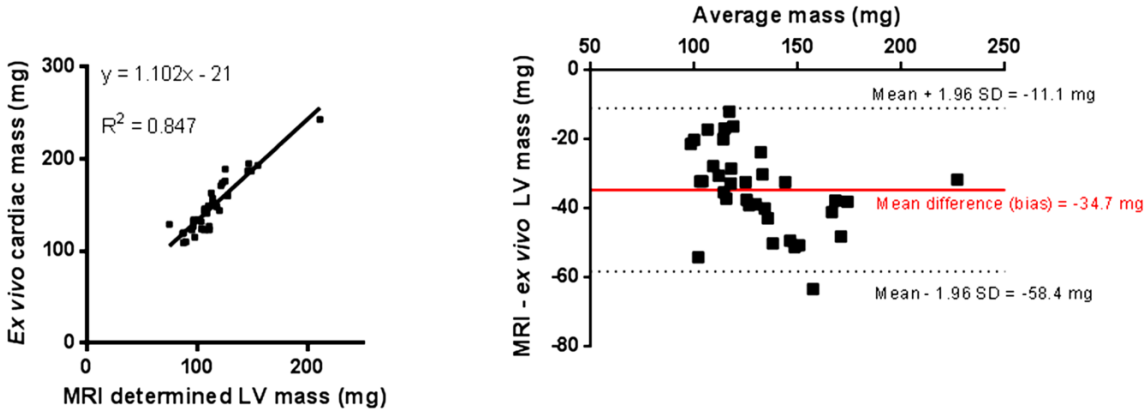


Figure 40. Left – Linear regression analysis of LV mass estimated by cine-MRI and cardiac mass measured *ex vivo*. Right – Bland-Altman analysis of the difference between cine-MRI-determined LV mass and *ex vivo* measurement plotted against the mean of the two measures.

In this cohort of mixed genetic background, it is notable that there were no statistically significant differences between genotypes in either mean heart rate achieved during cine-MR image acquisition, or in body weight at each of the time points assessed (Figure 41). Full results of cine-MRI imaging are tabulated in Appendix 3.

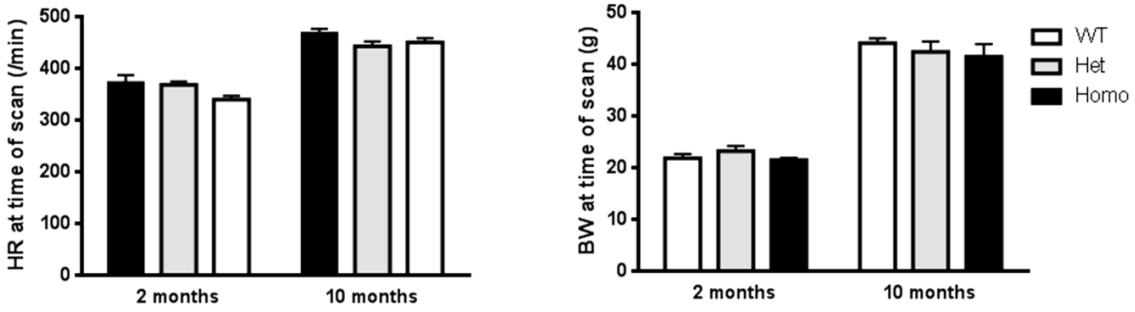


Figure 41. Heart rate (HR) and body weight (BW) at time of cine-MRI scan (N=7-19/genotype). Two-way ANOVA revealed a trend (*P*=0.06) to an effect of genotype on HR.

3.3.2.e Invasive haemodynamics and contractile reserve assessment at 12 months

As a further evaluation of the cardiac functional consequences of the R299Q γ2 mutation, the cohort of mice that had undergone evaluation of cardiac volumes by MRI also underwent terminal measurement of *in situ* aortic and LV haemodynamics using a closed-chest preparation via a

carotid arteriotomy[177]. Accurate measurements of the pressure waveform using a micro-catheter tipped with a high-fidelity pressure sensor permitted analysis of invasive aortic, LV systolic (LVSP) and diastolic (LVDP) pressures, in addition to heart rate and derived isovolumic indices of LV contractility and relaxation (e.g. dP/dt_{max} or dP/dt_{min})[178]. Given the subtlety of the cardiac phenotype at baseline, pharmacological challenge was administered in the form of dobutamine (β1-adrenoceptor agonist) inotropic stress to investigate contractile reserve. The concept of 'contractile reserve' relates to early clinical observations[179] that maximal LV pumping performance in response to pharmacological inotropic challenge is strongly related to outcome in patients with cardiac dysfunction. Other than risk-stratification, contractile reserve is also used to guide clinical decision-making regarding suitability for coronary revascularisation, valve surgery or cardiac transplantation[180]. In the context of phenotyping genetically altered mice, application of cardiovascular stress, either pharmacological or with forced exercise[181], is frequently used to disclose abnormalities not apparent in the resting state due to cardiac compensation.

Systemic blood pressures in R299Q γ2 mutant mice, including derived mean arterial pressure, were not significantly different to WT controls (Figure 42). LV end-diastolic pressures were comparable across groups (data not shown), with a reduction in baseline LV developed pressure (LVSP – LVDP) in homozygous mutant mice not reaching significance. However, in response to dobutamine challenge, significant effects for genotype were identified on several LV systolic function parameters, including LVSP and LV dP/dt_{max} (the maximal rate of LV pressure development).

Notably, genotype was observed to exert a marked effect on heart rate, both at baseline and in response to dobutamine infusion, with R299Q γ2 homozygous mutant mice manifesting lower heart rates at each dose in the protocol (0, 4 and 16 ng dobutamine/g body weight/minute) (Figure 42). An assessment of myocardial relaxation (lusitropic) indices (dP/dt_{min} and tau) revealed a clear signal for diastolic impairment in mutant mouse hearts (Figure 43). Full results of the invasive haemodynamics assessment are tabulated in Appendix 3.

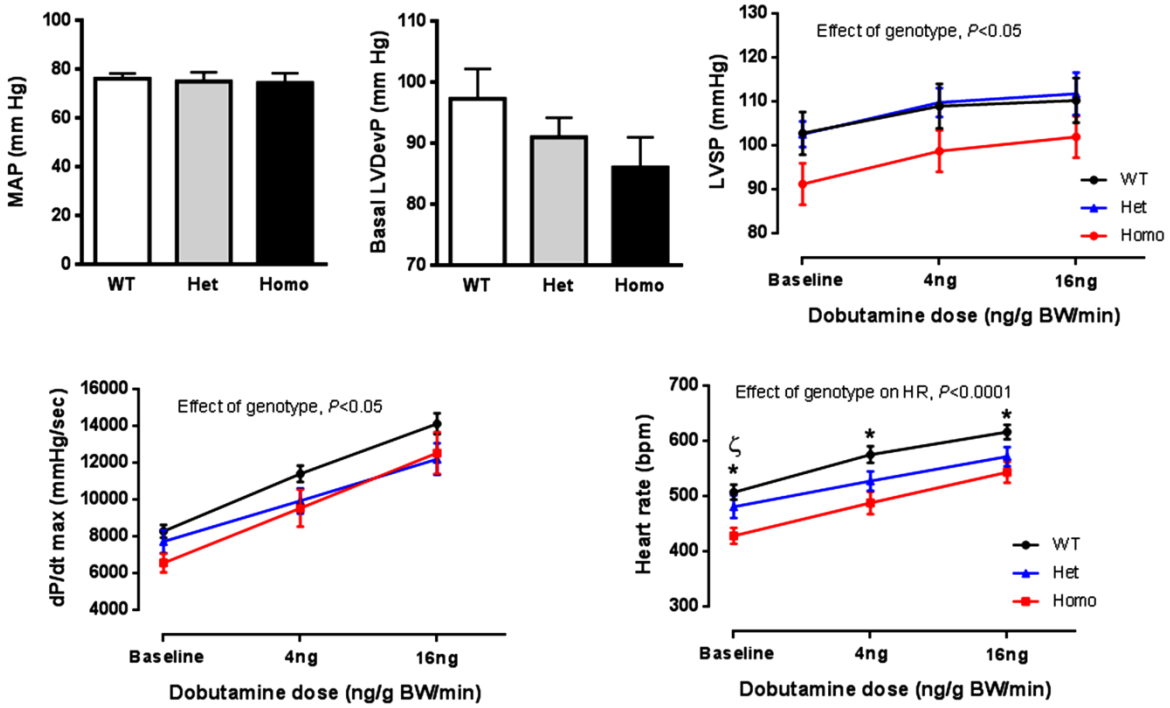


Figure 42. R299Q γ2 mutant mice have impaired contractile and chronotropic reserve at 12 months of age (N=10-18/genotype). *P<0.05 WT vs homozygote, ζ P<0.05 heterozygote vs homozygote, comparisons at time points indicated.

Upper panels – Mean arterial pressure (MAP); basal LV developed pressure (LVDevP) and LV systolic pressure (LVSP) in response to dobutamine infusion. BW, body weight. Lower panels – The effect of dobutamine stimulation on the maximal rate of rise in LV pressure (dP/dt max) and heart rate (HR).

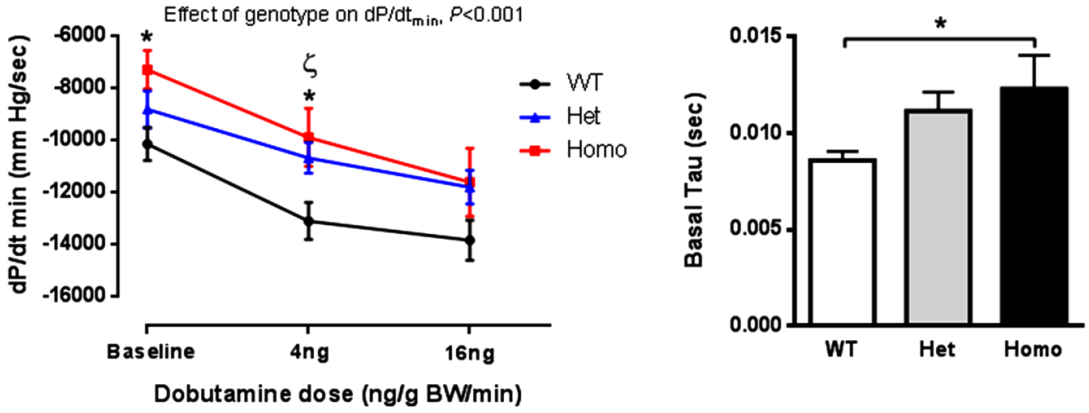


Figure 43. R299Q γ2 mutant mice display impaired LV relaxation (N=10-18/genotype). *P<0.05 WT vs homozygote, ζ P<0.05 heterozygote vs homozygote.

Left panel – Analysis of the steepest rate of LV pressure decline (dP/dt_{min}) – a marker of ventricular relaxation, revealed a significant effect of genotype. dP/dt_{min} is a frequently used diastolic parameter although, as a velocity measurement, is influenced by loading conditions and sensitive to the starting and final pressures in the LV. Right panel – Use of the time constant of isovolumic relaxation, tau (τ) – which represents the time taken for LV pressure to drop by a set proportion (to 1/e of its starting value during the relaxation period) and which is less sensitive to loading conditions – supported this finding of impaired lusitropy in R299Q γ2 homozygous mutant hearts.

3.3.2.f Ex vivo cardiac indices on a C57BL/6 genetic background

Given the importance of genetic strain in modifying mouse phenotype and the possibility that the mixed 129/C57BL/6 background may be influencing phenotype homogeneity, mice heterozygous for the R299Q γ2 mutation were backcrossed onto a C57BL/6 genetic background for 7 generations. Harvesting of hearts from 2 month old male mice on this incipient congenic C57BL/6 genetic background did not reveal any significant increase in absolute heart weight at this age (Figure 44). However, a significant signal for increased body weight was apparent in homozygous R299Q γ2 mutant mice. Normalisation of heart weight to either body weight or tibial length[182] did not identify any significant differences between genotypes at this age.

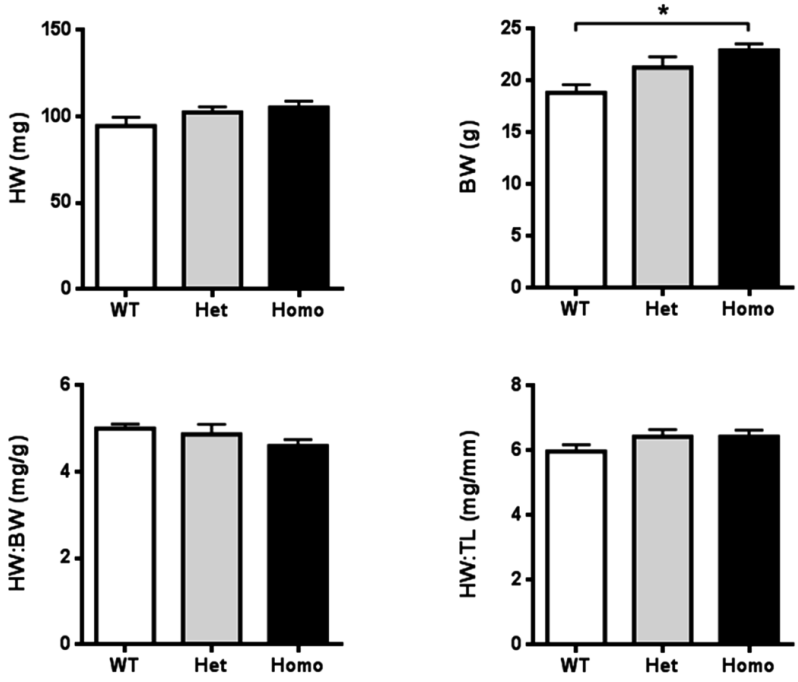


Figure 44. *Ex vivo* cardiac indices and body weight of R299Q γ2 mutant and WT male mice on a C57BL/6 genetic background aged 2 months (N=4-9/genotype). Abbreviations: HW, heart weight; BW, body weight; TL, tibial length. ****P*<0.05

Given the lack of significant differences in heart weight at 2 months, a cohort of mice were allowed to age further and tissues then harvested. By 12 months of age, R299Q γ2 mutant mice on a C57BL/6 background had significantly increased cardiac mass compared to WT controls, although accompanied by a marked increase in body weight (Figure 45). Normalisation of cardiac size to tibial length revealed a persistent signal for greater cardiac mass in mutant mice. This did not

appear to be specific for the heart, however, with clear increases in the mass of other organs including the liver and kidney – the latter persisting even when normalised to tibial length.

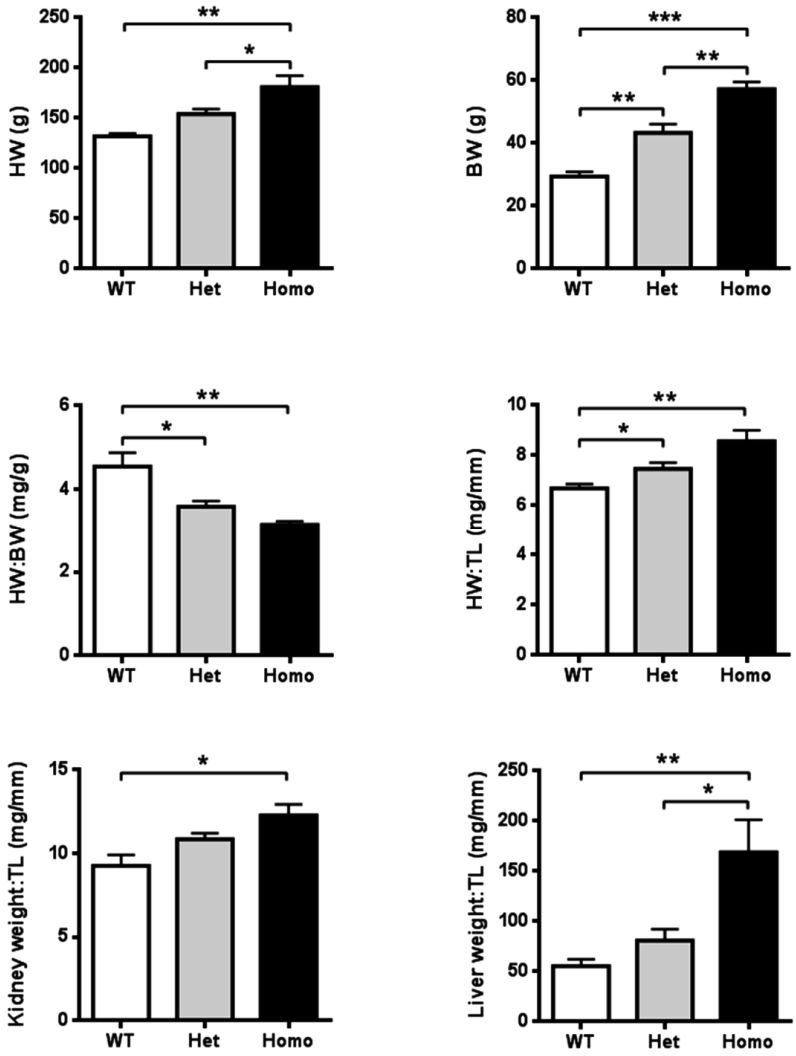


Figure 45. Heart weight, bodyweight and normalised *ex vivo* kidney and liver weights from male mice aged 12 months on a C57BL/6 background (N=6/genotype). ****P*<0.05, ** *P*<0.01, * *P*<0.001**

Overall, these data are consistent with increased cardiac mass in R299Q γ2 mutant mice on a C57BL/6 genetic background, but in the context of heavier animals with apparent *generalised* organ enlargement. Indeed, skeletal size, as judged by tibial length measured with digital calipers, was also significantly increased (*P*<0.05) at 12 months in homozygous mutant mice, measuring (mean ± SEM): WT 19.74 ± 0.33 mm, Het 20.62 ± 0.24 mm and Homo 21.06 ± 0.34 mm.

3.3.2.g Expression of cardiac stress markers

Pathological cardiac hypertrophy is frequently accompanied by a switch to a fetal pattern of gene expression[183]. Given the identification of signals for cardiac dysfunction in R299Q γ2 mutant mice using both non-invasive and invasive assessment methods, the expression of a panel of genes associated with cardiac stress or hypertrophy was investigated using qRT-PCR (Figure 46). This did not reveal any significant differences between the genotypes at two months of age, although there was a trend (*P*=0.09) towards upregulation of *Nppb*, encoding natriuretic peptide B.

The same panel of cardiac stress response genes was re-evaluated at 12 months (Figure 46). This identified the emergence of a significant 2.8-fold increase in *Nppb* expression in R299Q γ2 homozygous mutant mice, although no significant differences were apparent for the other genes assessed, including: skeletal muscle α-actin (*Acta1*), natriuretic peptide A (*Nppa*) and β-myosin heavy chain (*Myh7*).

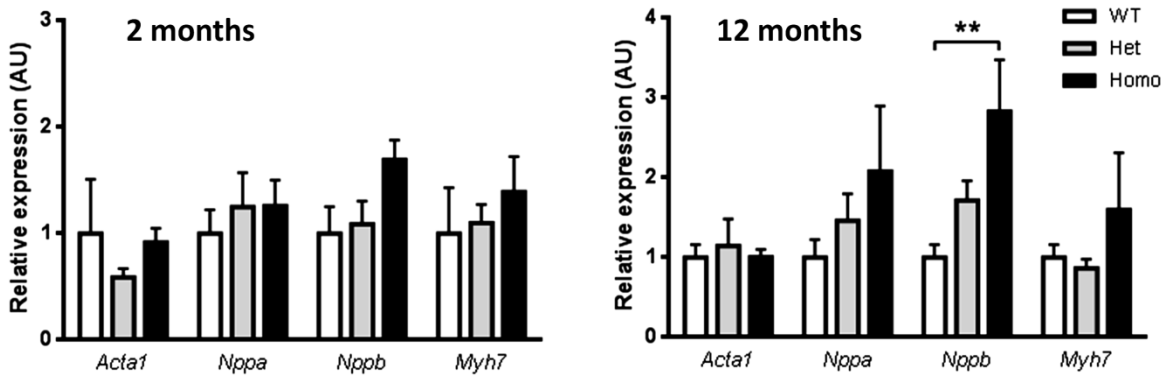


Figure 46. Relative mRNA expression of cardiac stress response genes at 2 and 12 months of age (N=6/genotype). *****P*<0.01

Importantly, these signals for isolated upregulation of *Nppb* were robust to genetic background, being present in mice of both mixed and C57BL/6 background (latter results presented). These changes in gene expression reinforced findings from prior functional and structural assessment, suggesting that R299Q γ2 mutant mice develop subtle LV systolic impairment, but not pathological LVH, with some evidence of a mutant gene dosage effect.

3.4 Discussion

3.4.1 Summary of principal chapter findings

Using a novel gene-targeted murine model for PRKAG2 cardiomyopathy bearing the R299Q mutation, the work presented in this chapter has identified:

i) Specific expression of the R299Q γ2 mutation at RNA level within whole heart in mutant mice. Although the targeting strategy did not readily permit the distinction between mutant and WT γ2 peptide, quantification of γ2 levels by Western blotting using an N-terminal γ2 antibody suggests comparable levels of expression across all three genotypes.

ii) No evidence was found for compensatory up-regulation of the remaining γ subunits at mRNA level. Although downregulation of γ3 transcript was identified by qRT-PCR in homozygous mice, this is of uncertain biological significance given the very low levels of γ3 expression in the heart.

iii) The apparent effect of the R299Q mutation on γ2-specific AMPK activity appears highly dependent on the extraction method used, with kinase activity assays of γ2-containing AMPK complexes obtained from perfusion-stabilised hearts failing to reveal the loss-of-function reported by transgenic mouse models overexpressing mutant R302Q γ2 in the heart[120, 124]. However, what can arguably be considered the biochemical hallmark of the *PRKAG2* mutations – namely interference with adenine nucleotide binding – was confirmed *in vitro* for the allosteric effect of AMP.

iv) No histological evidence of excess glycogen accumulation was apparent in mutant hearts, even up to 12 months of age. Although biochemical quantification of glycogen at this time point disclosed a significant increase in glycogen content in homozygous mutant mice, this was still orders of magnitude lower than that seen in a 'traditional model' of GSD. However, the presence of this discernible increase does provide support, albeit indirect, for the concept that the primary effect of the mutation is to (inappropriately) activate γ2 AMPK complexes.

v) Signals compatible with mild LV systolic dysfunction were identified in R299Q γ2 mutant mice using a range of non-invasive and invasive techniques. Older mice also exhibited LV diastolic

dysfunction. A signal for bradycardia was also discerned in R299Q γ2 homozygous mutant mice. This feature is explored further in chapter 4.

vi) On a mixed 129/C57BL/6 genetic background, R299Q γ2 mutant mice display no evidence of LV hypertrophy (LVH). However, mice backcrossed onto a C57BL/6 inbred genetic background do exhibit increased cardiac mass, but in the setting of greater body and internal organ size, indicating a wider, systemic effect of the mutation. The latter is investigated in chapters 6 and 7.

Several of these findings are discussed in more detail in the following sections.

3.4.2 Insights gained into the effect of γ2 mutations on AMPK activity

Crystal structures of mammalian γ1 with superimposed γ2 mutations would predict that these should largely affect adenine nucleotide binding[23]. In agreement with this and prior *in vitro* studies investigating the consequences of these mutations, the murine R299Q γ2 mutation is observed to cause a loss of sensitivity to allosteric stimulation by AMP *in vitro*.

The true *in situ* effect of the R299Q mutation on γ2-specific activity has, however, proven to be more challenging to delineate. Indeed, using an overexpressing transgenic (TG) approach to model the disease, the effect of γ2 mutations on AMPK activity has been controversial, with apparently different effects ('gain-' or 'loss-of-function') induced by the different mutations[119-121] at varying disease time points. One way of reconciling these findings is to invoke a key role for progressive glycogen accumulation – dramatically increased in TG hearts – in modulating AMPK activity with time. Thus, when assayed at a late time point, AMPK activity appears lower due to glycogen-induced inhibition via the GBD on the β-subunit. Conversely, assaying AMPK activity very early on (e.g. at 1 week of age), before significant glycogen deposition has taken place, reveals an increase in activity[119]. That the latter represents the true, primary effect of the mutation (independent of glycogen) is supported by experiments using an acute adenoviral-mediated approach to overexpress mutant γ2 in cultured cardiomyocytes[124].

Measurement of γ2-specific activity from AMPK complexes derived from rapidly harvested hearts immediately snap-frozen in liquid nitrogen identified dramatically *lower* activity in R299Q γ2

homozygous mutant mice compared to WT controls. At first sight this would suggest that the R299Q mutation behaves as a hypomorphic allele, resulting in *loss* of γ2 function. However, this simple analysis fails to take into account the conditions under which the AMPK complexes were harvested and thus the ambient adenine nucleotide status of the complexes. Under conditions of ATP depletion (as occur during organ anoxia and ischaemia during tissue harvesting), WT AMPK complexes would be expected to be markedly activated. The lower activity of mutant R299Q γ2 complexes can therefore be interpreted as a lack of appropriate activation by an ATP-deplete state. Conditions of tissue harvesting are not likely to accurately reflect the true basal state of AMPK complexes *in vivo*, a scenario where ATP levels are not anticipated to be significantly limiting. Therefore, in order to obtain a true reflection of basal activity *in situ*, an approach utilising *ex vivo* perfusion of harvested hearts to stabilise cellular energetic state was used. Under these conditions, rather than an apparent loss of γ2-specific AMPK function, there was a trend (P=0.07) in favour of *greater* basal activity of mutant γ2 complexes compared to WT. That this result failed to reach significance may point to the low signal-to-noise ratio attendant on working with a mutation conferring only a modest degree of activation in a minority cardiac isoform that is expressed at physiological levels via gene-targeting, in contrast to dramatic overexpression of mutant transgene.

Investigation of the TG^{N488I} model using an *ex vivo* cardiac perfusion approach, in combination with a period of no-flow global ischaemia to manipulate cellular nucleotide concentrations[149], provides support for this more nuanced interpretation of the consequences of γ2 mutations on AMPK activity (Figure 47). Assessment of pan α-Thr172 phosphorylation (as a marker of total AMPK activity) from hearts subjected to global ischaemia indicated lower phosphorylation in TG^{N488I} hearts compared to non-TG WT. This finding is consistent with formal measures of γ2-specific AMPK activity using the SAMS peptide assay from R299Q γ2 complexes harvested without a prior period of stabilising perfusion.

An alternative approach to 'locking' the enzyme in its true basal physiological state by freeze-clamping of tissue during stabilised *ex vivo* cardiac perfusion, is to utilise a recently described

fluorescent-based activity reporter[184] to assess AMPK activity (albeit total rather than γ2-specific) in live primary cells (e.g. hepatocytes or cardiomyocytes).

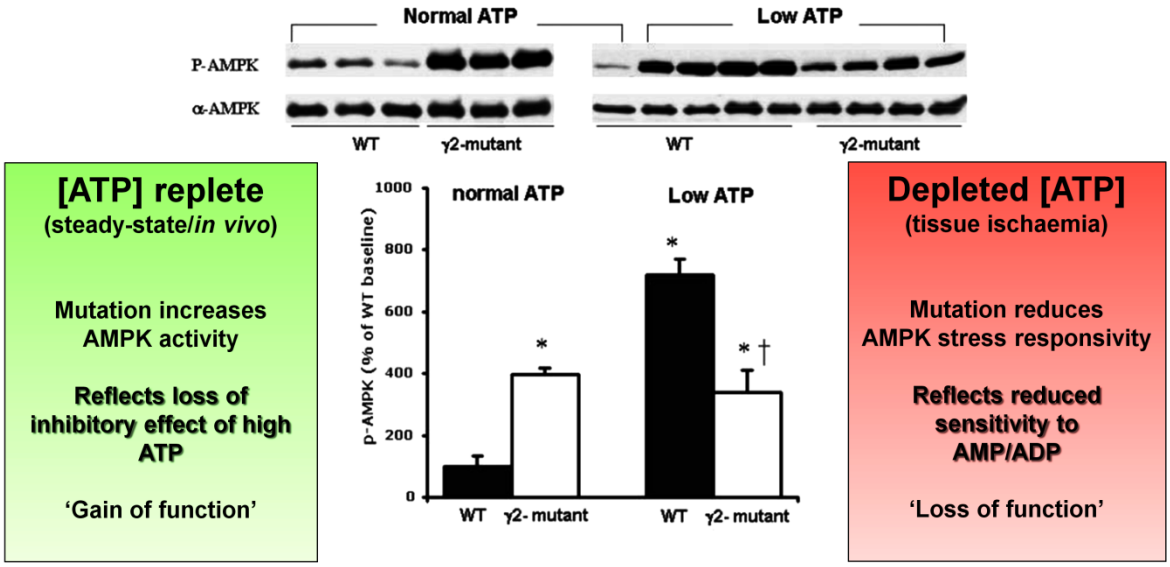


Figure 47. The effects of γ2 mutations on AMPK activity are complex, with evidence of bidirectionality dependent upon ambient adenine nucleotide status.[ff]

3.4.3 Cardiomyopathy in the absence of gross glycogen accumulation

The phenotype of the R299Q γ2 KI model exhibits clear differences to existing mouse models which utilise an over-expressing transgenic approach to model PRKAG2 cardiomyopathy, most notably the absence of massive glycogen deposition in the heart. Standard histological techniques for the visual detection of glycogen are limited in their sensitivity by the difficulties in fixing glycogen, readily leading to losses during traditional processing methods[74, 175] and compounded by its extremely rapid metabolism. Notwithstanding this, the absence of overt cardiomyocyte vacuolation on staining with H&E or PAS is in keeping with the notion that the R299Q γ2 gene-targeted model does not have *gross* cardiac glycogen accumulation. Quantitative determination of absolute cardiac glycogen content biochemically did reveal a mild increase in older homozygous mutant mice however. This is suggestive of a chronic, low-grade elevation in glucose uptake, with channeling of excess intracellular glucose moieties into glycogen synthesis at a rate exceeding that of glycogen breakdown or oxidation.

[ff] Adapted from figure 5 Zou et al. *Circ Res* 2005;97:323-328.

The reason for the marked discrepancy in glycogen accumulation between the R299Q γ2 KI and the TG models is unclear, but may reflect the effects of overexpression and, speculatively, differences in efficiency of mutant human versus murine γ2 to promote excessive cardiomyocyte glucose uptake. In the mouse it would appear that the presence of a γ2 mutation which predominately functions as 'activating' throughout life and which is expressed at relatively 'physiological levels' is, even in the homozygous state, simply insufficient to induce marked perturbation of carbohydrate metabolism. The finding that overexpression of human WT *PRKAG2* transgene alone results in a 10-fold elevation in cardiac glycogen content *in vivo*[124], would suggest that expression of mutant γ2 has to reach a sufficient absolute threshold to overwhelm the normal regulatory influences maintaining tissue glycogen homeostasis. What about in comparison to clinical cases of PRKAG2 disease, with clear reports[82, 106] of profound glycogen excess in human *heterozygotes*? The lack of identification of *any* increase in glycogen content biochemically in R299Q γ2 heterozygotes may simply indicate a low signal-to-noise ratio obscuring a small but real increase. Speculatively, this may also reflect significant interspecies differences in the metabolic efficiency of glycogen turnover between mouse and human.

The aforementioned considerations conceptualise PRKAG2 cardiomyopathy as a 'simple' Mendelian inherited disease, uniformly leading to glycogen excess in humans. This belies the true complexity of Mendelian disorders. Indeed, the inconsistent correlation between genotype and phenotype in human Mendelian disease has prompted some geneticists to argue that the phenotypes of Mendelian 'single gene' disorders are more accurately depicted as complex traits, with the recognition that the pathogenic mutation is itself one component of a complex network of genetic (e.g. independently inherited polymorphisms) and environmental influences[185, 186]. In this regard, it is salutary to note that clinical reports of symptomatic *PRKAG2* mutation carriers have identified cases with otherwise typical phenotypic disease features, but in the absence of *any* demonstrable glycogen excess[110, 116].

The observation of discernible cardiac functional abnormalities (impaired systolic and diastolic function), upregulation of a molecular marker of cardiac stress and signs of

electrophysiological disturbance (chronotropic incompetence and lower baseline heart rate) in R299Q γ2 homozygous mutant mice, occurring in the absence of gross glycogen accumulation, further point to a potential disconnect between the two. By providing an experimental platform relatively free of glycogen accumulation, a particular strength of the R299Q γ2 gene-targeted model may therefore be envisaged as its ability to aid dissection of *primary* versus secondary effects of mutations in *PRKAG2*.

3.4.4 Genetic background and modifier genes

It is increasingly apparent that the genomic landscape or 'background' in which the mutation finds itself has the ability to interact with the causal gene variant and thereby critically influence phenotype. Consideration of genetic background is thus crucial to understanding phenotype.

As with the majority of gene-targeted models, the R299Q γ2 mutation was initially established on a mixed genetic background, with gene-targeted, 129/Ola-derived embryonic stem (ES) cells being injected into C57BL/6 blastocysts to form chimeras, followed by crossing with C57BL/6 to test for germ-line transmission. The use of 129 ES cells as the strain of choice in gene-targeting experiments is traditional and largely relates to practical considerations of greater robustness and stability compared to C57BL/6 ES cells in culture[187]. The poor fecundity of 129 mice, however, prompts backcrossing onto a C57BL/6 genetic background, both to increase fertility and subsequent ease of phenotypic characterisation[188]. Whilst gene targeting can now be undertaken in C57BL/6-derived ES cells, this process is still significantly less efficient, with greater difficulty in culturing C57BL/6 ES cells and reduced efficacy of chimera formation described[188]. However, this may be offset by greater fertility of progeny once germ-line transmission of the mutation is achieved, in addition to avoiding the need for repeated backcrossing to create a fully congenic strain (i.e. one achieved after 10 generations of backcrossing)[188].

Mouse background strain is known to have potentially dramatic effects on the phenotype resulting from a genetic modification. A striking example of this is the dilated cardiomyopathy associated with cardiac overexpression of the sarcoplasmic reticulum calcium-binding protein, calsequestrin (CSQ). A single backcrossing of CSQ transgenic mice from a DBA/2J to C57BL/6 background

results in a reduction in survival of progeny from a mean of 157 to 52 days and acceleration of the cardiomyopathy phenotype[189]. Indeed, simple strain alone, even in the absence of any introduced genetic modification, influences baseline measures of *in vivo* and *ex vivo* cardiac function[190]. Modifier alleles present in the background strain genome are thought to affect mutant gene expression by several mechanisms, including altered gene transcription rates or mRNA stability and epigenetic effects resulting in altered DNA methylation or chromatin packaging[191].

The majority of the functional cardiac phenotyping of R299Q γ2 mutant mice was performed on a mixed genetic background. Whilst this demonstrated mild LV systolic dysfunction, there was no evidence of increased cardiac mass as determined by highly sensitive imaging with cine-MRI or measurement of post-mortem heart weight. Whilst phenotyping on a mixed background is expedient, such an approach is limited by the lack of a defined background and greater attendant heterogeneity. On backcrossing mice 7 generations onto a C57BL/6 genetic background to generate an incipient congenic line (i.e. between 5-10 generations backcrossed), a signal for greater cardiac mass was identified – but only in older mutant mice – both absolute and when normalised to tibial length. However, this was not accompanied by a clear pattern of re-expression of multiple fetal genes characteristic of the development of pathological hypertrophy.

The interpretation of increased cardiac mass of R299Q γ2 mutant mice on a C57BL/6 background is further complicated by the emergence of altered somatic and internal organ size. Whilst small cohorts of heterozygote and homozygote R299Q γ2 mutant mice on a mixed 129/C57BL/6 background were noted very early on in the course of the project to exhibit greater body weight, this was inconsistent amongst different litters and did not always reach statistical significance. However, after backcrossing these mice 7 generations to the C57BL/6 inbred strain, in comparison to WT littermate controls, R299Q γ2 homozygous mutant mice exhibited significant increases in the mass of the whole body (up to 2-fold), liver (~3.5 fold), interscapular brown adipose tissue (~2.5 fold), kidney (~1.4 fold) and heart (~1.4-fold), with heterozygotes displaying an intermediate signal. The emergence of this systemic phenotype points to a potential biological role for γ2 outwith the heart (albeit in the context of a pathogenic mutation) and is explored further in chapters

6 and 7. However, it also highlights a key, but unexpected, disadvantage of the total somatic gene-targeting strategy used to model the human R302Q γ2 mutation: namely the confounding effect of producing larger mice, inherently limiting the utility of the R299Q γ2 KI model to function as a platform with which to explore mechanisms of LVH in PRKAG2 cardiomyopathy.

Findings suggestive of an electrophysiological phenotype in R299Q γ2 mutant mice were robust to genetic background, appeared to have a high degree of penetrance, recapitulated key features of the human disease and, critically, preceded the development of significant alterations in body size. Accordingly, this aspect of the cardiac phenotype, presented in the next chapter, was explored in greater detail in the knowledge that any mechanistic processes elucidated were likely to be robust to the somatic phenotype.

Chapter 4. Electrophysiological phenotype and disease mechanisms

4.1 Aims and objectives

The focus of the work presented in this chapter was to define the electrophysiological (EP) phenotype of R299Q γ2 KI mutant mice, particularly with regard to the presence of ventricular pre-excitation and then to uncover novel disease mechanisms for the cardiac phenotype. A non-hypothesis-driven approach using a microarray identified a strong molecular candidate for one aspect of the EP phenotype, namely sinus bradycardia. This association was explored further using a combination of *in vivo*, isolated whole-organ and cell-based approaches.

Accordingly, the specific objectives of the experiments presented here were:

i) To define the basic electrophysiological phenotype of R299Q γ2 KI mutant mice using a combination of conscious and anaesthetised ECG recordings.

ii) To investigate for the presence of ventricular pre-excitation.

iii) To use whole-genome gene expression profiling to systematically probe the mutant *Prkag2* transcriptome to uncover molecular candidate(s) for the cardiac phenotype.

iv) Based on the microarray identification of downregulation of a transcript encoding an ion channel known to be highly enriched in sinoatrial node (HCN1), to address the hypothesis that the bradycardia of R299Q γ2 KI mutant mice was associated with a reduction in the 'funny' current, I_f, encoded by HCN (hyperpolarisation-activated, cyclic nucleotide-gated channel) proteins.

v) To begin to delineate mechanisms whereby AMPK γ2 may affect *Hcn* expression levels.

4.2 Chapter-specific materials and methods

4.2.1 Intrinsic heart rate

Measurement of intrinsic heart rate was undertaken during *ex vivo* cardiac perfusion (described in chapter 2).

4.2.2 ECG telemetry

ECG biopotentials were recorded in conscious, freely moving male R299Q γ2 mutant mice and WT controls (N=2-3/genotype) by subcutaneous implant of radiofrequency transmitters (TA10-EA-F20 from Data Sciences International, DSI, St. Paul, MN) at 4 months of age under isoflurane general anaesthesia using a protocol designed in accordance with welfare guidelines[192]. Mice received pre-operative saline (500 µL subcutaneously) and eye protection (Viscotears). A heating pad was used to maintain murine temperature homeostasis. Surgery was performed under sterile conditions after chlorhexidine-based skin disinfection and within a heated extraction hood. Paired bipolar electrode leads were tunnelled subcutaneously and secured parasternally in a lead II configuration using 6/0 mersilk. The telemeter body was then positioned in a pre-fashioned subcutaneous pocket in the right lower flank and wounds closed with 6/0 vicryl. Buprenorphine analgesia was administered intra-operatively (0.1 mg/kg) and mice recovered in a heating chamber before being housed individually post-surgery. Mice were allowed to fully recover from instrumentation for 14 days prior to any recordings. ECGs were acquired using Dataquest A.R.T. acquisition software (DSI) and analysed off-line for arrhythmia using Ponemah Telemetry Data Review and ECG PRO (DSI) software.

4.2.3 Invasive electrophysiology study (EPS)

A detailed series of conduction parameters were assessed in a cohort of 3 month old R299Q γ2 mutant mice and WT littermate controls on a C57BL/6 background, based on modifications of a published EPS protocol for mouse[193] (Figure 48). A 1.1F octapolar electrophysiology catheter (EPR-801, Millar Instruments) allowing simultaneous recording and pacing was introduced into the right atrium and ventricle via the right internal jugular vein under 1.5% isoflurane anaesthesia. High-fidelity intracardiac electrograms were filtered at 0.5-500 Hz and continuously recorded using

PowerLab and LabChart software (ADInstruments, Oxford). Correct catheter placement was verified by the presence of large ventricular electrograms on the distal poles and a predominately atrial signal on the proximal poles. After obtaining a baseline surface ECG, programmed atrial pacing protocols were performed as described[194] using a pacing stimulator with pacing output set at twice diastolic threshold (s88 Grass stimulator, Grass technologies, USA).

Conduction parameters measured during the protocol included:

- Sinus cycle length (SCL).
- Sinus node recovery time (SNRT): this was determined by delivering an atrial pacing train at a cycle length of 100 ms for 15 s x 3. SNRT was calculated as the maximum interval from the last paced atrial complex to the first spontaneous complex after cessation of pacing.
- Antegrade AV nodal conduction properties: AV Wenckebach cycle length (AVW) and AV 2:1 cycle length were determined using burst atrial pacing by progressively reducing the pacing cycle length from that of baseline in decrements of 10 ms until 1:1 AV conduction was reliably lost (Wenckebach cycle length) or resulted in failure of conduction of every other signal (2:1 cycle length).
- AV nodal effective refractory period (AVNERP): this was determined using programmed atrial extrastimulus pacing. An eight stimuli atrial drive train (S1) delivered at 100 ms was followed by a single premature stimulus (S2) which was progressively decreased until loss of ventricular conduction. AVNERP was defined as the longest S1-S2 coupling interval where S2 failed to generate a conducted beat.
- Ventriculoatrial (VA) conduction was also assessed using ventricular extrastimulus and incremental right ventricular pacing, with planned ventricular tachycardia (VT) stimulation if feasible during the experiment as determined by duration of the procedure and subject viability.

Following this, right atrial programmed electrical stimulation was used in an attempt to induce an atrioventricular re-entrant tachycardia (AVRT)[gg] and thereby potentially implicate an accessory pathway. An atrial double extrastimulus technique was used with an 8 stimuli primary drive train (S1) delivered at a fixed cycle length of 100 ms, followed by premature stimuli (S2 and S3) coupled at 80 ms and decremented to refractoriness. Further provocation for AVRT included atrial burst pacing at fixed cycle length, including following β-adrenoceptor stimulation by isoproterenol administration (1 ng/g i.v.).

As a further challenge for the presence of a concealed accessory pathway, measurement of standard surface ECG intervals was repeated following administration of 30 μg/g i.v. procainamide (to increase refractoriness and therefore slow conduction preferentially in a putative accessory pathway) and 1 mg/kg i.p. CCPA (2-chloro-N^6-cyclopentyladenosine), an adenosine A_1 receptor agonist which acts to induce transient AV nodal block whilst not affecting a potential accessory pathway. Analysis of recordings was performed off-line, blind to genotype using LabChart software (ADInstruments).

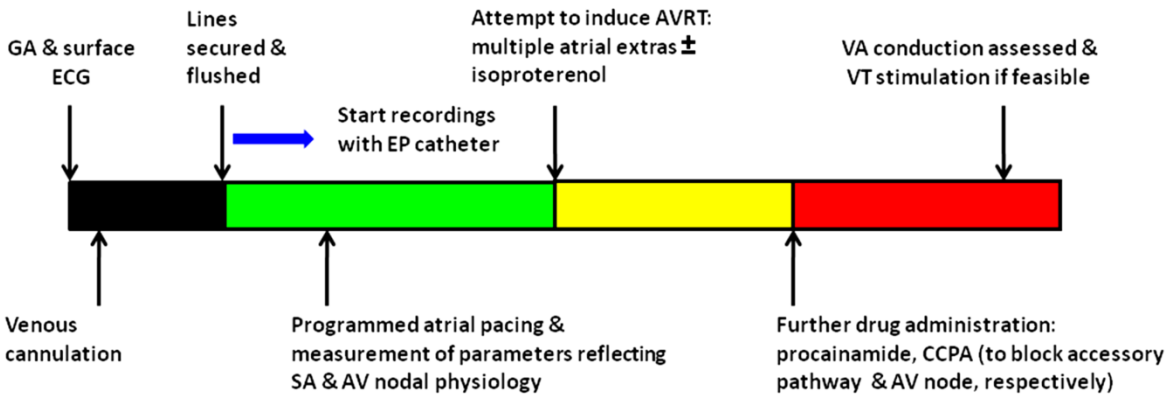


Figure 48. Overview of EPS protocol used for invasive evaluation of cardiac conduction.

Abbreviations: GA, general anaesthetic; AVRT, Atrioventricular re-entrant tachycardia; VA, ventriculoatrial; VT, ventricular tachycardia; SA, sinoatrial; AV, atrioventricular.

4.2.4 Microarray study and data analysis

Experiment design and data collection were in compliance with the Minimal Information About a Microarray Experiment (MIAME) guidelines[195]. The cohort consisted of male R299Q γ2

[gg] AVRT occurs due to delay in the AV node allowing the ventricular part of the accessory pathway to be activated and retrograde conduction to occur via the accessory pathway to the atria. The AV node is then no longer refractory, allowing conduction to proceed in an antegrade direction down the His-Purkinje system, completing the circuit.

homozygote and heterozygote mutant and WT littermate mice aged ~40 days, with 6 replicates per genotype. Total RNA was extracted from powdered whole heart using an RNeasy fibrous tissue minikit (Qiagen) with proteinase K treatment. Residual genomic DNA was removed with DNAase treatment. RNA yield was determined by spectrophotometry (NanoDrop ND1000). RNA quality and integrity were assayed using the RNA 6000 Nano assay on an Agilent Bioanalyzer. All samples used for the array had an RNA integrity number of >7.0. Whole-genome gene expression analysis was performed using the Illumina Single Colour Mouse WG-6_V2_0_R0_11278593 BeadChip containing 45,200 annotated transcripts. Biotinylated cRNA was generated using the Illumina TotalPrep-96 RNA Amplification Kit (# 4393543 Ambion, Inc., Austin, TX) from 300 ng total RNA from each sample. Briefly, this includes a first- and second-strand reverse transcription step, followed by a single *in vitro* transcription amplification that incorporates biotin-labelled nucleotides. This was followed by a direct hybridisation assay (Illumina, San Diego, CA) according to the manufacturer's directions, including array hybridisation, post-hybridisation washing, blocking and streptavidin-Cy3 staining. Fluorescence emissions by Cy3 were imaged using an Illumina BeadArray scanner. Raw data quality was checked using the Illumina Genome Studio software v.1.0.6 (Illumina, San Diego, CA) and converted into raw intensity values for each probe.

Raw intensity data were then imported into the R statistical programme (v.2.10, http://www.r-project.org/, R Foundation for Statistical Computing, Vienna, Austria) for further quality control and processing. The raw data was background corrected using array-specific measures of background intensity based on negative control probes and subsequently underwent transformation and normalisation using the variance stabilisation algorithm 'vsn' package (BioConductor) to correct for systematic non-biological bias in the data. The normalised data was then analysed and graphs visualised using Partek Genomics Suite software (Partek, St. Louis, MO). Initial exploration of data was made with principal components analysis to visualise sources of variation and technical factors. Determination of genes differentially expressed between genotypes was performed by ANOVA followed by application of a 5% cut-off rate using the Benjamini-Hochberg false discovery rate algorithm by adjusting raw *P*-values to correct for multiple testing. Genes were annotated using Illumina's annotation file for the BeadChip used.

4.2.5 Sino-atrial node and cardiac regional dissection for qRT-PCR

Male WT inbred C57BL/6 mice aged 8 weeks underwent euthanasia with an overdose of isoflurane followed by cervical dislocation. Hearts were immediately excised and placed in a Petri dish containing Tyrode solution (140 mM NaCl, 5.4 mM KCl, 1.8 mM $CaCl_2$, 5.5 mM D-glucose, and 5 mM HEPES-NaOH buffer, pH 7.4). Ventricles were removed and sections of free right and left ventricular and atrial walls were individually snap-frozen in liquid nitrogen. The sinoatrial node (SAN) was isolated as the intercaval region adjacent to the crista terminalis using a dissecting microscope as described[196] and immediately snap frozen. In brief, after excision of both ventricles, the right atrium and interatrial septum were opened and pinned to reveal the endocardial surface of the right atrium. SAN was anatomically delineated bilaterally by crista terminalis and interatrial septum, superiorly by the superior vena cava and inferiorly by the inferior vena cava and right branch of the sinoatrial ring bundle (Figure 49). Total RNA was isolated from 4 pools of 3 mice each for SAN and individually (i.e. non-pooled) for mice for other cardiac regions (N=12 total) using the method for RNA extraction described in chapter 2.

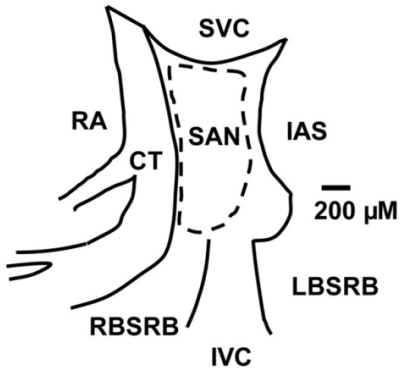


Figure 49. Intercaval region illustrating landmarks used in SAN dissection. Abbreviations: SVC, superior vena cava; RA, right atrium; CT, crista terminalis; IAS, interatrial septum; RBSRB, right branch of the sinoatrial ring bundle; IVC, inferior vena cava; LBSRB, left branch of the sinoatrial ring bundle.[hh]

4.2.6 Sinus node electrophysiology and I_f recordings

The SAN region was isolated as above and single SAN cells dissociated using an enzymatic solution containing collagenase (224 U/mL, Worthington Biochemical, NJ), elastase (1.42 U/mL) and protease (0.45 U/mL) and kept in Tyrode solution. I_f recordings were performed by voltage-

[hh] Adapted from figure 1 Mangoni et al. *Proc Natl Acad Sci* 2003;100:5543-5548.

clamping SAN myocytes in the whole-cell configuration at 35 ± 0.5°C with 1 mM $BaCl_2$ and 2 mM $MnCl_2$ added to the Tyrode superfusate to minimise interference of other currents (K^+ and Ca^{2+}, respectively)[197]. Patch-clamp pipettes were drawn from borosilicate glass and contained an intracellular-like solution[197]: 130 mM potassium aspartate, 10 mM NaCl, 5 mM EGTA-KOH (EGTA, ethylene glycol tetraacetic acid), 2 mM $CaCl_2$, 2 mM $MgCl_2$, 2 mM ATP as sodium salt, 5 mM creatine phosphate and 0.1 mM GTP as sodium salt, pH 7.2. I_f current density was obtained by measuring current amplitudes during steps between -55 and -125 mV, then normalising to cell capacitance (latter calculated by independent experimental measurements where voltage steps from -35 mV to -45 mV were delivered to the cell; at these voltages no ionic current flows in/from the cell and thus the current is fully attributable to capacitative charge/discharge). The voltage-dependence of activation was determined by using a standardised protocol where step tests at different potentials were followed by a step to -125 mV. Tail currents recorded at -125 mV were then normalised to the maximum amplitude and the obtained data points fitted with the Boltzmann function, providing the activation parameters of the channels as a function of membrane potential[197]. HCN current traces and action potentials were acquired and on-line filtered with pCLAMP software and an Axon Axopatch 200B amplifier (both Molecular Devices, CA).

4.2.7 Heterologous expression in HEK293 cells and I_f recordings

Human Embryonic Kidney cells (HEK293, Phoenix) were cultured in DMEM plus GlutaMAX-I supplemented with 10% FBS (GIBCO BRL) and antibiotics (100 U/mL penicillin/100 µg/mL streptomycin [Life Technologies]) and incubated at 37°C with 95% air/5% CO_2 at 95% relative humidity. For heterologous expression experiments, HEK293 cells were transiently co-transfected with pCDNA 1.1 vector containing human HCN4 construct (1 µg) and the pIRES-hrGFP II vector containing the WT or R299Q *Prkag2* mutant construct (or empty vector, both at 1 µg) using FuGENE HD transfection reagent (Roche). Prior assessment of GFP expression by immunofluorescence microscopy, or expression of WT and mutant γ2 protein by Western blotting using an anti-FLAG antibody, had confirmed transfection and translation of WT and mutant *Prkag2* constructs under these conditions. Electrophysiology experiments were conducted 48-72 hours after transfection. Cells were detached and dispersed by 0.05% trypsin and plated at low

density on a 35 mm Petri dish. Cells were allowed to settle for 3 hours and then currents were recorded from visually-selected GFP positive cells using the whole-cell patch-clamp technique at RT as outlined for SAN (section 4.2.6). The recording pipettes contained: 10 mM NaCl, 130 mM potassium aspartate, 0.5 mM $MgCl_2$, 1 mM EGTA-KOH, 1 mM HEPES-KOH, 2 mM ATP as sodium salt, 0.1 mM GTP as sodium salt) and 5 mM phosphocreatine, pH 7.2. The control extracellular solution was a modified Tyrode solution designed to increase I_f current amplitude (110 mM NaCl, 30 mM KCl, 1.8 mM $CaCl_2$, 0.5 mM $MgCl_2$and 5 mM HEPES-NaOH buffer, pH 7.4, with $BaCl_2$ and $MnCl_2$ added to aid I_f dissection over other ionic currents).

4.3 Results

4.3.1 R299Q γ2 knock-in electrophysiology

4.3.1.a Surface ECG recordings and telemetry

To accurately determine ECG intervals, anaesthetised surface ECG recordings were undertaken (Figure 50). These revealed significant sinus bradycardia in R299Q γ2 homozygotes. No evidence of ventricular pre-excitation was seen in mutant mice, with normal mean PR interval duration and only mild prolongation of QRS duration. The latter was apparent, but non-progressive, in ECG recordings from R299Q γ2 homozygote mice up to 12 months of age.

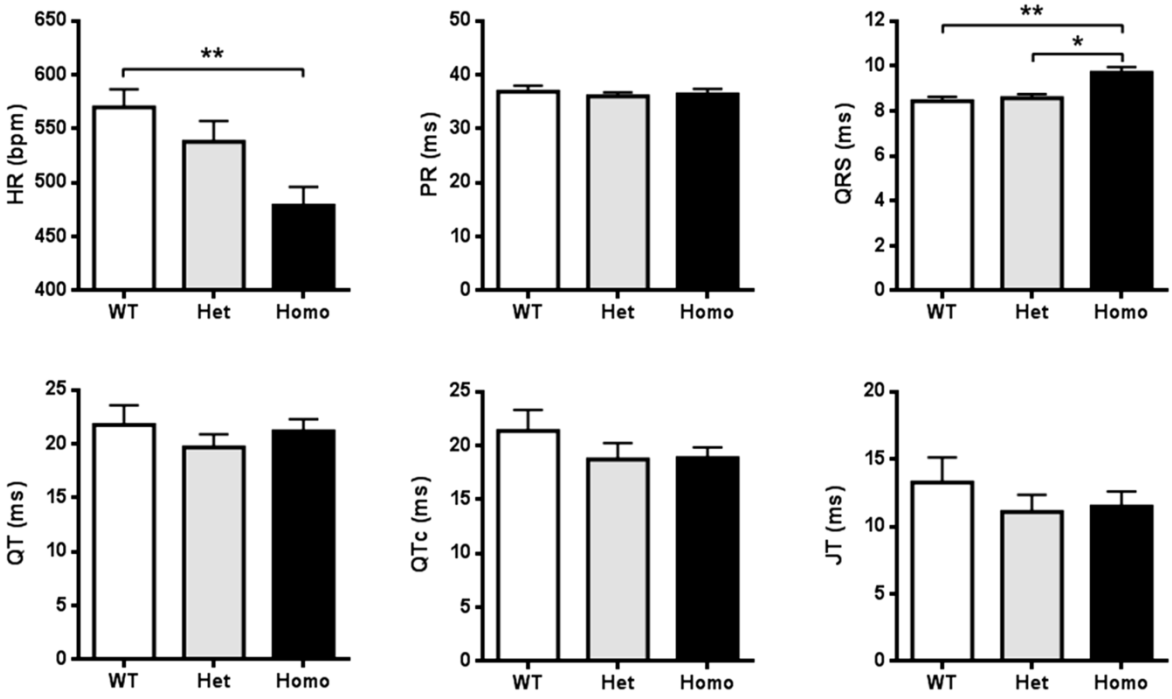


Figure 50. Anaesthetised surface ECG recordings from R299Q γ2 mutant mice and WT controls at 2 months of age (N=7-13/genotype). *P<0.05, **P<0.01

No significant differences were detected in markers of ventricular repolarisation, including QT, QTc (rate-corrected QT interval) or JTc interval[198].[ii] Serial conscious ECG recordings confirmed the signal for significantly lower heart rate of R299Q γ2 homozygous mutant mice without the confounder of anaesthetic, although this was not seen to progress over time (Figure 51).

[ii] JT_c is regarded as a more depolarisation-independent measure of ventricular repolarisation than QTc and thus may be particularly appropriate in cases of QRS abnormality, where JTc = QTc – QRS duration.

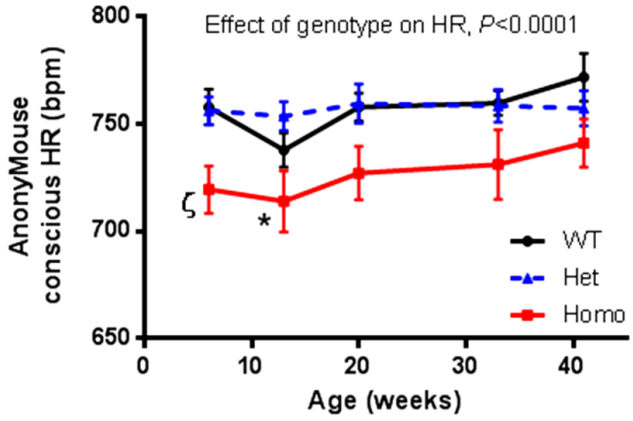


Figure 51. Longitudinal conscious ECG recordings (recorded using AnonyMouse platform) (N=6-12/genotype). ζ *P*<0.05 homozygote vs heterozygote and homozygote vs WT; **P*<0.05 homozygote vs heterozygote. Comparisons at time points indicated.

These conscious (albeit 'stressed' due to recordings being obtained on a foreign platform outside the mouse's home cage) ECG recordings occasionally revealed intermittent, subtle alterations in PR interval in a small number of R299Q γ2 homozygous mutant but not WT mice (Figure 52).

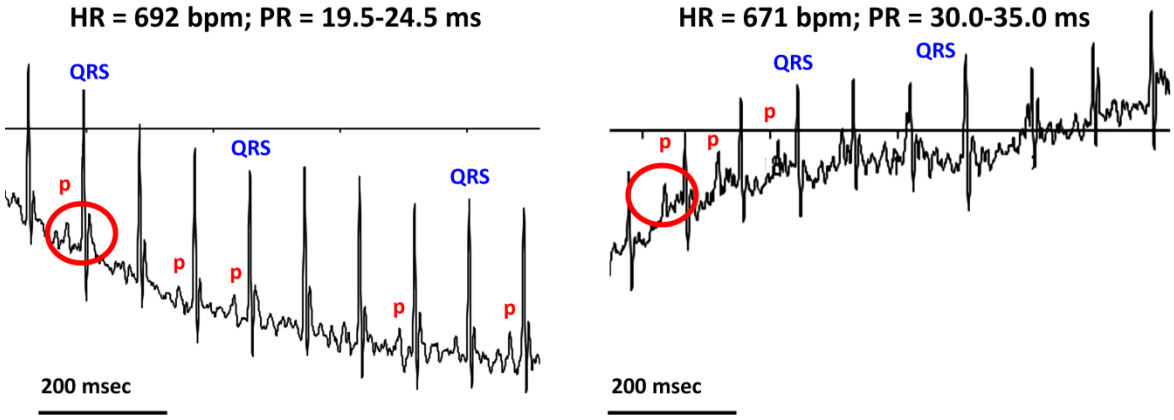


Figure 52. Two segments of the same conscious AnonyMouse ECG recording identifying labile PR interval duration in a male γ2 R299Q γ2 homozygote aged 8 months.

These changes were not typical of overt ventricular pre-excitation but were suggestive of potential AV nodal pathology. Accordingly, to be more confident of excluding intermittent ventricular pre-excitation, implantable biotelemetry (N=2-3/genotype) was utilised to provide longitudinal, high fidelity recordings in the conscious state and within the familiar environment of the animal's own cage. This did not show any evidence of ventricular pre-excitation in either R299Q γ2 mutant genotype, but reinforced the view that the predominant EP abnormality in homozygous mutant

mice was sinus node-related, with telemetry traces revealing runs of marked sinus bradycardia and sinus pauses (Figure 53). Heterozygous mutant mice evaluated were not seen to differ from WT.

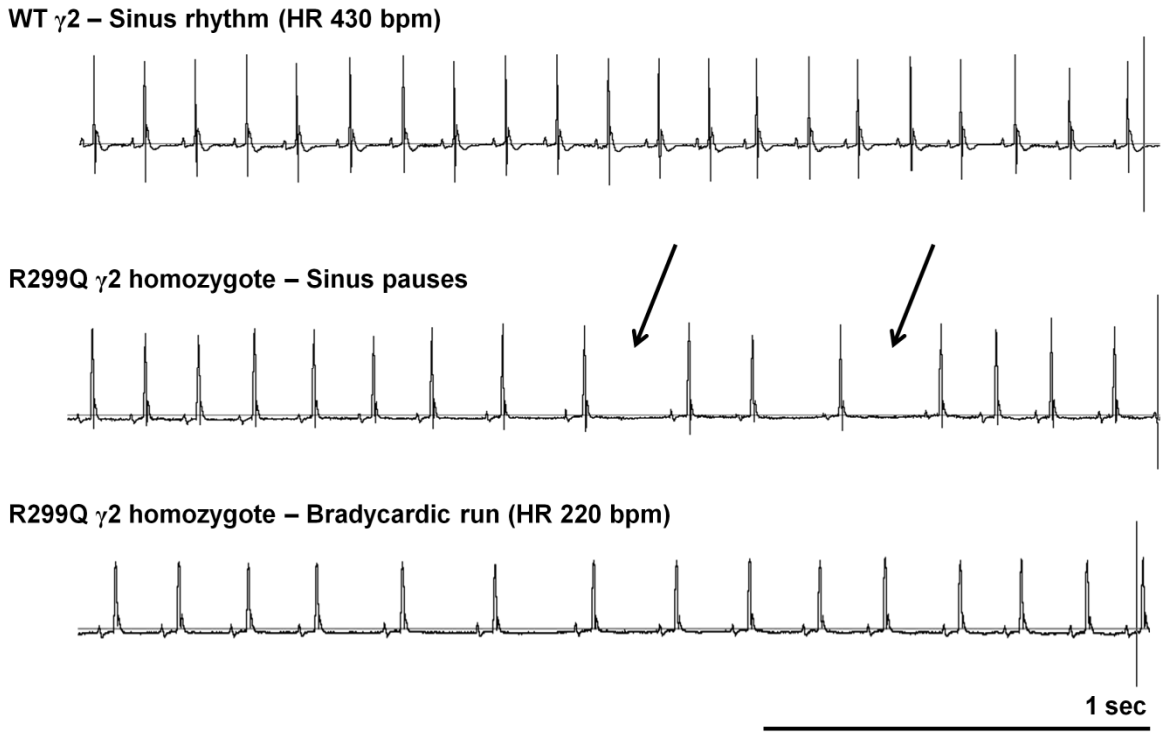


Figure 53. Implantable ECG telemetry traces from an age and sex-matched WT (upper trace) and R299Q γ2 homozygote mouse (middle and lower traces).

4.3.1.b Invasive electrophysiology study

Accessory atrioventricular (AV) connections are sometimes recognised as being 'concealed', with no apparent typical signs of pre-excitation on the surface ECG. This can occur if a pathway does not conduct in an antegrade direction. Furthermore, the appearances of pre-excitation have been described to differ between mice and humans, in particular relating to the appearance of a delta wave[199]. In humans the delta wave reflects a fusion of ventricular depolarisation and activation via both the native AV conduction system *and* the accessory pathway. Mice, however, have a relatively long AV delay in comparison to total ventricular activation time, thus the appearance of a fusion complex is less likely to occur if antegrade conduction down the accessory pathway is sufficiently fast to be able to completely activate the ventricle[199].

Given the limited sensitivity of surface ECG or telemetry recordings to detect conduction disturbances compatible with *concealed* accessory pathways, an invasive electrophysiology study (EPS) approach was utilised. EPS in mice[193] uses clinical pacing protocols derived from standard invasive assessments of human conduction used as part of arrhythmia diagnosis or treatment. The protocol applied (section 4.2.3) focused on evaluation of baseline sinus and AV nodal conduction in response to atrial pacing, followed by programmed electrical stimulation to unmask ventricular pre-excitation, in conjunction with use of pharmacological agents to preferentially block conduction in the AV node (with CCPA) or accessory pathway (with procainamide). Thus, pre-excitation can be increased by enhancing the AV delay either pharmacologically with AV nodal blocking drugs, or by extrastimulus pacing. In addition, atrio-hisian pathways may be detected by measuring the PR interval and atriofasicular or fasiculoventricular pathways by evaluating for a QRS complex.

Using this protocol, no evidence for ventricular pre-excitation was found at EPS, either at baseline (Table 6) or following programmed electrical stimulation. Double premature atrial extrastimuli were associated with greater recovery time in R299Q γ2 homozygous mutant mice, but there was no significant increase in the formal measure evaluated – sinus node recovery time (SNRT). A clear increase in sinus cycle length (SCL) of R299Q γ2 homozygous mutant mice mirrored the sinus bradycardia already identified.

Table 6. Baseline conduction parameters at EPS.[jj] *P<0.05 vs heterozygote & P<0.001 vs WT

BASELINE	WT (n = 11)	R299Q γ2 Heterozygote (n = 7)	R299Q γ2 Homozygote (n = 13)
Baseline SCL (ms)	104.4 ± 9.0	112.3 ± 10.2	126.9 ± 13.1*
SNRT (ms)	104.3 ± 35.3	110.1 ± 16.78	115.6 ± 21.89
AVW (ms)	67.7 ± 12.8	63.4 ± 8.2	67.3 ± 4.5
AV 2:1 (ms)	53.1 ± 10.7	48.1 ± 6.2	52.5 ± 6.0
AVNERP (ms)	43.9 ± 14.6	39.2 ± 6.3	40.8 ± 8.1

[jj] Abbreviations: SCL, Sinus cycle length; SNRT, sinus node recovery time; AVW, atrioventricular (AV) Wenckebach cycle length; AV 2:1, AV 2:1 cycle length; AVNERP, AV nodal effective refractory period.

4.3.1.c Intrinsic heart rate

Whilst a variety of *in vivo* techniques on separate cohorts had identified sinus bradycardia in R299Q γ2 homozygous mutant mice, these *in vivo* rate measurements reflected a composite of both intrinsic heart rate driven by the sinoatrial node (SAN) and autonomic nervous system (ANS) activity. Accordingly, to determine whether the bradycardia was intrinsic to the heart in the absence of autonomic influences, intrinsic rate was measured from isolated beating hearts perfused *ex vivo*. This proved to be the case, with an even more marked heart rate difference between homozygous mutant mice and the other two genotypes (Figure 54).

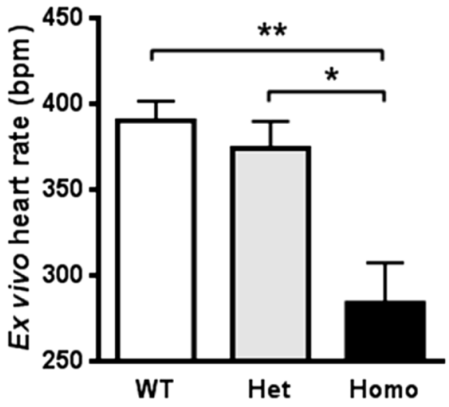


Figure 54. Intrinsic rate of *ex vivo* perfused R299Q γ2 mutant and WT hearts (N=6-11/genotype). *P<0.05, **P<0.01

4.3.2 Whole-genome gene expression profiling

In order to gain insights into the potential molecular correlates for the observed functional (chapter 3) and electrophysiological abnormalities, a non-hypothesis driven approach was used to systematically probe the mutant *Prkag2* cardiac transcriptome.

4.3.2.a Approach & experimental design

Given the identification of differences in body weight and size between R299Q γ2 mutant and WT mice emerging with age, comparative transcriptomic analysis of the genotypes was undertaken at a young age to minimise these potentially confounding factors. Whole-genome gene expression profiles were obtained from age-matched male mice on a C57BL/6 genetic background using an

Illumina-based microarray platform allowing for simultaneous profiling of over 45,200 transcripts (Table 7).

Table 7. Microarray cohort

	Wildtype γ2 (N=6)	R299Q γ2 Heterozygote (N=6)	R299Q γ2 Homozygote (N=6)
Age (days)	41 ± 0.4	42 ± 2	42 ± 2
Body weight (g)	20.2 ± 1.5	21.3 ± 2.3	21.0 ± 0.7
Tibial length (mm)	18.5 ± 0.8	18.7 ± 1	18.9 ± 0.9

4.3.2.b Primary dataset exploration

Initial exploration of the normalised data was performed using hierarchical clustering analysis[200] and principal components analysis (PCA) to visualise sources of variation arising from both biological (e.g. age, weight, genotype, litter source) and technical (e.g. BeadChip, RNA extraction batch) factors. In PCA plots the samples are represented as points, with each set of vectors (principal components) decreasingly capturing variation in the dataset[201]. PCA identified the individual hybridising chip as a large contributor to variability – i.e. a significant 'chip effect' (left panel, Figure 55). A balanced experimental design had been used, however, to ensure that different genotype groups were equally distributed across the BeadChips (right panel, Figure 55).

Different mixed-model ANOVAs, incorporating both fixed (e.g. genotype) and random (e.g. chip) effects, were used to further explore the major sources of variability in the dataset and to help determine the most important factors to include in an ANOVA model[202]. Consistent with the PCA findings, chip was seen to be a significant source of variation in the data and inclusion of this in a two-way ANOVA modestly increased the effect of genotype by accounting for a significant part of the noise in the data. Models including more covariates (e.g. litter origin, age and body weight) did not explain significantly more variability and so were not utilised in the final ANOVA to avoid reducing the model's overall statistical power to detect true differential gene expression.

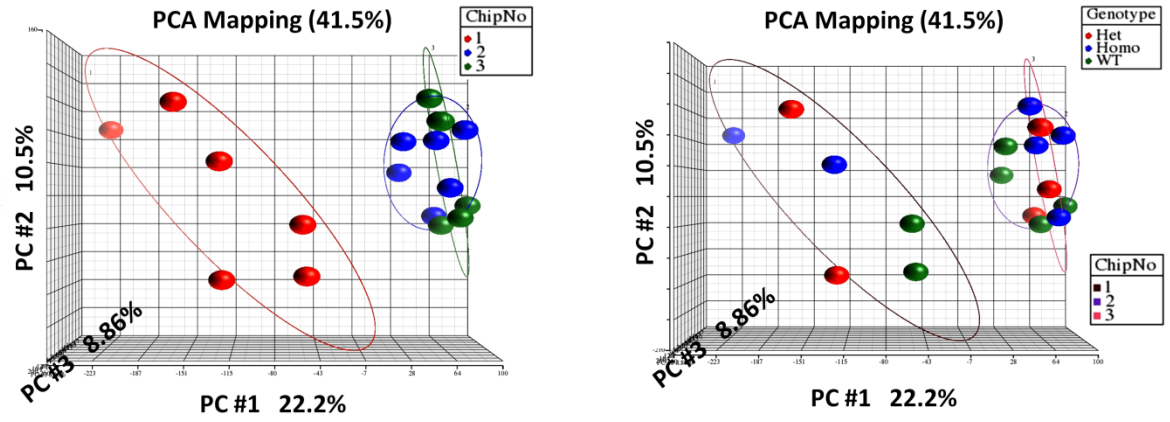


Figure 55. Preliminary exploration of microarray data using PCA.

Fixed-content whole-genome array panels from Illumina are designed such that multiple samples are hybridised onto a single BeadChip. Thus, each BeadChip effectively represents an individual experimental block. All samples on an individual BeadChip then undergo the same processing steps, such that samples on the same BeadChip may share common effects[203].

Left – Affirming this, PCA of the microarray dataset revealed that principal component 1 (PC#1) accounted for a large proportion of the variability in the experiment (>22%) and appeared to largely depict a chip effect: samples hybridised to chips 2 and 3 (blue and green) were seen to cluster together, signifying broadly similar pan-genome expression compared to those hybridised to chip 1 (red). Right – PCA scatter plot of microarray data coloured according to genotype. Block randomisation was used such that randomly selected samples were hybridised to each chip (coloured ellipses) with the restriction that N=2 of each genotype (denoted by colouration of sphere) were utilised per BeadChip[203].

4.3.2.c Microarray results

A two-way ANOVA model, incorporating genotype and chip, identified significant differential gene expression. Adjustment of raw *P* values to correct for multiple testing using a 5% Benjamini-Hochberg false discovery rate[200] identified ~40 genes to have differential expression in homozygote mutant versus WT mice (Appendix 4). Hierarchical clustering analysis showed 3 distinct groups corresponding to genotype, with heterozygous samples displaying patterns of gene expression closer to homozygous samples than to WT (Figure 56). Heat map depiction showed intermediate levels of differential expression for samples from heterozygous mice.

4.3.2.d Validation by qRT-PCR

Using the same samples, qRT-PCR was used to confirm gene expression results obtained by microarray analysis for select transcripts (chosen as the most differentially expressed transcripts that were annotated)[204]. qRT-PCR verified 6 out of 8 of these to be significantly differentially regulated, all of which were concordant in direction of expression with the microarray (Figure 57).

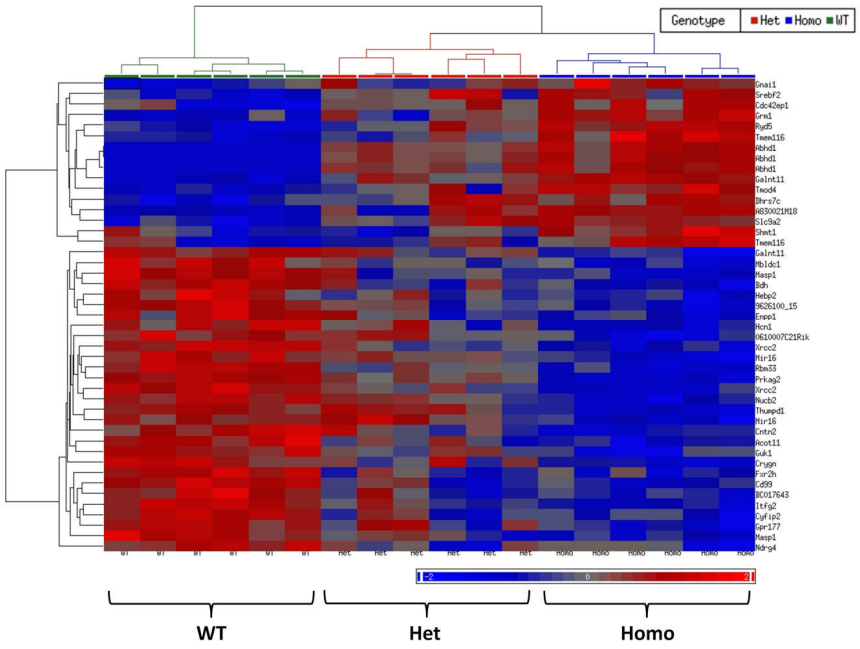


Figure 56. Heat map with hierarchical clustering of differentially expressed genes. The rows represent genes, whilst the columns indicate individual samples from different genotypes. Colour scale denotes quantification for gene expression, with red denoting upregulation and blue denoting downregulation of gene expression.

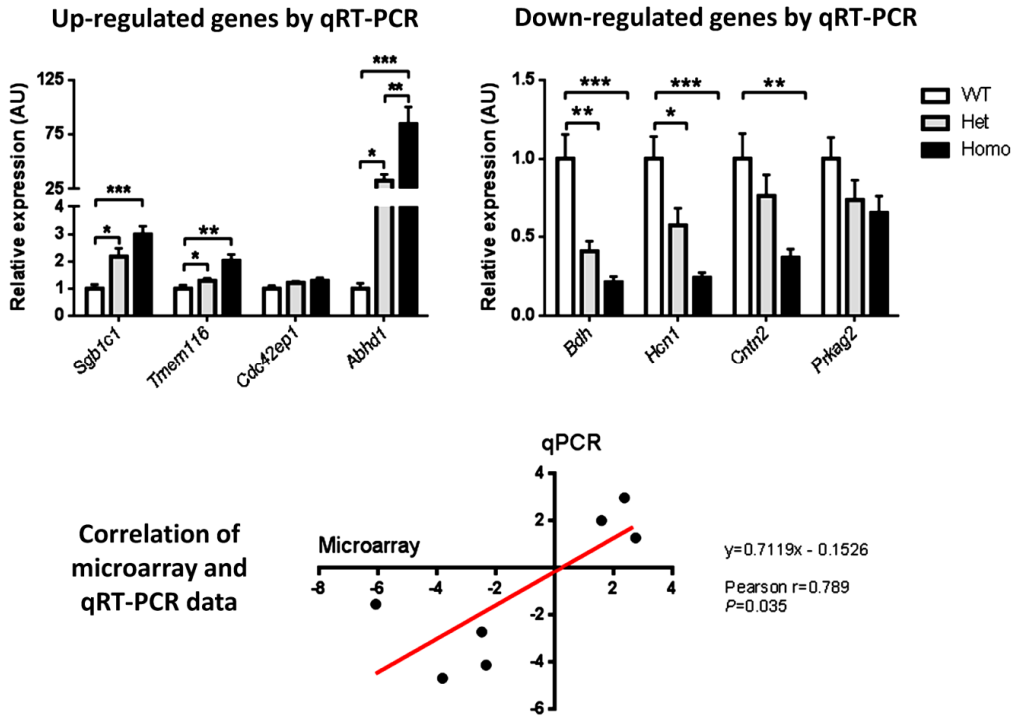


Figure 57. Validation of selected microarray analysis results by qRT-PCR (N=6/genotype). ****P*<0.05, *****P*<0.01, ******P*<0.001.

Upper row – Selected expression data obtained from the microarray platform was largely in good agreement with qRT-PCR. Apparent changes in expression in *Cdc42ep1* and *Prkag2* from the microarray did not achieve significance using qRT-PCR. Lower row – Significant correlation of fold-change (FC) in expression was identified between the two techniques. NB *Abhd1* excluded here on account of skewing the graph, although the correlation remains significant with its inclusion at *P*<0.05.

4.3.2.e Microarray data interpretation and follow-up

Attempts at gene-set enrichment analysis using on-line pathway databases (including KEGG, BioCarta, Reactome, Sigma-Aldrich pathways and Signaling gateway) revealed that the modest size of the gene list (WT vs. homozygote comparison 43 genes, WT vs heterozygote comparison 4 genes, with False Discovery Rate set at 5%) did not lend itself well to reliable identification of biological processes distributed across the level of gene networks, rather than at the individual gene level. Accordingly, the homozygote versus WT differential gene list was functionally annotated using DAVID (the Database for Annotation, Visualization and Integrated Discovery, DAVID Bioinformatics Resources 6.7; NIAID, NIH), supplemented with searches of Entrez Gene (NCBI) and the Mouse Genome Database (Mouse Genome Informatics, The Jackson Laboratory, Maine) and scrutinised. In the context of the phenotype of sinus bradycardia in R299Q γ2 homozygous mutant mice, the most promising molecular candidate for further exploration appeared to be *Hcn1*.

Hcn1 is one of four genes (*Hcn1-4*) encoding the molecular subunits of f-channels, known as hyperpolarisation-activated, cyclic nucleotide-gated channel proteins. Within the heart, f-channels conduct the pacemaker 'funny' current, I_f, which is thought to play an integral role in the spontaneous activity of SAN cells and the modulation of heart rate by the ANS. Basic biophysical properties of the channels (homo- or hetero-tetramers of HCNs) conducting I_f include: an unusual opening (and hence depolarisation) upon hyperpolarisation; opening in the diastolic depolarisation voltage range of the pacemaker action potential (AP); mixed conductance of Na^+ and K^+ ions; and direct modulation by cAMP via a cyclic-nucleotide binding domain. Whilst HCN4 is the predominant HCN isoform present in mammalian SAN (including man, rabbit and rodent), constituting between 60-80% of total *Hcn* mRNA transcript, HCN1 is recognised as contributing to I_f and being the second most abundant transcript in murine SAN[205], with HCN2 playing a minor role and HCN3 not expressed in SAN.

Accordingly, the expression of the remaining *Hcn* isoforms in whole-heart were investigated from an independent cohort of mice aged 40 days (Figure 58). This confirmed: a 75% reduction in *Hcn1*, and a 40% reduction in *Hcn4* in homozygous mutant mice; significant downregulation of *Hcn1* and

Hcn4 in heterozygous mice; and a mild increase of *Hcn2* in homozygous mutant mice, of uncertain significance.

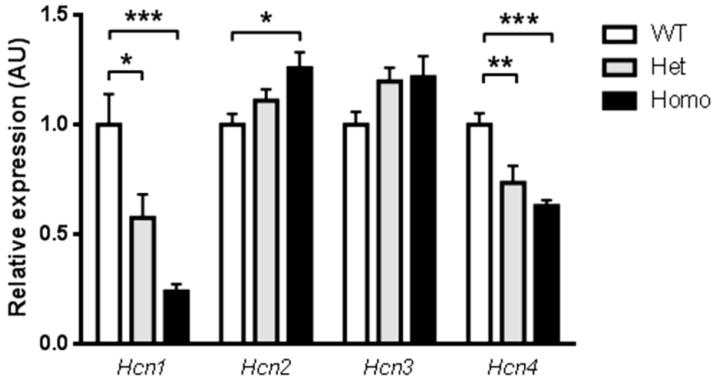


Figure 58. Expression of *Hcn* isoform mRNA from whole-heart in female WT and R299Q γ2 mutant mice aged 40 days (N=7-8/genotype). *P<0.05, **P<0.01, ***P<0.001

4.3.3 Sinoatrial node cellular electrophysiology

The identification of intrinsic sinus bradycardia associated with downregulation of key cardiac transcripts encoding a pacemaker current, argued for a direct effect of the R299Q γ2 mutation on altering SAN myocyte electrophysiological properties, in particular by perturbing I_f. Accordingly, the electrophysiology of isolated SAN myocytes was evaluated, with specific reference to I_f.

4.3.3.a Spontaneous rate & maximum diastolic potential

The spontaneous rate of single SAN myocytes isolated from both R299Q γ2 heterozygous and homozygous mutant mice was lower than that of age-matched WT, indicating reduced automaticity of pacemaker cells (Figure 59).

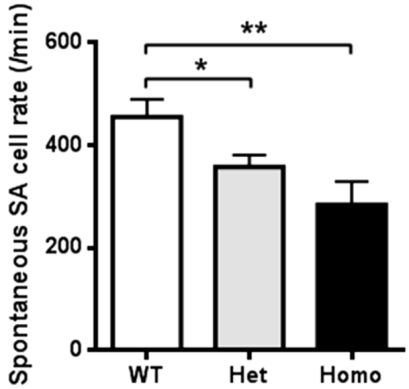


Figure 59. Mean SAN cell beating rate (N=5-11 cells/genotype). *P<0.05, **P<0.01

Unlike non-automatic cells, pacemaker cells do not have a stable resting membrane potential, but instead exhibit a maximum diastolic potential (MDP)[kk] at the onset of phase 4 of the AP, followed by a gradual and spontaneous phase 4 depolarisation[206]. Pacemaker discharge frequency is dependent upon a number of factors, including: MDP; the slope of the slow diastolic depolarisation of phase 4; the threshold voltage for firing; and the duration of the recovery phase, all of which are capable of modulation by autonomic influences[207]. Measurement of MDP revealed no differences between genotypes (Figure 60).

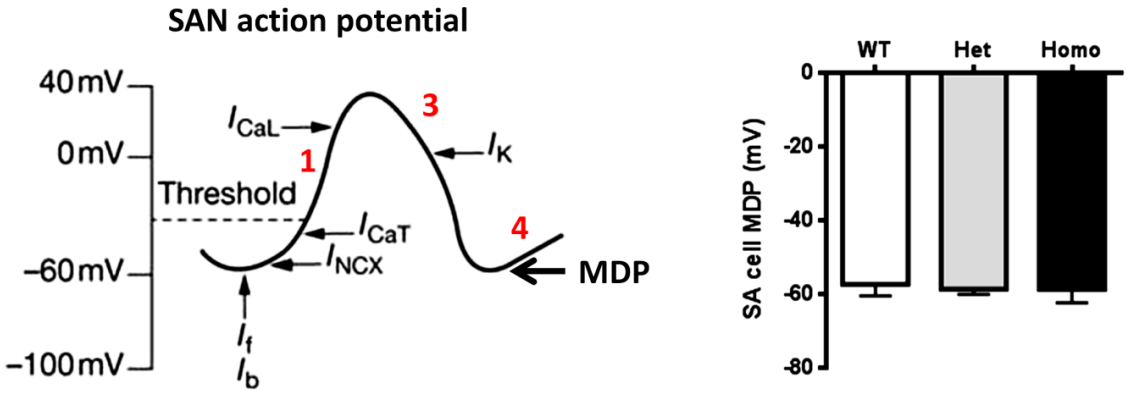


Figure 60. Left – Schematic illustrating an SAN action potential (AP) with phases numbered in red[ll]; Right – Levels of maximum diastolic depolarisation (MDP) from R299Q γ2 mutant and WT SAN myocytes (N=5-11 cells/genotype).

Abbreviations: I_f, funny current, I_b; background inward Na^+ current; I_{NCX}, inward sodium-calcium exchanger current; I_{Ca}, inward calcium current, with T, transient current or L, long-acting current.

This finding of no difference in MDP is significant for several reasons (Professor Baruscotti, personal communication): i) any alteration in MDP has an indirect effect on all other currents activated after the MDP, including I_f, I_{Ca} (inward Ca^{2+} current) and I_{Na} (inward Na^+ current), since their activation/ inactivation state is dependent upon the MDP; ii) Altered MDP *per se* is suggestive of an alteration in I_K (an outward K^+ current); iii) A more positive or negative MDP will alter the duration of the pacemaker phase (i.e. the time taken for the SAN cell to reach threshold for AP firing) independent of any change in the slope of the phase 4 diastolic depolarisation.

[kk] The most negative potential reached by the SAN myocyte between successive APs, largely driven by K^+ currents.

[ll] Adapted from figure 2 Yusuf & Camm *Nat Clin Pract Cardiovasc Med* 2005;2:44-52.

4.3.3.b I_f density & voltage-dependence of current activation

The clear reduction in *Hcn1* and *Hcn4* transcript, together with their key role in mediating the majority of mammalian I_f, argued for an effect of the R299Q γ2 mutation on I_f current density and/or its properties. To address this hypothesis, recordings of I_f were undertaken by patch-clamping isolated SAN myocytes (Figure 61). These revealed a significant and generalised reduction in I_f current density in both R299Q γ2 mutant genotypes, which was more marked for homozygous than heterozygous mutant cells. Assessment of the voltage dependence of activation did not reveal any difference between homozygous mutant or WT mice however, suggesting that (independent of the number of f-channels per cell) the voltage at which individual channels opened was unaffected.

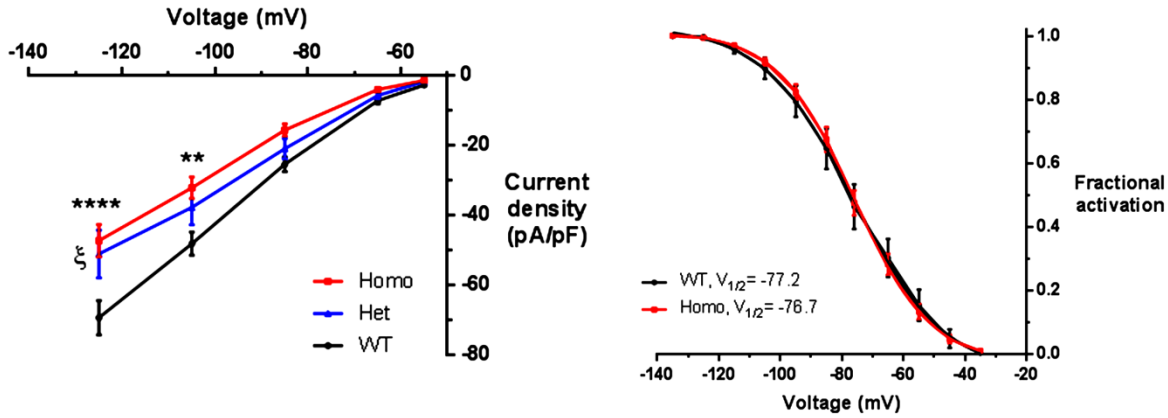


Figure 61. Left – mean steady-state current density plotted against membrane voltage (N=17-29 cells/genotype). ζ *P*<0.01 WT vs heterozygote, ***P*<0.01 WT vs homozygote, *****P*<0.0001 WT vs homozygote

Right – membrane voltage-dependence of activation (N=4-15 cells/genotype).

4.3.3.c Heterologous transfection experiments

The preceding data suggest that the effect of R299Q mutant γ2 on I_f is primarily mediated through a reduction in HCN channel expression, with consequent reduced current density. In order to verify that mutant R299Q γ2 protein was not also exerting a direct/indirect effect on f-channels as a post-translational event, a heterologous expression approach using WT γ2 and R299Q γ2 expressing vectors was used. Initial transfection experiments in HEK293 cells confirmed these to express on transient transfection, based both on GFP fluorescence and anti-FLAG immunoblotting (Figure

62). The latter indicated less robust protein expression of mutant *Prkag2* compared to WT, however, suggesting that over-expressed mutant protein may be less stable than its WT counterpart.

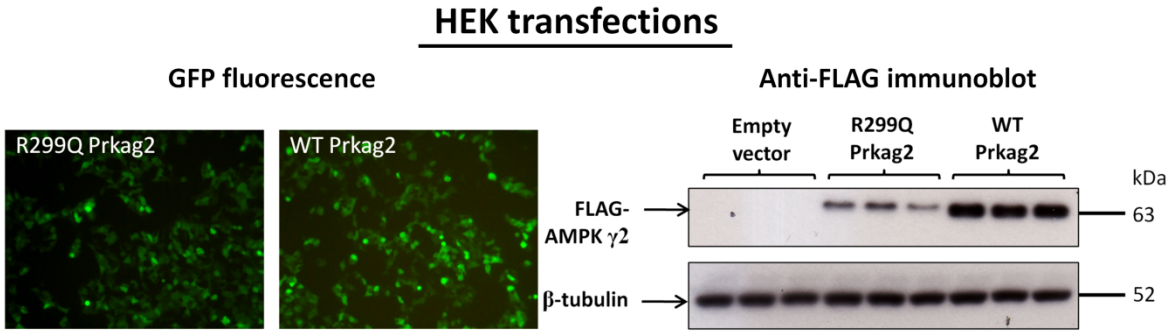


Figure 62. GFP fluorescent images and anti-FLAG immunoblot of HEK293 cells transiently transfected with mammalian expression vectors expressing WT or mutant *Prkag2*. Empty vector treated and untransfected cells exhibited no immunofluorescence (data not shown).

Subsequent transient co-transfection of HEK293 cells with a plasmid constitutively expressing human HCN4 and WT or R299Q mutant γ2 hrGFP II-expressing vector was followed by patch-clamping of GFP fluorescent HEK cells (Figure 63). This revealed no difference in either I_f current density or the voltage-dependence of activation between empty vector, R299Q *Prkag2* or WT *Prkag2* plasmid transfected cells, arguing against a primary effect of R299Q mutant γ2-containing AMPK heterotrimers on modulating HCN4 channels (the latter constituting the majority subunits of native SAN f-channels in both human and mouse).

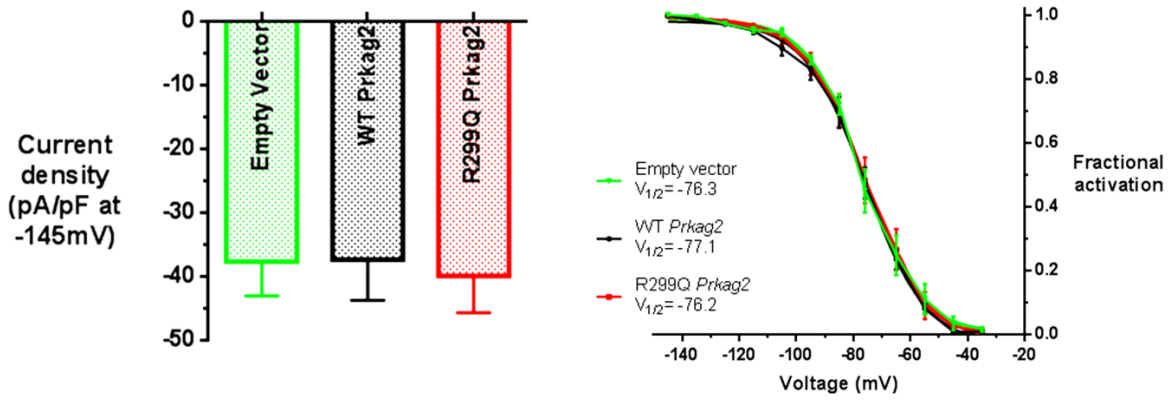


Figure 63. Effect of R299Q mutant γ2 and WT γ2 on heterologously expressed human HCN4 channels.

Left – I_f current density with individual HEK293 cell membrane voltage held at -145 mV (N=10-12 cells/group). Right – fractional activation curve (N=5-6 cells/group).

4.3.4 Initial exploration of mechanisms underlying altered *Hcn* expression

Whilst the factors regulating *Hcn* gene expression within the SAN are not well-described, a number of transcription factors have been reported to be involved in (murine) SAN development and transcriptional programme regulation, including TBX3, SHOX2 and NKX-2.5.[208-210] To determine whether the altered *Hcn* expression identified in R299Q γ2 mutant mice might reflect a wider disturbance of SAN gene expression patterns, the expression of several genes and transcription factors known to play a role in the SAN was examined using qRT-PCR. Genes selected included those thought to act downstream of the transcriptional repressor, TBX3, which suppresses the expression of atrial myocardial genes, e.g. *Cx40*, *Cx43* and *Nppa*.[208] This approach was limited by extraction from whole heart, with failed amplification of several transcripts interrogated due to very low levels of expression, including $K_v1.1$, *Cx 30.2* and *Shox2*. However, it did reveal a significant reduction in *Cacna1g*. This encodes $Ca_v3.1$, one of three pore-forming subunits of the voltage-dependent T-type Ca^{2+} channel responsible for the transient type calcium current $I_{Ca,T}$ and thought to have a role in diastolic depolarisation. Of note in this regard, mice with a disruption in the *Cacna1g* gene display mild sinus bradycardia (although only significant under conditions of ANS blockade) and delayed AV conduction (manifest as a prolonged PQ interval)[211].

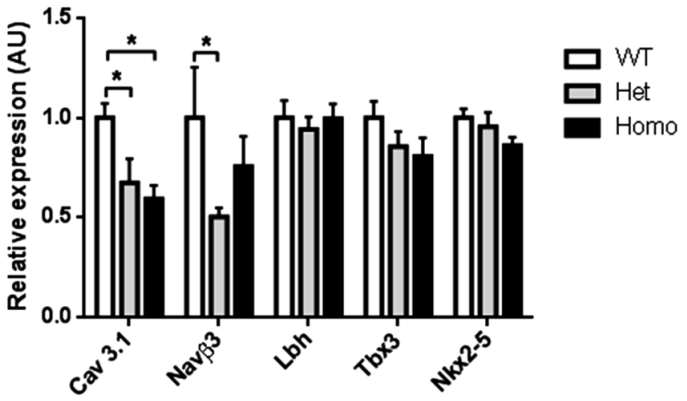


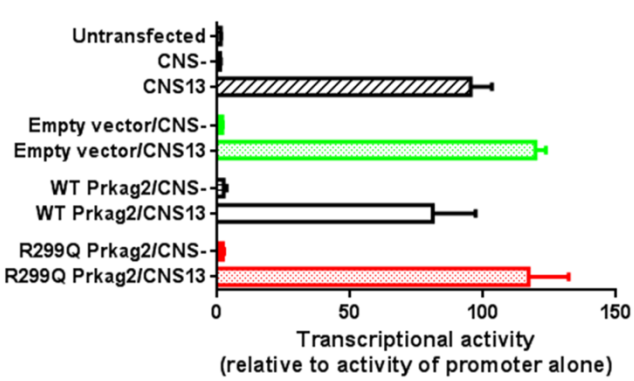
Figure 64. SAN gene and transcription factor profile (N=8/genotype). *P<0.05

$Na_v\beta3$ encodes one of the voltage-gated Na^+ channel β-subunits preferentially expressed in SAN; Lbh encodes a putative suppressor of *Nppa* expression.

Using a luciferase reporter gene assay, Takano's group has identified the transcription factors myocyte enhancer factor-2 (MEF2) and activator protein-1 (AP1) to bind to a conserved non-

coding sequence (termed CNS13) within the first intron of *Hcn4*, conferring prominent enhancer activity on the *Hcn4* promoter[212]. To explore whether R299Q mutant γ2 may exert its effect on *Hcn4* expression levels via a CNS13-*Hcn4*-dependent transcriptional mechanism, the effect of R299Q mutant γ2 and WT γ2 on *Hcn4* transcriptional activity was assessed using an *Hcn4*-luciferase reporter assay. Neonatal rat cardiomyocytes (NRCM) were co-transfected with: hrGFP II expression vector containing either WT *Prkag2*, R299Q mutant *Prkag2* or empty vector; a luciferase reporter construct containing the *Hcn4* promoter fused to the synthetic firefly luciferase reporter gene (*luc2*), with or without the CNS13 enhancer fragment ('CNS13' or 'CNS13-'); and an internal control vector (pGL4.74) encoding the *Renilla* luciferase gene (*hRluc*) reporter.

Transfection of the CNS13-*Hcn4* luciferase reporter was seen to induce marked upregulation in *Hcn4* transcriptional activity, either alone or when co-expressed with empty/WT *Prkag2*/R299Q *Prkag2*-containing vector, replicating the report of significant *Hcn4* enhancer function conferred by this regulatory fragment[212] (Figure 65). Conversely, overexpressing WT *Prkag2* (or R299Q *Prkag2*) had negligible effect on *Hcn4* transcriptional activity as measured by luciferase readout in the absence of the CNS13 enhancer. Notably, the effect of overexpressing R299Q or WT *Prkag2* in the presence of CNS13 on *Hcn4* transcriptional activity was not different to empty vector.



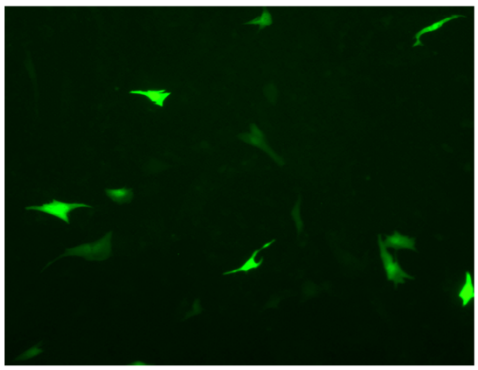


Figure 65. Left – Relative *Hcn4* promoter activity with or without the CNS13 enhancer fragment in response to co-transfection of NRCMs with pIRES-hrGFP II containing WT *Prkag2* or R299Q mutant *Prkag2* constructs. Error bars represent SEM from 3 independent experiments performed in at least quadruplicate.

Right – Representative fluorescent image of NRCMs transiently transfected with an AMPK construct and exhibiting GFP fluorescence. Non-transfected controls showed no GFP fluorescence (data not shown).

4.4 Discussion

4.4.1 Summary of principal chapter findings

Using a combination of whole-animal *in vivo*, *ex vivo* organ and cell-based approaches, the work presented in this chapter has sought to characterise the EP phenotype of R299Q γ2 mutant mice and identify novel disease mechanisms. This has identified:

i) Intrinsic sinus bradycardia in R299Q γ2 homozygous mutant mice.

ii) A mild prolongation of the QRS complex in R299Q γ2 homozygous mutant mice. Both this finding and that in (i) were non-progressive until the final time point assessed of ~10 months.

iii) No evidence of ventricular pre-excitation in mutant mice as determined by surface ECG recordings, telemetry or invasive EPS.

iv) Significant differential cardiac gene expression between mutant and WT mice as early as 40 days of age, indicating the presence of a differential transcriptome in the absence of marked glycogen accumulation.

v) Downregulation of *Hcn1* and *Hcn4* transcripts in whole heart samples from R299Q γ2 homozygous mutant mice, with intermediate signals present in heterozygous mutant mice. Notably, HCN1 and HCN4 are recognised as the major contributors to the mammalian 'funny' current, I_f, a key current subserving SAN pacemaking.

vi) Reduced automaticity of individual sinus node cells from both R299Q γ2 mutant genotypes, more marked for homozygous mutant SAN cells.

vii) As a corollary of a downregulation in *Hcn1* and *Hcn4* expression, a reduction in I_f current density, effectively constituting less f-channels per SAN cell.

viii) No evidence was identified to support a role for R299Q mutant γ2 in altering HCN channel kinetics and thereby contributing to bradycardia. Further, there was no evidence for expression of an R299Q mutant *Prkag2* construct modifying the biophysical properties of heterologously

expressed human HCN4 *in vitro*.

ix) A reduction in whole-heart *Cacna1g* gene expression in homozygous mutant mice. This encodes a pore-forming subunit of the voltage-dependent T-type Ca^{2+} channel, a molecular component of the transient type calcium current $I_{Ca,T}$ known to be enriched in SAN and thought to play a role in the diastolic depolarisation of SAN myocytes. This finding raises the possibility that the sinus bradycardia of R299Q γ2 mutant mice – and by inference humans with PRKAG2 cardiomyopathy – may not simply relate to an isolated HCN channelopathy.

x) In a preliminary exploration of potential mechanisms underlying the observed reduction in *Hcn4* expression, no evidence was identified to support an effect of R299Q mutant γ2 perturbing the enhancer function of CNS13 (via a reported MEF2-AP1 interaction) on the *Hcn4* promoter.

Specific aspects of these observations are discussed in greater detail below.

4.4.2 Electrophysiological disturbance – moving beyond glycogen

On a background of existing transgenic mutant PRKAG2 models, the striking absence of both ventricular pre-excitation and gross glycogen accumulation in the R299Q γ2 KI model strongly suggests that a large, critical mass of glycogen accumulation is a necessary pre-requisite for the development of accessory pathways in PRKAG2 cardiomyopathy. However, the finding of a robust intrinsic bradycardia caused by reduced sinus pacemaker automaticity in homozygous mutant mice, coupled with the finding of a discernible mutant transcriptome and perturbed cardiac ion channel expression as early as 40 days, points to primary effects of mutant γ2 complexes on ion channel expression likely to be entirely independent of glycogen.

4.4.2.a Sinus bradycardia of Prkag2 cardiomyopathy – an HCN'opathy?

The identification of reduced expression of *Hcn1* and *Hcn4* – both of which are highly enriched in SAN and the prime molecular constituents of SAN I_f – together with reduced I_f current density in R299Q γ2 homozygous mutant mice, provides a clear substrate for their sinus bradycardia and, by inference, may explain the prominent burden of sinus node disease features in patients carrying *PRKAG2* mutations. Whilst the magnitude of *Hcn* reduction observed in homozygous mutant mice

was greatest for *Hcn1* (24% of WT mRNA levels), the smaller reduction in *Hcn4* (63% of WT mRNA levels) is still likely to be far from biologically insignificant. Indeed, the observed spontaneous rate of SAN cells isolated from R299Q γ2 homozygous mutant mice closely approximates to that of a tamoxifen-inducible cardiac-specific HCN4 knockout (ciHCN4-KO) mouse model after ~2 days of tamoxifen injection[197]. The latter has a mean survival of only 4.9 days due to progressive, severe bradycardia. Notably, the primary I_f abnormality in ciHCN4-KO mice is a reduction in current density, with no alteration in the kinetic properties of I_f. These findings are similar to but more marked than that observed in R299Q γ2 homozygote mice and both can be conceptualised as less f-channels expressed per SAN cell. Moreover, it would suggest that a reduction in I_f current density alone – without invoking the need for additional post-translational modification(s) of HCN channels by mutant AMPK (e.g. via phosphorylation) – is sufficient to account for the magnitude of bradycardia observed. The findings from heterologous expression experiments co-expressing human HCN4 and mutant R299Q γ2 support this, although they do not formally exclude a direct effect of mutant γ2 on HCN1 channels.

The ionic mechanisms underlying SAN automaticity are recognised to be complex, with significant controversy as to the precise contribution of I_f to mammalian pacemaking. Two current paradigms exist to explain the spontaneous diastolic depolarisation of phase 4; these are conceptualised as a 'membrane voltage clock' and a 'calcium clock'[213]. The former reflects a net disequilibrium induced by a time- and voltage-dependent decay in the outward delayed rectifier K^+ current (I_K) and synchronous time- and voltage-dependent increase in multiple inward currents, including I_f but also I_b (background inward Na^+ current), $I_{Ca,L}$ and $I_{Ca,T}$ (L- and T-type Ca^{2+} currents)[213, 214]. The calcium clock refers to the spontaneous, rhythmic release of intracellular Ca^{2+} from sarcoplasmic reticulum Ca^{2+} stores via a Ca^{2+}-release channel (the ryanodine receptor 2) in diastole[213]. This then drives the influx of Na^+ ions by being extruded through the electrogenic myocyte Na^+-Ca^{2+} exchanger, resulting in a significant inward current, I_{NCX} ($3Na^+$ ions exchanged for 1 Ca^{2+} ion).

Importantly, these mechanisms are not likely to be mutually exclusive nor can they entirely be, given that multiple currents temporally overlap even within a single SAN myocyte (Figure 66)[215].

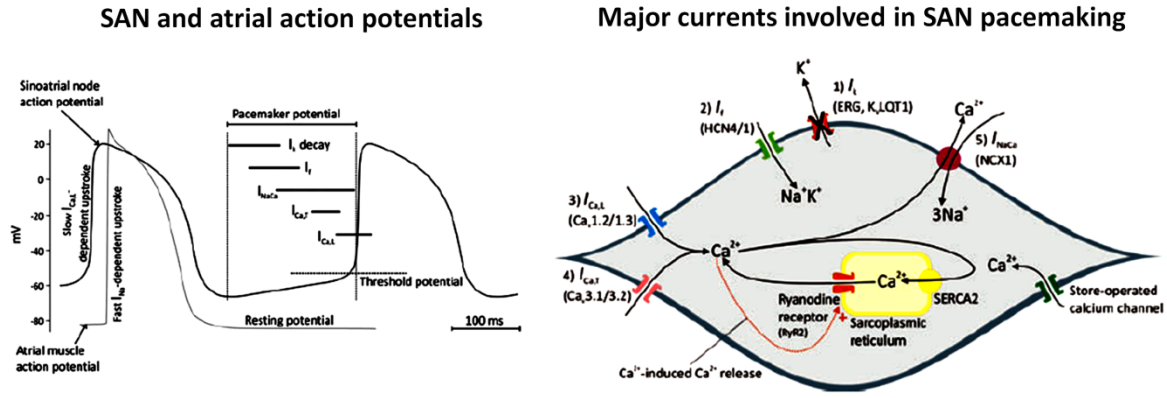


Figure 66. Left – Typical profile of an SAN and atrial muscle AP illustrating the temporal profile of major diastolic currents contributing to diastolic pacemaker potential. Right – Schematic depicting an SAN myocyte with 5 major ionic currents and illustrating the interplay between the membrane voltage and subsarcolemmal Ca^{2+} clocks.[mm]

What then are the implications of a finding of a reduction in *Cacna1g*, encoding the major pore-forming subunit of $Ca_v3.1$ Ca^{2+} channels which conduct the T-type Ca^{2+} current ($I_{Ca,T}$), in both R299Q γ2 homozygous and heterozygous mutant mice? $I_{Ca,T}$ has been identified in all myocytes which display automaticity, including the SAN, although their precise contribution to SAN pacing has been debated[214]. Deletion of the $Ca_v3.1$ subunit alone is sufficient to ablate $I_{Ca,T}$ in murine SAN and result in a ~10% reduction in heart rate compared to WT (albeit only apparent with autonomic blockade rather than on resting ECGs)[211]. Moreover, corrected sinus node recovery times (cSNRT) in $Ca_v3.1$ KO mice are significantly prolonged. However, whilst $Ca_v3.1$ is present to a greater degree in SAN than atria in both mice and humans[196, 216], its degree of enrichment is far less than that of HCN1 and HCN4. Furthermore, in contrast to components of $I_{Ca,T}$, loss-of-function mutations in HCN4 have been identified to cause sinus bradycardia in humans, whilst a selective I_f blocker (ivabradine) is in clinical use as an effective and highly specific heart-rate reducing agent, both highlighting the important contribution and relevance of I_f to human SAN pacemaking[217].

Moving beyond the SAN, it is important to note that the observed reduction in *Hcn* expression in R299Q γ2 KI mutant mice was identified from *whole-heart* tissue extracts that would include other regions where HCNs are known to be enriched, notably the AV node. Intriguing in this regard is the observation that ciHCN4-KO mice die not from sinus arrest, but rather from progressive AV

[mm] Adapted from figures 5 & 6 Monfredi et al. *Pacing Clin Electrophysiol* 2010;33:1392-406.

nodal dysfunction culminating in complete AV block. This is associated with a 63% reduction in I_f from AV nodal myocytes of ciHCN4-KO mice after 5 days of tamoxifen treatment[197]. With this observation and the present work's findings in mind, the high incidence of progressive AV nodal block necessitating permanent pacemaker implantation in humans with *PRKAG2* mutations could well relate to a loss of HCN function in the AV node.

Whether perturbed HCN function outside the heart could account for some rarer features described in patients with *PRKAG2* mutations, e.g. epilepsy, remains speculative. However, the fact that HCN channels are widely expressed in neurons and play an important role in modulating intrinsic excitability (through the neuronal equivalent of I_f, termed I_h), together with the association between loss of HCN function and epileptogenic activity both in mice and humans[218], does raise this possibility.

One limitation of the phenotypic findings presented is that the human disease, which is autosomal dominant in inheritance, does not appear to be adequately modelled by R299Q γ2 heterozygous mutant mice. Whilst the heart rate of heterozygous mutant mice (measured both by *in vivo* surface ECG recordings and during *ex vivo* perfusion) was clearly intermediate between that of WT and homozygous mutant mice, this did not reach statistical significance. However, heterozygous mutant mice did manifest significant reductions in *Hcn1* and *Hcn4* mRNA expression, I_f current density and spontaneous SAN cell beating rate, in addition to a significant reduction in *Cacna1g* expression. These findings indicate a gene-dosage effect with respect to R299Q mutant γ2 and highlight a modest but discernible heterozygote EP phenotype with clearly reduced sinus node automaticity, but which is likely to require significant statistical power to detect a population difference for parameters with poorer signal-to-noise ratios such as surface or *ex vivo* ECG recordings.

4.4.2.b Pathway linking AMPK γ2 and altered I_f

The data presented in this chapter provide strong evidence for reduced automaticity of R299Q γ2 homozygous mutant mice in concert with a clear reduction in I_f current density. The mechanisms linking mutant γ2 heterotrimers and alterations in *Hcn* expression levels are not clear and were

subject to only very preliminary exploration as part of this work. Nevertheless, the finding of a downregulation in multiple key *Hcn* isoforms, together with *Cacna1g*, may point to a potential reprogramming of the SAN transcriptome attendant upon mutant γ2 protein expression. Coordinated repression of *several* key molecular components of the complex, interacting array of ionic currents involved in SAN pacemaking may provide the substrate for the high burden of sinoatrial pathology in humans with *PRKAG2* mutations. It also raises the prospect of whether this is an aberrant gain-of-function by mutant peptide, or whether WT AMPK γ2 has a similar (albeit less marked) function to enable it to regulate heart rate physiologically *in vivo* – this issue is explored further in chapter 5.

An attractive mechanism for coordinate downregulation of expression in this regard is a direct/indirect interaction of AMPK with a transcription factor. One potential candidate is TBX3, a transcriptional repressor expressed in the SAN and cardiac conducting tissue. Use of *in silico* phosphorylation prediction algorithms (ScanSite 3.0 beta[219] and PhosphoNET[220]) identifies a region surrounding Thr203 (QWMSKVVTFHKLKLT, human numbering) as closely fitting the canonical AMPK sequence recognition motif – φ[X,B]XX[Ser/Thr]XXXφ, where φ is a hydrophobic residue (M, V, L, I or F) at the P-5 and P+4 positions, B is a basic residue (R, K or H) at the P-3 or P-4 position and X is any residue[55] – with a BLAST (Basic Local Alignment Search Tool, National Centre for Biotechnology Information)[221] search indicating a high degree of conservation of these residues in TBX3 across species. Within the SAN, TBX3 suppresses expression of the atrial gene programme and promotes an SAN gene programme (including *Hcn1*, *Hcn4* and $Ca_v3.1$)[208]. A preliminary exploration of expression of other key SAN genes was limited by measurement at the level of the whole-heart rather than SAN which, for certain transcripts, prevented reliable amplification and detection, even with highly sensitive qRT-PCR. A read-out of multiple putative transcriptional targets downstream of TBX3 direct from SAN itself would help refine the hypothesis of an SAN AMPK γ2-TBX3 pathway more directly. If implicated, the role of TBX3 in disease pathogenesis may even extend beyond the SAN given that TBX3 is expressed in the AV node and that some TBX3 hypomorphic alleles are associated with pre-excitation in mice[222].

The described interaction[212] between the transcription factors MEF2, AP-1 and the CNS13 enhancer in the first intron of *Hcn4* prompted the investigation of whether R299Q mutant γ2 might exert its effects on *Hcn4* expression through this mechanism using NRCMs. No compelling effect of mutant γ2 was demonstrated in altering the prominent enhancer activity conferred by CNS13 on *Hcn4* transcription, however.

4.4.2.c Is the phenotype of R299Q γ2 KI mice developmental in origin?

The use of a gene-targeted approach has advantages, including expression of mutant protein in its endogenous physiological context and with the native developmental profile; in the case of γ2 in the heart, this expression is expected to be at an embryonic stage[49]. Consequently, the bradycardic phenotype of the R299Q γ2 KI could be a result of abnormal SAN development. One approach to address the developmental question is to ablate R299Q mutant γ2 product from the SAN in adult life. The presence of *loxP* sequences surrounding the R299Q *Prkag2* mutation, together with the availability of transgenic lines which permit temporal regulation of recombination in adult heart using a tamoxifen-inducible Cre recombinase (MerCreMer) under the control of the α-MHC promoter[223] (known to excise in SAN[197]), provides a ready means of doing this. Thus, an assessment of heart rate in mice homozygous for the R299Q γ2 mutation which express the tamoxifen-inducible MerCreMer transgene (both pre- and post-tamoxifen) will help delineate whether the bradycardic phenotype is reversible postnatally, arguing against a major developmental aetiology.

4.4.2.d Other potential mechanistic players in the PRKAG2 mutant EP phenotype: CNTN2

In the absence of ventricular pre-excitation, the origin of the prolonged QRS interval in R299Q γ2 homozygous mutant mice is more enigmatic, given that the QRS complex occurs during ventricular depolarisation, with the anatomical region responsible potentially localising to any of the specialised conducting tissue inclusive of or between the AV node and Purkinje-ventricular myocyte junction. Altered conduction velocity resulting in QRS prolongation could potentially relate to: an effect of the mutation on prolonging voltage-gated Na^+ current (as has been

postulated)[141]; altered cardiac gap junction protein expression, function or distribution; or significant deposition of glycogen selectively within the specialised cells of the cardiac conducting system. The microarray finding of marked downregulation of contactin-2, encoded by *Cntn2*, is intriguing in this regard. Contactin-2 is a cell adhesion/recognition molecule classed as a member of the immunoglobulin superfamily and implicated in neural adhesion, migration and ion channel clustering[224]. More recently, contactin-2 has been identified as a novel marker preferentially expressed throughout the specialised cardiac conduction tissue of the heart and represents the most highly enriched transcript in Purkinje fibres[225]. Mechanistically, it is conceivable that altered conduction system patterning or dysregulation of Purkinje ion channel organisation – consequent upon downregulated *Cntn2* – may contribute to the high frequency of bundle branch block described in patients with *PRKAG2* mutations[113] and correspond to the signal of prolonged QRS duration observed in R299Q γ2 homozygous mutant mice.

4.4.3 Potential correlates for other phenotypic manifestations

The molecular correlates of the cardiac dysfunction in the R299Q γ2 KI model are unclear but, in the absence of bulk glycogen accumulation in the cardiomyocyte, may ensue downstream of the impaired sensing of metabolic stress (ADP/AMP) that the CBS domain mutation entails. Failure to sense and respond to immediate energy needs in key cellular subcompartmental regions by mutant γ2-containing heterotrimers at times of fluctuation in energy availability may result in adverse consequences, such as impaired functioning of a variety of ATP-dependent transporters in the cardiomyocyte – e.g. the myosin ATPase and the sarcoplasmic reticulum Ca^{2+} reuptake pump – with consequent impaired contractility and relaxation.

Impaired sensing of cellular stress may not be limited to abrogated recognition of elevated intracellular ADP/AMP levels, however. AMPK is increasingly recognised to function as both a redox sensor and modulator of ROS production. AMPKα2 has been shown to promote endothelial function by suppressing endothelial NADPH (nicotinamide adenine dinucleotide phosphate) oxidase-derived ROS production *in vivo*[226]. Germline deletion of AMPKα1 results in reduced erythrocyte lifespan due to elevated oxidative stress[227], whilst loss of the AMPK α1 subunit has

also been observed to enhance endothelial *Nox2* expression[228] . In addition to inhibiting ROS production by NADPH oxidases, AMPK regulates mitochondrial ROS production by enhancing UCP2 expression[229], as well as augmenting endogenous anti-oxidant defence mechanisms such as thioredoxin[230]. Notably, oxidative stress and altered nitric oxide-redox balance have been implicated in both human and experimental animal models of arrhythmia, including sinus node dysfunction[231] and atrial fibrillation[232], both highly prevalent clinical features of PRKAG2 cardiomyopathy.

Against this background, the identification of an 85-fold increase in expression of *Abhd1* by qRT-PCR – validating the finding of the most highly upregulated transcript on microarray profiling of homozygous mutant hearts – is intriguing. *Abhd1* codes for a protein predicted to contain an N-terminus transmembrane domain and to form α/β hydrolase folds, a domain found in a wide range of esterase & lipase hydrolytic enzymes[233]. It has been found to be expressed in most tissues examined, including heart, but its biologic function remains unknown. Recent insights into its potential function emerged from investigation of D5 dopamine receptor KO mice. These constitute a renal model of systemic hypertension and increased systemic oxidative stress characterised by increased NADPH oxidase expression & activity. Microarray transcriptional profiling of kidneys from D5 dopamine receptor KO mice identified *Abhd1* as the most highly upregulated transcript[234]. Subsequent stable overexpression of *Abhd1* in a renal proximal tubular cell line (a site rich for D5 receptors) revealed significant reduction in the levels of O_2^-, prompting the authors to propose that upregulation of *Abhd1* constituted a defence mechanism against enhanced oxidative stress[234].

In summary, the identification of an abnormal transcriptome, altered intrinsic cardiac electrophysiological characteristics and reduced LV systolic and diastolic function in the R299Q γ2 KI model, all occurring in the absence of the gross glycogen accumulation that is a hallmark of transgenic mutant *PRKAG2* models, highlights the complexity of PRKAG2 disease. Moreover, it suggests that an adequate working model for disease mechanisms (Figure 67) is best obtained through integration of insights gleaned from both contemporary transgenic and the novel gene-targeted approach.

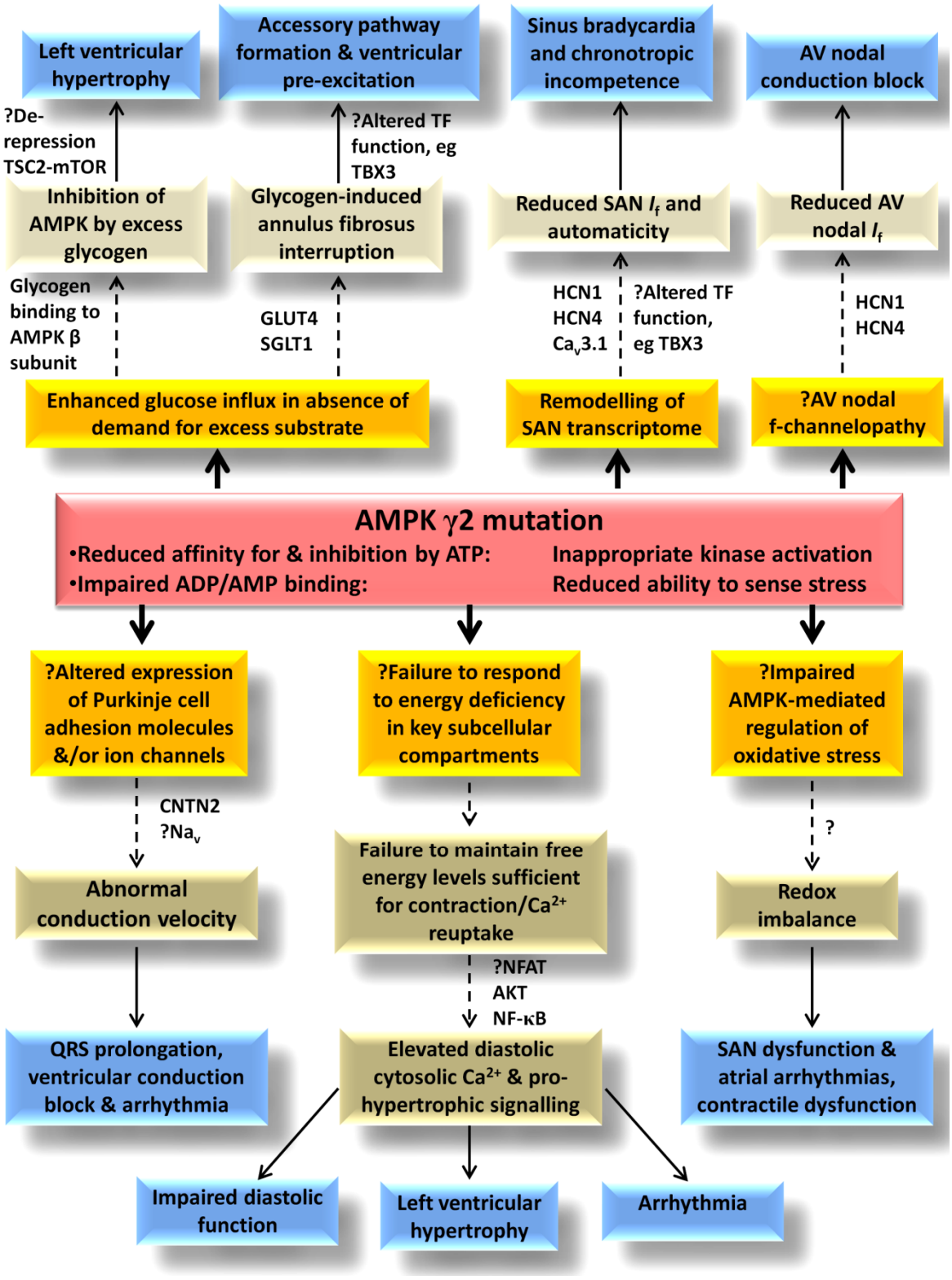


Figure 67. Pathophysiological model for the clinical manifestations of PRKAG2 cardiomyopathy. Question marks highlight areas of uncertainty or hypotheses to be tested.

Chapter 5. Exploring the physiological role of γ2 in heart rate regulation

5.1 Aims and objectives

The EP findings from the R299Q γ2 mutant KI model provided strong support for an effect of mutant γ2 on influencing I_f and SAN automaticity, but did not address whether WT γ2 might play a role in the *physiological* regulation of heart rate. Accordingly, the focus of the work presented in this chapter was to generate and subsequently characterise the EP phenotype of the first global γ2 gene KO (using a Sox2 promoter-driven Cre) in order to investigate the potential role of γ2 as a *physiological* regulator of heart rate.

The specific objectives of the experiments presented here were:

i) To ascertain whether γ2 exhibited regional cardiac enrichment patterns that might point to a specific role(s) for this isoform in the heart and explain the high burden of sinus nodal and atrial disease features of *PRKAG2* mutation carriers.

ii) To explore the potential *physiological* role of γ2 in regulating heart rate by generating a global γ2 KO mouse model using the Sox2cre transgenic line.

iii) To develop a successful PCR-based genotyping strategy and validate the Sox2cre γ2 KO with respect to excision of R299Q mutated exon 7, ablation of γ2 protein and loss of γ2 function.

iv) To assess for compensatory γ isoform changes as a result of early embryonic γ2 deletion.

v) To undertake a basic assessment for the presence of cardiomyopathy, including histology and non-invasive assessment of cardiac structure and function.

vi) To define the effect of loss of γ2 on heart rate and *Hcn1* and *Hcn4* expression.

vii) To test whether acute silencing of gene expression in a cardiac cell-based system recapitulates the cardiac *Hcn* isoform gene expression signature of Sox2cre-driven γ2 KO mice.

5.2 Chapter-specific materials and methods

5.2.1 Sox2cre mice

Sox2cre mice backcrossed for 6 generations onto a C57BL/6 genetic background were originally a gift from Dr Andrew McMahon (Harvard University). Sox2cre transgenic mice express Cre recombinase under the control of a 12.5 kb enhancer/promoter element from the *Sox2* gene[235]. *Sox2*, or SRY- (sex determining region Y) box containing gene 2, is a transcription factor that regulates the expression of a number of developmental genes and is expressed in early epiblast and extraembryonic ectoderm[236]. By directing *Cre* expression to early epiblast (derived from the inner cell mass and containing all the cells that will generate the actual embryo), Sox2cre mice permit conditional deletion of floxed sequences (flanked by *loxP*) in the embryo proper by day E6.5.[235, 236] R299Q γ2 KI mice bred onto a C57BL/6 genetic background were crossed with Sox2cre transgenic mice to achieve global deletion of γ2 by generating Sox2cre γ2 KO mice. Mice heterozygous for the Sox2cre transgene but WT for *Prkag2* (i.e. 'WT Cre+') were used as controls for all experiments involving Sox2cre γ2 KO mice. The WT Cre+ colony was maintained by breeding heterozygous WT Cre+ mice with WT mice from the R299Q γ2 colony. For some experiments, heterozygous floxed R299Q γ2/Sox2cre carrying mice (i.e. Het fl Cre+) and independently generated R299Q γ2 homozygous mutant mice were used as additional controls or, in the case of the former, to assess whether the presence of only a single WT γ2 *Prkag2* allele was associated with a phenotype.

5.2.2 Sox2cre transgene PCR

Genotyping for the presence of the Sox2cre transgene was performed on gDNA using the following primers and PCR conditions (Table 8), generating a specific amplicon of 500 bp:

Forward primer (S2CF) 5'-CTGGTGTAGCTGATGATCCG-3'

Reverse primer (S2CR) 5'-CTCAGTGGTATTTGTGAGCC-3'

Table 8. Reaction mix and PCR conditions for detection of the Sox2cre transgene

Sox2cre PCR Mix			Reaction conditions			
			Step	**Temp.**	**Time**	**Cycles**
Genomic mouse DNA	100.0	ng	Initial step	95°C	600s	1x
Primers	0.5	µmol				
dNTPs	0.16	mM	Denaturing	95°C	30s	
Immolase Reaction Buffer	0.1	Vol	Annealing	67°C	45s	12x
$MgCl_2$	3	mM	Extension	72°C	60s	-1°C/cycle
Taq Polymerase (Immolase)	1.0	U				
			Denaturing	95°C	30s	
Reaction Volume	20.0	µL	Annealing	54°C	45s	20x
			Extension	72°C	60s	
			Completion	72°C	300s	1x
			Hold	4°C	-	

5.2.3 gDNA sequencing for detection of *Prkag2* exon 7 deletion

Genomic DNA (gDNA) was extracted from cardiac tissue and PCR amplified with KPI1-H1 and RV2 primers (Table 9). PCR products were run on a gel and the bands excised under UV light and then cleaned using a purification kit (QIAquick, Qiagen). Sanger DNA sequencing was performed on these in the forward and reverse directions using KPI1-H1 and RV2 primers by Source BioScience (Oxford), with subsequent sequence alignment using MegAlign (DNASTAR).

Forward primer (KPI1-H1) 5'-CACCTGAAGTTGCCGTGTGACCTCC-3'

Reverse primer (RV2) 5'-AGAAGGCAGAGACACGGGATCGG-3'

Table 9. Reaction mix and PCR conditions for genomic excision PCR

Sox2cre genomic excision PCR Mix			Reaction conditions			
			Step	**Temp.**	**Time**	**Cycles**
Genomic mouse DNA	100.0	ng	Initial step	95°C	600s	1x
Primers	0.5	µmol				
dNTPs	0.16	mM	Denaturing	95°C	30s	
Immolase Reaction Buffer	0.1	Vol	Annealing	71°C	45s	16x
$MgCl_2$	3	mM	Extension	72°C	180s	-½°C/cycle
Taq Polymerase (Immolase)	1.0	U				
			Denaturing	95°C	30s	
Reaction Volume	20.0	µL	Annealing	62°C	45s	19x
			Extension	72°C	180s	
			Completion	72°C	600s	1x
			Hold	4°C	-	

5.2.4 PCRs for specific detection of intact or excised *Prkag2* exon 7 from gDNA

Two separate genotyping PCRs were established to detect intact exon 7 (using primers Ex7 FW1 and Ex7 RV1) and excised exon 7 (based on an amplicon size difference using primers KO FW1 and KO RV1). All primers were designed using Primer3 (http://frodo.wi.mit.edu/). A schematic of primer binding sites and the expected product sizes is shown in section 5.3.3. Primers and PCR conditions (identical for both primer sets) are listed below (Table 10).

Forward primer (Ex7 FW1) 5'-TGTTTCTGGTTTCTTTCCAGGTCAA-3'

Reverse primer (Ex7 RV1) 5'-TGCAAAAGCCAGAAAGTTCTTCAAC-3'

Forward primer (KO FW1) 5'-GGTGTGCACAGCATCCAGCAACA-3'

Reverse primer (KO RV1) 5'-AGGCTGAGCTCACCGTTACTCGTG-3'

Table 10. Reaction mix and PCR conditions used to detect intact or excised exon 7

Specific Exon 7 PCR Mix			**Reaction conditions**			
			Step	**Temp.**	**Time**	**Cycles**
Genomic mouse DNA	100.0	ng	Initial step	95°C	600s	1x
Primers	0.5	µmol				
dNTPs	0.16	mM	Denaturing	95°C	30s	
Immolase Reaction Buffer	0.1	Vol	Annealing	70°C	30s	14x
$MgCl_2$	3	mM	Extension	72°C	60s	-½°C/cycle
Taq Polymerase (Immolase)	1.0	U				
			Denaturing	95°C	30s	
Reaction Volume	20.0	µL	Annealing	61°C	30s	20x
			Extension	72°C	60s	
			Completion	72°C	300s	1x
			Hold	4-10°C	-	

5.2.5 End-point PCR for detection of exon 7 excision from cDNA

Cardiac cDNA from the Sox2cre γ2 line was synthesised and subject to PCR using the following primers and reaction conditions, with PCR products run on a 2% agarose gel:

Forward primer (G2Ex7P3FW) 5'-TGGCGTTTATATGCGATTCA-3'

Reverse primer (G2Ex7P3RV) 5'-TCATAAATCTGTACCATGGGTGA-3'

Table 11. Reaction mix and PCR conditions used to detect *Prkag2* exon 7 excision from cDNA

Exon 7 cDNA PCR Mix			**Reaction conditions**			
			Step	**Temp.**	**Time**	**Cycles**
Genomic mouse DNA	100.0	ng	Initial step	95°C	600s	1x
Primers	0.5	µmol				
dNTPs	0.16	mM	Denaturing	95°C	30s	
Immolase Reaction Buffer	0.1	Vol	Annealing	70°C	45s	12x
$MgCl_2$	3	mM	Extension	72°C	60s	-1°C/cycle
Taq Polymerase (Immolase)	1.0	U				
			Denaturing	95°C	30s	
Reaction Volume	20.0	µL	Annealing	58°C	45s	18x
			Extension	72°C	60s	
			Completion	72°C	300s	1x
			Hold	4°C	-	

5.3 Results

5.3.1 Cardiac regional expression of *Prkag2*

As an initial step to identify whether WT γ2 might play a role in the *physiological* regulation of heart rate, regional expression patterns of *Prkag2* were investigated in C57BL/6 inbred mice using qRT-PCR (Figure 68) – both to see whether *Prkag2* was enriched in any particular cardiac region and if its pattern of expression differed from that of *Prkag1*.

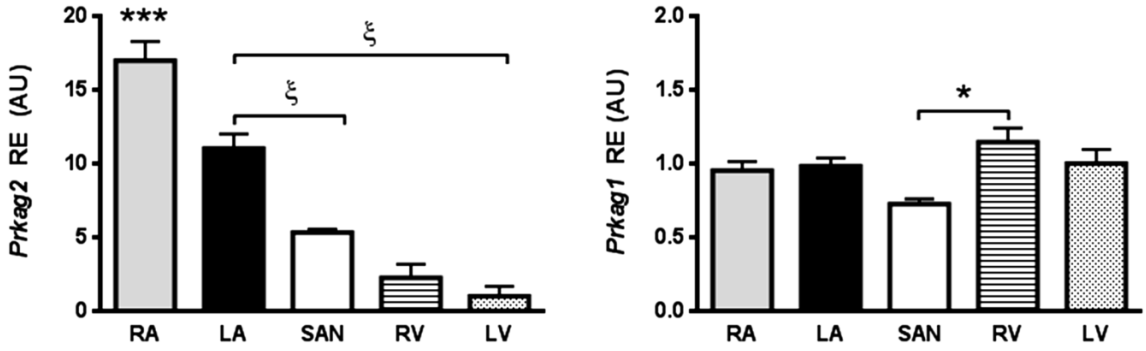


Figure 68. Cardiac regional expression of *Prkag2* and *Prkag1* in C57BL/6 inbred mice aged 8 weeks (N=4-12/region). **P*<0.05, ζ *P*<0.001, ****P*<0.001 vs all other regions

Whilst comparable levels of *Prkag1* expression were seen across both the atria, SAN and ventricles for *Prkag1*, *Prkag2* exhibited marked regional enrichment patterns, being most abundantly expressed in the atria and SAN compared to the ventricles. This regional enrichment pattern was replicated with a separate cohort of inbred mice. The same SAN samples were markedly enriched for *Hcn4* and *Hcn1*, confirming accuracy of SAN dissection (Figure 69).

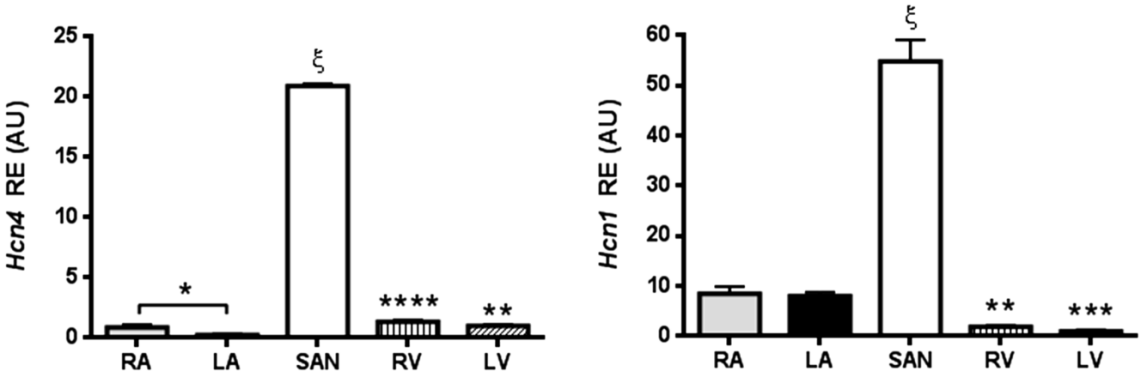


Figure 69. Relative expression of *Hcn4* and *Hcn1* in C57BL/6 mouse heart (N=4-12/region). Left panel – **P*<0.05, ***P*<0.01 vs LA, *****P*<0.0001 vs LA, ζ *P*<0.0001 vs all other groups Right panel – ***P*<0.01 vs atria, ****P*<0.001 vs atria, ζ *P*<0.0001 vs all other regions

5.3.2 Generation of a Sox2cre-driven γ2 KO

The regional distribution of *Prkag2* expression suggested that it may have a specific physiological role in the atria and SAN compared to γ1. Whilst no report of a γ2 KO has been published, a global γ1 KO has no described cardiac phenotype[237]. In order to determine whether γ2 plays a non-redundant role in regulating mammalian heart rate, a γ2 KO model was generated.

The existing γ2 KI model was designed with *loxP* sites flanking the R299Q mutated exon 7 of *Prkag2*. Whilst using the KI did not readily permit a satisfactory conditional approach to specific deletion in the heart (i.e. it would leave the R299Q mutated exon 7 intact and hence active elsewhere), it did permit a global KO approach using an embryonically active promoter to drive Cre recombinase expression (Figure 70). Thus, R299Q γ2 homozygous mutant mice were crossed with Sox2cre transgenic mice, the latter directing excision of floxed sequences in all epiblast-derived tissue (which giving rise to the embryo proper) from day E6.5.[235, 236] Resulting progeny which were heterozygous for the floxed (i.e. flanked by *loxP*) R299Q exon 7 mutation and carrying the Sox2cre transgene (i.e. 'Het fl Cre+'), were further crossed with R299Q γ2 homozygous mutant mice to generate the putative KO (i.e. 'Homo fl Cre+').

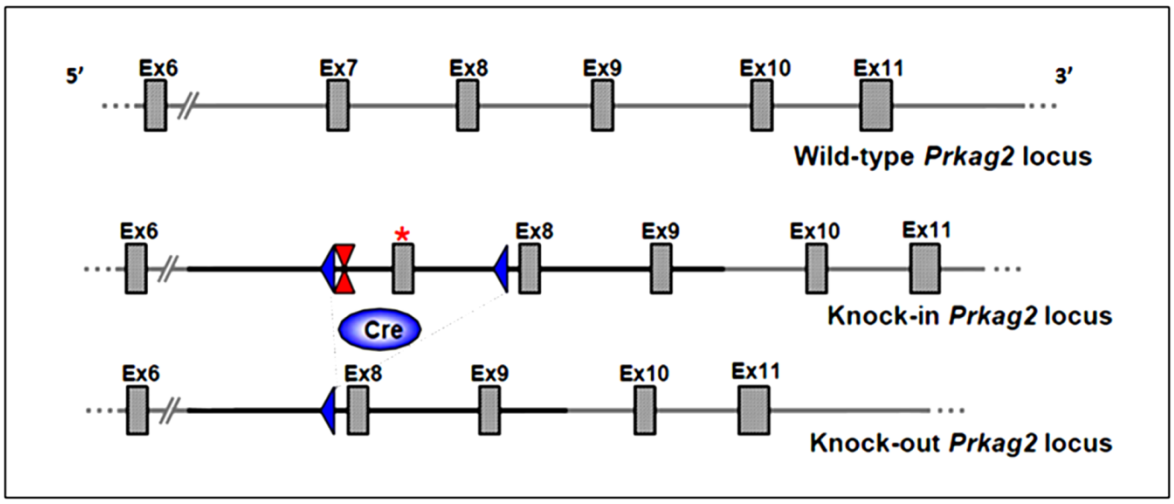


Figure 70. Schematic outline of WT, KI and KO *Prkag2* loci. * indicates site of R299Q mutated exon 7 of *Prkag2*; *loxP* sites are indicated by single blue triangles; the residual *FRT* sequence is denoted as inverted facing red triangles.

5.3.3 Genotyping of Sox2cre γ2 KO

Genotyping of litters obtained from the above final cross with primers KPI1-H1 and KPI1-H2 (used for genotyping the R299Q γ2 gene-targeted line) identified mice with no clear single band at 475 bp typical of an R299Q γ2 homozygous mutant animal but which carried the Sox2cre transgene (identified using a separate *Cre*-specific PCR). This was suggestive of a Homo fl Cre+ genotype – i.e. the putative γ2 KO – indicating that mice with global deletion of γ2 might be viable. This initial genotyping also identified mice positive for the Sox2cre transgene, but exhibiting only a WT *Prkag2* band (i.e. Het fl Cre+ mice), consistent with mice which had a single floxed R299Q mutated exon 7 excised *in utero* by Cre recombinase, leaving the non-floxed WT allele intact.

Excision of exon 7 of *Prkag2* was sequence verified from cardiac gDNA of Homo fl Cre+ mice using primers KPI1-H1 and RV2, with RV2 binding specifically to the small region of intronic sequence immediately between the residual *loxP* (left after Cre-mediated recombination in the putative γ2 KO) and the start of exon 8 (Figure 71). The size of the large intronic region before exon 7 meant that this product would be readily detected for the excised exon 7 locus (239 bp), but relied on generating an unwieldy 2572 bp amplicon under the same PCR conditions in the case of the intact WT *Prkag2* locus. Surprisingly, use of these primers for genotyping from ear-notch gDNA also identified some mice which were homofloxed for the R299Q *Prkag2* allele and clearly negative for *Cre*, but nevertheless had evidence of exon 7 excision.

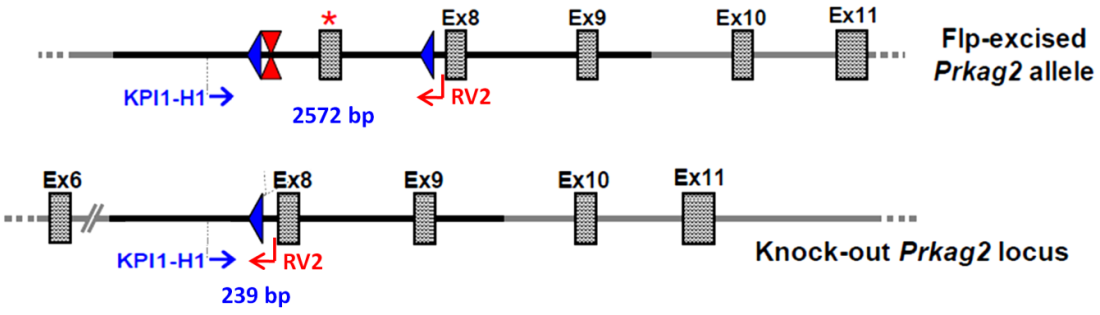


Figure 71. Primer design used for sequence verification of *Prkag2* exon 7 deletion from gDNA. Both KI and KO alleles are illustrated. Arrows indicate primer positions.

Maternal inheritance of Cre recombinase activity has been described[236, 238] with the Sox2cre line, whereby all progeny from a Sox2cre carrying female which carry floxed sequences undergo

excision regardless of their inheritance of the *Cre* transgene. This has been ascribed to the activation of this promoter during folliculogenesis (differentiation of the female germline), such that synthesised Cre protein may be stored in the oocyte allowing early recombination to occur after fusion of pronuclei on fertilisation. Cognizant of this, initial crosses set up to establish the Sox2cre γ2 line utilised males carrying the Sox2cre transgene to facilitate genotype interpretation. Whilst *paternal* inheritance of Cre recombinase activity has not been formally published with Sox2cre, it is alluded to in the original study[236] and clearly described for other promoters[239], although it appears to occur less frequently than the maternal effect. Analogous to the maternal effect, this would be suggestive of Cre-negative gametes (in this case spermatozoa) carrying sufficient Cre protein/mRNA to allow recombination of floxed sequences in the early zygote[239].

Exacerbated by the disparate sizes of the amplicons, the genomic excision PCR was not always found reliable in producing amplification. Accordingly – and in view of the added difficulty in genotype interpretation due to (variable) inheritance of parental Cre recombinase activity – primers were designed for two separate PCRs to specifically detect either intact exon 7 (with Ex7 FW1 and Ex7 RV1), or the recombined locus with exon 7 excised (KO FW1 and KO RV1). Together with the original R299Q γ2 KI PCR (KPI1-H1 and KPI1-H2) and a PCR to detect *Cre*, these four PCRs formed the basis of subsequent genotyping of the Sox2cre γ2 line (Figure 72).

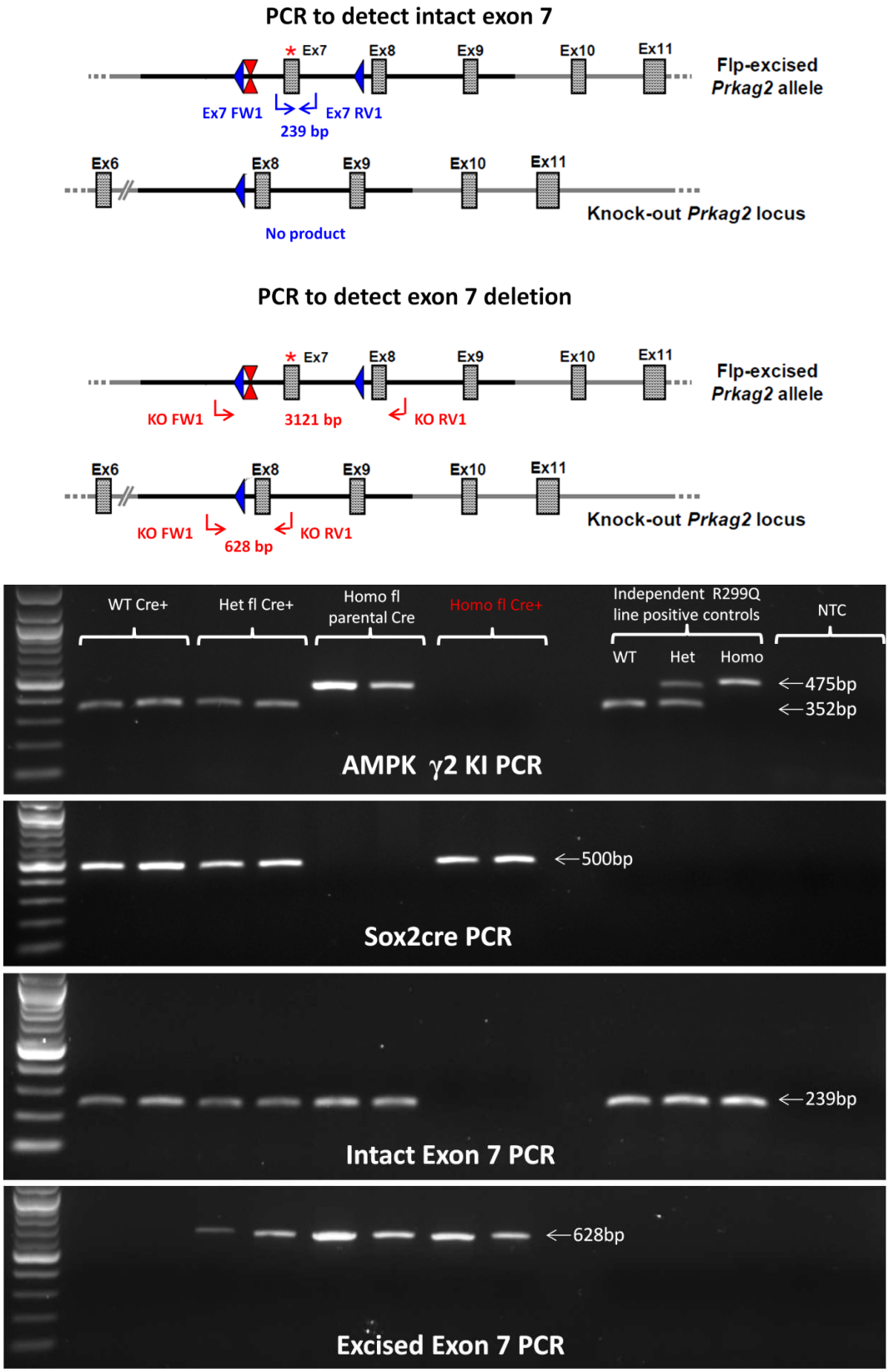


Figure 72. Position of primers used to detect intact and excised exon 7 from gDNA and PCR products visualised on agarose gel electrophoresis.

2-log DNA ladder (NEB) used for all gels. NTC – No template control (no input DNA). 'Homo fl parental Cre' refers to mice exhibiting exon 7 deletion in the absence of inherited Cre, consistent with parental inheritance of Cre recombinase activity.

5.3.4 Validation of Sox2cre γ2 KO – RNA level

Primers were designed to bind exon 6 and the exon 8-9 junction of *Prkag2* cDNA to detect the exon 7 excision event at mRNA level (Figure 73). End-point PCR on cardiac cDNA confirmed this.

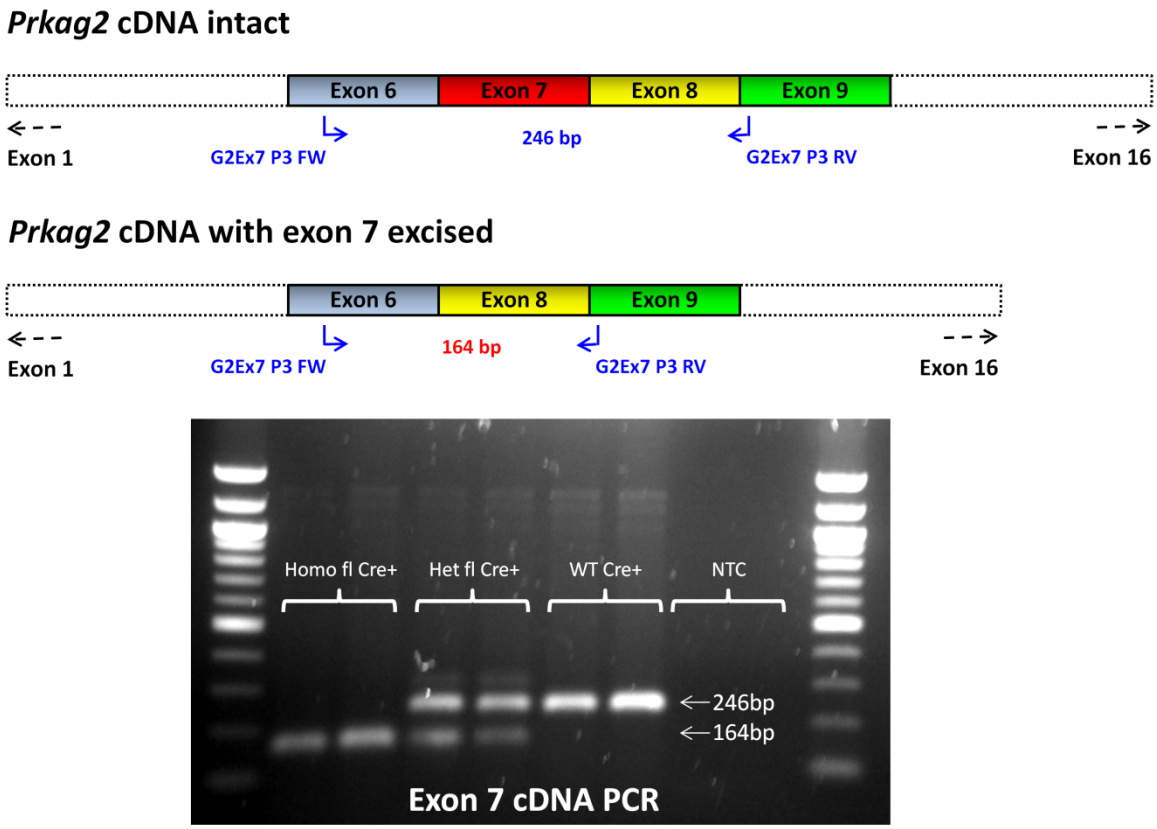


Figure 73. Primers designed to detect intact exon 7 and excision event at cDNA level (upper and middle schematic). Results from end-point PCR using these primers on cardiac cDNA (lower panel). 100 bp DNA ladder used. NTC – No template control (no cDNA).

Using allelic discrimination primers specific for WT or R299Q γ2 mutant *Prkag2* on cardiac cDNA, the fluorescent signals from Homo fl Cre+ mice were seen to cluster with no template controls, consistent with successful removal of the R299Q γ2 KI mutation (Figure 74).

To assess the degree of exon 7 excision, qRT-PCR was undertaken on whole-heart cDNA with a TaqMan assay directed against the exon 6-7 boundary. This confirmed absence of amplification in Homo fl Cre+ mice, with Het fl Cre+ animals exhibiting a modest reduction only (Figure 74). These results were also reproducible with a separate TaqMan gene expression assay targeting the exon 7-8 boundary (results not shown).

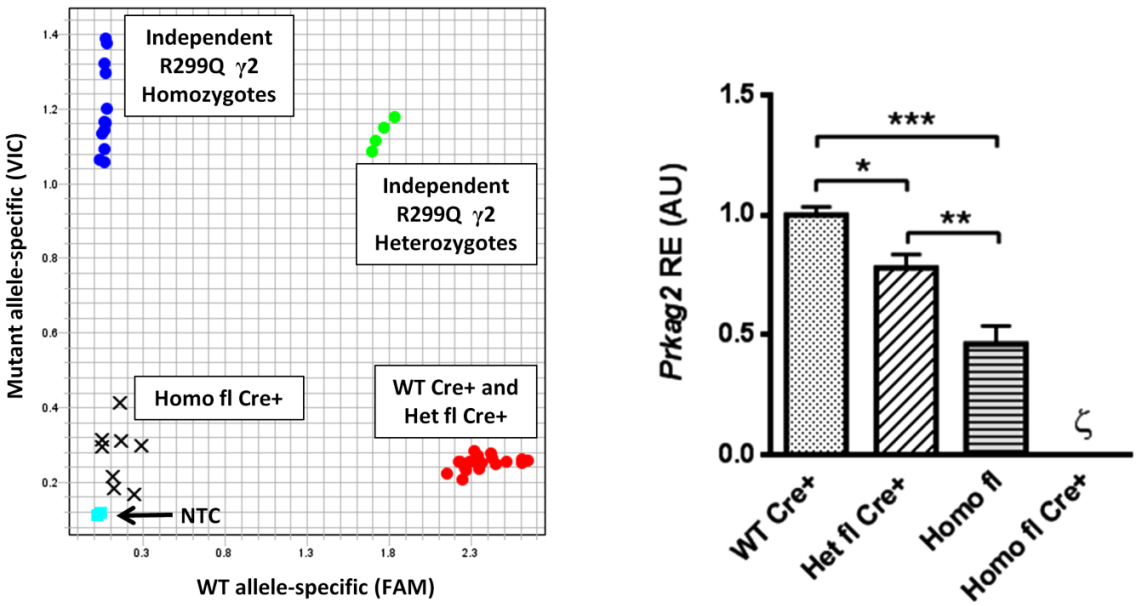


Figure 74. Confirmation of *Prkag2* exon 7 deletion using qRT-PCR.[nn]

Left – Allelic discrimination plot on cardiac cDNA using WT and R299Q *Prkag2* mutant specific probes. NTC, no template control. Controls used included independent R299Q γ2 homozygous and heterozygous mutant mice from the original R299Q γ2 KI line.

Right – Quantification of *Prkag2* relative expression using qRT-PCR and a TaqMan assay directed against the *Prkag2* exon 6-7 boundary (Mm01134853_m1, ABI) (N=4-6/genotype). **P*<0.05, ***P*<0.01, ****P*<0.001, ζ *P*<0.001 vs all other groups

Assessment of cardiac *Prkag1* and *Prkag3* transcript expression did not reveal any significant differences between WT Cre+ and Homo fl Cre+ mice to indicate compensation (Figure 75).

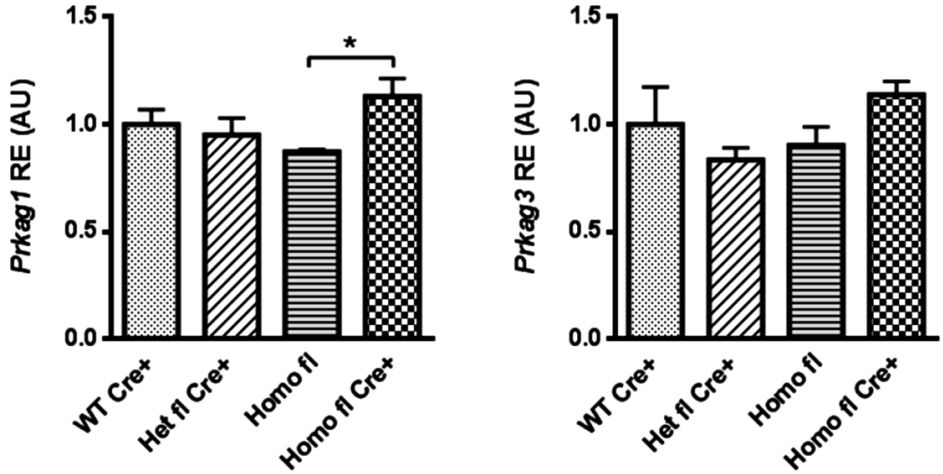


Figure 75. Relative expression of *Prkag1* and *Prkag3* at mRNA level from whole heart (N=5-6/genotype). **P*<0.05.

[nn] NB 'Homo fl' in Figure 74 and Figure 75 refers to a non-independent group of mice obtained from an R299Q γ2 homozygous mutant x R299Q γ2 heterozygous mutant/Sox2cre intercrossing. These 'Homo fl' animals displayed evidence of significant exon 7 excision despite not carrying *Cre*, consistent with a parental inheritance of Cre effect (as described in 5.3.3).

5.3.5 Validation of Sox2cre γ2 KO – protein level

Several commercially available anti-γ2 antibodies were extensively trialled with the aim of confirming γ2 deletion in Homo fl Cre+ mice at protein level. An antibody directed against the N-terminus of γ2 (stated epitope between 15-25 amino acids long and within amino acids 25-75 of human γ2; personal communication, Santa Cruz Technical Support) was found to be specific in demonstrating γ2 protein ablation across multiple organs of Homo fl Cre+ mice (Figure 76).

Quantification of the level of γ2 from whole-heart protein lysates of Homo fl Cre+ mice using densitometry of Western blots was consistent with *near*-complete ablation of γ2 (Figure 77). Consistent with the mRNA data, there was no evidence of compensatory change in γ1 protein level.

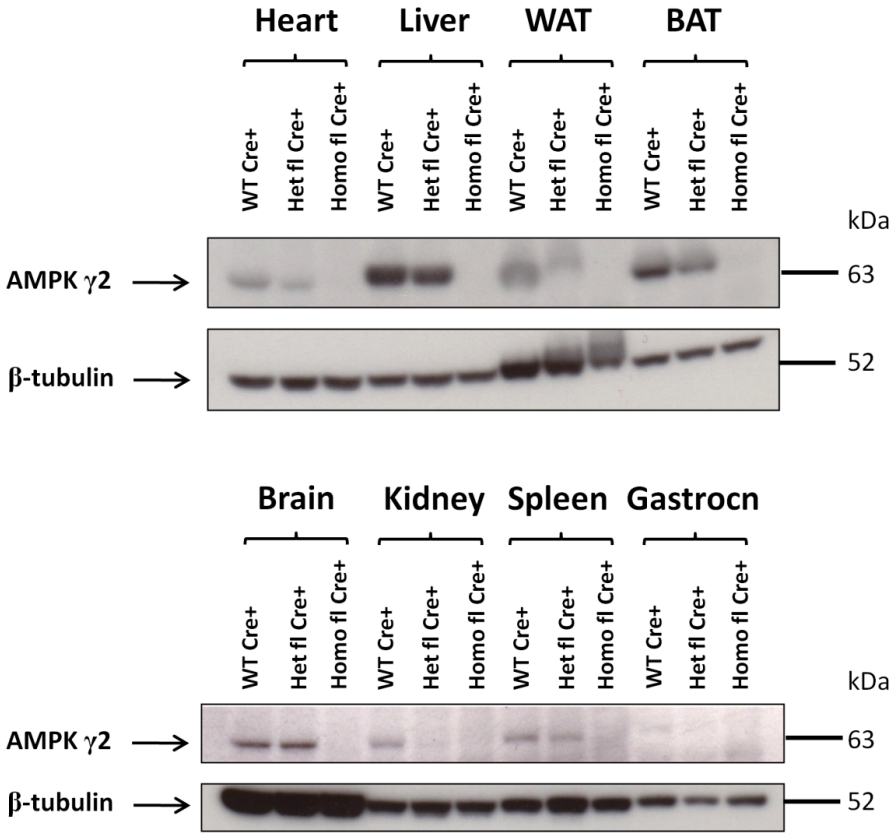


Figure 76. Western blotting across multiple organs in the Sox2cre γ2 line using an N-terminus anti-γ2 antibody. Abbreviations: Brain, refers to sample of cerebral cortex; WAT, white adipose tissue; BAT, brown adipose tissue; Gastrocn, gastrocnemius skeletal muscle.

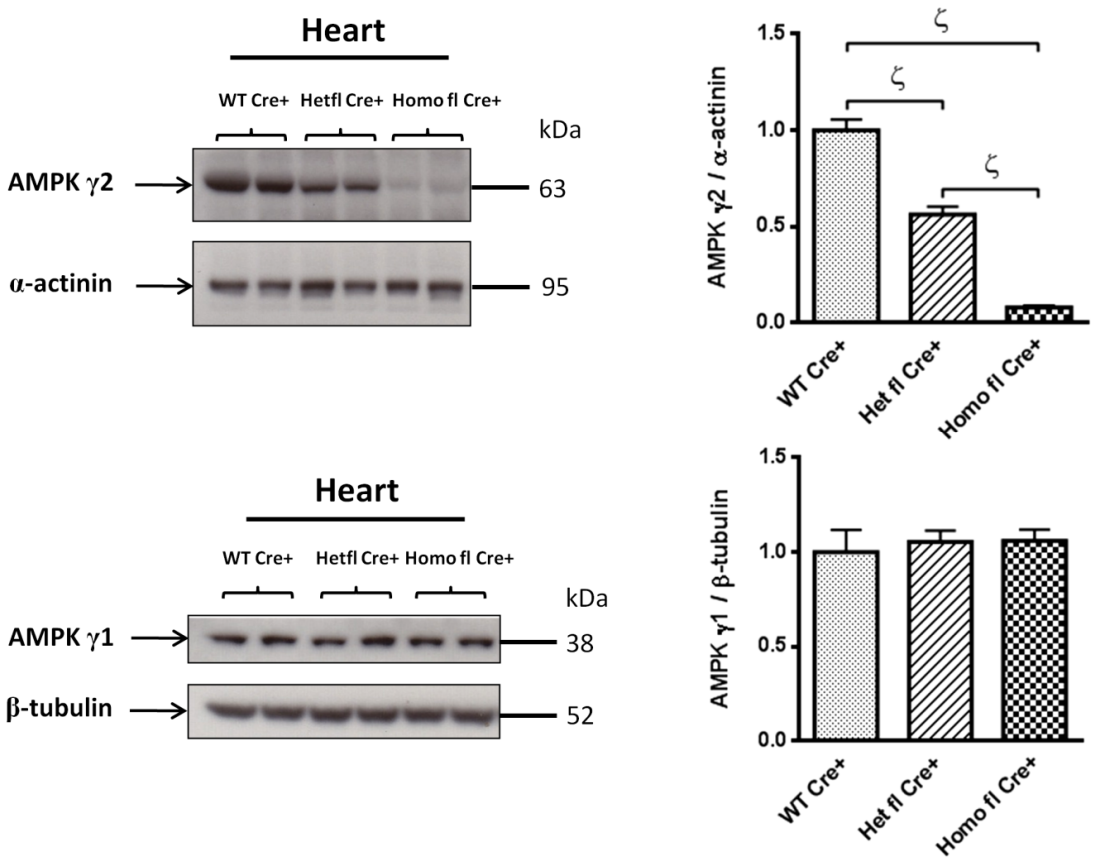


Figure 77. Whole-heart protein expression levels for γ1 and γ2 in the Sox2cre γ2 line (N=4-6/genotype). ζ *P*<0.0001

5.3.6 Validation of Sox2cre γ2 KO – functional level

Assessment of γ2-specific activity using a C-terminus anti-γ2 antibody to immunoprecipitate γ2-containing AMPK complexes from liver followed by the SAMS assay confirmed near undetectable levels of γ2-specific AMPK activity in Homo fl Cre+ animals (3% of WT Cre+ levels) (Figure 78).

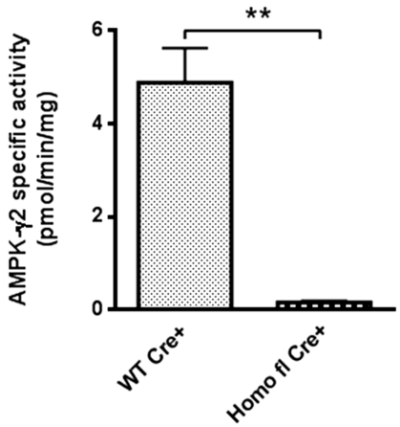


Figure 78. Hepatic γ2-specific AMPK activity in WT Cre+ and Homo fl Cre+ mice (N=5/genotype). *****P*<0.01

Extending these observations to whole heart samples revealed a substantial, although incomplete, loss of γ2-specific AMPK activity in Homo fl Cre+ mice, with Het fl Cre+ and Homo fl Cre+ 36% and 14% of WT Cre+ activity, respectively (Figure 79). No significant differences in either γ1-specific activity or total AMPK activity were detected between genotypes from the same cardiac samples.

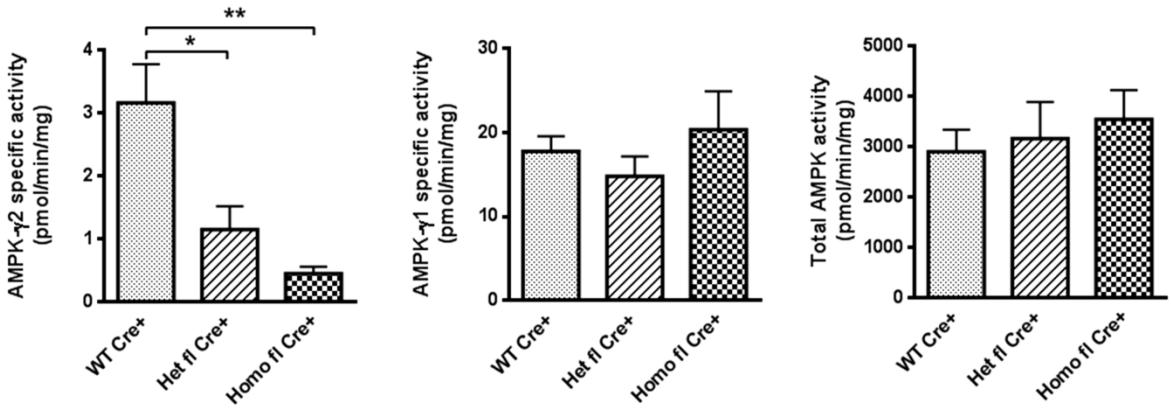


Figure 79. AMPK activity (γ1-/γ2-specific and total) from whole heart samples in the Sox2cre γ2 line (N=4-5/genotype). *P<0.05, **P<0.01

An assessment of phosphorylation of ACC – a downstream target of AMPK – revealed no significant change in overall phosphorylation level in the heart (Figure 80), in keeping with the total AMPK activity result.

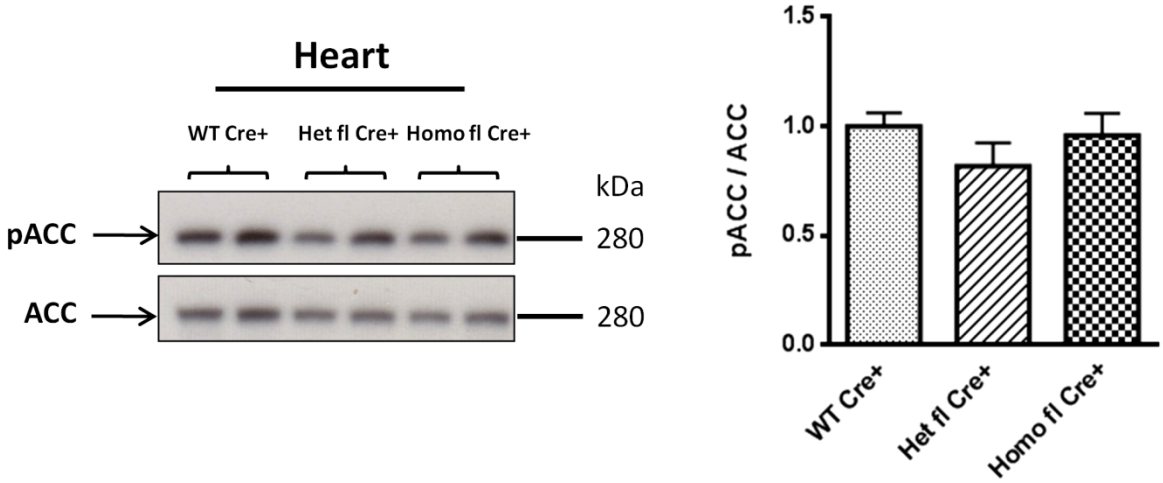


Figure 80. Phosphorylation of ACC from whole-heart samples in the Sox2cre γ2 line (N=4-5/genotype).

5.3.7 Baseline structure and function

Cardiac histology of Homo fl Cre+ mice appeared comparable to WT Cre+ controls with respect to morphology, glycogen deposition and degree of fibrosis.

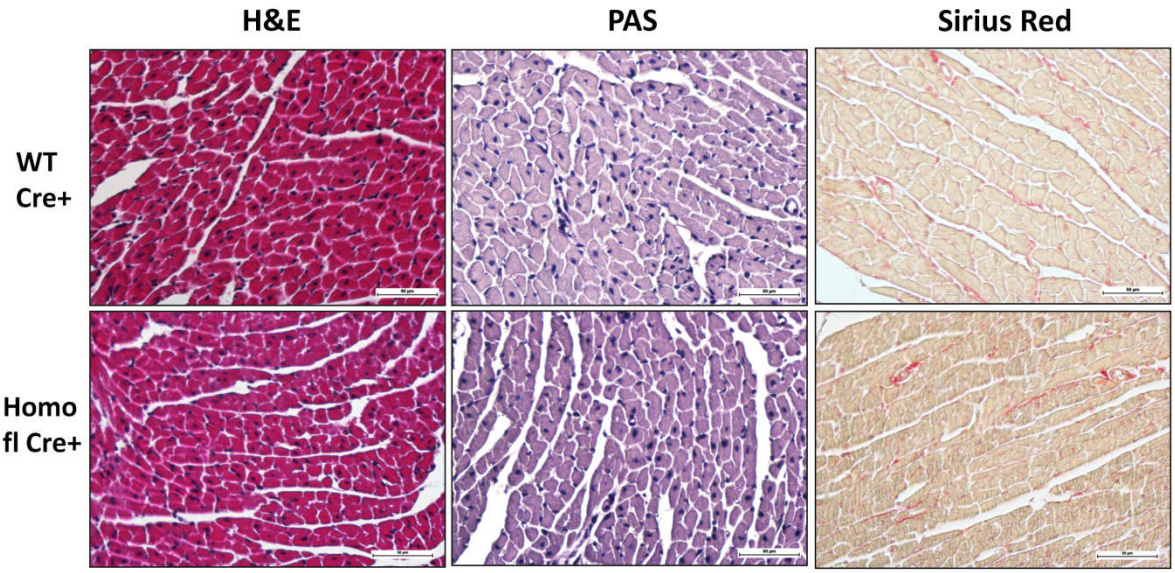


Figure 81. Histology of WT Cre+ and Homo fl Cre+ male mice at 3 months. Scale bar 50 µm.

Echocardiography of males at 6 weeks revealed no evidence for cardiomyopathy, with no significant LV systolic impairment, dilatation or hypertrophy in Homo fl Cre+ mice (Figure 82).

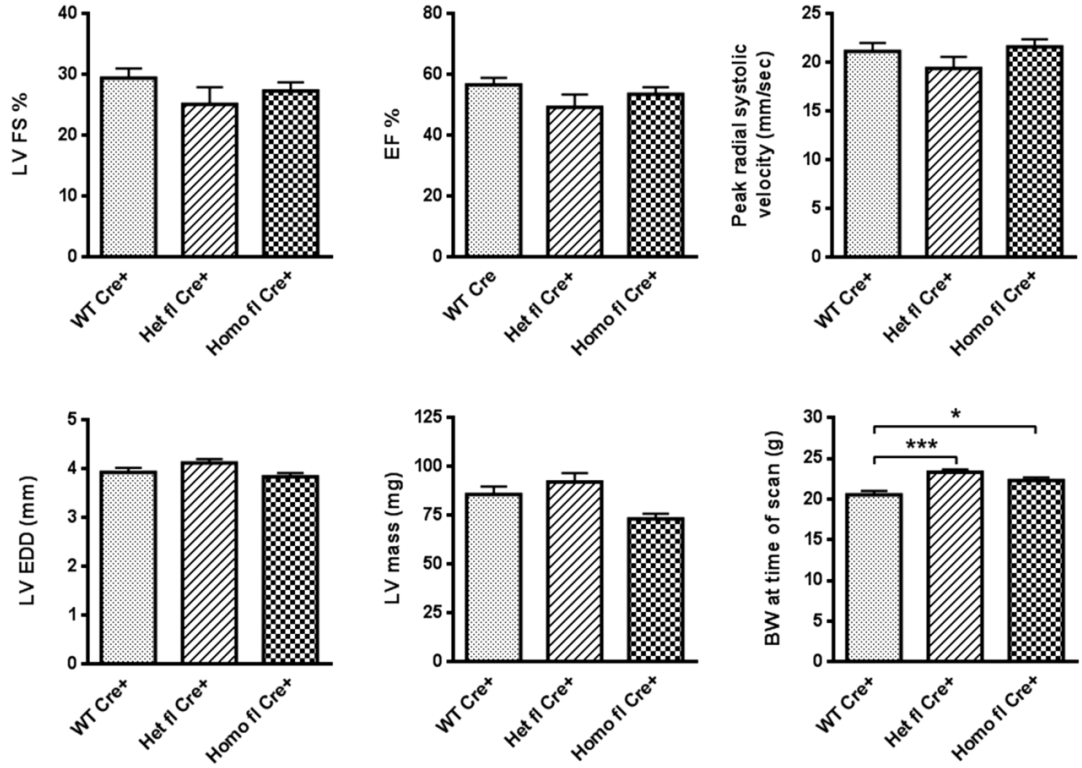


Figure 82. Echocardiography of Sox2cre γ2 line (N=9-12/genotype). *P<0.05, **P<0.001

Small but significant differences in body weight were apparent in this cohort, with both Het fl Cre+ and Homo fl Cre+ being heavier than WT Cre+ mice. Full results are detailed in Appendix 5.

5.3.8 Baseline EP phenotype

To explore the hypothesis that loss of γ2 would lead to changes in heart rate opposing that of the putatively basally activating R299Q γ2 KI, anaesthetised surface ECG recordings were undertaken. Homo fl Cre+ mice were found to have an increased heart rate compared to all other genotypes at 10 weeks of age. Mice which had genotypic findings consistent with transgene-independent Cre recombination from parentally-derived Cre (parental Cre effect, labeled 'Homo fl' in Figure 83) behaved similarly to R299Q γ2 homozygotes in terms of significant bradycardia and prolonged QRS duration, compatible with only partial excision of R299Q mutant *Prkag2* alleles.

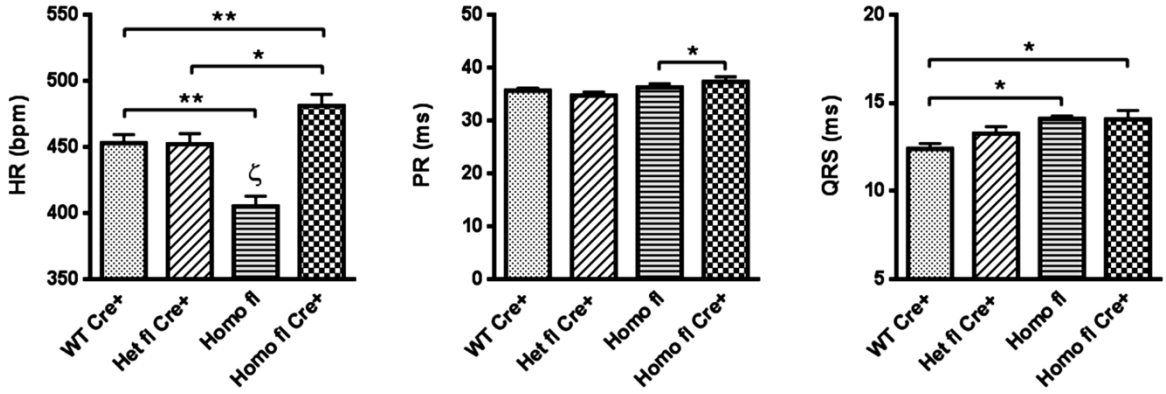


Figure 83. Anaesthetised ECG intervals from Sox2cre γ2 line aged 10 weeks (N=8-16/genotype). ****P*<0.05, *****P*<0.01, ζ *P*<0.001 Homo fl vs Homo fl Cre+ and Homo fl vs Het fl Cre+.[oo]

Inspection of individual ECG traces revealed no sustained arrhythmias during these short recordings and indicted that the increase in heart rate in Homo fl Cre+ mice was sinus in origin. To determine whether the latter feature was intrinsic to the heart, *ex vivo* cardiac perfusion was used to measure heart rate in the absence of autonomic influences (Figure 84). This confirmed an elevation in heart rate of Homo fl Cre+ mice, suggesting that this arose from altered intrinsic SAN pacemaker function. Whilst this signal for difference (Homo fl Cre+ vs WT, mean difference 53

[oo] NB As previously indicated, 'Homo fl' here refers to a non-independent group of mice obtained from an R299Q γ2 homozygous mutant x R299Q γ2 heterozygous mutant/Sox2cre intercrossing which displayed evidence of significant exon 7 excision despite not carrying *Cre*, consistent with a parental inheritance of Cre effect (described in section 5.3.3).

beats/minute) was more prominent than that obtained by *in vivo* ECG recordings, it was still not as marked as the corresponding *ex vivo* comparison between R299Q γ2 homozygous mutant and WT γ2 mice (mean difference 107 beats/minute).

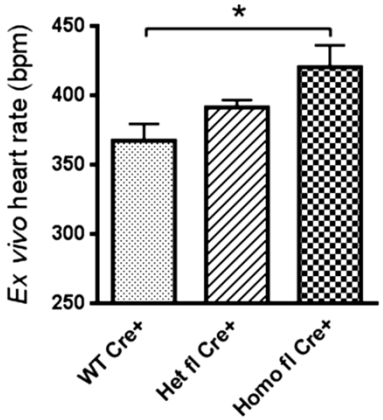


Figure 84. Intrinsic rate of isolated, *ex vivo* perfused Sox2cre γ2 line hearts (N=3-9/genotype). *P<0.05

5.3.9 *Hcn* expression profile

The elevation in sinus heart rate exhibited by a model of loss of γ2 function (Homo fl Cre+ mice) contrasted with the sinus bradycardia of R299Q γ2 homozygous mutant mice – the latter exhibiting downregulation in the two major murine SAN HCN transcripts, *Hcn1* and *Hcn4*. Accordingly, qRT-PCR was used to probe whether the heart rate increase observed in Homo fl Cre+ mice was associated with perturbations in *Hcn* expression (Figure 85). In keeping with the elevated heart rate of Homo fl Cre+ mice, upregulation of cardiac expression of both *Hcn1* and *Hcn4* was identified.

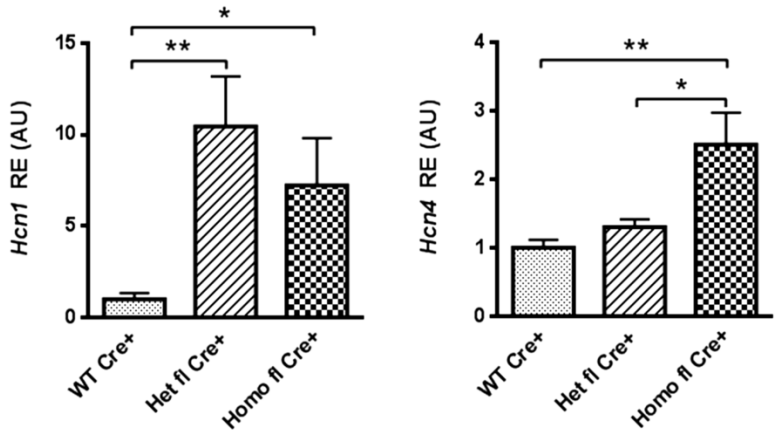


Figure 85. Relative expression of *Hcn* isoform 1 and 4 mRNA from whole-heart in Sox2cre γ2 line of mice (N=4-6/genotype). *P<0.05, **P<0.01

5.3.10 Silencing of *Prkag* isoform gene expression in HL-1 cells

The above data indicated that chronic loss of γ2 *in vivo* was associated with an elevation in intrinsic heart rate and augmented cardiac *Hcn1* and *Hcn4* expression. Given that the Sox2 promoter is active very early in embryonic development (causing recombination by day E6.5, or even earlier in the case of transgene expression in developing germ cells), experiments were undertaken to explore the effects of acute, transient reduction in γ isoforms on the expression of *Hcn1* and *Hcn4* using a small interfering RNA (siRNA) approach. In the absence of available sinoatrial nodal cell lines, RNA interference was undertaken using HL-1 cells. These are an immortal cardiac cell line, derived from atrial cardiomyocytes (section 2.8.2), that have been shown to display a hyperpolarisation-activated I_f and express all four HCN isoforms[240].

Exposure of HL-1 cells to *Prkag2*-targeted siRNA for 12 hours was effective in achieving silencing using an mRNA readout at 48 hours post-treatment, with 93% reduction in *Prkag2* and a 20% non-specific reduction in *Prkag1*, compared to treatment with non-specific siRNA (Figure 86). In contrast, siRNA-mediated silencing of *Prkag1* was less effective, with a 73% knockdown of *Prkag1* expression compared to non-specific siRNA and near two-fold up regulation of *Prkag2*.

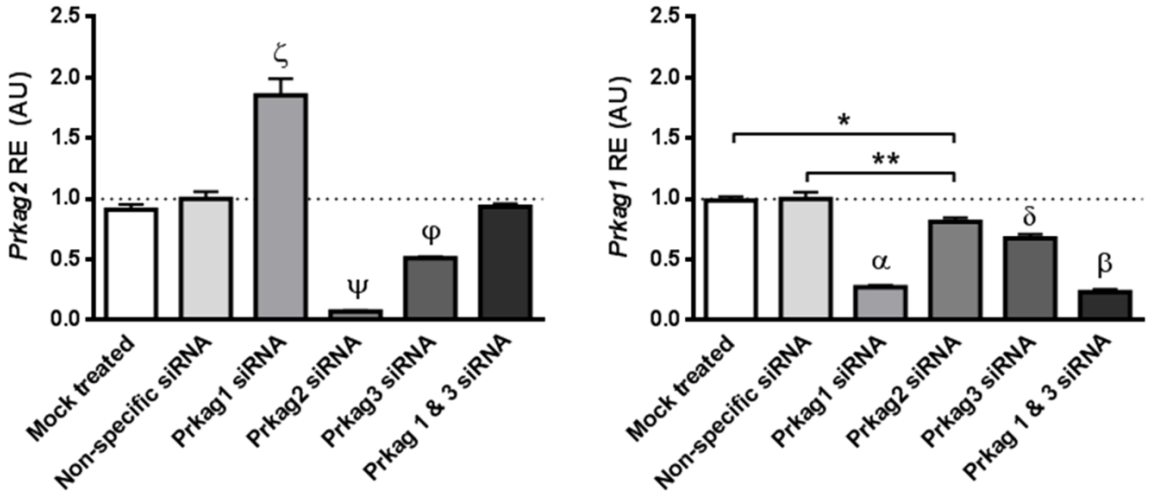


Figure 86. Effect of acute siRNA-mediated *Prkag* isoform gene knockdown on *Prkag2* and *Prkag1* expression in HL-1 cells (N=6 replicates per group).

Left – ζ *P*<0.001 vs all other groups; ψ *P*<0.001 vs all other groups; φ *P*<0.01 vs mock treated, non-specific siRNA and Prkag 1 & 3 siRNA

Right – **P*<0.05; ***P*<0.02; α *P*<0.001 vs all groups except Prkag 1 & 3 siRNA; δ *P*<0.001 vs mock treated or non-specific siRNA groups; β *P*<0.001 vs all other groups except Prkag1 siRNA

Acute knockdown with *Prkag1*- but not *Prkag2*-directed siRNA was observed to upregulate *Hcn1* and *Hcn4* expression. Indeed, knockdown of *Prkag2* had no effect on *Hcn1* expression and actually led to a reduction in *Hcn4* expression compared to HL-1 cells treated with non-specific siRNA. However, interpretation of the *Hcn4* expression data was complicated by the fact that non-specific silencing itself induced upregulation of *Hcn4* expression over mock transfected cells. Knockdown of *Prkag3* resulted in downregulation of both *Hcn1* and *Hcn4*. Double knockdown of *Prkag1* and *Prkag3* had no significant effect on the mRNA expression of either HCN isoform assessed.

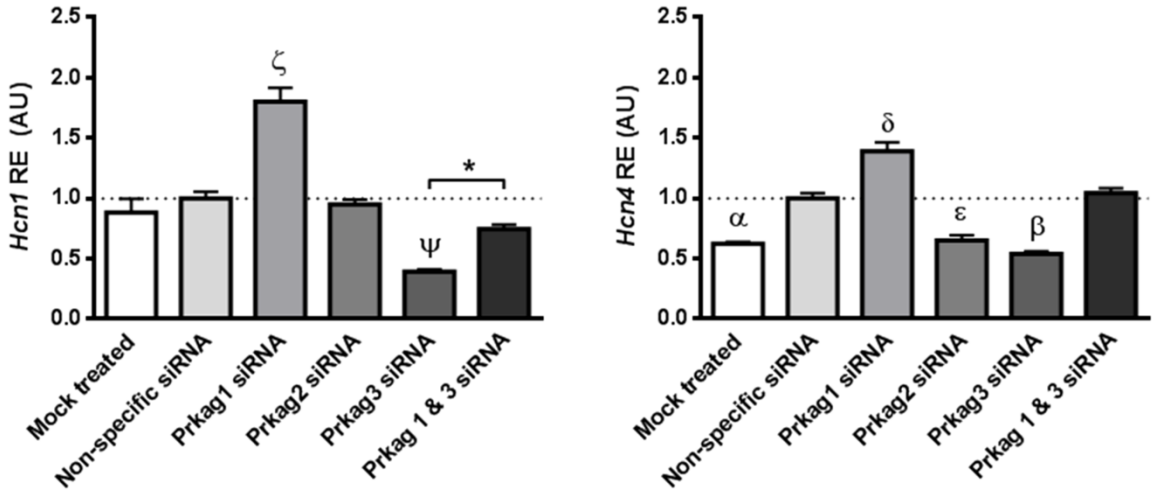


Figure 87. Effect of *Prkag* isoform silencing on *Hcn1* and *Hcn4* expression in HL-1 cells (N=6 replicates per group).

Left – ζ *P*<0.001 vs all other groups; ψ *P*<0.001 vs mock treated and Prkag2 siRNA groups; **P*<0.05

Right – α *P*<0.001 vs non-specific siRNA, Prkag1 siRNA and Prkag 1 & 3 siRNA groups; β *P*<0.001 vs non-specific siRNA, Prkag1 siRNA and Prkag 1 & 3 siRNA; δ *P*<0.001 vs non-specific siRNA, Prkag2 siRNA and Prkag 1 & 3 siRNA; ε *P*<0.001 vs non-specific siRNA and Prkag 1 & 3 siRNA

Use of HL-1 cells as an immortalised cardiac cell line has advantages, including standardisation, ease of use and adherence to the 3Rs principles (Replacement, Refinement and Reduction) as pertains to best ethical practice in animal experimentation. However, this may be offset by inadequate degree of differentiation, potential genomic instability through repeated passaging and, critically, by its physiological relevance to SAN (in terms of ion channel profile and corresponding action potential morphology), thereby potentially limiting its utility as a reductionist tool to dissect out pacemaker mechanisms.

5.4 Discussion

5.4.1 Summary of principal chapter findings

The work presented in this chapter has outlined the generation and initial characterisation of a global γ2 KO mouse model with a view to unlocking potential novel physiological role(s) for γ2 in the heart. These experiments have identified the following:

i) Unlike *Prkag1*, *Prkag2* displays regional enrichment patterns in the normal mouse heart, with *Prkag2* transcript being most abundantly expressed in the atria and SAN compared to the ventricles.

ii) Global deletion of γ2 using a strategy involving Sox2-driven Cre to excise exon 7 of *Prkag2* yields mice that are viable, fertile and appear comparable in appearance to WT Cre+ mice.

iii) The use of the Sox2cre transgene can be associated with parental inheritance of Cre recombinase activity. This refers to the phenomenon whereby recombination and excision of *loxP* flanked sequences occurs at the earliest stages of zygote development, irrespective of inherited *Cre* transgene in the offspring and is thought to be due to the presence of functioning Cre message or protein in the parental germline[236]. Whilst described and frequently encountered for progeny of crosses involving Sox2cre females (Professor Elizabeth Robertson, Oxford, personal communication), this phenomenon has not been formally published for Sox2cre males.

iv) The use of Sox2cre permits satisfactory removal of the floxed R299Q mutated exon 7 of *Prkag2* as judged by qRT-PCR and an end-point RT-PCR readout using mutant allele-specific primers.

v) Western blotting in Homo fl Cre+ mice using an N-terminus specific antibody suggests ablation of γ2 protein product in most organs assessed and a substantial, but incomplete, ablation in heart.

vi) AMPK activity measured by SAMS assay using a C-terminus antibody supports the Western blotting findings, with complete loss of AMPK γ2-specific activity in the liver, but low residual activity in the heart.

vii) No evidence was found for an upregulation of γ1 in response to loss of γ2, at the level of

mRNA, protein or kinase activity. Furthermore, total AMPK activity and ACC phosphorylation in whole hearts was comparable between Homo fl Cre+ and WT Cre+ mice.

viii) No evidence was found for significant structural remodelling or altered histological appearances in response to loss of γ2 in young adult Homo fl Cre+ mice, excluding a significant cardiomyopathy at this stage.

ix) Homo fl Cre+ mice manifest an elevation in intrinsic heart rate and expression of *Hcn1* and *Hcn4* compared to WT Cre+ controls, findings directionally opposite to that found in R299Q γ2 KI mice, in keeping with the concept of the R299Q γ2 mutation being primarily basally activating.

x) Acute silencing of *Prkag2* gene expression in an atrial cell line (HL-1 cells) does not replicate the findings from Homo fl Cre+ mice, although knockdown of *Prkag1* in HL-1 cells does lead to a modest upregulation of *Hcn1*and *Hcn4* expression.

Specific aspects of these findings are discussed in greater detail below.

5.4.2 *Sox2cre*-driven excision of *Prkag2* exon 7: adequate approach to KO γ2?

The starting point for generating a γ2 KO in this chapter's experiments was the gene-targeted R299Q γ2 homozygous mutant mouse which, by virtue of the presence of *loxP* sequences flanking the mutated exon 7, permitted removal of the mutation using a Cre recombinase-expressing mouse line. The selection of Cre line was governed largely by the need to remove the mutation throughout the body, given mutant R299Q γ2 expression under the endogenous promoter and the known widespread tissue distribution[41] of γ2. Accordingly, use of the *Sox2cre* transgene to direct exon 7 excision in early epiblast (by E6.5), allowing efficient deletion of floxed sequences in the embryo proper[236], appeared highly suitable. As a corollary of this, exon 7 was efficiently excised as judged by sequencing of cardiac gDNA, end-point real-time PCR with mutant or WT allele-specific primers on cardiac cDNA and qRT-PCR with exon 7-specific TaqMan gene expression assays.

What then are the consequences of excision of exon 7 of *Prkag2*? Removal of exon 7 is predicted to introduce a frameshift and introduce multiple stop codons in the remaining sequence, with the potential formation of a truncated protein product 293 amino acids in length which has an intact N-

terminal domain, but which lacks the full nucleotide-binding domains (NCBI Open Reading Frame Finder, http://www.ncbi.nlm.nih.gov/gorf/gorf.html). This predicted protein does possess a small portion of CBS1 that could, in theory, bind to the β subunit[241]. The other potential truncated protein product predicted is 253 amino acids in length and starts in the first Bateman domain and extends to include the remainder of the C-terminus of γ2. Notably, the latter lacks the conserved sequence N-terminal of CBS1 required for interaction with the β subunit and the production of a functional heterotrimer[241]. In addition, the expression of multiple nonsense mutations in the transcripts encoding these potential proteins (and several other smaller products) is *anticipated* to be detected by the cell's endogenous mRNA quality-control mechanisms and rapidly subject to nonsense-mediated decay[242]. Any bypassing of this surveillance system by aberrant mRNAs is still expected to produce truncated peptides that either lack the ability to bind adenine nucleotides and/or are unable to form a functional heterotrimeric AMPK complex.

Whilst the data were in support of deletion of exon 7 and hence removal of the R299Q γ2 mutation, the complexity of *Prkag2* splicing[49] and uncertainty in the protein-coding capacity of all the splice variants, coupled with a KO approach that could not generate a complete null allele to delete the entire protein coding sequence of *Prkag2*, made it vitally important to ascertain the protein status of γ2. This endeavour was complicated by the lack of an accepted and verified γ2 antibody for Western blotting. Whilst use of a commercial N-terminus antibody was found to be specific and consistent with loss of γ2 protein in the liver and the majority of other organs examined, it did indicate what appeared to be a small amount of residual, full-length γ2 protein in the heart. Subsequent assessment of γ2-specific activity by SAMS assay after immunoprecipitation of tissue with a C-terminus antibody indicated clear KO in the liver, but persistent low activity in whole heart (14% of WT Cre+ activity levels). While it is not straightforward to reconcile these findings, one approach is to invoke the alternative splicing patterns of *Prkag2*, which differ in liver and heart. Notably, original Northern hybridisation data[41] indicate that the liver almost exclusively expresses the γ2 long variant which the N-terminus antibody utilised for Western blotting would be expected to identify. The expression of smaller splice variants in the heart which differ in N-terminal length would not be adequately picked up by this antibody. However, the use of a C-

terminus antibody to obtain a read-out of γ2 AMPK function *in vitro* should circumvent these concerns. On this basis (and notwithstanding the *in silico* prediction), the kinase activity data are in keeping with low-level cardiac expression of γ2 (or a partial peptide thereof) that is able to form functional AMPK complexes which can phosphorylate SAMS peptide *in vitro*.

With these considerations in mind, as a direct consequence of targeted restriction to one domain, it is likely that the Sox2cre γ2 KO has either multiple partial or alternative transcripts that result in functional peptides in some organs[154]. Whilst a formal, exhaustive screening approach to identify or exclude these was not undertaken, it is important to highlight that the degree of ablation in the organ of primary interest – the heart – was substantial, not accompanied by confounding upregulation of competing γ isoforms and associated with a discernible cardiac phenotype, consistent with a non-redundant physiological role for γ2 in the heart.

5.4.3 EP phenotype of the γ2 KO and γ2 as a novel conserver of cardiac energy

As with its originating parent, the R299Q γ2 KI model, the most notable cardiac abnormality identified in the Sox2cre γ2 KO model was electrical in nature. Using *ex vivo* cardiac perfusion, hearts from Homo fl Cre+ mice were identified to exhibit an elevated intrinsic rate in association with significant upregulation in *Hcn1* and *Hcn4* expression. Whilst formal delineation of increased SAN cell automaticity, SAN HCN1 and HCN4 protein upregulation and augmented I_f current density has not yet been made for Homo fl Cre+ mice, taken together with the findings from the putative gain-of-function R299Q γ2 KI model, these observations support the concept that γ2 may act *physiologically* to modulate *Hcn* expression, I_f current density, sinus node firing rate and thus heart rate *in vivo*. The observation that γ2 is both enriched in the SAN and that it appears to act in coordinated fashion to downregulate expression of several ion channel moieties regulating the diastolic depolarisation phase that critically governs SAN myocyte automaticity – notably including the major contributors to mammalian I_f – lend credence to this proposal. Interpreted in this light, rather than an aberrant gain-of-function, in the SAN the R299Q γ2 mutation may arguably be conceptualised as an extreme version of the physiological norm.

Why might γ2 have evolved to physiologically regulate heart rate? Whilst this role is speculative,

chronic, mild downregulation of mammalian heart rate would act to decrease cardiac oxygen consumption and hence reduce the overall metabolic demands of the beating heart[243]. These considerations are not trivial when estimates for ATP consumption by the heart (weighing ~300-350 g in adult humans) are considered. These range from ~ 6 kg to ~ 30 kg of ATP each day (the latter corresponding to ~ 300mg ATP consumed per heart beat), with the great majority of this being expended for contractile activity (myosin ATPase), but also a significant consumption by the sarcolemmal Na^+/K^+-ATPase and sarcoplasmic reticulum Ca^{2+} ATPase (SERCA)[100, 243]. Seen in this light, even a modest reduction in heart rate has the capacity to save significant amounts of ATP. Beyond the heart, there is a close relationship between heart rate and whole-body oxygen consumption and hence energy expenditure[243]. As such, a putative function of γ2 to act as a physiological negative regulator of heart rate would not only serve to defend cardiac energy homeostasis, but also provide a means of reducing energy consumption by the body as a whole.

5.4.4 Limitations

Whilst the Sox2cre γ2 KO model presented has a clearly discernible EP phenotype, it does have limitations as a platform with which to interrogate the biology of γ2.

Within the heart, the presence of residual γ2 activity consequent upon a potentially altered hypoactive allele in a model that seeks to totally ablate all γ2 function is not ideal. Indeed, it could be argued that a more complete loss of γ2 would have led to a more overt phenotype, notably in terms of a larger signal for increased heart rate. The converse argument is that complete loss of protein function is inherently so unphysiological that it must invoke some compensatory mechanisms (and not simply restricted to that of remaining γ isoform upregulation) that confound reliable interpretation of the phenotype. Viewed in this manner, near-complete loss of γ2 in the heart, resembling a hypomorphic mutant, may provide more physiologically relevant information on the effects of isolated depletion of γ2.

The expression of the R299Q γ2 mutant protein outside of the heart precluded the perhaps most obvious approach to assessing the cardiac role(s) of γ2, namely the use of an organ or cell-specific promoter to allow conditional targeting of the recombination event to the heart, leaving γ2 function

intact elsewhere. Notable in this regard was the identification of small differences in body weight in young Homo fl Cre+ mice compared to WT Cre+ controls. Whilst this should, arguably, not detract from the heart rate and *Hcn* expression findings presented, the exaggeration of this difference over time (data not presented) would make it increasingly difficult to exclude a systemic component to the cardiac phenotype. Moreover, it also considerably complicates potential attempts to stress the model, e.g. with the use of surgical transverse aortic constriction to assess the consequences of cardiac pressure overload in the setting of absent γ2. By virtue of these considerations and the primary scope of the thesis, characterisation of the Sox2cre γ2 KO was focused on its validation, evaluation for a significant cardiomyopathy and targeted assessment to explore the hypothesis that the changes in heart rate and *Hcn* expression in R299Q γ2 mutant mice hinted at a fundamental physiological role for this γ isoform in heart rate regulation.

A criticism common to both the Sox2cre γ2 KO model and the R299Q γ2 KI model is that the EP changes reflect primarily *developmental* adaptations, making them less suitable models with which to make reliable inferences about the adult function(s) of γ2 in the heart. In seeking to address whether *acute* loss of γ2 would exert the effect to upregulate *Hcn1* and *Hcn4* expression – and thereby recapitulate the apparent effects of chronic γ2 loss – a specific reductionist approach was taken using RNA silencing in a cell-based system. Whilst technically satisfactory in terms of adequate knockdown of γ isoform gene expression, these experiments did not reproduce the findings from the Sox2cre γ2 KO model, although one interpretation of the findings is that acute loss of a *Prkag* isoform does have the potential to alter *Hcn* expression (as evidenced by the upregulation in *Hcn1* and *Hcn4* observed with *Prkag1* knockdown in HL-1 cells). The failure of acute silencing of γ2 gene expression to do so may both highlight the limitations of HL-1 cells in modelling SAN cellular physiology, as well as potentially pointing to an SAN-specific or conduction tissue-restricted pathway linking γ2 to HCN1 and HCN4 expression.

5.4.5 Future cardiac work involving the Sox2cre γ2 KO model

Future experiments will include investigation of the hypothesis that enhanced I_f current density is primarily responsible for the elevated heart rate of Homo fl Cre+ mice, in addition to more direct

measurement of the expression of HCN isoforms and other SAN ion channels from the SAN itself, including SAN expression of HCN protein. However, definitive identification of a putative upregulation in I_f current density in Homo fl Cre+ mice may be complicated by the small difference in intrinsic heart rate compared with WT Cre+ mice.

One potential means of investigating the role of γ2 in adult SAN is to attempt to *physiologically* activate SAN AMPK complexes *in situ*. Endurance exercise is known to activate AMPK both in rodents and humans, whilst AMPK is in turn thought to play a major role in the adaptation of skeletal muscle to chronic endurance exercise[244]. Chronic endurance training is associated with a bradycardia traditionally attributed to altered autonomic regulation of the heart. Studies have indicated, however, that training induces an intrinsic bradycardia[245, 246] not fully explained by enhanced cardiac vagal efferent activity[247]. In light of the data presented in this thesis, it is attractive to hypothesise that activation of SAN AMPK γ2 complexes is well-placed to mediate this effect via downregulation of *Hcn1* and *Hcn4* expression, with a consequent reduction in the I_f-driven membrane clock. In mice, 10 weeks of voluntary running wheel exercise has been shown to induce intrinsic bradycardia[248]. If repeated endurance exercise – as a state of chronic AMPK activation – induces sinus bradycardia via an AMPK γ2-dependent downregulation of sinoatrial f-channel expression and reduction in I_f, the corollary of this is that γ2 KO mice (i.e. Homo fl Cre+) should exhibit an abrogated, or even absent, intrinsic bradycardic response to chronic endurance training.

Chapter 6. The systemic phenotype and underlying peripheral mechanisms

6.1 Aims and objectives

Initial phenotyping of the R299Q γ2 mutant line indicated that the consequences of gene-targeting γ2 with this mutation extended well beyond the cardiovascular system. Mutant mice of both genotypes had evidence of altered body size and weight, a phenomenon that became more apparent on backcrossing mice from a mixed to a C57BL/6 genetic background and indicative of disrupted whole-body energy homeostasis. The focus of this chapter was therefore to characterise the systemic phenotype of R299Q γ2 mutant mice and explore underlying peripheral mechanisms.[pp]

Accordingly, the specific aims of the experiments presented were:

i) To characterise the natural history of body weight change and food intake in both male and female R299Q γ2 mutant mice compared to WT.

ii) To determine the cause for body weight change by assessing fat and lean contributions to body mass and determine whether this changed over the lifetime of the animal.

iii) To assess the effect of body weight changes on the plasma adipocytokine profile and correlate this with changes in white adipose tissue gene expression.

iv) To investigate glucose homeostasis in R299Q γ2 mutant mice.

v) To determine the spontaneous activity and exercise capacity of mutant mice.

vi) To examine the impact of the R299Q γ2 mutation on whole-body energy expenditure.

To better place these experiments into context, an introduction to the regulation of energy balance by AMPK follows next.

[pp] Probing of central mechanisms is discussed in chapter 7.

6.2 AMPK and the regulation of whole-body energy balance

6.2.1 AMPK as a mediator of systemic energy balance

Traditionally, AMPK has been viewed as an evolutionarily conserved sensor of cellular energy levels, acting to maintain energy balance at the *individual cell level*. Whilst this concept is fully applicable to the role of AMPK orthologues in unicellular eukaryotes, such as the yeast *Saccharomyces cerevisiae*, in higher multicellular eukaryotes the AMPK signalling system has evolved to respond to and integrate multiple hormonal, nutrient and peptide signals, particularly at the level of the hypothalamus[249]. In conjunction with AMPK's ability to modulate lipid and glucose metabolism, as well as influence mitochondrial biogenesis and protein synthesis in multiple peripheral tissues (e.g. muscle, adipose tissue, liver and pancreas), this positions AMPK to play a broader role in mammals in regulating energy homeostasis at the *whole body level* (Figure 88)[249].

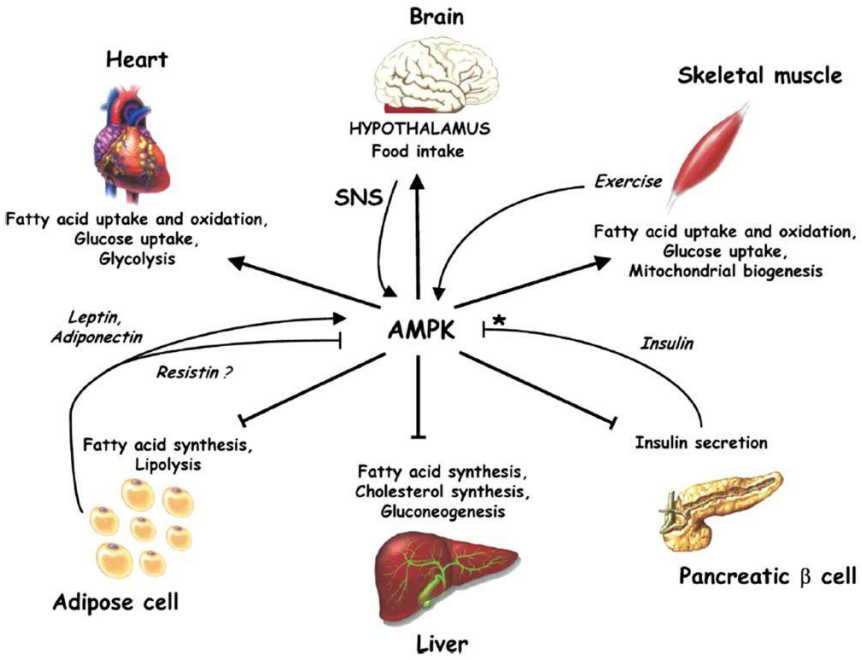


Figure 88. AMPK is able to influence metabolism in key peripheral metabolic organs as well as centrally integrate peripheral hormonal & nutrient signals, thereby playing a role in the regulation of energy balance at the systemic level.[qq]

[qq] Reproduced from figure 1 Kahn et al. *Cell Metab* 2005;1:15-25.

6.2.2 Effects of AMPK on peripheral metabolism

In addition to its well-described role in integrating signals of energy surfeit or depletion centrally, AMPK regulates important metabolic pathways in key peripheral organs such as liver, adipose, pancreas and skeletal muscle. Prominent amongst these is its ability to modulate fatty acid metabolism. AMPK's regulation of fatty acid metabolism centres on its ability to phosphorylate ACC and thereby reduce cellular malonyl-CoA content, simultaneously promoting fatty acid oxidation (via relief of allosteric inhibition of CPT1) and reduction in lipogenesis (as detailed in chapter 7)[250]. Within the liver, AMPK activation inhibits hepatic lipogenesis and the conversion of HMG-CoA to mevalonate in the cholesterol biosynthesis pathway (through its inhibition of HMG-CoA reductase), whilst promoting fatty acid oxidation to decrease hepatic lipid deposition[251].

6.2.2.a Regulation of glucose homeostasis – hepatic gluconeogenesis

AMPK plays an important function in glucose homeostasis through effects on hepatic glucose output and peripheral glucose uptake, notably by skeletal muscle[250]. In addition, AMPK has been identified as a modulator of insulin release from pancreatic islet β–cells[252, 253].

Activation of AMPK in the liver represses the transcription of key enzymes regulating gluconeogenesis (the generation of glucose from non-carbohydrate carbon sources such as pyruvate, lactate, glycerol and glucogenic amino acids): phosphoenolpyruvate carboxykinase (PEPCK) and glucose-6-phosphatase (G-6-Pase). TORC2 (transducer of regulated CREB activity 2), is a transcriptional co-activator and critical regulator of hepatic gluconeogenesis by mediating CREB-dependent transcription of PGC1α and its ensuing gluconeogenic targets PEPCK and G-6-Pase[251]. TORC2 is phosphorylated by AMPK, preventing its translocation to the nucleus and blocking its ability to enhance CREB-dependent expression of PEPCK and G-6-Pase[251, 254]. In keeping with this, mice deficient in AMPK's major upstream kinase in liver – LKB1 – display marked elevations in fasting glucose, but normal hypoglycaemic response to insulin (indicating unperturbed peripheral glucose uptake mechanism), in association with markedly reduced levels of phospho-AMPK[255].

6.2.2.b Regulation of glucose homeostasis – glucose uptake

The uptake of glucose by skeletal muscle is mediated through insulin-dependent and -independent mechanisms[254]. The principal glucose transporter mediating this uptake is GLUT4: a high-affinity glucose transporter that is predominately expressed in skeletal muscle and adipose tissue[256]. GLUT4 exists largely as a cytosolic transport pool which – in response to insulin and other stimuli such as contraction due to exercise in skeletal muscle – acutely redistributes to the plasma membrane[257]. Insulin-mediated acute recruitment of GLUT4 transporters to the cell membrane is thought to partly involve a canonical PI(3)K-dependent signalling pathway (Figure 89), whereby binding of insulin to its cell surface tyrosine kinase receptor leads to phosphorylation of insulin receptor substrate proteins (IRS)[256, 257]. Tyrosine phosphorylated IRS proteins recruit and activate PI3K, which in turn catalyses the production of phosphatidylinositol-3,4,5-trisphosphate (PIP3). PIP3 activates the serine/threonine kinase AKT (protein kinase B or PKB), a central insulin signalling intermediate that interacts with components of the GLUT4 exocytic machinery[256].

Fusion of GLUT4 vesicles with the plasma membrane requires members of the Rab family of small GTP-binding (guanosine triphosphate-binding) proteins – regarded as key regulators of intracellular membrane trafficking[257] – to be in their active GTP-bound state. In the basal state, this process is blocked by the association of Rab proteins with Rab-GTPase activator proteins (Rab-GAP), which promote the intrinsic GTP-hydrolysing activity of Rab proteins to convert Rab proteins to their inactive GDP-bound (guanosine diphosphate-bound) state[12]. One important AKT target in this regard is the Rab-GTPase activating protein TBC1D4 (TBC1 domain family member 4, also known as AS160 or AKT substrate of 160 kDa)[256]. Insulin-activated AKT phosphorylates AS160 leading to its interaction with 14-3-3 proteins, dissociation from GLUT4 vesicles and consequent activation of Rab proteins and vesicle-membrane fusion[12]. In addition to its phosphorylation by AKT, AS160 is also thought to be a substrate for AMPK at multiple phosphorylation sites[24]. AMPK is also known to phosphorylate another Rab-GAP, TBC1D1, promoting 14-3-3 binding and inactivation to permit GLUT4 exocytosis[12] (Figure 89). Notably,

whilst both AKT and AMPK can phosphorylate TBC1D1, only the latter increases 14-3-3 binding, suggesting that this may be the principal means by which AMPK promotes GLUT4 translocation[24].

In addition to acutely enhancing glucose uptake, activation of AMPK increases the expression of GLUT4 and hexokinase II (the enzyme catalyzing the phosphorylation of glucose as the first step in glycolysis)[250].

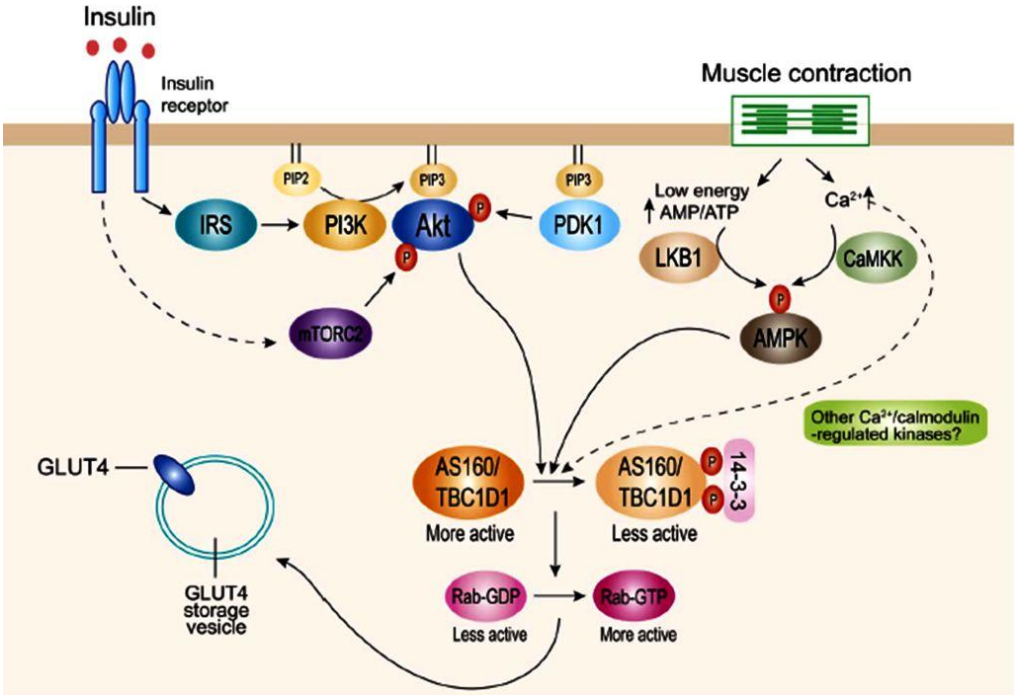


Figure 89. Model for glucose uptake in skeletal muscle demonstrating both insulin-dependent (left) and contraction-stimulated (right) signalling pathways[rr].

Activation of AKT by the insulin signalling pathway, or of AMPK by metabolic stress (elevation of AMP or ADP relative to ATP) or elevated intracellular [Ca^{2+}] occurring during muscle contraction, both lead to phosphorylation of AS160 and TBC1D1 at multiple sites. This renders them less active and triggers their dissociation from GLUT4 storage vesicles, allowing the now activated Rab-GTP complexes to interact with Rab effector proteins to mediate docking and/or fusion of GLUT4 vesicles with the plasma membrane.

6.2.2.c Role of AMPK in the hormonal regulation of peripheral metabolism

In addition to its role in regulating food intake by the hypothalamus in response to circulating leptin and ghrelin, AMPK has been identified as playing a key role in mediating many of the metabolic effects of hormones in the periphery (Table 12)[249, 250, 254, 258].

[rr] Reproduced from figure 1 Sakamoto & Holman *Am J Physiol Endocrinol Metab* 2008;295:E29-E37.

Table 12. Endocrine regulation of AMPK signalling and downstream effects which are dependent on AMPK in key metabolic organs[ss].

Hormone	Skeletal muscle (effect on AMPK & metabolism)	Adipose	Liver	Hypothalamus
Leptin	↑ AMPK (direct and via hypothalamo-sympathetic axis) ↑fatty acid oxidation Increased AMPK α2 and β2 protein content	↑ AMPK ↑fatty acid oxidation	No effect	↓ AMPK activity in ARC and PVN nuclei ↓ food intake
Adiponectin	↑ AMPK ↑fatty acid oxidation ↑glucose uptake	↑ AMPK ↑glucose uptake	↑ AMPK ↓ gluconeogenesis	↑ AMPK ↑ food intake
Resistin	↓ AMPK ↓ fatty acid oxidation ↓ fatty acid uptake	↓ AMPK ↑ lipoprotein lipase	↓ AMPK ↑hepatic glucose production	↑ AMPK ↓ food intake (link with AMPK unclear)
Ghrelin	No effect on AMPK	↓ AMPK ↑lipogenesis	↓ AMPK ↑hepatic glucose production	↑ AMPK ↑ food intake
Endo-cannabinoids	No effect on AMPK	↓ AMPK ↑lipogenesis	↓ AMPK ↑hepatic glucose production	↑ AMPK[259] ↑ food intake
IL-6	↑ AMPK ↑fatty acid oxidation ↑glucose uptake	↑ AMPK	↑ AMPK	Unknown
Ciliary neurotrophic factor (CNTF)	↑ AMPK ↑fatty acid oxidation	↑ AMPK ↑fatty acid oxidation	↑ AMPK in hepatoma cells	↓ AMPK ↓ food intake
Thyroid hormones (T3 and T4)	↑ AMPK (T3) ↑fatty acid oxidation	Unknown	↓ AMPK (T3)	↓ AMPK in VMH[260] ↑ *de novo* lipogenesis Sympathetic nervous system activation of BAT thermogenesis Weight loss, but no acute effect on food intake
Gluco-corticoids	No effect on AMPK	↓ AMPK ↑lipogenesis	↑ AMPK	↑ AMPK[261] ↑ food intake

[ss] Adapted from table 1 Dzamko & Steinberg *Acta Physiol* 2009;196:115-127. References for hormonal regulators not detailed in the original table have been indicated.

6.2.3 Animal models investigating the role of AMPK in energy homeostasis

Whilst pharmacological studies in eukaryotic cell-lines utilising the AMPK activator, AICAR, have provided the basis for much of our understanding of the metabolic pathways regulated by AMPK[57], insight into the *in vivo* role of the different subunits has required harnessing the power of mouse genetics. Several KO mouse models, both global and cell or tissue-specific, have been generated to better understand the physiological role of AMPK subunits in systemic metabolism. Somewhat surprisingly, given the extensive breadth of data implicating AMPK in the regulation of energy homeostasis, relatively few of these develop overt metabolic changes in the absence of challenges such as a high fat diet (HFD) (Table 13).

Why genetic disruption of AMPK subunits should lead to relatively subtle or even bland metabolic phenotypes, in contrast to the morbid obesity manifested by disruption of other genes involved in energy balance (notably leptin and its receptor or elements of the melanocortin pathway such as the POMC or the MC4 receptor), could have several causes. Prominent amongst these is the potential for developmental compensation induced by ablation of a critical gene/pathway/cell early in development due to network plasticity. An example of the latter is targeted ablation of orexigenic AgRP neurons: in the early postnatal period this has only a transient effect on food intake and body weight, whilst ablation in adulthood rapidly leads to starvation[262]. The mechanisms underlying such compensation are not well-described[263], but may involve upregulation of related genes[264]. Another form of inherent compensation involves redundancy of interactions or pathways; this may be particularly relevant in the regulation of vital physiological processes such as food intake or body fat mass, involving highly integrated neuroendocrine networks. Interpretation of whole-body gene deletions can also be complicated by competing effects of gene loss in different organs. Thus, in the whole-body β1 subunit KO, there is a substantial (90%) reduction in hepatic AMPK activity, which would be anticipated to promote gluconeogenesis, enhance triglyceride synthesis and reduce fatty acid oxidation; this is indeed the case in hepatocytes isolated from these mice[265]. Surprisingly though, *in vivo*, β1 null mice manifest no differences in fed or fasting glucose compared to controls and display reduced expression of the gluconeogenic enzyme G-6-Pase. This has been attributed to

the overriding effect of the (modest) reduction in hypothalamic AMPK activity causing hypophagia and weight loss, hence protecting against the deleterious effects of β1 loss in the liver[265].

Table 13. Selected AMPK KO mouse models and their associated metabolic phenotype

Model	Gene	Phenotype	Reference
Total α1 KO	PRKAA1	No detectable metabolic phenotype – normal body weight, fasting glucose/insulin & glucose tolerance	Jorgensen et al., 2004 [266]
Total α2 KO	PRKAA2	Normal body weight, food intake, body composition. Normal fasting glucose & insulin but impaired glucose tolerance with oral glucose challenge. Impaired insulin secretion associated with increased urinary catecholamine secretion Increased body weight & fat mass when fed a high fat diet	Viollet et al., 2003 [267] Villena et al., 2004 [268]
POMCα2 KO (i.e. POMC neurons)	PRKAA1	Mild obesity phenotype (15% greater body weight than littermate controls by age 11 weeks). Normal baseline food intake but exaggerated compensatory feeding response to fast. Normal glucose tolerance. Reduced energy expenditure. Preserved leptin sensitivity and response to melanocortin agonist. Absent electrophysiological responses to altered extracellular glucose Potentiation of obesity by a HFD with ensuing mild glucose intolerance	Claret et al., 2007[269]
AgRPα2 KO (i.e. AgRP neurons)	PRKAA2	Mild age-related reduction in body weight with increased sensitivity to a melanocortin agonist. Absent electrophysiological responses to altered extracellular glucose No significant effect of HFD on body weight phenotype	Claret et al., 2007 [269]
Total β1 KO	PRKAB1	Reduced food intake, body and fat mass. No effect on metabolic rate or physical activity. Improved hepatic insulin sensitivity Protection from HFD-induced hyperinsulinaemia, hepatic steatosis and insulin resistance. Concomitant significant loss of α1 and α2 subunits in liver and reduction in α1 in hypothalamus and white adipose tissue noted	Dzamko et al., 2010 [265]
Total β2 KO	PRKAB2	Normal body growth and glucose tolerance on chow diet. Reduced maximal exercise capacity and endurance. Reduced muscle and hepatic glycogen levels. Impaired AICAR-stimulated glucose uptake. Greater weight gain and susceptibility to hyperinsulinaemia and glucose intolerance. Compensatory increase in β1 in skeletal muscle, with marked reduction in α1 and α2 subunit expression in skeletal muscle	Steinberg et al., 2010 [270]
Total γ1 KO	PRKAG1	No overt metabolic phenotype Splenomegaly with haemolytic anaemia due to altered erythrocyte membrane elasticity (abnormally increased membrane rigidity with high resistance to osmotic haemolysis)	Foretz et al., 2011 [237]
Total γ3 KO	PRKAG3	Normal systemic glucose homeostasis and growth rate. Impaired skeletal muscle glycogen resynthesis *in vivo* post-exercise. Normal baseline glycogen content. Normal insulin-stimulated glucose transport	Barnes et al., 2004 [52]

6.3 Chapter-specific materials and methods

6.3.1 Body weight growth curves

A cohort of age-matched mice (7 generations backcrossed onto a C57BL/6J background) was single-housed shortly after weaning, allowed to acclimatise for one week, then subject to weekly body weight and food intake measurements. Mice were maintained on a standard rodent chow diet (Teklad Global Diet: 16% protein, 4% fat; Harlan Laboratories, UK).

6.3.2 Plasma chemistry

Blood glucose levels were measured using a hand-held glucometer (Acensia Contour, Bayer Healthcare). Blood was collected into EDTA-coated microvette tubes (Sarstedt, Germany) via tail nick after warming the animals in a heating chamber (Vet Tech Solutions, UK). Collected blood was stored briefly on ice, before centrifugation at 5000 x g for 5 minutes. The resulting plasma was stored at -80^{o}C. Adiponectin was measured in diluted plasma samples using an ELISA (Quantikine immunoassay, R&D systems). Multiplex measurement of plasma adipokines and other analytes was with the Milliplex MAP Mouse Serum Adipokine Panel (Millipore) and a Luminex xMAP system as per manufacturer recommendations. All samples were measured in at least duplicate.

6.3.3 Body composition

6.3.3.a Quantitative magnetic resonance (MR) relaxometry

Two separate cohorts of age-matched mice of all three genotypes were scanned using a quantitative MR instrument (EchoMRI, Echo Medical Systems) in the conscious state using three replicates. Mice were weighed before scanning and placed into a holding tube of appropriate dimensions for their size. Total scanning time was restricted to under 5 minutes.

6.3.3.b Dual-energy x-ray absorptiometry (DEXA)

DEXA measurement (Lunar Piximus 2 mouse densitometer, GE Medical, Bedford, UK) of fat and lean mass was carried out under inhaled isoflurane general anaesthesia after assessment of energy expenditure in older mice at 1 year, as well as at the end of the pair-feeding experiment (chapter 7).

6.3.4 Glucose handling

6.3.4.a Oral glucose tolerance test (OGTT)

OGTT was assessed at 6 weeks and 10 months of age in mice of the R299Q γ2 KI line. Mice were fasted for five hours prior to administration of glucose by oral gavage (2 g/kg). Lignocaine local anaesthetic was applied to the tail and blood microsamples obtained at -30, 0, +30, +60, +90, +120 and +180 minutes relative to glucose dosing. Blood glucose levels were measured with a glucometer (Acensia Contour, Bayer Healthcare). Tail nick blood samples were taken for insulin measurement at -30 and +30 minutes into EDTA-coated microvette tubes (Sarstedt, Germany), stored briefly on ice, centrifuged at 5000 x g for 5 minutes and the resulting plasma stored at -80^{o}C. Insulin content was determined by ELISA according to the manufacturer's instructions (Mouse Insulin ELISA Kit, Crystal Chem Inc) with a plate reader (SpectroMax 250, Molecular Devices).

6.3.4.b Insulin sensitivity test

Ten month old male R299Q γ2 KI mice and WT littermate controls underwent fasting for 5 hours followed by intraperitoneal (i.p.) administration of 1.5 U/kg of Actrapid insulin (Bayer Healthcare). Glucose measurements were then performed in similar manner to that described for the OGTT at -10, 0, +10, +20, +30, +45 and +60 minutes relative to the insulin injection, with data presented as absolute level of blood glucose and change relative to the starting value at the time of injection.

6.3.4.c Pancreatic insulin content

After removal, pancreas samples were weighed, then placed in ice-cold ethanol (75% v/v)/HCl (180 mM) buffer and minced rapidly. Samples were incubated overnight at 4°C and then centrifuged at 1800 x g for 20 minutes. Insulin content of the supernatant was determined by radioimmunoassay according to the manufacturer's instructions (Millipore), using mouse insulin standards and expressed relative to initial pancreatic weight.

6.3.5 Spontaneous activity assessment by infra-red beam breaks

Female R299Q γ2 mutant mice and WT littermates were singly housed in light-tight, ventilated enclosures, at constant temperature and humidity. Activity was measured using pyroelectric

detectors (passive infra-red, PIR, Panasonic AMN32111J, Farnell, UK). Activity data was collected and analysed using ClockLab software (Actimetrics, IL, USA). Activity under 12 hour light:12 hour dark conditions was averaged for 14 days for each animal (as average counts/min in 10 minute bins over 24 hours) and displayed as Zeitgeber time (ZT, lights on at ZT0).

6.3.6 Voluntary running assessment and data analysis

Exercise activity of R299Q γ2 KI mice was assessed by use of an in-house computerised running wheel system[271]. Female mice were singly housed at 7 weeks of age in IVC's containing a freely-rotating, angled running track (Lillico, UK), with wheel rotations monitored by use of a magnetic reed switch connected to a computerised exercise monitoring system (Micro 1401, CED, Cambridge) (Figure 90). Mice were allowed to acclimatise to single housing for several days and then data was continuously recorded throughout the experiment for 30 days, with acquisition and analysis performed using Spike2 software (CED). The following parameters were derived and quantified for each 24 hour period for all mice: total distance travelled, time spent running, average running speed, modal running speed ('cruising' speed), maximum running speed, number of running bouts and bout duration[271]. During the study, mice were monitored remotely daily by computer and cage disturbance kept to a minimum, with *ad libitum* access to the running wheel.

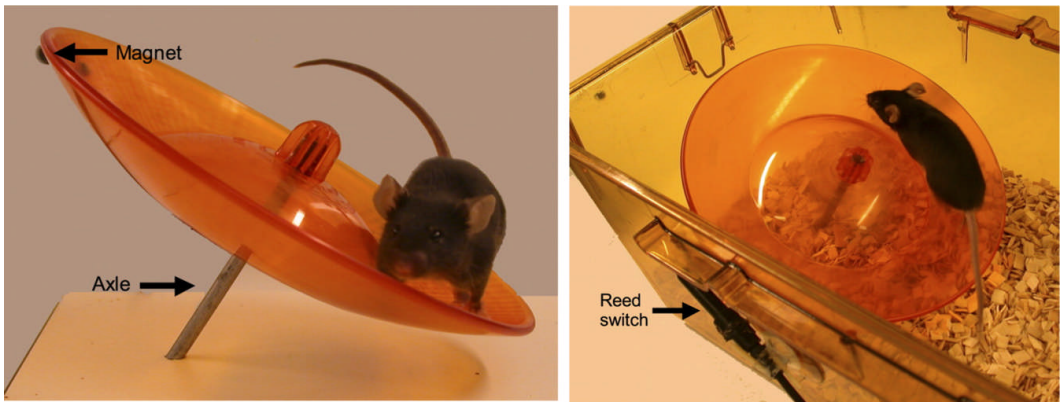


Figure 90. Angled running wheel track used for experiments illustrating magnet fastened to wheel rim (left) and reed switch on cage exterior (right) to pick up wheel rotations.[tt]

[tt] Reproduced from figure 1 De Bono et al. *Am J Physiol Regul Integr Comp Physiol* 2006;290:R926-R934.

6.3.7 Energy expenditure

Energy expenditure (EE) was measured by open-circuit indirect calorimetry over 24 hours, or for up to 5 hours following administration of a β3-adrenergic agonist (BRL-37344 at 250 mg/kg i.p.) in 6 week old mice. EE was calculated by customised software using the equation of Weir[272] and expressed on a whole animal basis over 24 hours. In line with recent guidance[273], analysis of data from older, obese mice was carried out using analysis of covariance (ANCOVA) with DEXA-determined lean body and fat mass as covariates (MedCalc Software version 12.3, Belgium).

6.3.8 Pancreatic islet β-cell isolation, culture and electrophysiology

Pancreatic islets were isolated from R299Q γ2 KI mice aged 8 weeks under sterile conditions as described with minor modifications[274]. The common bile duct was cannulated and its duodenal end occluded by clamping. The duct was injected with 2 mL of Liberase solution (Hank's Balanced Salt Solution, HBSS [Invitrogen]; 25 mM HEPES; 0.25 mg/mL liberase enzyme [Roche]) at 0.25 mg/mL to distend the pancreas. The pancreas was removed, shaken and incubated for 14 minutes at 37°C in quenching buffer (HBSS with 10% FBS and 1% penicillin/streptomycin). Digestion was terminated by addition of ice-cold quenching buffer. Crude pancreatic preparations underwent 3 rounds of washing with HBSS and centrifugation at 1000 x g and finally isolated islets were hand-picked in HBSS containing 25 mM HEPES under a dissection microscope. Once purified islets were obtained, individual β-cells were obtained by triturating through a fire-polished glass pipette and cells added to poly-L-lysine coated coverslips. Cells were maintained in DMEM containing 10% FBS and 1% penicillin-streptomycin for up to 7 days.

Cultured β-cells were superfused at RT with a saline solution (containing 135 mM NaCl, 5 mM KCl, 1 mM $MgCl_2$, 1 mM $CaCl_2$, 10 mM HEPES, pH to 7.4). Recording electrodes were drawn from borosilicate glass filled with a pipette solution (10 mM HEPES, 10 mM EGTA, 140 mM KCl, 5 mM $MgCl_2$, 3.8 mM $CaCl_2$, 3 mM ATP, pH 7.2). Membrane potential was measured by whole-cell current-clamp recordings (AxoPatch 200A, Axon Instruments) as described[253]. Extracellular glucose concentrations in the superfusate were altered after a minimum of 10 minutes stable recording.

6.4 Results

6.4.1 Appearance, body weight and food intake

Male and female R299Q γ2 homozygous mutant mice maintained on a standard chow diet were seen to be strikingly different in size to their WT counterparts, with heterozygous mutant males but not consistently female heterozygote mice, manifesting an intermediate phenotype (Figure 91).

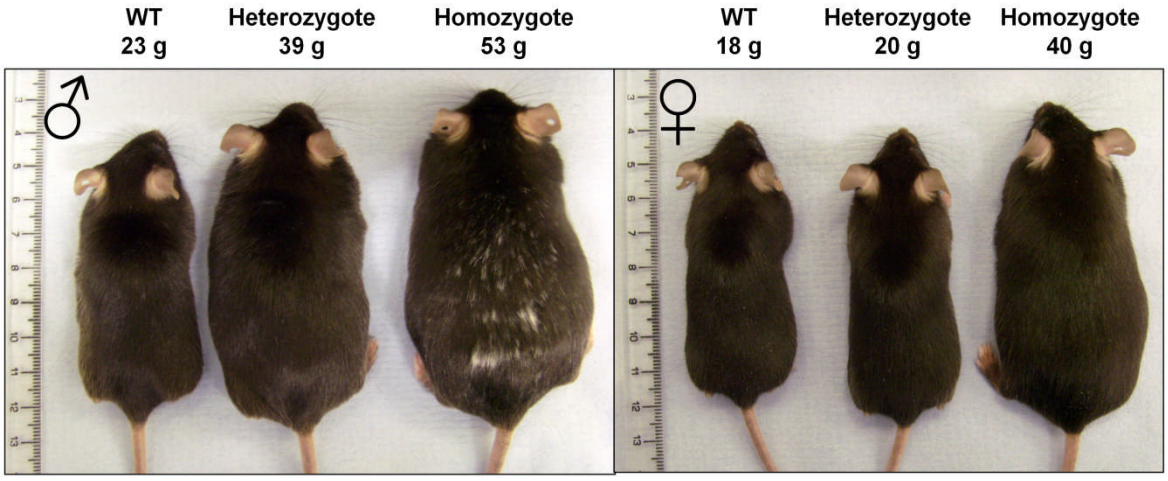


Figure 91. Male and female appearances on a C57BL/6 genetic background at 20 weeks.

Individual housing of mice to standardise environment and reduce within-group variance[275], revealed marked body weight divergences over time in homozygous mice of both sexes (Figure 92).

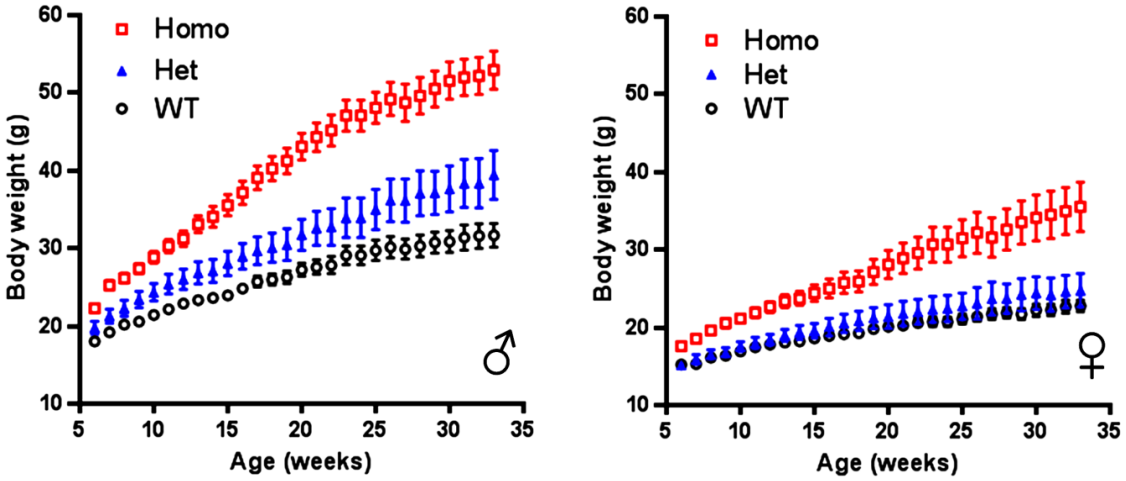


Figure 92. Body weight growth curves of individually housed male and female R299Q γ2 line mice fed a standard rodent chow diet (N=7-12/genotype each). Homozygote vs WT differences are significant from 11 and 17 weeks for males and females, respectively.

Assessment of food intake (Figure 93) disclosed hyperphagia in homozygous mutant mice of both sexes, with only a visual trend towards increased food intake in male heterozygotes relative to WT.

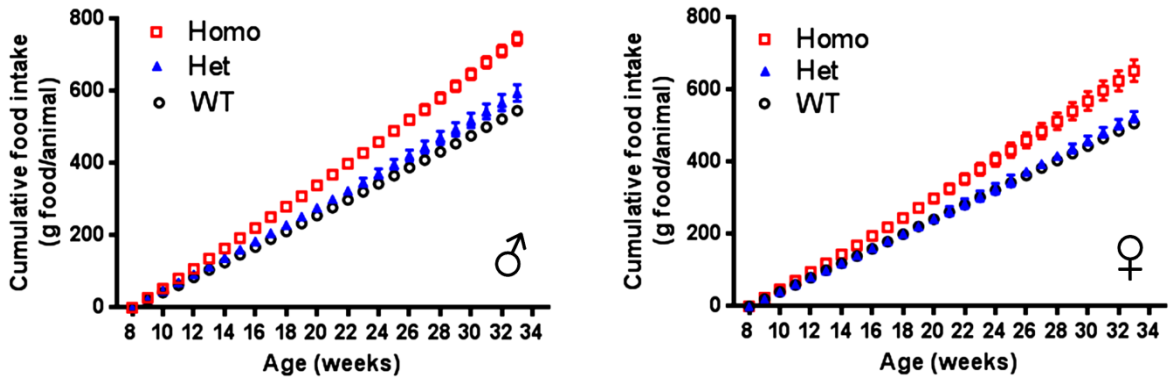


Figure 93. Cumulative food intake of R299Q γ2 line mice on a standard rodent chow diet. (N=7-12/genotype each). Homozygote vs WT differences are significant from 16 and 20 weeks for males and females, respectively.

6.4.2 Body composition

To examine the changes in body composition underlying these differences in body weight, non-invasive MR relaxometry[276] was performed at age 4 and 40 weeks. This identified an increase in 'lean' mass (representing non-fat mass) at 4 weeks in both male and female homozygous mutant mice (Figure 94). By 40 weeks, however, homozygous mice developed marked increases in fat mass, in addition to persistently increased lean mass (Figure 95).

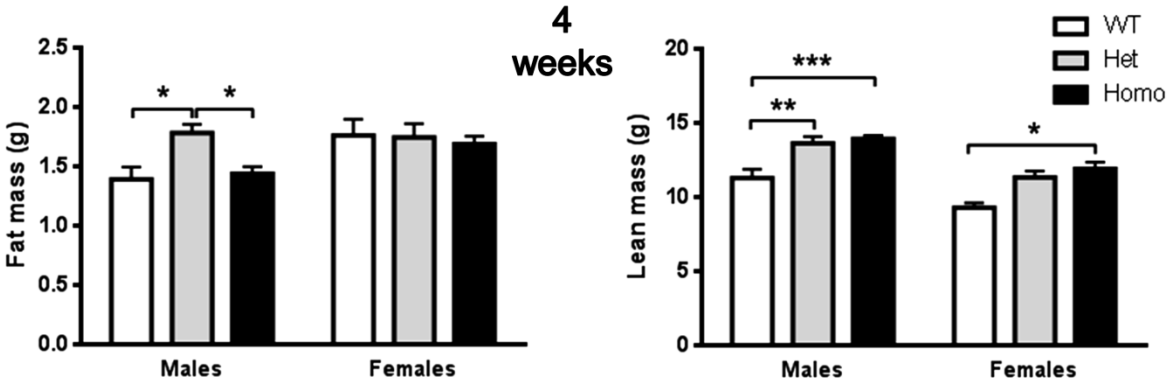


Figure 94. Quantitative MR assessment of body composition in R299Q γ2 line at 4 weeks (N=7-16/genotype for both sexes). *P<0.05, **P<0.01, ***P<0.001

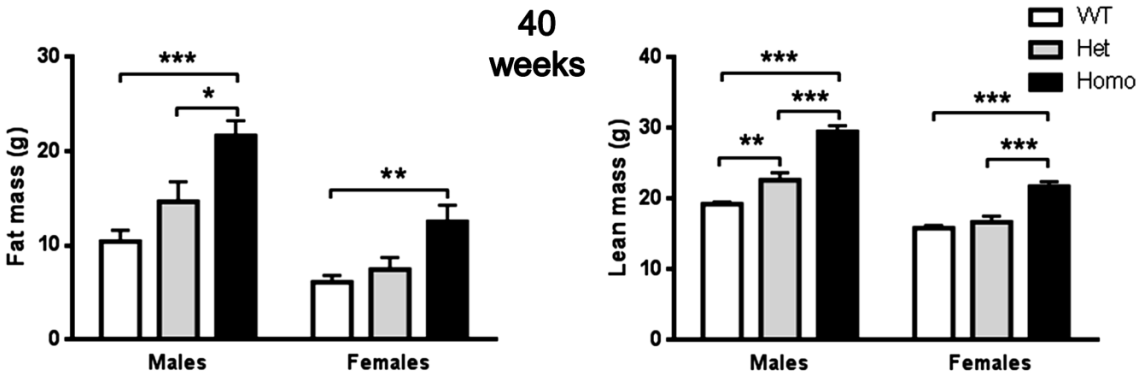


Figure 95. Quantitative MR assessment of body composition in R299Q γ2 line at 40 weeks (N=4-11/genotype for both sexes). *P<0.05, **P<0.01, ***P<0.001

Ex vivo measurement of discrete fat pads from 40 week old male mice confirmed a significant increase in mass of white adipose tissue depots in both R299Q γ2 mutant genotypes (Figure 96).

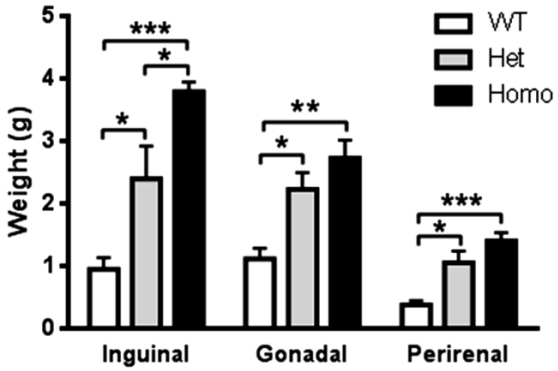


Figure 96. Regional white adipose tissue depot mass in males at 40 weeks (N=5/group). *P<0.05, **P<0.01, ***P<0.001

6.4.3 White adipose tissue (WAT) appearances and gene expression

Histology of epididymal WAT of 40 week old male homozygous mutant mice revealed white adipocyte hypertrophy (Figure 97), with a rightward shift in frequency distribution (Figure 98).

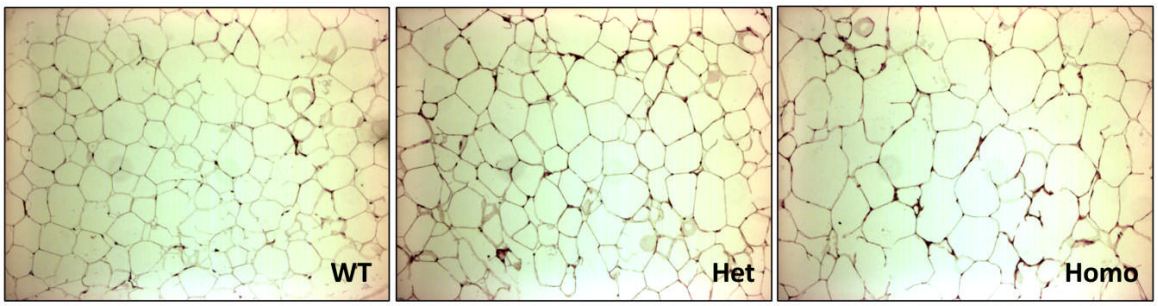


Figure 97. Representative H&E histology images from epididymal WAT at 40 weeks.

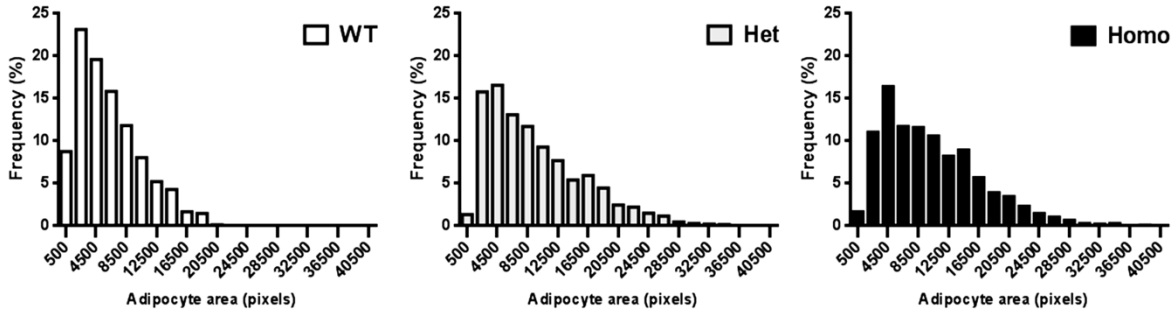


Figure 98. Frequency distribution of adipocyte areas from epididymal WAT at 40 weeks (N=5 animals/genotype with ≥250 cells evaluated/animal).

Given the emergence of obesity in mutant R299Q γ2 mice, gonadal WAT gene expression of 40-week old male mice was investigated with particular reference to macrophage and inflammation-related genes (Figure 99)[277]. This revealed significant upregulation in *Emr1* (encoding the macrophage-restricted cell surface glycoprotein F4/80), as well as the gene encoding the inflammatory cytokine, TNFα. Conversely, there was downregulation in *Adipoq*, encoding the anti-inflammatory, insulin-sensitising adipokine, adiponectin. These findings are consistent with the obese state and suggestive of an increase in both macrophage number and activation level in WAT of R299Q γ2 homozygous mutant mice.

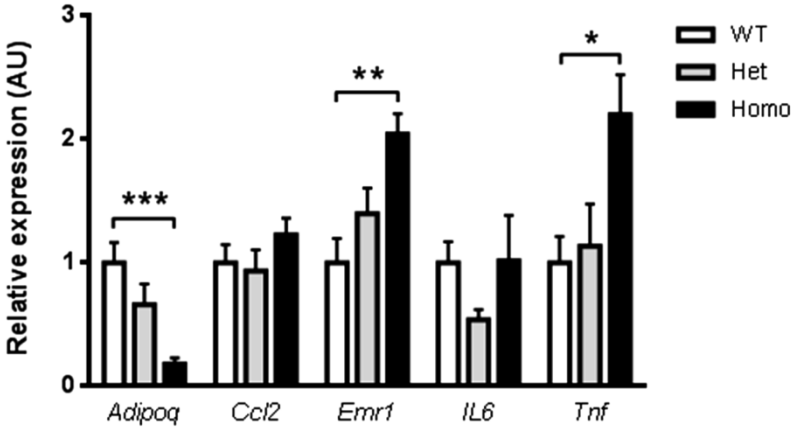


Figure 99. WAT mRNA expression profile of adiponectin, markers of macrophage infiltration (*Ccl2* and *Emr1*) and inflammatory cytokines (*Il6* and *Tnf*) in male mice at 40 weeks (N=5-8/genotype). **P*<0.05, ***P*<0.01, ****P*<0.001

6.4.4 Plasma adipocytokine profile

To investigate whether the development of obesity in mutant mice was associated with an adverse circulating adipocytokine profile, plasma was assayed both at an early time point (4-6 weeks),

when body weight was comparable across genotypes and a late time point (40-44 weeks), when obesity was clearly established (Figure 100).

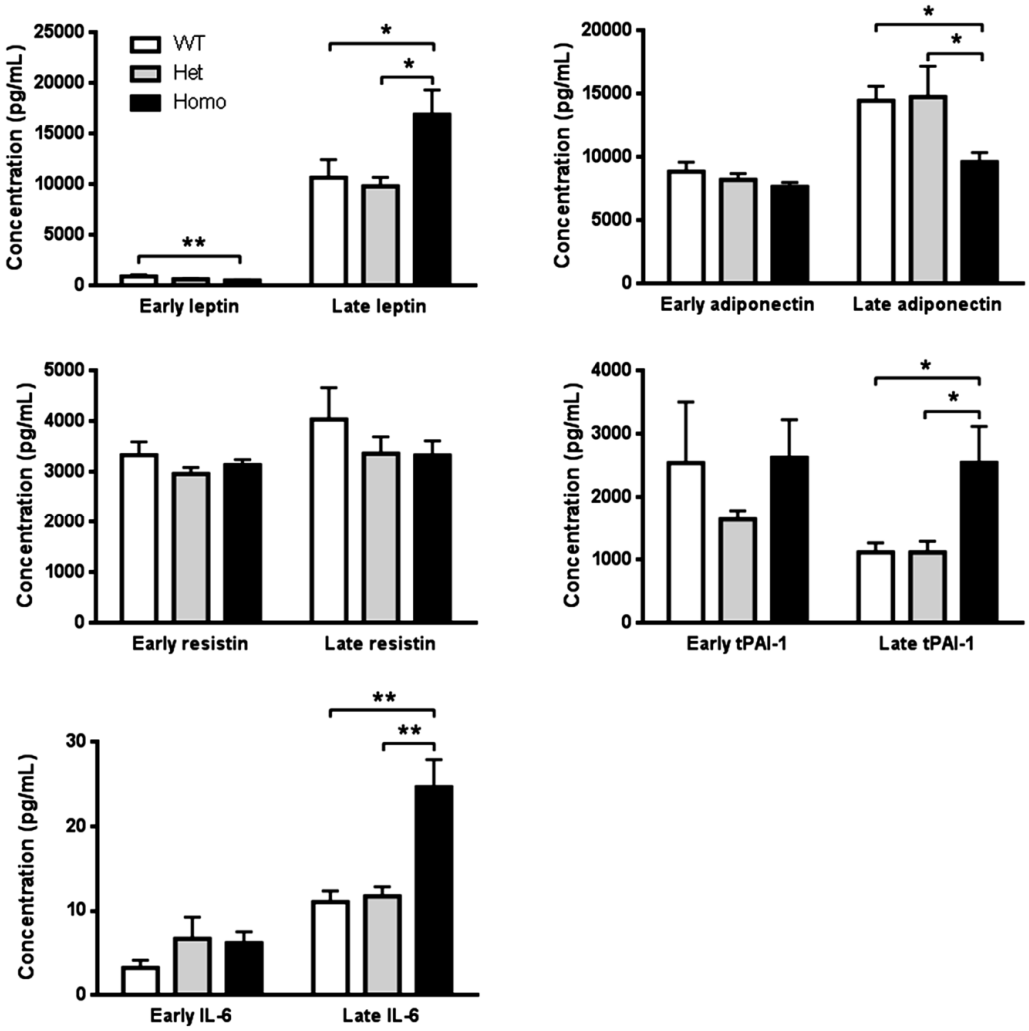


Figure 100. Plasma adipocytokine levels at early (4-6 weeks) and late (40 weeks) time points (N=7-19/genotype).

Except for a reduced plasma leptin level in young R299Q γ2 homozygous mutant mice (consistent with their reduced percentage fat mass), the plasma profile of the adipokines and analytes assessed was comparable amongst genotypes at the early time point. With age, however, R299Q γ2 homozygous mutant mice manifested an adverse plasma profile largely consistent with obesity, including hyperleptinaemia, hypoadiponectinaemia and elevated levels of tPAI-1 (tissue plasminogen activator inhibitor-1) and IL-6, the latter indicative of systemic inflammation.

6.4.5 Glucose homeostasis

6.4.5.a Glucose tolerance

In order to examine the effect of the R299Q γ2 mutation on glucose handling, oral glucose tolerance testing (GTT) was performed (Figure 101). This indicated intact glucose tolerance in response to an oral glucose load in young mice, but impaired glucose tolerance with elevated area under the curve (AUC) for glucose (in keeping with stimulated insulin resistance) in older mice.

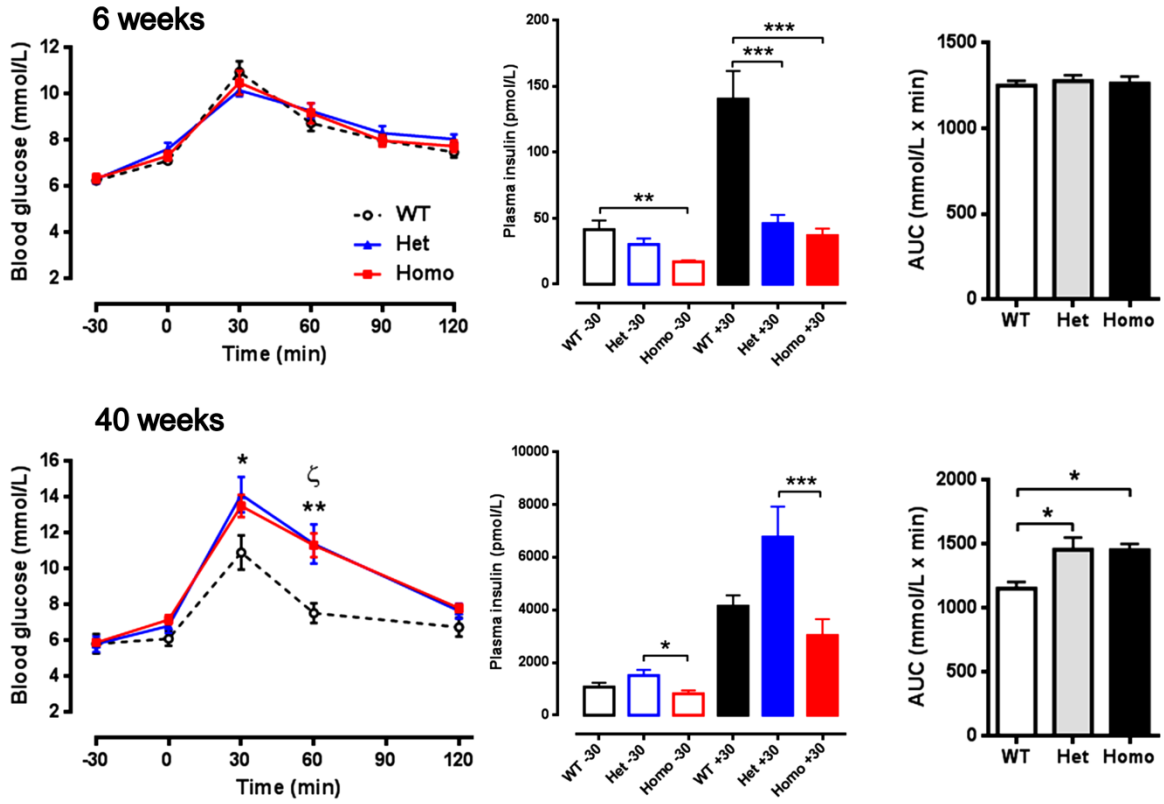


Figure 101. Oral glucose tolerance profile, corresponding plasma insulin levels 30 minutes pre- and post-glucose load and area under the curve (AUC) for glucose tolerance test in males at age 6 weeks (upper row) and 40 weeks (lower row) (N=15-23/genotype for 6 week time point; N=9-27 per genotype for 40 week time point).

40 week GTT - *P<0.05 vs WT, **P<0.01 Het vs WT, ζ P<0.001 Homo vs WT comparison. All other charts – *P<0.05, **P<0.01, ***P<0.001

Notably, young R299Q γ2 homozygous mutant mice displayed significantly lower fasting insulin levels, with both heterozygous and homozygous mutant mice exhibiting markedly blunted insulin response to oral glucose load in comparison to WT mice (Figure 101). Consistent with their obese state, older mutant mice had impaired glucose tolerance and elevated AUC in keeping with

stimulated insulin resistance, although basal insulin levels (pre-OGTT) were not significantly different to WT mice (Figure 101). Surprisingly, fasting insulin levels of older R299Q γ2 homozygous mutant mice were no different to WT controls, although lower than that of heterozygous mice. Both WT and heterozygous mutant mice responded to an oral glucose load with a clear insulin response, but this appeared blunted in the homozygous mutant mice, with comparable levels of insulin to WT at 30 minutes post-glucose bolus. These data suggest dynamic changes in glucose homeostasis with time in R299Q γ2 KI mice, with emergent impaired glucose tolerance but not the marked hyperinsulinaemia that often accompanies significant obesity.

6.4.5.b Whole-body insulin sensitivity and β-cell glucose sensing

To further probe the late time point GTT findings, whole body sensitivity to insulin was assessed based on evolution of glucose levels to an insulin bolus[278] (Figure 102).

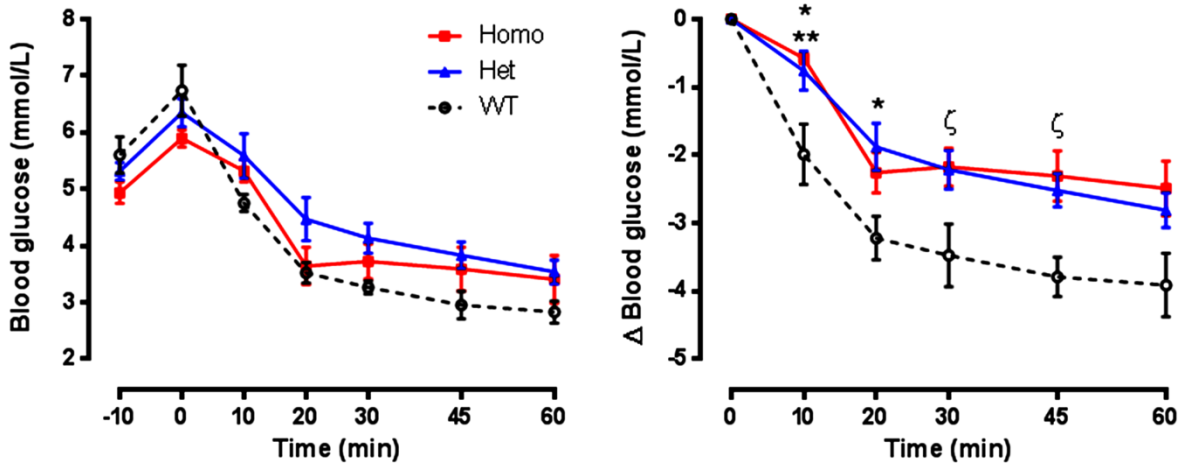


Figure 102. Response of 1 year old male mice to 1.5 U/kg actrapid insulin (N=6-13/ genotype). ****P*<0.05 Het vs WT, *****P*<0.01 Homo vs WT, ζ *P*<0.01 Homo vs WT. NB the effect of genotype on blood glucose levels was also highly significant (*P*<0.0001) by two-way ANOVA when plotted as % of baseline levels.

This revealed significantly reduced insulin sensitivity in both mutant genotypes, with a significantly slower initial rate of decline in glucose levels, typically indicative of diminished skeletal muscle insulin sensitivity. Based on these findings, reduced whole-body insulin sensitivity contributes to the phenotype of impaired glucose tolerance at the late time point. The finding of an inappropriately reduced insulin response to a glucose load suggested an additional primary

pancreatic component, in terms of reduced insulin secretion, however. As an initial step, pancreatic insulin content was measured from 1 year old mutant mice (Figure 103). This was unchanged in mutant mice, suggesting that the abnormal *in vivo* insulin response to glucose was due to either impaired sensing of glucose by the β-cells of the pancreatic islets and/or reduced insulin secretion. To examine whether the impaired *in vivo* glucose-stimulated insulin secretion (GSIS) was associated with altered islet glucose sensing, β-cell electrical responsiveness was measured from individual isolated β-cells (Figure 103). This revealed no evidence for a defect in electrical glucose sensing, with normal, reversible membrane hyperpolarisation response to hypoglycaemia (10 mM to 2 mM glucose) in R299Q γ2 mutant β-cells, suggestive of appropriate membrane potential response by K_{ATP} channels, ATP-sensitive potassium channels which play a fundamental role in linking changes in cellular metabolism following glucose influx to β-cell membrane potential[279]. Taken together, the impaired *in vivo* GSIS of R299Q γ2 mutant mice is likely K_{ATP} channel-independent, with a reduced ability to secrete insulin, either intrinsic to the pancreas or potentially secondary to altered autonomic nervous influence.

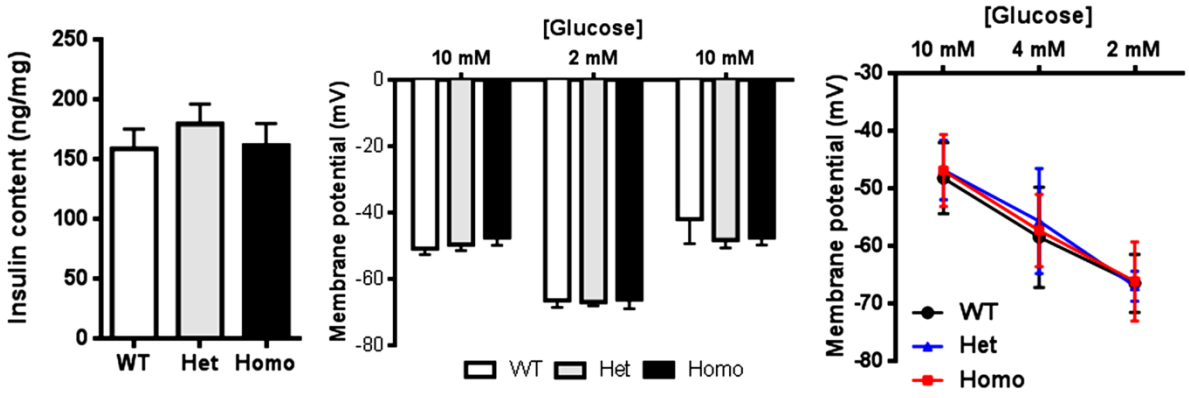


Figure 103. Left panel – Pancreatic insulin content in male mice at 1 year (N=6-10/genotype). Middle and right panels – Hyperpolarisation of β-cells from 6-8 week old mice in response to lowered glucose concentration (N=6-10 individual β-cells/recording).

6.4.6 Activity assessment

6.4.6.a Spontaneous activity

To determine whether altered physical activity contributed to the weight gain of R299Q γ2 KI mutant mice, spontaneous locomotor activity of a cohort of 7-8 week old female mice monitored

individually in their home cages was assessed using passive infra-red sensors (Figure 104).

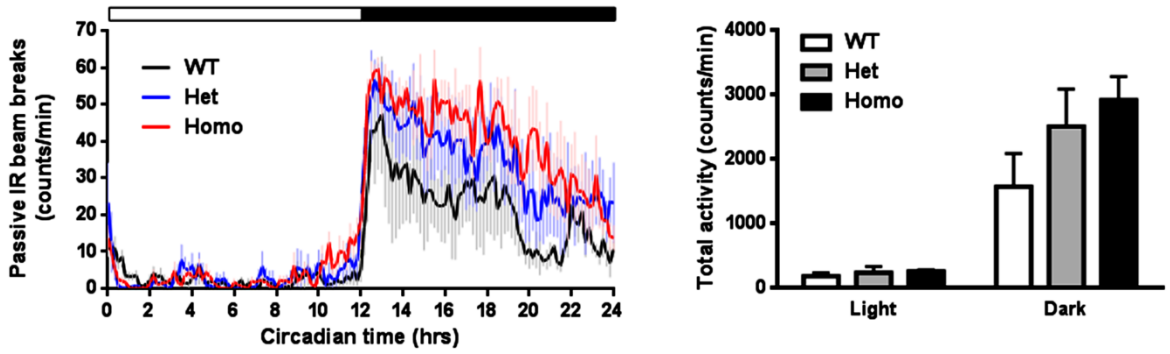


Figure 104. Spontaneous locomotor activity in female R299Q γ2 mutant mice and WT littermates aged 7-8 weeks (N=4/genotype).

As expected, this revealed a diurnal rhythm of physical activity in all mice, with minimal light-phase activity and a dramatic surge in locomotor behaviour at the onset of the dark phase. Surprisingly, R299Q γ2 mutant mice of both genotypes exhibited trends to greater locomotor activity throughout the dark phase. Notably, the high levels of activity within the initial hours of onset of the dark phase rapidly settled in WT mice, but were far more prolonged in mutant mice.

6.4.6.b Spontaneous exercise performance

Whilst the passive infra-red detector data suggested increased volitional drive to movement in R299Q γ2 mutant mice, they did not provide insight as to whether their exercise capacity was altered. To investigate whether the R299Q γ2 mutation affected voluntary exercise performance, a cohort of 7 week old female mice were individually housed with a computer-linked running wheel[271] for 30 days. The body weights of mice at the start of running were not significantly different (WT, 16.0±0.5 g; Het, 18.3±2.9 g; Homo, 18.2±1.8 g, mean±SEM). Notably, whilst both male and female mice run spontaneously when given access to a wheel, C57BL/6 female mice run significantly further and for a longer time than their male counterparts[271]. Female mice have also been demonstrated to have more day-to-day variability in total time spent running[271].

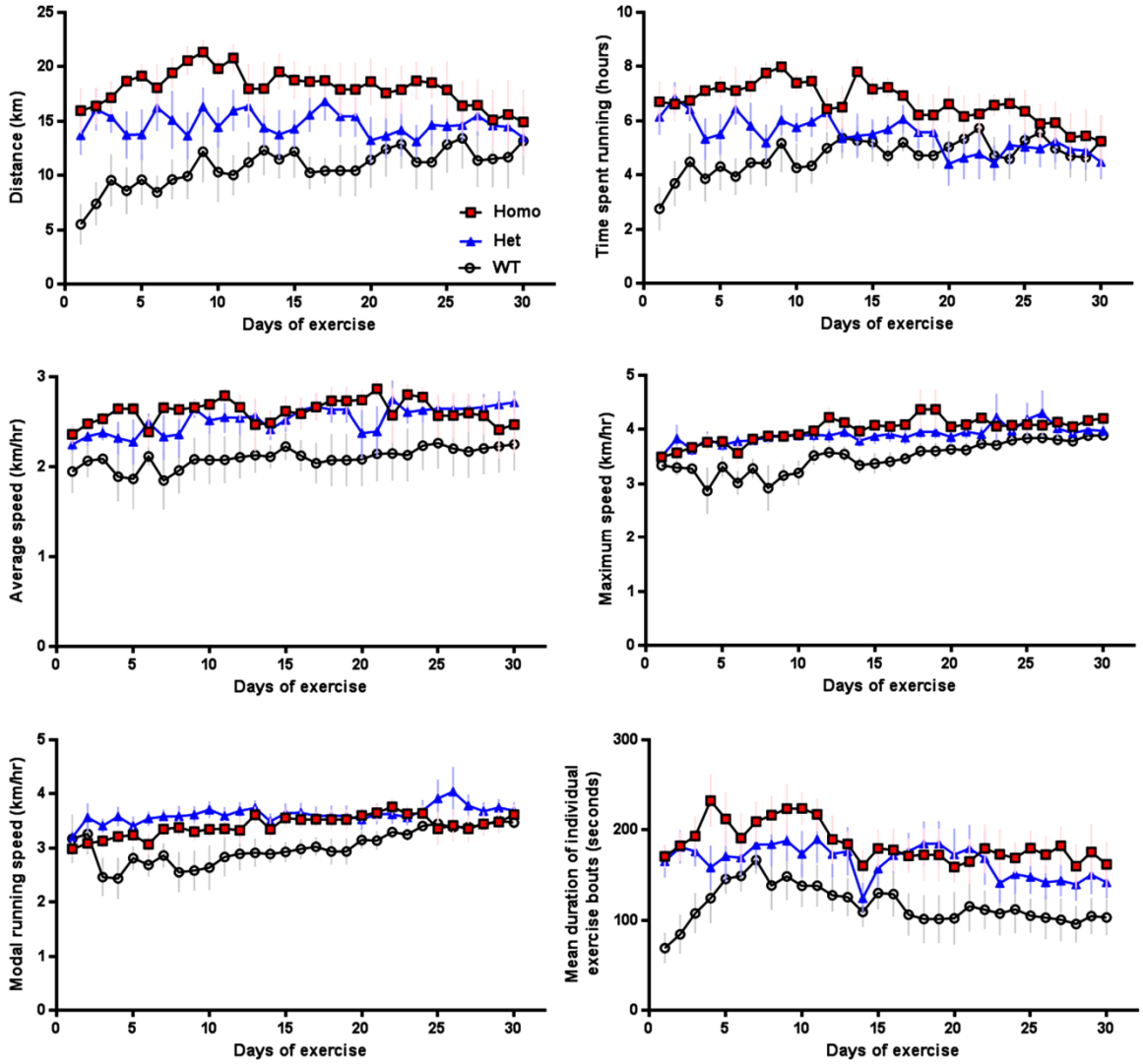


Figure 105. Voluntary wheel running parameters in female R299Q γ2 KI mice and WT littermates starting at age 7 weeks (N=7-10/genotype). The effect of genotype was highly significant for all parameters assessed by two-way ANOVA (*P*<0.001).

Compared to WT, homozygous mutant mice had greater distance run, total time spent running, average duration of running bout and a faster average speed ($P<0.05$ for all parameters) (Figure 105). Trends were also seen for greater maximal speed ($P=0.07$) and modal speed ($P=0.09$) for mutant genotypes. Intriguingly, whilst WT mice exhibited a clear 'training effect' – with initial progressive increases in distance and time spent running – mutant mice already appeared maximally 'trained', with no further improvement seen in these parameters with time.

6.4.6.c Quadriceps gene expression profile

The running wheel data indicated greater exercise capacity in mutant mice. To probe the potential molecular correlates of this, an examination of gene expression of slow and fast phenotype-associated markers, as well as biomarkers of oxidative function, was undertaken in quadriceps muscle in untrained mice at 8 weeks.

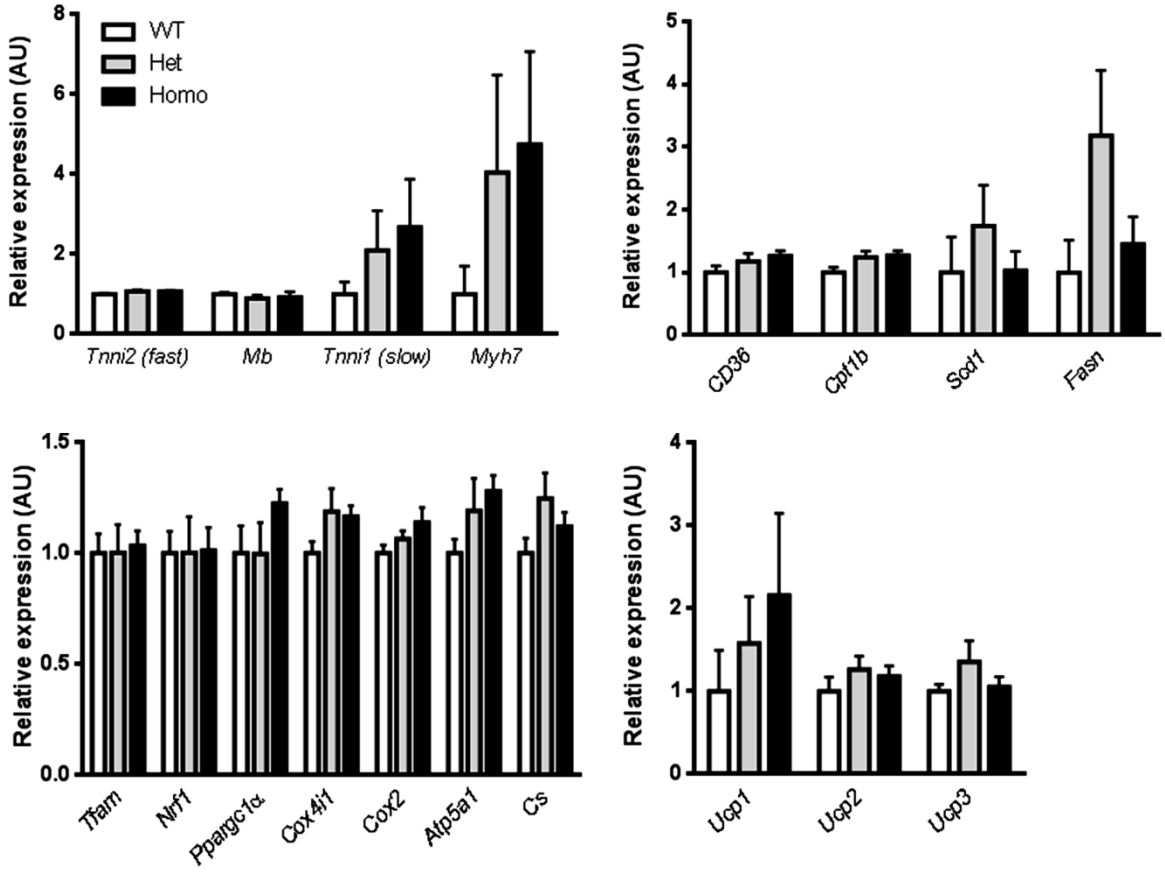


Figure 106. Relative gene expression levels of slow and fast muscle phenotype markers (upper left), biomarkers of fatty acid metabolism (upper right) and mitochondrial function (lower panels) in quadriceps muscle at 8 weeks (N=8/genotype).

In this cohort of 8 mice per genotype, no statistically significant differences were identified in the markers assessed. Trends were seen to modest upregulation of several mitochondrial biomarkers (e.g. *Cox4i1, Cox2, Atp5a1*) and slow muscle fibre phenotype markers (*Tnni1*) in R299Q γ2 mutant mice, suggestive of a potential subtle coordinated alteration in gene expression in mutant mice favouring enhanced endurance and exercise performance.

6.4.7 Energy expenditure

6.4.7.a Indirect calorimetry in young adult mice

To determine whether reduced energy expenditure (EE) may contribute to the development of obesity in R299Qγ2 mutant mice, EE was measured at an early time point, when differences in body weight were minimal, using indirect calorimetry (Figure 107). This uses gas-tight cages with a constant flow of fresh air and calculates EE indirectly based on oxygen consumption and carbon dioxide production in the home cage of the mice[273].

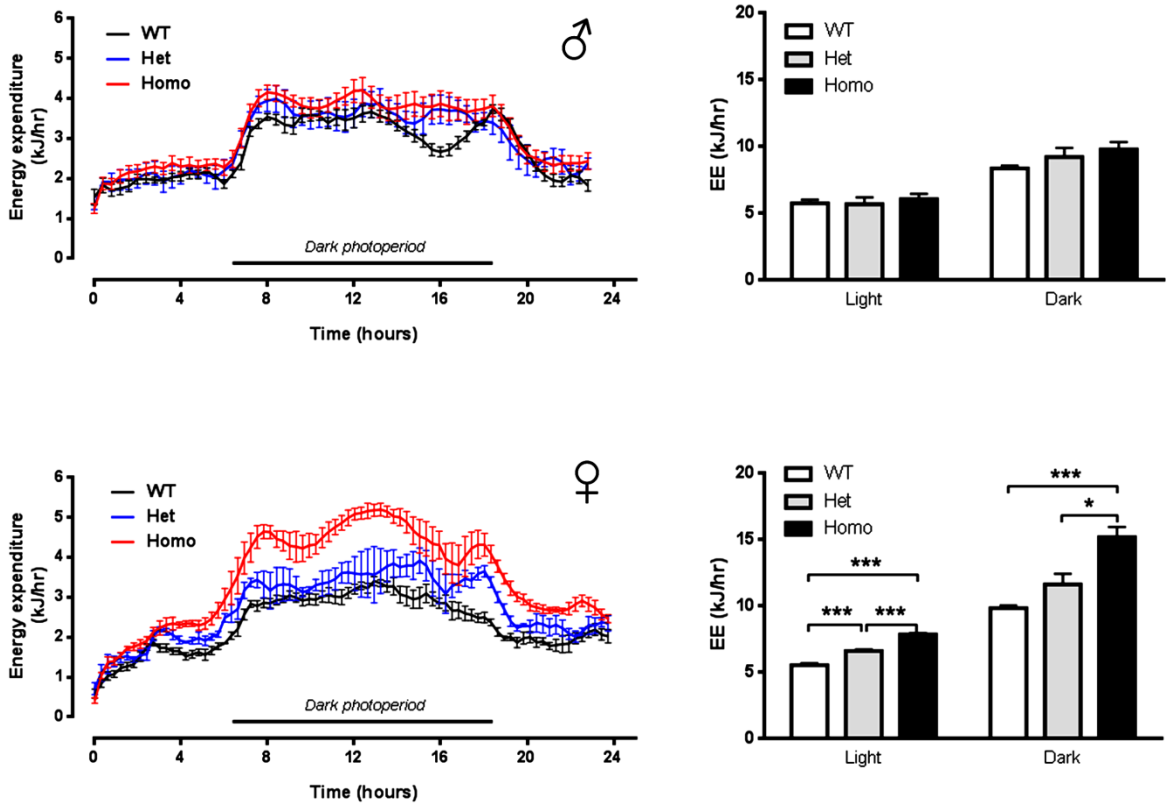


Figure 107. Energy expenditure over 24 hours determined by indirect calorimetry at room temperature in mice aged 6 weeks, expressed on a whole animal basis (N=4-8 cages of 3/genotype). ****P*<0.05, ******P*<0.001

Indirect calorimetry revealed no evidence for reduced EE in either male or female R299Q γ2 mutant mice. Indeed, in keeping with the greater spontaneous locomotor activity of female homozygous mutant mice, significant *increases* were identified in EE, most marked for the dark phase, with male homozygous mutant mice exhibiting a trend to increased EE (*P*=0.07).

6.4.7.b Thermic capacity and brown adipose tissue gene expression profile

One important aspect of EE in the rodent is adaptive thermogenesis – primarily mediated by the action of brown adipose tissue (BAT) – and which takes place in response to either altered environmental conditions or diet-induced thermogenesis. Brown adipose tissue is thought to play a major role in adaptive thermogenesis and possesses several features that make it uniquely well-placed to serve this function[280]: rich sympathetic innervation; a high degree of vascularisation; elevated mitochondrial density, with unique expression of the mitochondrial uncoupling protein 1 (UCP1) on the inner mitochondrial membrane, permitting uncoupling of oxidative phosphorylation from ATP synthesis to generate heat. Activation of β3-adrenoceptors located on BAT adipocyte membranes by norepinephrine, released from sympathetic nerve terminals, induces a rise in intracellular cAMP; this activates hormone sensitive lipase, stimulating lipolysis to provide free fatty acid thermogenic substrate for BAT mitochondria[281]. To determine whether the R299Q γ2 mutation affected thermic capacity, a β3-adrenoceptor-selective agonist (BRL 37344) was administered to young male mice (Figure 108). This did not identify a significant difference in capacity for stimulation of EE by this sympathomimetic compound.

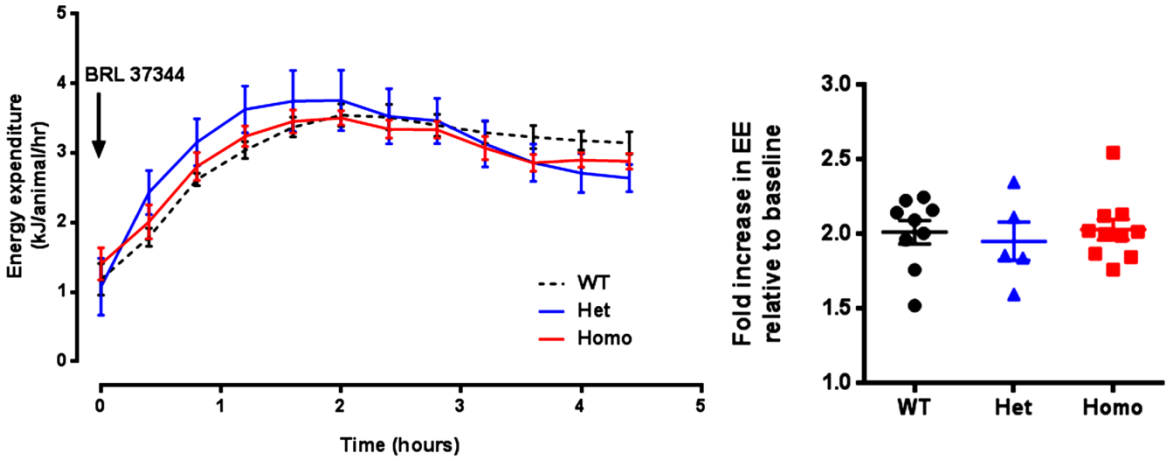


Figure 108. Acute thermogenic response to the β3-adrenoceptor-selective agonist BRL 37344 (0.25 mg/kg i.p.) in males at 6 weeks, expressed per mouse (N=5-10/genotype).

No significant differences were identified in interscapular brown adipose tissue mass of young mice, whether expressed as absolute values (Figure 109) or normalised to body weight, although there were visual trends to greater values in mutant genotypes. In support of the indirect

calorimetry data which suggested that altered EE was not a major contributor to the emerging obesity of R299Q γ2 KI mice, no differences were identified in the expression of key thermogenic genes[281] in the BAT of 6 week old mice (Figure 109). This included genes encoding: the β3-adrenoceptor (*Adrb3*); UCP1 (*Ucp1*); type II deiodinase responsible for conversion of thyroxine to bioactive triiodothyronine in BAT (*Dio2*); factors enhancing mitochondrial capacity such as PGC1α (*Ppargc1a*); and a transcriptional regulator of brown adipogenesis (*Prdm16*).

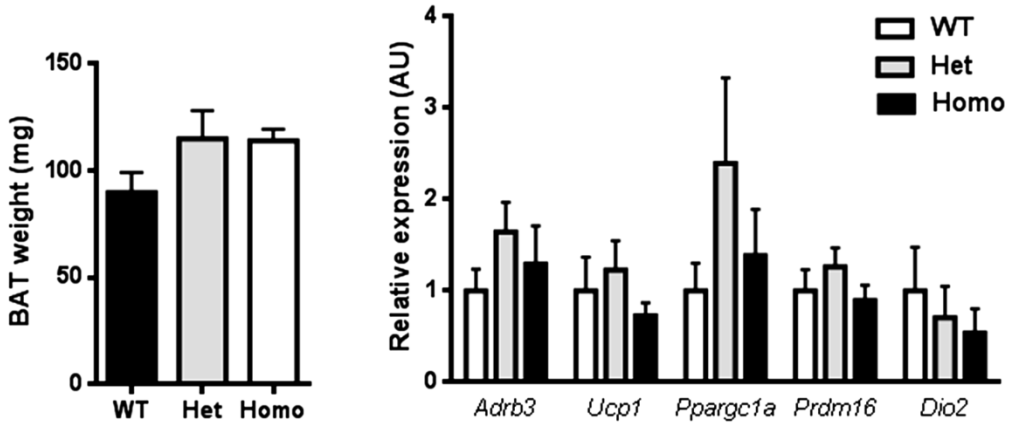


Figure 109. Left – Weight of interscapular brown adipose tissue from 8 week old male mice (N=8/genotype). Right – Thermogenic gene expression from interscapular brown adipose tissue of 6 week old male mice (N=5-6/genotype).

6.4.7.c Energy expenditure in older mice

EE was reassessed in older mice to see whether this might contribute to the obesity phenotype with time. Indirect calorimetry of mice at one year did not provide any evidence for reduced EE in mutant mice of either sex. Indeed, when the raw data was expressed on a whole animal basis (in line with recent recommendations[273]), this indicated trends to *increased* EE in mutant mice, with a significant increase identified in R299Q γ2 homozygote females compared to WT in the dark phase (Figure 110). Interpretation of these findings is complicated by the significant differences in size that emerge with age between genotypes, however, with body size *per se* known to exert a strong and independent effect on EE. Nevertheless, taking into account the effects of body composition on EE using an analysis of covariance (ANCOVA)[273] still did not identify any reduction in EE in mutant mice, with in fact visual trends suggesting *greater* adjusted EE in mutant genotypes (Figure

111).

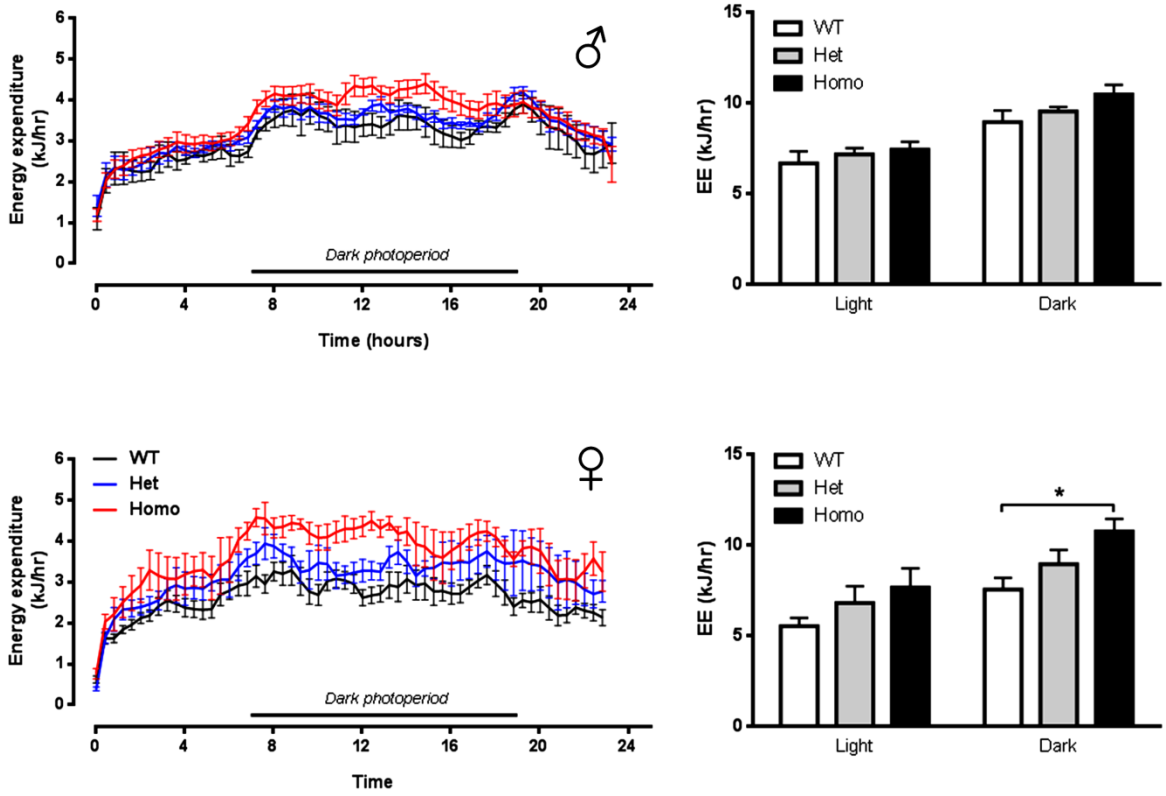


Figure 110. Energy expenditure over 24 hours determined by indirect calorimetry at room temperature in mice aged 1 year, expressed on a whole animal basis (N=3-4 cages of 3/genotype for females; N=4-10 cages of 3/genotype for males). *P<0.05

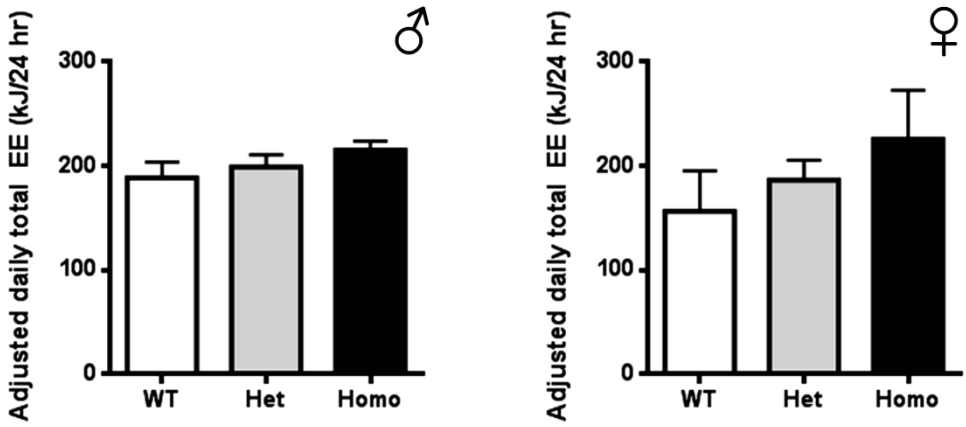


Figure 111. Adjusted daily energy expenditure (EE) at 1 year using ANCOVA with DEXA-determined lean body mass and fat mass as covariates, expressed as kJ/24 hours (N numbers as above).

6.5 Discussion

6.5.1 Summary of principal chapter findings

The experiments presented in this chapter have sought to characterise the systemic (i.e. extra-cardiac) phenotype of the R299Q γ2 KI. Initial phenotyping indicated a clear age-related onset of obesity. Accordingly, the assessment of underlying mechanisms (in both this and the subsequent chapter) was targeted to an 'early' time point (~7-8 weeks of age) when differences in body weight and composition were minimal and genotypes far more comparable. Descriptive phenotyping was undertaken at this time point and also at a 'late' time point when obesity was clearly established. Mechanistic-based investigation was not focused on this latter stage to avoid the confounding effect of metabolic alterations secondary to obesity obscuring primary changes due to the mutation[273].

The principal findings of the experiments presented in this chapter are:

i) R299Q γ2 mutant mice are larger and heavier than their WT counterparts, most marked for homozygotes of both sexes. Heterozygote males manifest a broadly intermediate phenotype of body weight gain, whilst heterozygote females tend on average to not exhibit any significant increase in weight over age-matched WT mice.

ii) Homozygous mutant mice of both sexes are clearly hyperphagic, including younger animals at a time point when body size is comparable to WT.

iii) R299Q γ2 mutant mice exhibit dynamic changes in body composition. At a young age, mutant mice display largely comparable fat mass to WT littermates, but with a clear signal for increased lean mass. With age, whilst the signal for greater lean mass continues in mutant mice, there is a marked accumulation of fat mass such that homozygotes exhibit ~2-fold greater total fat mass compared to WT at age 40 weeks.

iv) Histology identifies clear white adipocyte hypertrophy in mutant mice of both genotypes, most marked for homozygote mice. Changes occur in gene expression of white adipose tissue from older homozygous mutant mice consistent with a pro-inflammatory state.

v) In line with the evolving change in body composition, the plasma profile of adipokines alters with age. Young mutant mice have a largely normal adipocytokine profile. Notably, consistent with their reduced percentage fat mass, young homozygous mutant mice have hypoleptinaemia. Older mutant mice exhibit an adverse plasma profile, however, with homozygous mutant mice developing hypoadiponectinaemia, hyperleptinaemia, elevated tPAI-1 and an increase in IL-6 levels compared to age-matched WT.

vi) The R299Q γ2 mutation exerts complex effects on glucose homeostasis, with intact glucose tolerance in young mice, but impaired glucose tolerance in older mice and reduced glucose-stimulated insulin secretion (GSIS) at both time points. Pancreatic insulin content is preserved even in older mutant mice, whilst electrical glucose sensing is comparable across genotypes in younger mice, suggestive of a potential primary defect in islet insulin secretion as the cause of impaired GSIS. Consistent with their obesity, older mutant mice have impaired whole-body sensitivity to insulin.

vii) Intriguingly, young mutant mice are spontaneously more active than their WT counterparts and show enhanced voluntary exercise capacity, in terms of distance, speed and duration of running. Gene expression changes in favour of modest increases in skeletal muscle oxidative capacity in mutant mice did not reach significance with the cohort size examined.

viii) No clear evidence was identified to support a reduction in EE as a major contributor to the emergent obesity phenotype of mutant mice. Indeed, the available data are in keeping with an increase in EE, at least in part accounted for by their increased (and highly metabolically active) lean mass levels, but also likely to reflect elevated locomotor activity levels. Furthermore, brown adipose tissue thermogenic gene profile, mass and response to stimulation by a sympathomimetic compound are comparable across genotypes, arguing against the mutation inducing a significant perturbation in adaptive thermogenesis.

Specific aspects of these findings are discussed further in the following sections.

6.5.2 Why investigate the systemic phenotype of the R299Q γ2 KI model?

Whilst the rationale for generating and comprehensively characterising a gene KO are relatively easy to define in terms of deciphering the physiological role of a gene, it is perhaps less immediately apparent why a mouse model of a rare mutation presenting predominately with a cardiomyopathy in humans should merit detailed systemic work-up. One potential argument is the compelling nature of the obesity phenotype, whereby the degree of alteration in body composition and size on a standard laboratory rodent diet rivals or even exceeds that of any other published model involving genetic modification of AMPK, many of which have either subtle metabolic abnormalities[266, 269, 282] or require a HFD challenge[268] to manifest a discernible phenotype.

An alternative argument is based on the putative predominate effect of the R299Q γ2 mutation *in vivo*, namely that of mild AMPK activation. Given the major threat to global public health posed by the ongoing obesity epidemic and the relatively poor efficacy and safety of current anti-obesity pharmacotherapy, the recognition of AMPK as an indirect target of antidiabetic therapy (including metformin and the thiazolidinediones), coupled with AMPK's ability to regulate multiple facets of lipid and glucose metabolism, have highlighted AMPK as an attractive drug target for treatment of obesity and diabetes. Whilst relatively short-term *in vivo* administration of AMPK activators is associated with beneficial metabolic effects in experimental obesity models[283-285], the chronic sequelae of these drugs remain unexplored. Interpreted in this light, the R299Q γ2 KI model, likely functioning to induce a subtle but life-long increase in basal (γ2-containing) AMPK complex activity, can be considered the first tractable model wherewith to better elucidate the effects of chronic pharmacological AMPK activation *in vivo*.

6.5.3 The complex systemic phenotype of the R299Q γ2 KI

The consequences of gene-targeting exon 7 of *Prkag2* with the R299Q mutation in the mouse are seen to extend well beyond the cardiovascular system. In keeping with AMPK's myriad metabolic effects, the systemic phenotype of the R299Q γ2 KI is complex, reflecting the dynamic interplay of multiple organs and energy homeostatic mechanisms.

6.5.3.a Early phenotype

The data presented in this chapter are consistent with the view that the *initial* consequences of the R299Q γ2 mutation are largely metabolically beneficial. Thus, young mutant mice exhibit increases in lean muscle mass, greater spontaneous activity and reduced plasma leptin and fasting insulin levels. In addition to the increase in spontaneous activity, mutant mice display a strikingly enhanced exercise capacity, both in terms of endurance and speed, with mean total distances run of 324, 443 and 543 km over 30 days in young age-matched WT, heterozygote and homozygote female mice, respectively. Whilst WT mice were seen to markedly increase their running distance over the initial week – suggestive of the development of adaptive responses to enhance running performance – this feature was not apparent in mutant mice, as they already exhibited 'maximal' levels of endurance from the start of the experiment. One caveat to this interpretation is the use of a voluntary paradigm which, whilst enabling assessment of exercise capacity in a stress-free setting within the normal diurnal pattern of mouse behaviour, does not (unlike forced exercise paradigms) readily permit dissociation of pure physical capacity from volitional behavioural influences. Although not definitively verified with the group sizes assessed, it is likely that the mutation induces a remodelling of the skeletal muscle transcriptome towards a pro-endurance phenotype which, whilst subtle on an individual gene level, acts in a coordinated fashion across the level of gene networks to effect greater exercise performance. Notable in this regard is the finding that 4 weeks administration of AICAR to sedentary mice increases their maximal exercise capacity and induces genes linked to oxidative metabolism [286].

Regular handling of mice readily indicated that homozygous mutant mice were, on average, not just heavier than their WT counterparts, but also more muscular, particularly evident for older homozygote males. This increased lean mass in young homozygous mutant mice may contribute both to their enhanced exercise capacity and their insulin response to a glucose load, by improving insulin sensitivity at the whole-body level. The aetiology of the increase in lean mass is unclear and was not formally investigated, but is likely to reflect, at least in part, the contribution of hyperphagia and increased nutrient availability to muscle growth. Notable in this regard are

observations in neonatal pigs identifying both peripheral and visceral tissue protein synthesis to be far more responsive during early development, driven in part by higher ribosomal content and greater translation efficiency, leading to a profound stimulation of protein synthesis with feeding[287].

Thus, hyperphagia in homozygous mutant mice may act to fuel increased somatic growth during the growth phase by maximising availability of nutrients such as glucose and amino acids. This would serve to stimulate multiple intracellular pathways to promote protein synthesis, including growth factor signalling (e.g. insulin/PI3K/AKT pathway) and enhanced signalling of the mammalian target of rapamycin (mTOR) – a highly conserved serine-threonine kinase that plays a critical role in the regulation of protein synthesis and cellular growth as part of a mammalian TOR complex 1 (mTORC1) – both in response to the positive upstream action of PI3K-AKT activation and greater amino acid availability[288]. The net effect of this may well serve to outweigh the direct inhibitory effects of AMPK activation on protein synthesis[289] which are mediated via AMPK's phosphorylation of TSC2, acting to repress the activity of Rheb (a downstream small G protein activator of TORC1), as well as direct AMPK-mediated phosphorylation of raptor (a key mTORC1 binding subunit) leading to inhibition of mTORC1.

6.5.3.b Late phenotype

With age, R299Q γ2 homozygous mutant mice (and to a less marked and more variable extent the heterozygotes) develop obesity, with marked increases in body weight primarily due to an increase in fat mass, but also a significant ongoing contribution from lean mass. Mutant mice display several adverse metabolic features largely compatible with their obese state, including hyperleptinaemia, hypoadiponectinaemia, evidence of systemic and WAT inflammation and impaired glucose tolerance. The latter finding is noteworthy in being associated with *reduced* fasting and post-glucose load insulin levels in homozygous mutant male compared to WT male mice, contrasting with the hyperinsulinaemia typical of the metabolic syndrome and common polygenic obesity in humans. Whilst any beneficial effects on glucose tolerance and insulin sensitivity induced by increased muscle mass and AMPK activation within skeletal muscle are likely to persist to some degree in older mutant animals, these may be outweighed by the

consequences of the R299Q γ2 mutation in the pancreas. Homozygous mutant mice were seen to exhibit inappropriately low insulin secretion in response to a glucose load. In young mice this effect was likely outweighed by greater insulin sensitivity peripherally, but in older mice this was associated with frank glucose intolerance. The observation that both pancreatic insulin content and islet electrical glucose sensing were normal suggests that impaired pancreatic insulin secretion may be the underlying cause. Indeed, studies[252] using isolated primary rat islets and clonal MIN6 β cells have found both pharmacological (using AICAR) and genetic (with adenoviral-mediated overexpression of constitutively active α1 AMPK) activation of AMPK to inhibit GSIS, likely through both transcriptional means (e.g. inhibition of activity of the preproinsulin gene promoter[252]) and direct inhibitory effects on distal secretory steps (e.g. vesicle dynamics[290]). Together with the data outlined in this chapter, these findings highlight the (largely overlooked) potential negative effects of activating AMPK within the pancreas, a potential significant limitation in the development of novel specific AMPK activators to treat diabetes and the metabolic syndrome.

The obesity phenotype of older R299Q γ2 mutant mice is notable for its combination of increased linear growth, lean mass and fat mass. Together, these features are seen in some (e.g. obese yellow or agouti syndrome mice[291] and melanocortin-4 receptor KO mice[49]) but not all (e.g. the leptin-deficient *ob/ob* mouse) rodent models of obesity and in humans with altered melanocortin-4 receptor function. The mechanisms underlying increased somatic growth in these models are poorly understood, but elevated plasma IGF-1 levels and direct or indirect effects on bone (e.g. altered osteoclast-mediated bone resorption) have been invoked[291].

Ultimately, the effects of chronic caloric surfeit consequent upon increased food intake in excess of energy expenditure serve to outweigh any beneficial effects of the R299Q γ2 mutation in the periphery (e.g. on skeletal muscle) and result in frank obesity with attendant adverse metabolic changes. The latter include an abnormal *in vivo* whole-body response to insulin in keeping with reduced insulin sensitivity and pro-inflammatory changes in plasma and WAT. They serve to highlight the complexity of AMPK activation on a whole-body level, with a multitude of

competing effects in different organs. This scenario is likely to be even more complex in heterozygous mutant mice, where the presence of a single normal allele may be sufficient to compensate for the negative effects of the mutation in some organs, but not others, potentially providing an explanation as to why their phenotype is not seen to be strictly intermediate for many of the parameters assessed. The findings from older R299Q γ2 mutant mice suggest that the effects of central AMPK activation on promoting food intake come to dominate any beneficial effects of AMPK activation in the periphery. Accordingly, the next chapter investigates the central consequences of the R299Q γ2 mutation in greater detail.

Chapter 7. The systemic phenotype of the R299Q γ2 KI: central mechanisms

7.1 Aims and objectives

Initial systemic phenotyping had identified clear adult-onset progressive obesity in R299Q γ2 homozygous mutant mice. Given the identification of preserved or even increased energy expenditure (EE) and spontaneous activity, hyperphagia appeared to be the main driver behind weight gain and it is this factor which is probed in more detail in this chapter. This was focused on potential hypothalamic signalling pathways responsible for hyperphagia of mutant mice at an early, pre-obese time point to minimise confounding effects associated with systemic obesity. The aims of the experiments presented here were to:

i) Determine the relative contribution of hyperphagia to weight gain by use of pair-feeding.

ii) Investigate orexigenic and anorexigenic neuropeptide expression in the hypothalamus.

iii) Ascertain whether γ2 is expressed in the normal murine hypothalamus.

iv) Determine whether perturbations in leptin or melanocortinergic signalling underpin the phenotype by assessing food intake responses to leptin and a melanocortinergic agonist.

v) Investigate the response of R299Q γ2 mutant and WT mice to fast-refeeding.

vi) Explore whether mutant mice exhibit an exaggerated feeding response to exogenous ghrelin.

vii) Investigate hypothalamic signalling pathways downstream of ghrelin receptor activation, both at baseline and in response to exogenous ghrelin administration.

viii) Attempt to rescue the mutant hyperphagic phenotype with antagonism of a putative key pathway predicated on mechanistic insights obtained in (iv), (vi) and (vii).

To place these experiments into context, a discussion of the regulation of food intake (FI) by the hypothalamus, with a particular focus on the role of AMPK, follows next.

7.2 The hypothalamus and the regulation of appetite

7.2.1 Overview of hypothalamic regulation of appetite

The hypothalamus is located beneath the thalamus and above the pituitary and is found in all mammals[292]. Structurally, it is organised into anatomically-defined neuronal clusters (Figure 112) – termed nuclei – which interconnect via projected axons, including the: ventromedial (VMH), dorsomedial (DMH), paraventricular (PVH) and arcuate (ARC) nuclei, and the lateral hypothalamic area (LHA)[293].

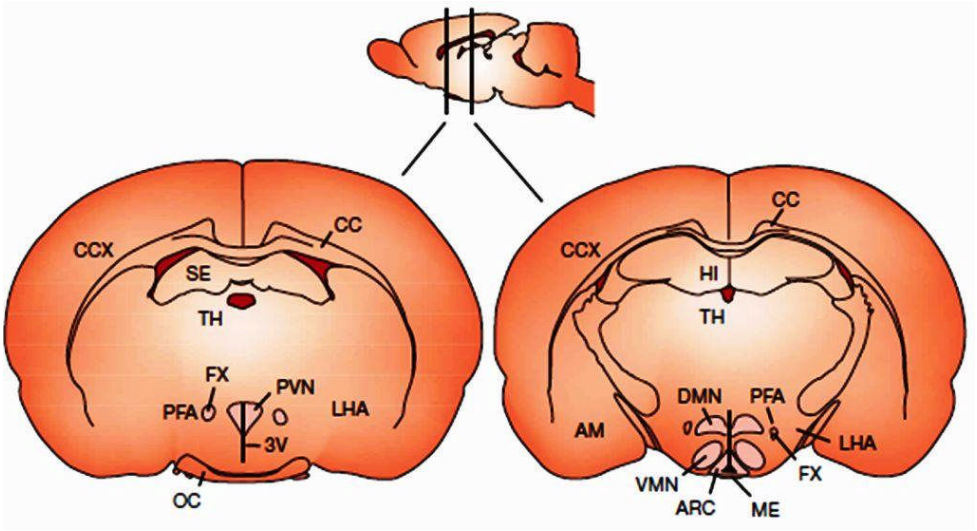


Figure 112. Anatomical distribution of major hypothalamic nuclei implicated in energy homeostasis in the rat brain. Additional abbreviations: CCX, cerebral cortex; CC, corpus callosum; SE, septum; TH, thalamus; FX, fornix; PFA, perifornical area; 3V, third ventricle; OC, optic chiasm; HI, hippocampus; AM, amygdala; ME, median eminence.[uu]

The hypothalamus definitively emerged as an appetite and body weight regulatory centre in 1940 when large, bilateral electrolytic lesions of the hypothalamus applied stereotaxically were noted to induce obesity in rats[294]. Subsequent studies refined this by identifying regions within the hypothalamus where targeted bilateral lesions would induce either hyperphagia with attendant obesity (VMH), or anorexia and weight loss (lateral hypothalamus)[294]. These findings led to the early 'dual centre model' for the regulation of feeding in mammals, with the concept of the existence of a hypothalamic 'feeding' and 'satiety centre'[294]. Whilst implicating discrete

[uu] Reproduced from figure 3 Schwartz et al., *Nature* 2000;404:661-671.

hypothalamic regions in the modulation of food intake (FI), it was clear that these regions could not function effectively as energy homeostatic centres without some means of receiving and responding to the energy needs of the organism.

In 1953, Kennedy proposed an 'adiposity negative feedback' model for mammalian energy homeostasis. This hypothesised that peripheral circulating signals feedback the status of the body's fat reserves to areas of the brain implicated in energy homeostasis; these then, in turn, adjusted energy balance over time to stabilise body adiposity[295]. Crucial support for this concept of long-term endocrine regulation of fat mass emerged in 1994, when Jeffrey Friedman's group identified the mouse obese gene (*ob*) as the locus affected by recessive mutations causing a well-recognised monogenic severe obesity syndrome in mice (termed *ob/ob*)[296, 297]. *Ob* encodes for a 167 amino acid protein expressed in and secreted by white adipocytes in proportion to body adiposity and functioning as an afferent signal to modulate FI and body weight[298]. Mutations in the gene encoding the long leptin receptor isoform (*Lepr*) were subsequently identified as responsible for a similar phenotype of hyperphagia, obesity and severe insulin resistance in *db/db* mice and Zucker *fa/fa* rats[299]. LEPR was found to be expressed in multiple hypothalamic nuclei known to be involved in appetite regulation – including the ARC, VMH, DMH and LHA – affirming a fundamental role for the hypothalamus as a recipient of afferent feedback signals of nutritional status from the periphery[300]. Furthermore, the discovery of leptin invoked a paradigm shift in the scientific community's perception of white adipose tissue: extending its role beyond that of passive depot for excess energy stores, to an active endocrine organ and integral component of the body's energy homeostatic mechanism (Figure 113).

It is now recognised that the regulation of appetite is highly complex, with hypothalamic nuclei forming part of a much wider interconnected neural circuitry that acts to influence FI, including regions of the hindbrain that receive gastrointestinal satiety inputs from vagal afferent fibres (e.g. the nucleus tractus solitarius, NTS) and brain regions involved in food reward (e.g. ventral tegmental area, and nucleus accumbens)[295]. Within this network, core neural circuits residing in the hypothalamus play a fundamental role in integrating peripheral hormonal and nutrient signals,

which feedback information on the nutritional and metabolic status of the body, to appropriately influence feeding behaviour, energy expenditure and metabolic activity[300].

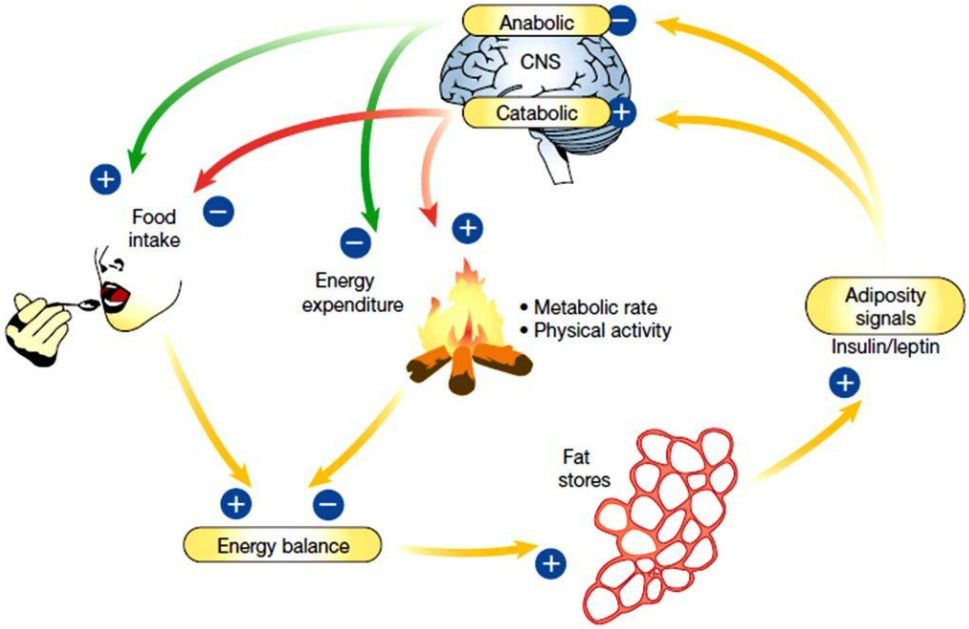


Figure 113. The lipostat model for the regulation of energy balance and adiposity.

Via a negative feedback loop, the release of afferent hormones – leptin and insulin – in proportion to fat mass acts centrally to inhibit anabolic and promote catabolic downstream effector pathways.[vv]

7.2.2 The arcuate nucleus – a primary locus for hypothalamic integration of peripheral metabolic signals influencing appetite

A key area of convergence of central and peripheral metabolic signals is the arcuate nucleus of the hypothalamus (ARC), now regarded as a primary centre for FI control. Anatomically, the ARC lies below the VMH on either side of the third ventricle. Through its position immediately adjacent to fenestrated capillaries in the median eminence – a site where the blood-brain barrier is semi-permeable – the ARC is uniquely positioned to sense alterations in circulating hormonal and nutrient feedback signals[293]. Within the ARC reside two anatomically intermingled populations of what are conventionally regarded as first-order neurons[293] (Figure 114). Both of these actively receive, coordinate and transduce peripheral satiety (e.g. leptin and insulin) and feeding cues (e.g. ghrelin) to second order neurons in other appetite-regulating nuclei (including the DMH, LHA,

[vv] Reproduced from figure 1 Schwartz et al., *Nature* 2000;404:661-671.

PVH and VMH), with the net effect of stimulating directionally opposing effects on appetite behaviour[301]. These key appetite-regulating neuronal populations are: i) NPY/AgRP neurons co-expressing the potent orexigenic (FI promoting) neuropeptides neuropeptide Y (NPY) and agouti-related peptide (AgRP); and ii) POMC (proopiomelanocortin) neurons expressing the anorexigenic (FI inhibiting) processing products of POMC, namely α-melanocyte-stimulating hormone (α-MSH) and the cocaine- and amphetamine-regulated transcript (CART)[300].

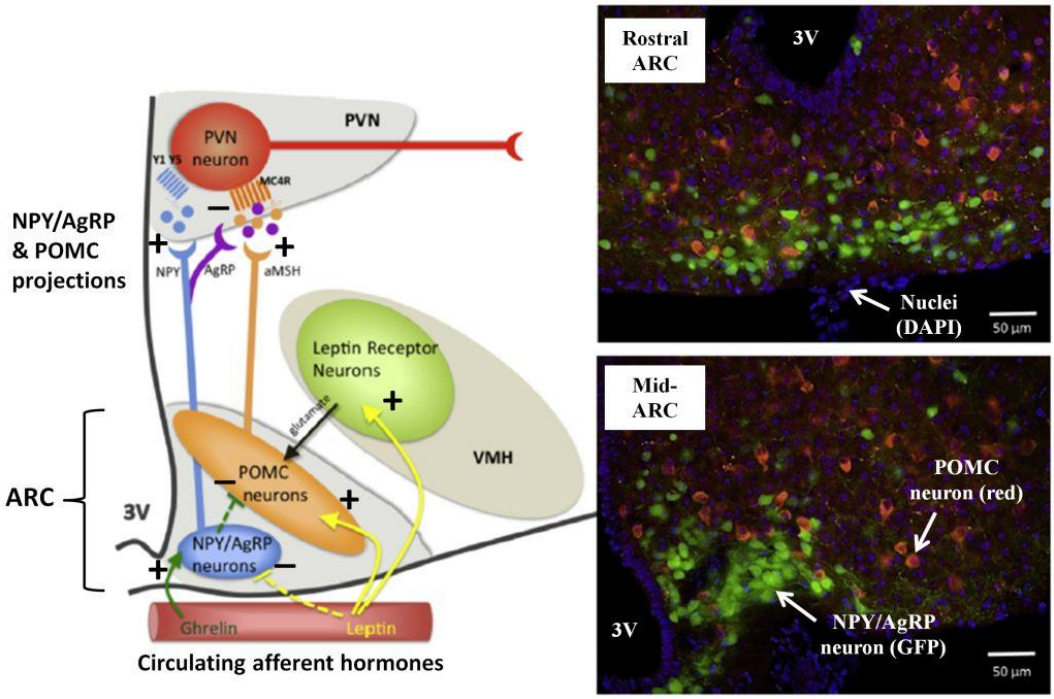


Figure 114. Core hypothalamic circuitry regulating food intake.

Schematic demonstrating key hormonal inputs to ARC NPY/AgRP and POMC neurons (left) and sections through the ARC showing close anatomical relationship between these two neuronal subpopulations (right top and bottom).[ww]

7.2.3 Neuropeptide Y (NPY) and its regulation by leptin and ghrelin

NPY – a 36 amino acid peptide synthesized by both central and peripheral neurons – is the most powerful orexigenic stimulant known, with acute central administration inducing robust FI across multiple species (even when satiated) and chronic administration resulting in obesity[302]. In the central nervous system, NPY localises most strongly to the hypothalamus – and within this to the ARC and DMH – but it is also widely expressed in other brain areas as well as in sympathetic

[ww] Adapted from figure 1 Stark et al., *Mol Cell Endocrinol* 2012 Jul 9 {Epub ahead of print].

nerves of the peripheral nervous system, suggesting a role beyond appetite control. NPY's orexigenic effects are thought to be principally mediated through the action of Y_1 and Y_5 receptor isoforms[292]. Elevated ARC NPY expression has been noted in association with (physiological) states of negative energy balance such as acute fasting and long-term caloric restriction, as well as in several animal models of obesity, including obese (*ob/ob*) and diabetic (*db/db*) mice[292]. Accordingly, the firing rate of ARC NPY/AgRP neurons is increased in hypothalamic brain slices from food-deprived mice[303].

Leptin has been implicated as an important negative regulator of hypothalamic NPY expression. NPY and leptin receptors are co-expressed in approximately 50% of ARC NPY/AgRP neurons[302]. Leptin administration results in a downregulation of ARC NPY gene expression as well as hyperpolarising NPY/AgRP neurons to inhibit their signal activity[292]. Further evidence for the close interplay between NPY and leptin comes from the partial rescue of the hyperphagia and extreme obesity phenotype of the leptin-deficient *ob/ob* mouse upon crossing with mice genetically deficient in NPY[302]. In invertebrates such as the fruitfly *Drosophila melanogaster* (which lacks leptin)[297], insulin plays a key role as a negative feedback signal of energy surfeit and body fuel stores[304]. In keeping with this ancestral role, in mammals there is overlap in the hypothalamic signal transduction pathways downstream of leptin or insulin binding, notably activation of the IRS-PI(3)K (insulin receptor substrate-phosphatidylinositol-3-OH kinase) pathway[295]. Thus, insulin is also a negative regulator of NPY/AgRP neurons, sharing leptin's ability to hyperpolarise and inactivate ARC NPY/AgRP neurons, leading to a reduction in FI[292]. Overall, however, leptin is thought to play a more critical role in the maintenance of energy homeostasis. In support of this, diabetic hyperphagia occurring in the context of severe, uncontrolled insulin deficiency – and associated with low leptin, reduced body adiposity and elevated hypothalamic NPY synthesis and release – is corrected by selective replenishment of leptin alone[305].

In contrast to the anorexigenic hormones leptin and insulin – which act as physiological inhibitors of NPY/AgRP neurons – the orexigenic hormone ghrelin conveys a signal of negative energy balance to the ARC through its activation of NPY/AgRP neurons. Ghrelin is a 28 amino acid

peptide originally isolated from rat stomach and identified as the endogenous ligand for a previously orphan growth hormone secretagogue receptor (GHSR), stimulating growth hormone release from the pituitary[306]. The stomach is the main source of circulating ghrelin, although it is expressed widely[307]. Ghrelin levels rise before a meal and are suppressed post-prandially, suggesting that it may have a role in meal initiation as a 'hunger hormone'[299, 307]. In keeping with this, the active ghrelin receptor (GHSR-1a) is expressed throughout the hypothalamus and is co-expressed with leptin receptors on NPY/AgRP neurons[300], with approximately 90% of ARC NPY/AgRP neurons expressing GHSR-1a [293].

Central administration of ghrelin potently stimulates feeding after a single dose. This effect is associated with c-*fos* immunoreactivity in ARC NPY/AgRP neurons and an increase in hypothalamic NPY and AgRP mRNA expression[308, 309]. Blockade of NPY (with pre-administration of anti-NPY IgG or dual Y1/Y5 receptor blockade) abolishes ghrelin's acute orexigenic effect[308]. Similarly, antagonism of AgRP's action by use of either α-melanocyte stimulating hormone (α-MSH) or anti-AgRP IgG, suppresses ghrelin-induced feeding[308]. Chronic peripheral administration of ghrelin promotes carbohydrate over fat utilisation and leads to increased adiposity[310]. In keeping with their opposing actions on appetite, ghrelin has been shown to activate specific ARC NPY/AgRP conditional pacemaker neurons to induce their burst firing – a recognised effective stimulus for neuropeptide release – whilst leptin suppresses pacemaker activity[311].

7.2.4 Agouti-related peptide (AgRP) and the melanocortinergic system

AgRP is a highly potent orexigenic neuropeptide which – unlike NPY – is synthesized in the brain exclusively in ARC neurons where it is co-expressed with NPY[302]. The 132-amino acid AgRP shares significant sequence homology with the 131-amino acid, agouti protein[312]. Agouti is normally expressed exclusively in hair follicular epithelial cells, where it acts in paracrine fashion on follicular melanocytes to regulate melanin expression. By antagonising the action of α-MSH on melanocortin-1 receptors (MC1-R), agouti promotes a switch from eumelanin (brown-black) to phaeomelanin (yellow-red), giving rise to the agouti coat colour[291, 302, 313]. Dominant alleles of the *agouti* locus have been recognised to give rise to a severe obesity syndrome in mice known as the

obese yellow or agouti syndrome, the best characterized allele being the *agouti lethal yellow* (A^y) mutant (the homozygous mutation being embryonic lethal)[291]. In addition to maturity-onset obesity, heterozygous A^y mice exhibit hyperphagia, hyperinsulinaemia, hyperglycaemia, hyperleptinaemia, hypometabolism, increased linear growth and yellow fur[291, 314]. The syndrome results from widespread ectopic overexpression of agouti protein due to spontaneous chromosomal deletions that place the *agouti* gene under the regulation of nearby constitutively expressed promoters[314]. The hyperphagia of these mice is thought to be mediated by inhibition of hypothalamic melanocortinergic receptors caused by aberrant expression of agouti protein. In support of this, agouti has been found to be a high affinity antagonist of both MC1 and MC4 receptors (MC4-R) *in vitro*. Whilst MC1-R is expressed in skin and hair melanocytes, MC4-R is principally expressed throughout the brain, including the PVH, VMH, DMH and LHA nuclei[313]. Targeted disruption of the *Mc4r* gene recapitulates much of the phenotype of A^y mutant mice[313]. Mutations at the *MC4R* locus in humans have also been identified in association with morbid obesity[315].

The endogenous agonists for the MC receptors are the melanocortins, a group of peptides cleaved from the polypeptide precursor molecule POMC. In the brain, POMC is near-exclusively expressed in the ARC and the NTS of the brainstem. POMC is cleaved by prohormone convertases to yield a number of peptides, including α-, β- and γ-MSH, adrenocorticotrophic hormone and the endogenous opioid β-endorphin[302]. α-MSH is the principle ligand and agonist for the MC4-R, promoting satiety and reducing FI. In keeping with this, direct interference with POMC – via POMC genetic deletion or neuron ablation – induces dramatic hyperphagia[316]. The action of POMC-derived α-MSH at the MC4-R is directly antagonised by AgRP. Thus, AgRP functions as the endogenous counter-regulator of the melanocortinergic system (Figure 115) [303]. In common with NPY, AgRP expression is upregulated in response to fasting and states of genetic leptin deficiency[302] and its central administration potently increases FI, although over a much longer time course than NPY (days rather than hours)[302].

The melanocortinergic system is thought to play a key role in mediating the central anorexigenic and energy-expenditure promoting effects of leptin. Both leptin's receptor and key components of

its downstream signalling cascade, including pSTAT3 (phosphorylated signal transducer and activator of transcription 3) and SOCS-3 (suppressor of cytokine signalling 3), are expressed in ARC POMC neurons[291]. Leptin promotes POMC neuronal signalling by increasing POMC synthesis, as well as depolarisation and activation of POMC neuronal firing[317]. Furthermore, leptin dynamically regulates excitatory synaptic projections onto ARC POMC neurons from the VMH in response to feeding[318].

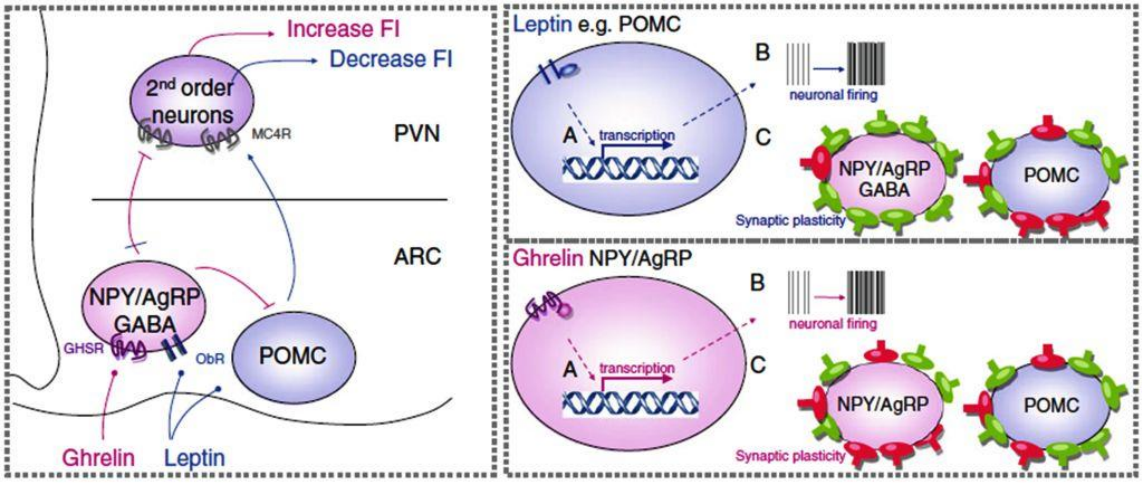


Figure 115. The interplay between ARC NPY/AgRP-POMC melanocortin neural circuitry and circulating afferent hormonal signals.[xx]

Both leptin and ghrelin reciprocally modulate feeding behaviour through a combination of altered: gene transcription, neuronal firing frequency and neuronal connectivity by modulating synaptic plasticity (with green and red boutons denoting inhibitory and excitatory input, respectively)[300, 309]. Note that NPY/AgRP neurons project inhibitory connections to POMC neurons, allowing ghrelin-mediated activation of orexigenic NPY/AgRP neurons to be complemented by a reduction in POMC neuronal activity via NPY/AgRP synaptic release of the inhibitory neurotransmitter γ-aminobutyric acid (GABA)[295, 319].

Underlining the pivotal role of the melanocortinergic system, POMC-null mice develop hyperphagia and severe obesity – partially rescued by peripheral administration of α-MSH – in addition to altered pigmentation and defective adrenal function and development[320]. Delineation of the physiological importance of orexigenic signalling to appetite regulation and maintenance of body weight has been less straightforward, however. Mice deficient in AgRP, or AgRP and NPY, through gene-targeted disruption of the endogenous locus, both exhibit surprisingly normal feeding

[xx] Reproduced from figure 2 Shan & Yeo, *Rev Endocr Metab Disord* 2011;12:197-209.

behaviour, body weight and response to fasting[312]. Using a different approach, selective ablation of NPY/AgRP *neurons* – by targeting the human diphtheria toxin receptor to the *AgRP* locus in mice (which normally lack a diphtheria toxin receptor) coupled with injection of diphtheria toxin – causes rapid, life-threatening starvation in adulthood but not infancy[262]. Conversely, selective photostimulation of NPY/AgRP neurons to increase their electrical activity is sufficient to rapidly induce voracious feeding in mice[303]. Intriguingly, stimulation of NPY/AgRP neurons in A^y mice (which have blockade of their melanocortin receptor signalling due to constitutive ectopic agouti protein expression) still strongly evokes feeding, indicating that acute NPY/AgRP-evoked feeding behaviour is not dependent on inhibition of melanocortin receptors[303]. These studies serve to illustrate the compensatory plasticity of hypothalamic signalling pathways regulating FI and energy balance in early life, as well as underline the vital importance of the NPY/AgRP neuron (as opposed to solely their anabolic effector peptides) in mediating central orexigenic drive[263].

7.3 Hypothalamic AMPK - an integrator of peripheral hormonal and nutrient signals of energy status

AMPK has recently emerged as an integral component of the neuroendocrine feedback control of energy homeostasis in mammals[293]. Through linking afferent hormonal and nutrient signals of energy balance to coordinate activity in hypothalamic neural circuits critical to FI and energy expenditure, AMPK is able to regulate energy homeostasis at the level of the whole organism.

7.3.1 Modulation of hypothalamic AMPK activity affects food intake

AMPK is expressed in key hypothalamic nuclei, including the ARC, PVH, VMH and LHA[293]. In rats, central pharmacological activation of AMPK using AICAR – administered either via the intracerebroventricular (ICV) route or directly into the PVH – acutely increases FI[321]. Using a genetic approach, expression of constitutively active (CA, H150R mutation in γ1 subunit) AMPK in the medial hypothalamus (predominately affecting the ARC, VMH and DMH) using recombinant adenoviruses increases FI and body weight in normal mice[322]. Conversely, co-

expression of dominant negative (DN) α1 and α2 AMPK subunits in the medial hypothalamus results in anorexia and weight loss[322]. These changes in FI were associated with altered expression of key neuropeptides influencing FI: expression of DN-AMPK suppressed mRNA expression of the orexigenic neuropeptides *Npy* and *Agrp* in the ARC in *ad libitum* fed mice; in contrast, CA-AMPK expression enhanced the normal fasting-induced increase in these neuropeptides in the ARC[322, 323]. Interestingly, POMC expression was appropriately suppressed by fasting in CA-AMPK-treated mice and was downregulated in freely-fed DN-AMPK-expressing mice, the latter an appropriate physiological response to mice of lower body weight and leptin level[322]. Thus, genetic modulation of AMPK activity in the hypothalamus had clear effects on enhancing the central orexigenic signalling response to food deprivation, but did not alter the physiological response of POMC neurones to fasting.

7.3.2 Hypothalamic AMPK and the response to leptin

That hypothalamic AMPK is regulated under physiological circumstances is highlighted by the finding that its activity is modulated by feeding state: feeding represses hypothalamic AMPK activity whilst fasting increases it[322]. These feeding states are associated with altered glucose and insulin levels which may contribute to the changes in AMPK activity[249]. Accordingly, peripheral or ICV administration of glucose (the latter not inducing hyperglycaemia) results in suppression of α2 AMPK activity in all hypothalamic regions but not in cerebral cortex[322]. Similarly, ICV injection of insulin – a potent anorexigenic signal – also reduced α2 AMPK activity in the same anatomical pattern[322].

In contrast to its action in the periphery[324], administration of leptin by the intraperitoneal (i.p.)[321, 322] or medial intrahypothalamic[322] route inhibits AMPK activity, associated with reduced FI. This effect is seen to be restricted to α2-containing AMPK complexes in the ARC and PVH - hypothalamic regions traditionally regarded as first- and second-order neuronal components of the melanocortinergic circuitry regulated by leptin (Figure 115). The hyperphagia of mice with hypothalamic expression of CA-AMPK fails to respond to the usual inhibitory effect of leptin, although they manifest slightly enhanced (i.e. preserved) STAT3 phosphorylation[322]. In contrast,

the anorectic response to leptin is unaffected by expression of DN-AMPK[322]. These results have been interpreted to indicate that AMPK may function as an initial gatekeeper for the satiety-inducing effects of leptin[323]. Thus, significant activation of AMPK complexes in the ARC and PVH (indicating short-term energy deficit) would override anorexigenic signalling by leptin in an attempt to defend whole-body energy balance by driving FI. Conversely, loss of AMPK function – as modelled by DN-AMPK expression – does not impede leptin's ability to inhibit FI and lead to weight loss. Moreover, the effects of CA- or DN-AMPK on modulating acute responses to leptin are not explained by changes in phosphorylation of the transcription factor STAT3, leading to the suggestion that AMPK-related modulation of anorexigenic leptin effect operates in parallel to, or downstream of, STAT3-regulated gene transcription[322].

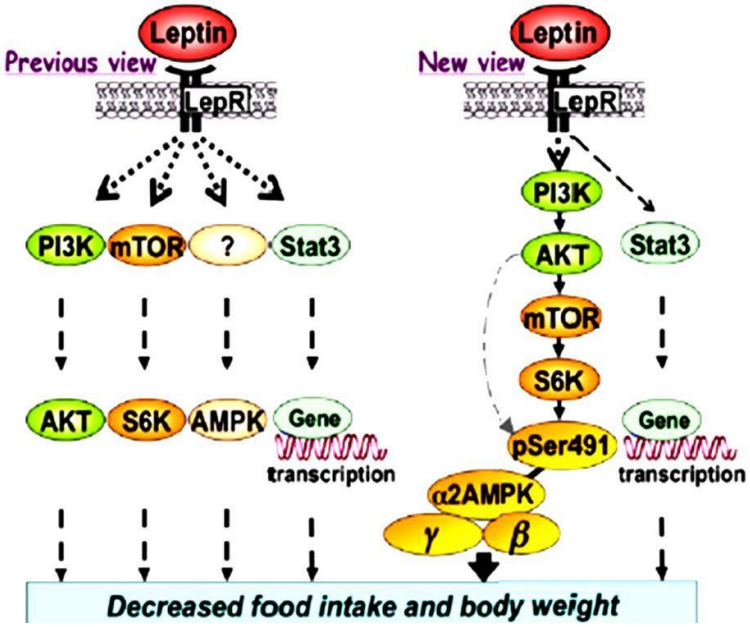


Figure 116. A recent model for the acute anorexigenic effects of leptin involving the unification of what were previously regarded as separate pathways (left) in a hypothalamic signalling cascade converging on phosphorylation of Ser491 of the α2-subunit of AMPK (right)[325].

Activation of this pathway leads to AMPK inhibition and reduced FI. The acute effects of PI(3)K-dependent inhibition of α2-AMPK are also likely to be complemented by the rapid PI(3)K-dependent depolarisation and activation of ARC POMC neurons in response to leptin[326].[yy]

[yy] Reproduced from figure 4 Dagon et al. *Cell Metab* 2012;16:104-112.

A recent study[325] has shed light on this by proposing a unifying mechanism for leptin-induced *acute* inhibition of FI (Figure 116): activation of LEPR acts, via a PI(3)K-AKT-mTOR-S6K phosphorylation cascade, to inhibit AMPK activity by phosphorylation of a key serine[491] residue on the α2-subunit, with *long-term* regulation of body weight by leptin more reliant on STAT3-mediated signalling.

7.3.3 Modulation of hypothalamic lipid metabolism by AMPK regulates feeding

In contrast to the effect of leptin, peripheral administration of ghrelin at a dose shown to stimulate FI increases hypothalamic AMPK activity and enhances phosphorylation of AMPK's downstream target, ACC[321, 327]. ACC catalyses the carboxylation of acetyl-CoA to malonyl-CoA. Malonyl-CoA is both a metabolic precursor in *de novo* fatty acid biosynthesis (important in lipogenic tissues such as liver) and a regulator of long-chain fatty acid oxidation through its potent allosteric inhibition of carnitine palmitoyltransferase 1 (CPT1), important in cardiac and skeletal muscle. CPT1 is a key enzyme involved in the transport of activated fatty acids (fatty acyl-CoA's) into the mitochondria for β-oxidation. ACC phosphorylation consequent upon AMPK activation is therefore expected to reduce malonyl-CoA levels, disinhibiting CPT1 and increasing fatty acid oxidation (Figure 117).

Hypothalamic malonyl-CoA is regulated physiologically, being markedly induced by feeding, whilst fasting reduces its levels[327, 328]. Ghrelin administration acutely reduces hypothalamic malonyl-CoA levels in association with increased CPT1 activity and feeding[327]. Given the marked pre-prandial rise in plasma ghrelin levels, activation of an AMPK-malonyl CoA-CPT1 axis may play a role in the acute triggering of FI after a fast[327]. Thus, the hypothalamic malonyl-CoA pool can be conceptualised as an important signal of nutrient abundance involved in the regulation of FI[328]. In further support of this, chronic reduction of malonyl-CoA levels in rat mediobasal hypothalamus by adenoviral-mediated overexpression of MCD (malonyl-CoA decarboxylase) – the enzyme which catalyses the decarboxylation of malonyl-CoA – results in marked hyperphagia and sustained weight gain[329].

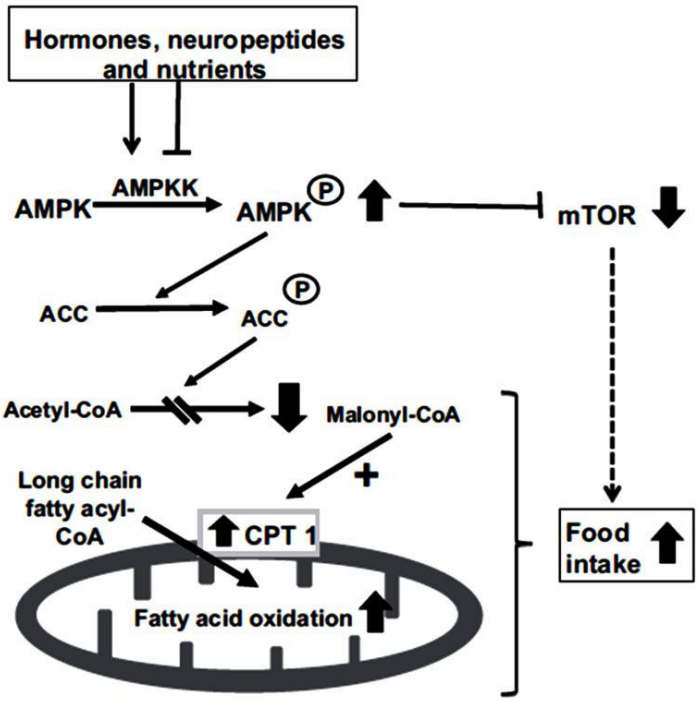


Figure 117. A model for the potential effects of altered AMPK activity on malonyl-CoA levels in the hypothalamus to regulate FI[323].

Note that AMPK activation also inhibits mTOR (mammalian target of rapamycin) signalling. mTOR is an evolutionarily conserved serine/threonine kinase that plays a central role in integrating nutrient and hormonal signals to regulate cellular growth with its anabolic actions perhaps best-recognised in skeletal muscle[330]. mTOR co-localises with both NPY-AgRP and POMC in the ARC. Fasting has been observed to downregulate mTOR activity, whilst both feeding and leptin promote its signalling[331]. Central stimulation of mTOR by the amino acid $_{L}$-leucine suppresses FI and, as with leptin's acute effect on FI, this effect is inhibited by the mTOR inhibitor, rapamycin[331].[zz]

7.3.4 Ghrelin stimulates appetite via a mechanism involving AMPK and UCP2

A recent study[229] has identified events downstream of ACC phosphorylation by AMPK as integral to the orexigenic action of ghrelin in NPY-AgRP neurons, implicating an AMPK-CPT1-UCP2-dependent mitochondrial mechanism. UCP2 (uncoupling protein 2) is a member of the UCP family of inner mitochondrial membrane proteins, the archetype of which is UCP1 found in brown adipose tissue (BAT) and responsible for regulation of non-shivering thermogenesis in the newborn and states of hibernation or cold-acclimatisation in mammals[332]. UCPs function to uncouple oxidative phosphorylation from ATP synthesis by permitting controlled leak of protons from the intermembrane space back into the mitochondrial matrix, serving to dissipate the proton motive

[zz] Reproduced from figure 3 Minokoshi et al. *Nutrition* 2008;24:786-790.

force that drives ATP synthase[332]. Whilst this functions to divert the energy derived from substrate oxidation to heat in BAT, it also serves an important role in reducing production of reactive oxygen species (ROS) – and thereby oxidative stress – by diminishing the mitochondrial membrane potential (MMP). Coupled mitochondria have a significant MMP established by the proton gradient across the inner mitochondrial membrane[332]. Elevated MMP is thought to enhance stochastic single electron transfer reactions between components of the electron transport chain and molecular oxygen. Consequently, chronic uncoupling can function as an anti-oxidant defence mechanism. Interestingly, UCP2 expression is itself induced by ROS[332], suggesting a protective positive feedback cycle to limit an excessive MMP, which would otherwise promote toxic levels of ROS. Whilst acute uncoupling reduces ATP production on a per-mitochondrion basis, chronic uncoupling promotes mitochondrial biogenesis and proliferation. In so doing, mild chronic uncoupling is thought to be beneficial through mitochondrial ROS suppression (limiting their generation to levels that can be controlled by endogenous antioxidant defence mechanisms), whilst not compromising ATP production[332]. Furthermore, by dissipating the MMP, UCP action can promote mitochondrial calcium release (through a potential-driven calcium uniporter) into the cytosol, thereby limiting potential mitochondrial calcium overload[332].

These mechanisms may play a particularly important role in energy–intensive neuronal synaptic transmission, such as occurs with the release of hypothalamic neuropeptides in response to orexigenic signals such as ghrelin. UCP2 is known to be richly expressed in hypothalamic nuclei integral to FI regulation – including the ARC, PVH, VMH and DMH nuclei – both in humans and rodents[332]. In response to ghrelin administration, activation of AMPK should increase CPT1 activity, enhancing long-chain fatty acid influx into mitochondria and promoting their oxidation. In accordance with this, Andrews and co-workers[229] have demonstrated that ghrelin stimulates palmitate-driven respiration in isolated hypothalamic mitochondria, as well as increasing basal uncoupling status after inhibition of ATP synthase with oligomycin. Both of these effects were seen to be absent in *Ucp2* null mice, indicating the effect of ghrelin on mitochondrial respiration and uncoupling to be UCP2-dependent. Following ghrelin treatment, an increase in mitochondrial number in NPY neuronal perikarya was identified, together with upregulation of nuclear

respiratory factor 1 (*Nrf1*) expression[229]. *Nrf1* encodes a transcription factor that acts on nuclear genes required for mitochondrial respiratory chain expression and function.

Increased fatty acid β-oxidation post-ghrelin stimulation is expected to generate more mitochondrial ROS as a by-product. Administration of ghrelin was observed to increase hypothalamic ROS both *in vitro* and *in situ* in NPY-AgRP neurons in *Ucp2* null but not WT mice, suggesting that UCP2 acts to buffer ROS levels[229]. i.p. ghrelin administration was also observed to increase hypothalamic *Ucp2*, *Cpt1* and *Npy* mRNA expression, an effect blocked by concurrent central inhibition of either AMPK (using compound C) or CPT1 (using etomoxir)[229]. Ghrelin-induced hyperphagia was markedly attenuated in *Ucp2* KO mice (although the anorectic response to leptin is preserved), whilst ICV injection of either compound C or etomoxir suppressed ghrelin-induced FI in WT mice.

Taken together, these findings suggest that ghrelin-induced hypothalamic fatty acid oxidation elicits a number of effects selectively in NPY-AgRP neurons, including: enhanced mitochondrial respiration and energy production from fatty acids following AMPK activation; elevated ROS buffering via UCP2 to manage increased ROS generation by fatty-acid oxidation; promotion of mitochondrial biogenesis and capacity, in part to compensate for the effects of UCP2-mediated uncoupling on ATP generation (Figure 118). In concert, these processes are likely to play a critical adaptive role in permitting sustained firing and release of orexigenic neuropeptides by NPY-AgRP neurons in states of negative energy balance to protect the mammal from starvation[319]. The absence of these processes in anorexigenic POMC neurons (the majority of which lack the GHSR) has been speculated to indicate their greater susceptibility to oxidative stress, highlighting an innate selective survival advantage of the hypothalamic orexigenic mechanism which may contribute to age-related onset of obesity[229].

A recent study[63] has identified the link between ghrelin binding to the GHSR and AMPK activation in the hypothalamic pathway leading to increased NPY expression, as involving the upstream AMPK kinase, CaMKK2 (CaMKKβ).

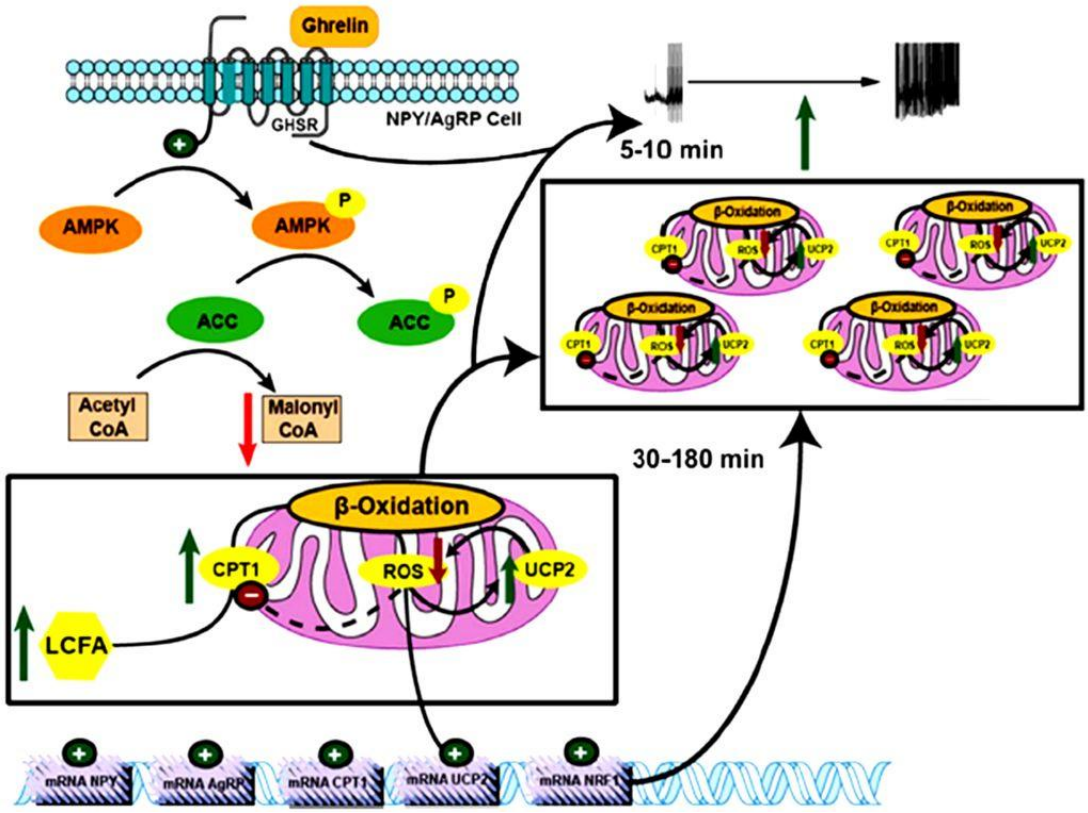


Figure 118. Schematic outline of the intracellular AMPK-ACC-CPT1-UCP2 pathway activated by ghrelin binding to the GHSR in NPY-AgRP neurons to promote FI.[aaa]

Ghrelin has been shown to increase intracellular calcium in isolated ARC NPY neurons[333]. The underlying mechanism for this is thought to involve ghrelin binding to the $G\alpha_q$-coupled GHSR, resulting in recruitment of phospholipase C to the cell membrane and the production of inositol-1,4,5-trisphosphate (IP3) by hydrolysis of membrane phosphatidylinositol 4,5-bisphosphate[293]. IP3 acts as a soluble second messenger, able to mobilise calcium from stores in the endoplasmic reticulum which interacts with calmodulin (CaM) to trigger activation of CaMKK2 [293].

CAMKK2 expression is observed to be 20-fold enriched in the ARC region of the hypothalamus, correlating with expression of both NPY-AgRP and POMC neurons[63]. CAMKK2 null mice exhibit lower baseline hypothalamic expression of *Npy* and *AgRP* mRNA, and fail to respond to the food-stimulatory effects of exogenous ghrelin[63]. That AMPK activation is still able to promote FI in these mice is supported by the finding that 2-deoxyglucose (which should bypass the GHSR and activate AMPK via an AMP/LKB1-dependent mechanism) still stimulated FI however[63]. These

[aaa] Reproduced from supplementary figure 9 Andrews et al. *Nature* 2008;454:846-851.

findings, suggesting the importance of CAMKK2 in regulating AMPK activity in NPY-AgRP neurons, were supported by *in vivo* experiments using the CAMKK inhibitor, STO-609 [334]. Central administration of STO-609 reduced FI in WT mice with ensuing weight loss and was associated with a reduction in hypothalamic *Npy* and *Agrp* expression. CAMKK2 null mice were also seen to be protected against high-fat diet-induced obesity and associated glucose intolerance[63].

7.3.5 AMPK-dependent regulation of synaptic plasticity onto AgRP neurons

Whilst much attention has been focused on the role of AMPK in the ARC NPY-AgRP neuron in the response to ghrelin and fasting, a recent study[64] has highlighted a novel mechanism for the regulation of FI involving pre-synaptic AMPK. Traditionally, the NPY-AgRP neurons in the ARC have been regarded as first-order neurons in ARC neurocircuitry, acting as the initial responders sensing peripheral hormonal signals of overall metabolic status, such as ghrelin and leptin[335]. Patch-clamp recordings of acute ARC hypothalamic slice preparations had clearly identified the ability of these hormones to regulate synaptic plasticity of inputs to POMC and NPY neurons[318]. Thus, leptin-deficient *ob/ob* mice have been observed to exhibit an increase in excitatory inputs (known as excitatory post-synaptic currents, EPSCs) to NPY-AgRP orexigenic neurons, whilst displaying a reduction in inhibitory synaptic inputs to the anorexigenic POMC neurons[318]. These electrophysiological changes favouring hyperphagia were accompanied by corresponding ultrastructural evidence of altered excitatory and inhibitory synaptic density onto NPY-AgRP and POMC neurons. Strikingly, leptin administration to *ob/ob* mice induced rapid rewiring of these circuits (within 6 hours) to reverse the changes in synaptic number and synaptic activity prior to inducing behavioural change[318]. Ghrelin was seen to modulate synaptic input density in a direction opposite to that of leptin[318], consistent with fundamentally opposing functional roles for these two hormones in the regulation of mammalian appetite[336].

Using miniature EPSCs (mEPSCs) as a measure of spontaneous neurotransmitter release from pre-synaptic terminals, Yang et al.[64] identified that food deprivation results in increased mEPSC frequency (f_{mEPSC}) and therefore excitatory synaptic input onto ARC NPY-AgRP neurons sufficient to increase their firing rate. This effect was dependent on ghrelin-activation of the GHSR and

involved a pre-synaptic calcium-dependent signalling process which activates CAMKKβ and thus AMPK[64]. Critically, the mechanism features an AMPK-dependent positive feedback loop whereby AMPK itself triggered internal calcium release via ryanodine receptors to both increase spontaneous excitatory synaptic activity and probability of neurotransmitter release, as well as further activate AMPK via CAMKKβ. The observation that elevated f_{mEPSC} in hypothalamic slices treated briefly with ghrelin was still present after 5 hours, has been suggested to indicate that this positive feedback loop allows sustained feeding in response to a pulse of ghrelin, which persists after cessation of the ghrelin stimulus. Administration of the counter-regulatory hormone leptin to food-deprived mice 3 hours prior to slice preparation was observed to reduce f_{mEPSC} to that of fed levels. This resetting of persistent excitatory synaptic activity by leptin was identified to involve a POMC neuron-derived opioid (likely β-endorphin) which acts on pre-synaptic neurons to reverse AMPK-mediated persistent activity. Taken together, the identification of a presynaptic AMPK-dependent positive feedback loop, the ability of ghrelin to activate this loop to induce feeding and the presence of an opioid-receptor mechanism, activated by leptin, which resets persistent activity to induce satiety, led the authors to propose a bistable state of presynaptic neurons involving pre-AgRP synaptic memory (Figure 119). Thus, ghrelin-mediated signalling of the food-deprived state confers sustained activation of pre-synaptic neurons until flipped into a low activity state by leptin-induced POMC-mediated inhibition of the AMPK pathway[335].

How these findings integrate with those of Andrews et al.[229] is not immediately clear, particularly given that pharmacological manipulation of AMPK activity in the post-synaptic patch-clamped AgRP neuron did not alter f_{mEPSC} [64]. One possibility is that the mechanism uncovered by Yang et al.[64] is primarily responsible for the *acute* electrical response of elevated AgRP neuron firing following food deprivation or exogenous ghrelin stimulus, whilst the cell-autonomous AMPK-ACC-CPT1-UCP2-dependent model[229] underlies *more chronic* induction of adaptive metabolic changes to maintain (energetically costly) AgRP neuronal firing and promote expression of orexigenic neuropeptides.

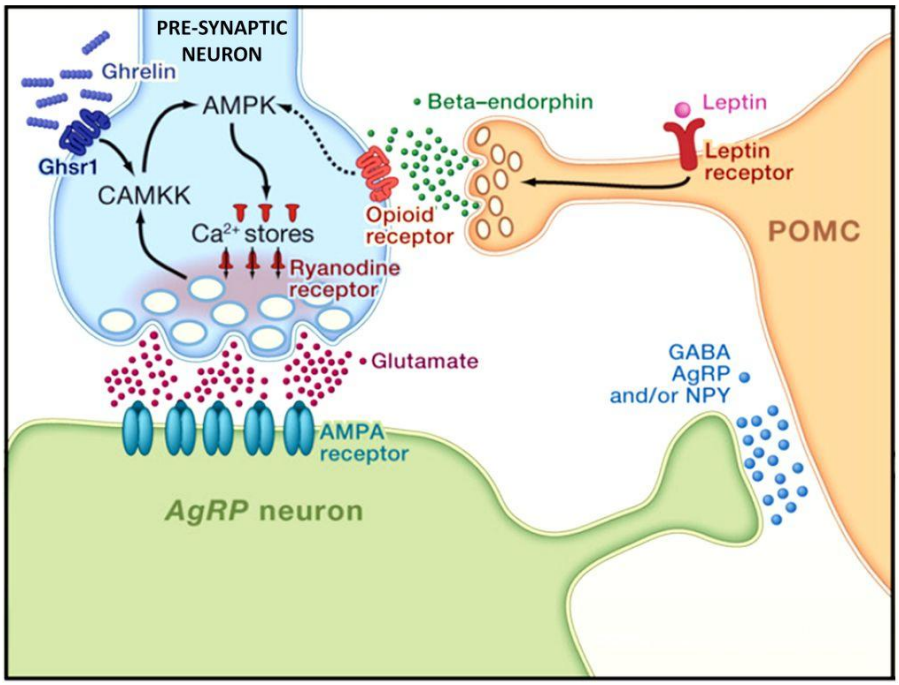


Figure 119. A model for the regulation of AgRP neuronal excitability by pre-synaptic AMPK.[bbb]

Stimulation of the GHSR by ghrelin in states of negative energy balance triggers the activation of a pre-synaptic positive feedback loop to drive FI. The mobilisation of calcium from IP3-sensitive internal stores induced by activation of the G-protein ($G\alpha_q$) coupled GHSR, leads to AMPK activation via CAMKK, with activated AMPK itself promoting further calcium release via the ryanodine receptor[64]. This increases excitatory neurotransmission to (NPY-) AgRP neurons by enhancing glutamate release onto ionotropic glutamate receptors, thereby inducing a depolarising post-synaptic current favouring action potential firing[64]. This signal continues even in the absence of ghrelin by virtue of the positive feedback loop – i.e. it exhibits hysteresis – until reset by leptin's action on neighbouring POMC neurons to promote opioid release, binding to pre-synaptic μ opioid receptors and turn off the AMPK-dependent positive feedback loop[335].

[bbb] Adapted from figure 1 Dietrich & Horvath *Cell* 2011;146:863-865.

7.4 Chapter-specific materials and methods

7.4.1 Pair-feeding (PF)

AMPK R299Q γ2 homozygous mutant mice and WT littermate controls were individually housed at 5 weeks of age and allowed to acclimatise for a further week. WT mice were freely fed and homozygous mutant mice were randomly allocated to one of two groups, either freely fed (non-PF) or fed the same amount of standard chow diet as consumed by the WT group in the preceding 24 hours (PF group) and provided daily at 10 am. Body weight was measured 3 times weekly. Mice underwent assessment of body composition by DEXA scanning at the end of the study.

7.4.2 Hypothalamus dissection

Murine hypothalamus was dissected as described[337] with minor modifications. Animals were euthanized by rapid cervical dislocation. The skull was opened with dissecting scissors and the brain removed and placed ventral side-up in a Petri dish containing ice-cold 1 X PBS. Hypothalamus was identified according to landmarks (rostrally: optic chiasm; caudally: mamillary bodies; laterally: optic tract) and a mediobasal hypothalamic block excised with curved forceps and immediately snap-frozen for subsequent RNA extraction. For some experiments, whole brains were immediately wrapped in aluminium foil and frozen on dry ice for subsequent hypothalamic dissection.

7.4.3 *In situ* hybridisation (ISH)

Whole mouse brains from male R299Q γ2 mutant and WT mice aged 9-10 weeks (N=4/genotype) were frozen in OCT (Merck, Darmstadt, Germany) on dry ice and 12 μm coronal cryosections cut and mounted on positively charged slides. Sequences for riboprobe synthesis were amplified by PCR from whole-brain cDNA to yield ~750 bp of the coding sequence of the gene of interest. Resulting cDNA fragments were cloned into the pCR4-TOPO vector as recommended by the manufacturer (Invitrogen). Sequenced clones were linearised prior to use. *In vitro* transcription and digoxigenin (DIG)-labeled riboprobe synthesis and hybridisation were performed essentially as described previously[338]. Briefly, slides were fixed in 4% paraformaldehyde and subjected to

acetylation treatment (consisting of: 442 mL 0.1% DEPC [diethyl pyrocarbonate]-treated water, 5.69 mL triethanolamine, 780 µL conc. HCl, 1 mL acetic anhydride) to decrease background before pre-hybridisation. Probe hybridisation was carried out for 16 hours at 60°C followed by stringency washes in saline-sodium citrate (SSC) buffer at 5 X SSC and 0.2 X SSC at 70°C (from a 20 X SSC stock composed of: 3 M NaCl, 0.3 M Na citrate, pH 7.0). After blocking with 10% bovine serum in PBS, the slides were incubated with a 1:5000 dilution of an anti-DIG antibody fused to alkaline phosphatase for 16 hours at 4°C, followed by generation of the hybridisation signal by adding alkaline phosphatase substrate (NBT/BCIP [nitro blue tetrazolium chloride/5-bromo-4-chloro-3-indolyl-phosphate], Roche) solution for 16 hours in all cases. Reactions were stopped in parallel once the desired level of intensity was reached by washing 2 x 5 mins in PBS. Slides were mounted in 80% glycerol and coverslipped. Signal intensities were quantified using ImageJ (NIH) on multiple matched sections. Sequences of upstream and downstream primers used for probe synthesis were:

Prkag2 forward primer	5'-CTTCTGCCTGGCCTTTCA-3'
Prkag2 reverse primer	5'-AAATACTGCGAGCGGTGC-3'
Agrp forward primer	5'-AAAGCTTTGTCCTCTGAAGCTG-3'
Agrp reverse primer	5'-GTTCTGTGGATCTAGCACCTCC-3'
Bsx forward primer	5'-CGAGGACATTCTGCTACACAAG-3'
Bsx reverse primer	5'-CTTCATCCCCAATGTCCACTT-3'

7.4.4 Drug sensitivity challenges

7.4.4.a Leptin sensitivity

Individually housed R299Q γ2 mutant and WT male mice aged 6 weeks received 1.5 mg/kg i.p. recombinant murine leptin (PeproTech, London, UK) or vehicle (saline) twice daily at lights on/off for 3 days with daily measurement of FI and body weight for 7 days after the start of injections. At

the end of the experiment, hypothalami were extracted for assessment of STAT3 phosphorylation by Western blotting.

7.4.4.b Melanocortin agonist

Individually housed R299Q γ2 homozygous mutant and WT male mice aged 6 weeks were fasted overnight (16 hours), then administered 1 mg/kg or 10 mg/kg i.p. of the melanocortin agonist, melanotan II (MT-II, Bachem, Bubendorf, Switzerland) and provided with free access to rodent chow at the start of the light-phase. Cumulative FI was determined by measurement at 2, 4, 8, 24, 48 and 72 hours. Final dose selection was based on initial pilot studies using age-matched male C57BL/6 mice (Charles River) with the dose-range of MT-II tested (1-10 mg/kg) based on previous studies[269, 339, 340] which had used MT-II.

7.4.4.c Ghrelin sensitivity

Male mice aged 6 weeks were individually housed and administered 30 μg i.p. human ghrelin (Bachem, Bubendorf, Switzerland) or an equivalent volume of saline in the non-fasted state one hour into the start of the light phase (i.e. mice satiated and settled). FI was measured at 1 hour post-injection. Final dose selection was based on pilot studies using age-matched male C57BL/6 mice, with the range of doses of human ghrelin tested (3, 10, 30 and 60 μg) guided by the literature[341-343]. To evaluate the molecular response to ghrelin, brains were rapidly removed 3 hours after i.p. administration of 30 μg human ghrelin and then frozen on dry ice prior to hypothalamic dissection for protein extraction and assessment by Western blotting.

7.4.5 Fast-refeeding

Male mice aged 6 weeks were individually housed and fasted overnight (16 hours) followed by access to food *ad libitum*. Cumulative FI was assessed at 2, 4, 8, 12, 24 and 48 hours post-cessation of fast.

7.4.6 Active (acylated) ghrelin levels

Blood samples for measurement of basal acylated ghrelin were obtained from freely-fed male mice aged 6 weeks at lights-on (7am). Sample collection and treatment to ensure stability of active

ghrelin were as recommended by the manufacturer of the ELISA kit used (Millipore, Billerica, MA, USA). Whole blood samples were drawn into tubes containing EDTA and AEBSF (4-[2-Aminoethyl]benzenesulfonyl fluoride hydrochloride) immediately added to a final concentration of 1 mg/mL. Samples were immediately centrifuged at 3000 x g for 15 minutes at 4°C to obtain plasma. Plasma was removed and acidified with HCl to a final concentration of 0.05 M and stored at -80°C. Samples were subject to no more than a single freeze-thaw cycle and acylated ghrelin concentration determined by ELISA (Millipore, Billerica, MA, USA) according to the manufacturer's instructions.

7.4.7 Ghrelin receptor antagonism

7.4.7.a Acute ghrelin receptor antagonism

WT and R299Q γ2 homozygous mutant male mice aged 6 weeks were individually housed, fasted overnight (16 hours) and then treated with a single dose of 200 nmol i.p. of the ghrelin receptor antagonist [D-Lys-3]-GHRP-6 (Tocris Bioscience, Bristol, UK) and provided with food *ad libitum*. Cumulative FI was measured at 0.5, 1, 2, 4 and 24 hours post-injection. Final dose selection was based on pilot studies with the dose-range of [D-Lys-3]-GHRP-6 tested (100-300 nmol) based on previous studies[344-346].

7.4.7.b Chronic ghrelin receptor antagonism - hyperphagic rescue

6 week old male WT and R299Q γ2 homozygous mutant mice were individually housed and randomly allocated to one of two groups to receive either vehicle (saline) or 100 nmol of the ghrelin receptor antagonist [D-Lys-3]-GHRP-6 (dissolved in saline) administered i.p. twice daily at lights on/off for 29 days.

7.5 Results

7.5.1 Pair-feeding

To dissect the relative contribution of energy intake and expenditure, pair-feeding was undertaken in 6 week old male mice to determine whether matching homozygote daily FI to those of WT, restored their body weight (BW) and body composition to that of WT (Figure 120). Pair-feeding of homozygous mutant mice to the daily intake of WT mice normalised their BW to that of WT and led to a reduction in fat mass below that of WT mice, suggesting greater homozygote EE.

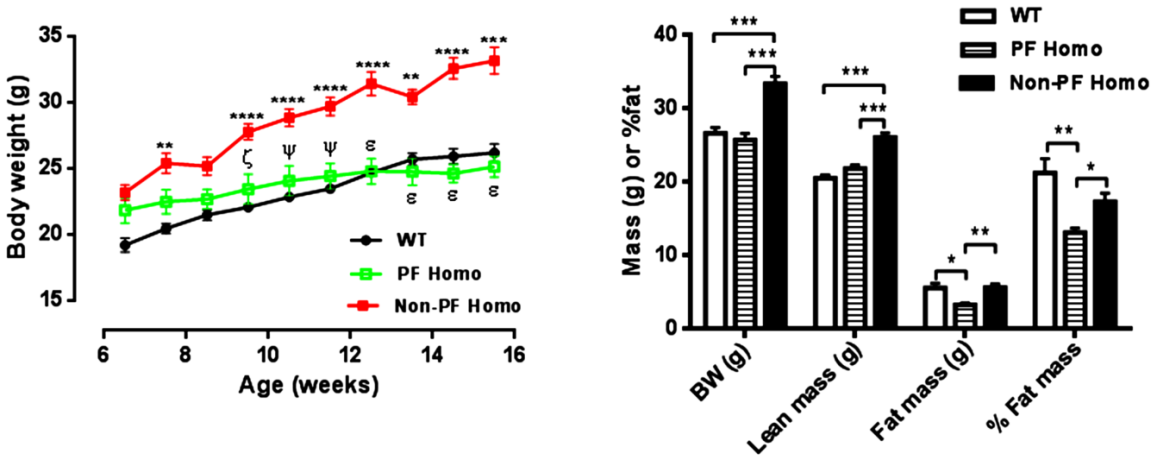


Figure 120. Effect of pair-feeding male R299Q γ2 homozygous mutant mice to FI of age-matched male WT mice (N=6-12/group). Abbreviations: PF Homo, pair-fed homozygote; Non-PF homozygote, non-pair-fed homozygote; BW, body weight.

Left – serial BW gain over the course of the pair-feeding experiment. *****P*<0.01 vs WT, ******P*<0.001 vs WT, *******P*<0.0001 vs WT, ζ *P*<0.01 vs non-PF homozygote, ψ *P*<0.001 vs non-PF homozygote, ε *P*<0.0001 vs non-PF homozygote. Right – DEXA analysis of body composition at the end of 10 weeks of pair-feeding. ****P*<0.05, *****P*<0.01, ******P*<0.001

7.5.2 Neuropeptide signalling profile

The results of the pair-feeding experiment were consistent with the concept that hyperphagia was the primary driver of weight gain and eventual development of obesity in R299Q γ2 homozygous mutant mice. To gain further insight into the molecular correlates of this, orexigenic and anorexigenic neuropeptide expression was measured in the hypothalamus of freely-feeding 6 week old male mice and their ratios compared (Figure 121), as described[269]. This revealed a pro-orexigenic signalling profile, with a significantly increased ratio of *Agrp* to *Pomc* in R299Q γ2 homozygous mutant mice compared to WT and heterozygote mice displaying a signal intermediate

between the two other genotypes. To confirm this signal for increased *Agrp, in situ* hybridisation was used specifically in WT and homozygote mice (Figure 121). This confirmed a greater than two-fold increase in *AgRP* mRNA expression in the arcuate nucleus of homozygous mutant mice.

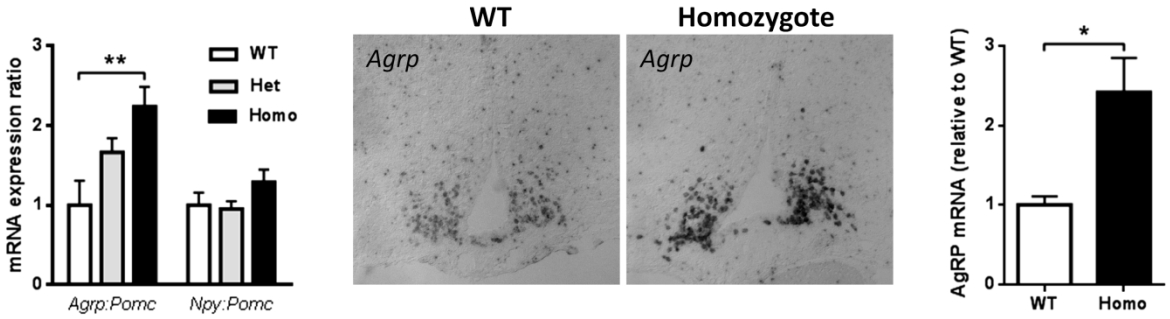


Figure 121. Left panel – Expression ratio of key hypothalamic pro-orexigenic (*Agrp, Npy*) to anorexigenic (*Pomc*) neuropeptides in freely-fed 6 week old male mice (N=6/genotype). Centre panels – Hypothalamic *Agrp* expression by *in situ* hybridisation and quantification (right panel) from freely-fed 8 week old male mice (N=4/genotype).

7.5.3 Gross neuroanatomy and hypothalamic γ2 expression

To ascertain whether the R299Q γ2 mutation affected gross brain morphology, Nissl staining (which stains both neurons and glia) was used on brains that had undergone perfusion fixation *in situ* (Figure 122). This revealed comparable gross anatomical brain appearances across genotypes.

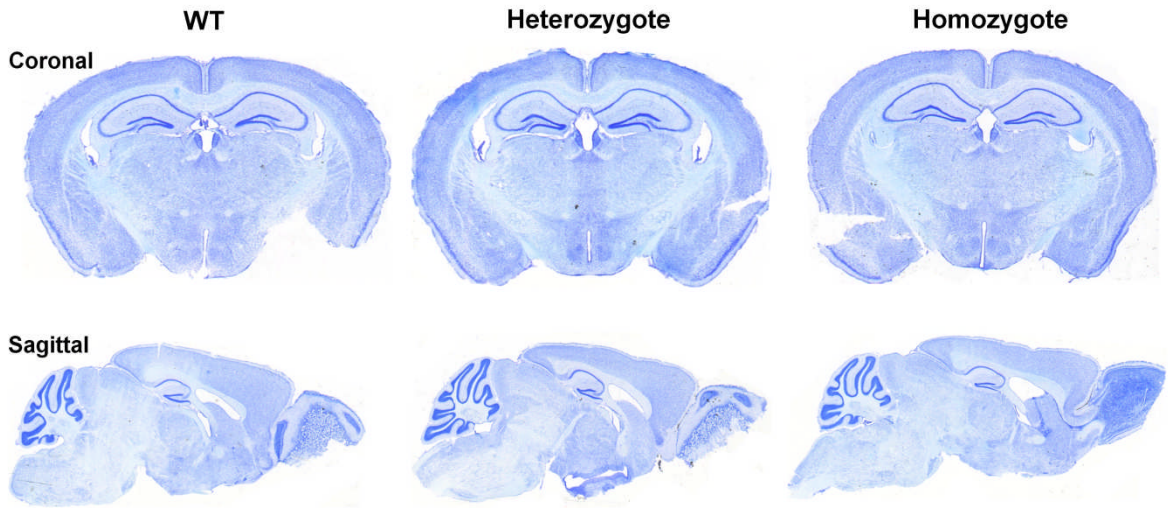


Figure 122. Brain Nissl staining appearances from male WT and R299Q γ2 mutant mice.

The preceding data indicated that FI and the balance of key neuropeptides regulating appetite were perturbed in R299Q γ2 homozygous mutant mice. To determine the regional expression pattern of

the *Prkag2* isoform in the normal hypothalamus, in particular in nuclei regulating FI, *in situ* hybridisation was used (Figure 123). This revealed γ2 to be highly expressed in the hypothalamus, including the arcuate nucleus.

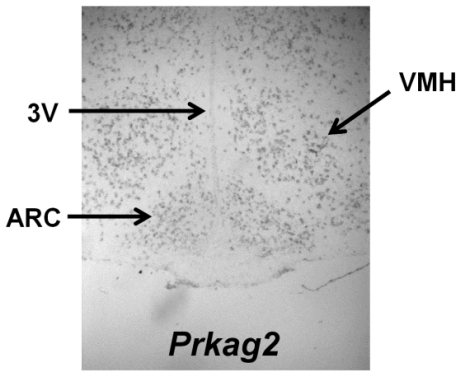


Figure 123. *In situ* hybridisation of a coronal hypothalamic section demonstrating expression pattern of *Prkag2* from an 8 week old male WT mouse. Abbreviations: 3V, third ventricle; ARC, arcuate nucleus; VMH, ventromedial hypothalamic nucleus.

Multiplexed PCR using mutant and WT allele-specific probes on hypothalamic cDNA confirmed expression of R299Q γ2 in the mediobasal hypothalamus of both mutant genotypes. Relative quantification of hypothalamic *Prkag2* mRNA expression with qRT-PCR using an inventoried TaqMan assay indicated comparable expression across genotypes (Figure 124).

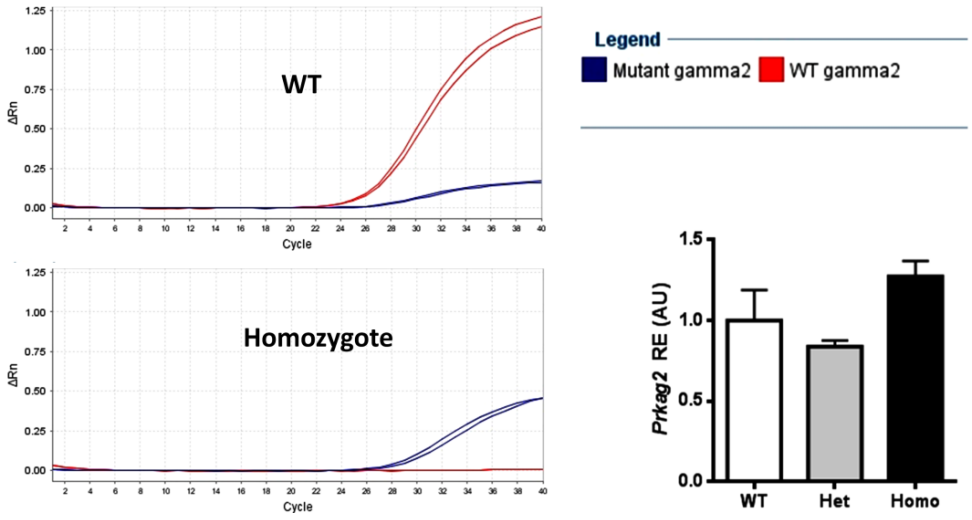


Figure 124. Left –PCR amplification plots from hypothalamic cDNA using WT and R299Q γ2 mutant specific probes. Lower right – relative quantification of hypothalamic *Prkag2* mRNA by qRT-PCR using an inventoried TaqMan probe (N=5-6/genotype).

7.5.4 Leptin sensitivity

Leptin is a key peripheral satiety signal and reported to act in part via AMPK. To explore whether the R299Q γ2 mutation affected central leptin signalling, the impact of peripherally administered leptin on FI was investigated. This revealed more prolonged satiety and signals in favour of a greater magnitude of anorectic effect in homozygous mutant mice in response to twice daily leptin administered for three days (Figure 125). To gain further insight into this, phosphorylation of STAT3 (signal transducer and activator of transcription 3), a key transcription factor mediating leptin's transcriptional regulation of the melanocortinergic pathway[347], was assessed (Figure 126). In keeping with the FI response, homozygous mutant mice displayed significantly greater hypothalamic STAT3 phosphorylation following a single dose of leptin.

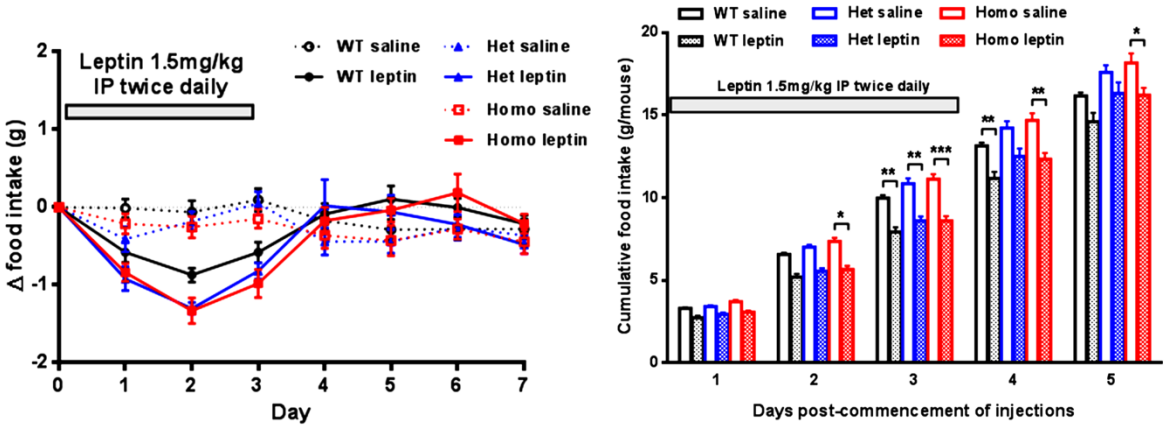


Figure 125. Effect of 1.5 mg/kg leptin i.p. administered twice daily for 3 days on FI (N=11-12/genotype).

Left – change in FI compared to baseline pre-leptin. Leptin had a significant effect on reducing FI vs saline for all genotypes by day 2 (WT, *P*<0.01; Het and Homo, *P*<0.0001). Post-ANOVA WT vs Homo multiple comparison testing did not identify a significant difference in change in FI between mutant and WT leptin-treated groups.

Right – Cumulative FI in response to 3 days peripheral leptin administration. **P*<0.05, ***P*<0.01, ****P*<0.001

To determine whether components upstream or downstream of STAT3 phosphorylation[347] were perturbed in the basal, freely-fed state, the expression of the active, long-form of the leptin receptor (LEPR) and mRNA expression of SOCS3 (suppressor of cytokine signalling 3), a feedback inhibitor of LEPR signaling, were examined by Western blotting and qRT-PCR, respectively (Figure 126). Non-significant trends suggestive of potential subtle upregulation of LEPR

expression (*P*=0.15 for effect of genotype) and lower *Socs3* mRNA expression (*P*=0.14 for effect of genotype) were observed, both of which would act to enhance central leptin action.

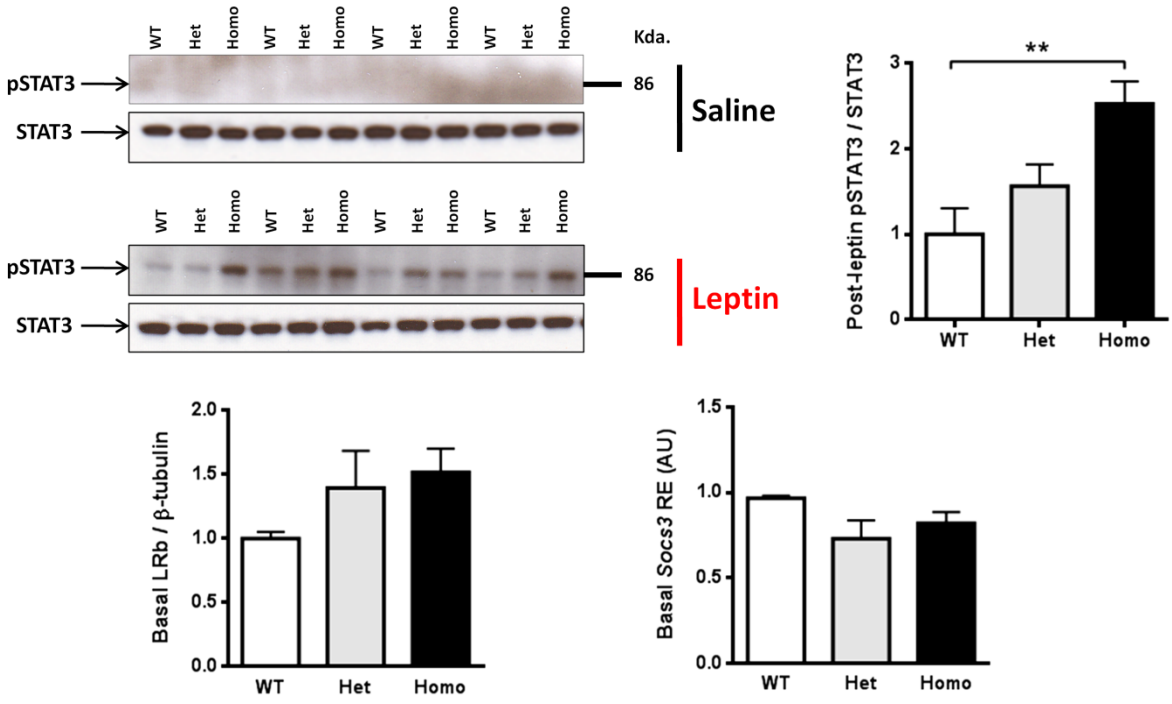


Figure 126. Upper panels – induction of hypothalamic pSTAT3 in response to a single i.p. injection of 1.5 mg/kg of leptin and densitometry quantification (N=4-5/genotype). *****P*<0.01

Lower panels – Quantification by Wwestern blotting of the long-form of the leptin receptor (LEPR or LRb) (N=4-5/genotype) and *Socs3* mRNA levels (N=5-6/genotype) in the hypothalami of freely-fed male mice at 6 weeks of age.

7.5.5 Response to melanocortinergic activation

R299Q γ2 homozygous mutant mice manifest hyperphagia, maturity-onset obesity, greater lean mass and increased linear growth, a phenotype highly similar to heterozygous A^y (agouti yellow) mice and MC4-R KO mice, classical models of severe melanocortinergic dysfunction. Accordingly, to determine whether melanocortinergic dysfunction contributed to the systemic phenotype of R299Q γ2 mutant mice, the FI response to the MC3/4-R agonist melanotan II (MT-II) was assessed. All genotypes responded with an appropriate reduction in FI to a single peripheral dose of MT-II at both 10 mg/kg (not shown) and 1 mg/kg (Figure 127), indicating that the pathway downstream of MC3/4-R activation was grossly intact in mutant mice. Notably, in response to 1 mg/kg MT-II, WT mice had a longer duration of reduced FI compared to homozygous mutant mice

(up to 8 hours compared to 4 hours), with a non-significant trend (*P*=0.15) to lower anorectic response in homozygote mice at 2 hours post-MT-II.

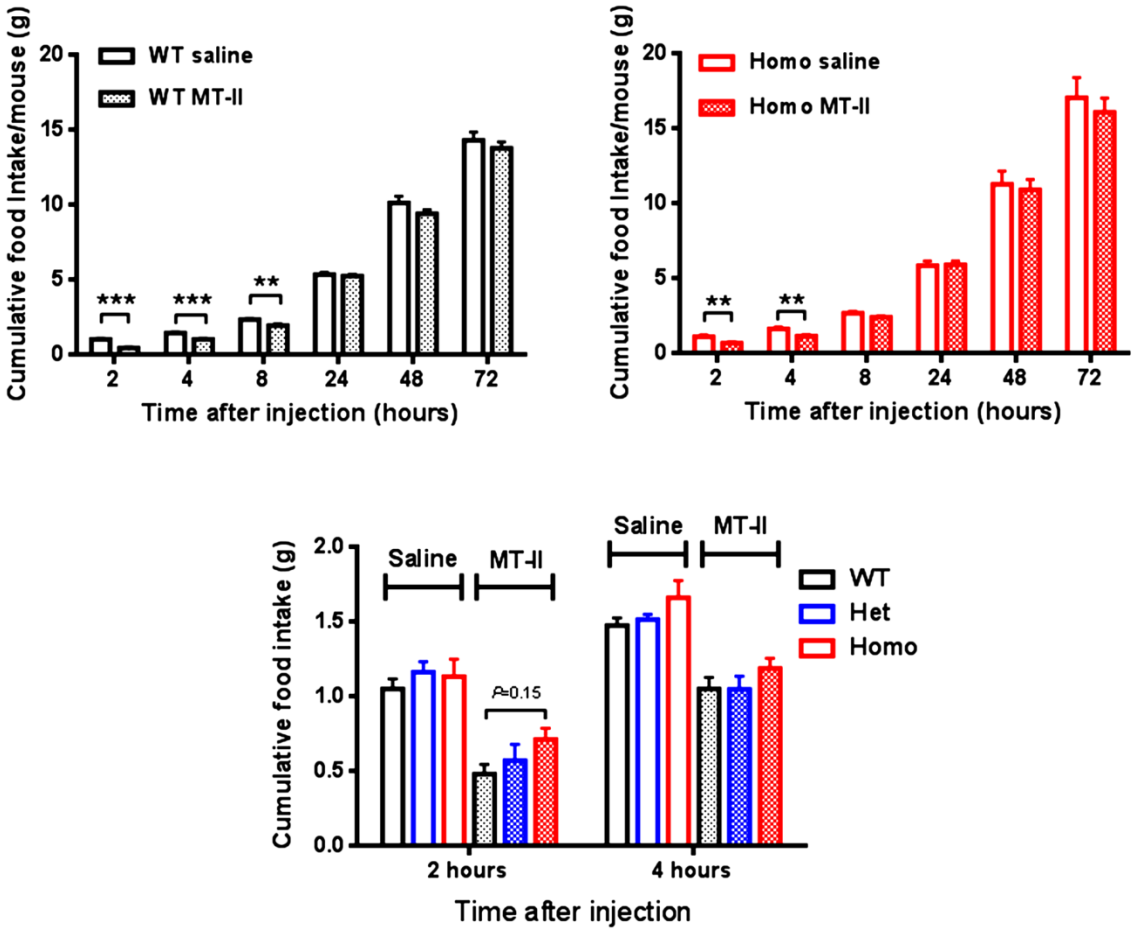


Figure 127. Upper panels – cumulative FI response of 6 week old WT and homozygous mutant mice following i.p. administration of 1 mg/kg melanotan-II (MT-II) or vehicle (saline) (N=12-13/group). *****P*<0.01, ******P*<0.001

Lower panel – cumulative feeding response to i.p. 1 mg/kg MT-II in all three genotypes at 2 and 4 hours.

7.5.6 Fast-refeeding and the response to ghrelin

The preceding data suggested that perturbations in pathways which promote anorexigenic neuropeptide and electrophysiological signalling, namely central leptin and melanocortinergic signalling, could not account for the hyperphagia of mutant mice. Indeed, in the case of leptin, there was evidence to support an *increased* sensitivity of the pathway, an effect which would actually tend to reduce FI in mutant mice. This, coupled with the finding of elevated *Agrp* expression, suggested a primary enhancement of central orexigenic signalling rather than reduced melanocortinergic tone as the prime driver of hyperphagia in R299Q γ2 mutant mice. As an initial

step, the cumulative feeding response following a potent physiological stress – fasting – was assessed (Figure 128). In contrast to a published model[342] of melanocortinergic dysfunction, namely the heterozygous A^y mouse, R299Q γ2 homozygous mutant mice had an intact or even exaggerated feeding response to an overnight fast.

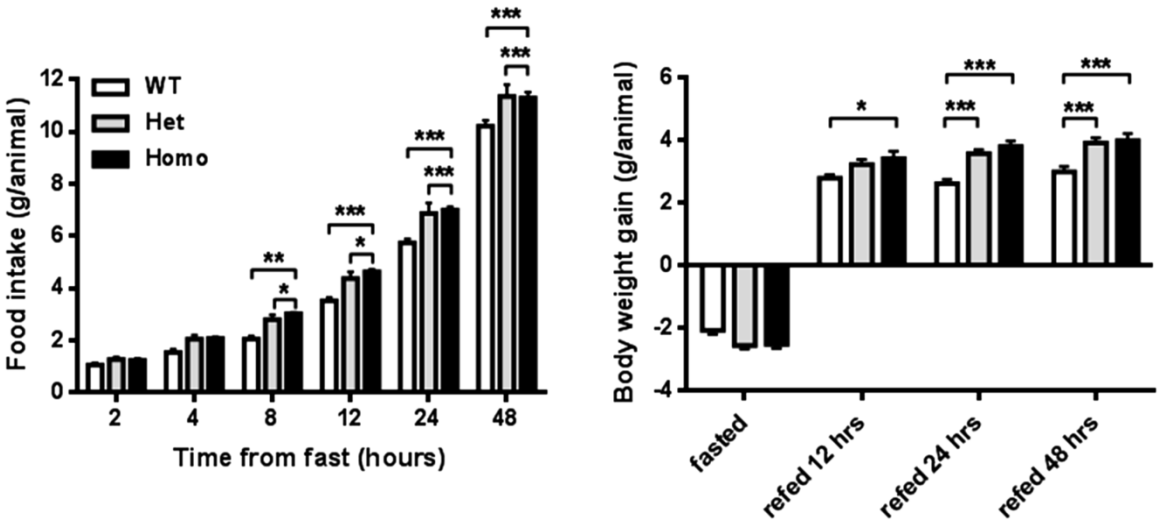


Figure 128. Cumulative FI (left) and BW change (right) in response to an overnight fast followed by free access to food (N=11-12/genotype). *P<0.05, **P<0.01, ***P<0.001

During fasting, the orexigenic hormone ghrelin conveys a signal of negative energy balance to the ARC through its activation of NPY/AgRP neurons. Given the response to fast-refeed and the role of AMPK in the central pathway downstream of ghrelin receptor activation, the acute feeding response to peripheral ghrelin administration was assessed (Figure 129). R299Q γ2 homozygous mutant mice displayed an exaggerated hyperphagic response to exogenous ghrelin compared to both WT and heterozygous mutant mice. In contrast to leptin levels, no differences were identified between genotypes in plasma concentrations of active ghrelin in the freely-fed state (Figure 129).

To investigate the potential molecular correlates underpinning a heightened feeding response to exogenous ghrelin administration, the hypothalamic protein expression of signalling intermediaries implicated in the pathway downstream of central ghrelin receptor (GHSR-1a) activation were assessed from mediobasal hypothalamus following ghrelin injection (Figure 130 and Figure 131).

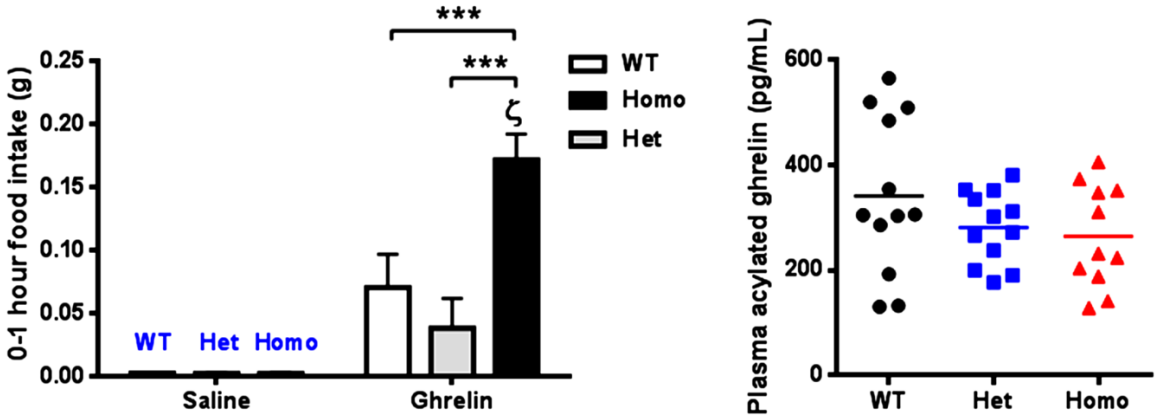


Figure 129. Left – Feeding response at 1 hour following 30 µg i.p. human ghrelin in 6 week old male mice (N=6-7/group). ζ *P*<0.0001 vs all genotypes treated with saline, ****P*<0.001. Right – Basal plasma acylated (active) ghrelin in 6 week old male mice taken at the onset of the light phase (N=11-12/genotype).

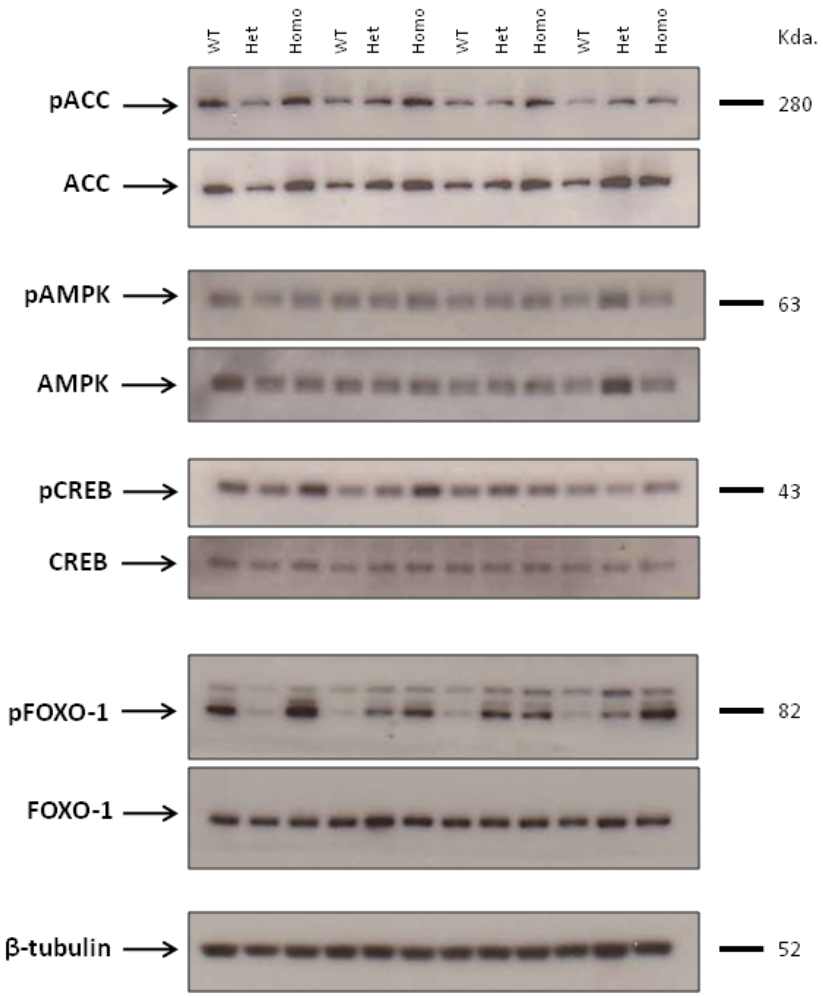


Figure 130. Western blotting of hypothalamic lysates from R299Q γ2 mutant and WT mice following 30 µg i.p. human ghrelin.

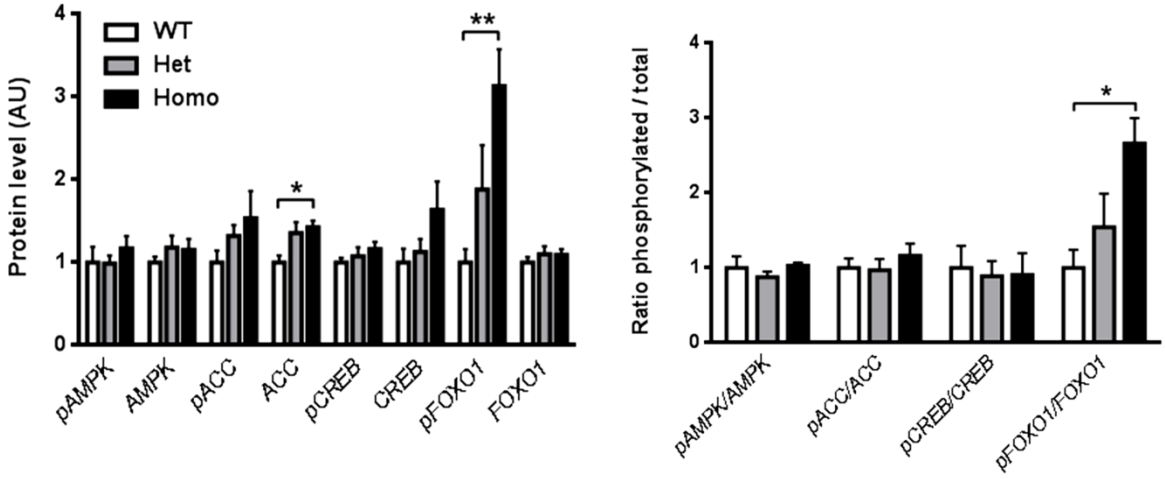


Figure 131. Hypothalamic protein levels of AMPK, ACC, CREB, FOXO1 and their phosphorylated forms measured by Western blot (normalised to β-tubulin) following administration of 30 µg i.p. human ghrelin. Values quantified by densitometry (N=6-7/genotype). Right – ratios of phosphorylated to total protein. *P<0.05, **P<0.01

The orexigenic response to ghrelin has been shown to involve inhibition of *de novo* fatty acid biosynthesis via AMPK in the VMH[327]. Accordingly, the levels of total and α-Thr172 phosphorylated AMPK (pAMPK), as well as total and phosphorylated ACC (pACC) were assessed from whole mediobasal hypothalamic extracts. No significant differences were seen in pAMPK, but total ACC content was significantly elevated in R299Q γ2 homozygous mutant mice, together with a non-significant trend to increased pACC. Ghrelin's promotion of orexigenic neuropeptide expression (*Npy* and *Agrp*) is recognised as being mediated via several transcription factors[348]: the brain-specific homeobox factor (BSX); phosphorylated cAMP response-element-binding protein (pCREB); and the forkhead box O1 (FOXO1). Examination of the protein levels of these factors following peripheral administration of ghrelin identified markedly higher levels of phosphorylated FOXO1 (pFOXO1) in response to ghrelin administration in homozygote mice but only non-significant trends to increases in FOXO-1 and pCREB.

7.5.7 Investigation of basal levels of central ghrelin signalling

In order to identify whether the heightened feeding response to exogenous ghrelin administration reflected an increase in *basal* ghrelin signalling, the hypothalamic expression of AMPK, ACC, CREB, FOXO1 and their phosphorylated forms were assessed from mediobasal hypothalamic samples in freely-fed mice by Western blotting and subsequent densitometry (Figure 132). No

significant differences in protein levels or the ratio of phosphorylated to total protein were identified between WT and homozygous mutant mice, although homozygotes exhibited significantly higher levels of pACC compared to heterozygotes.

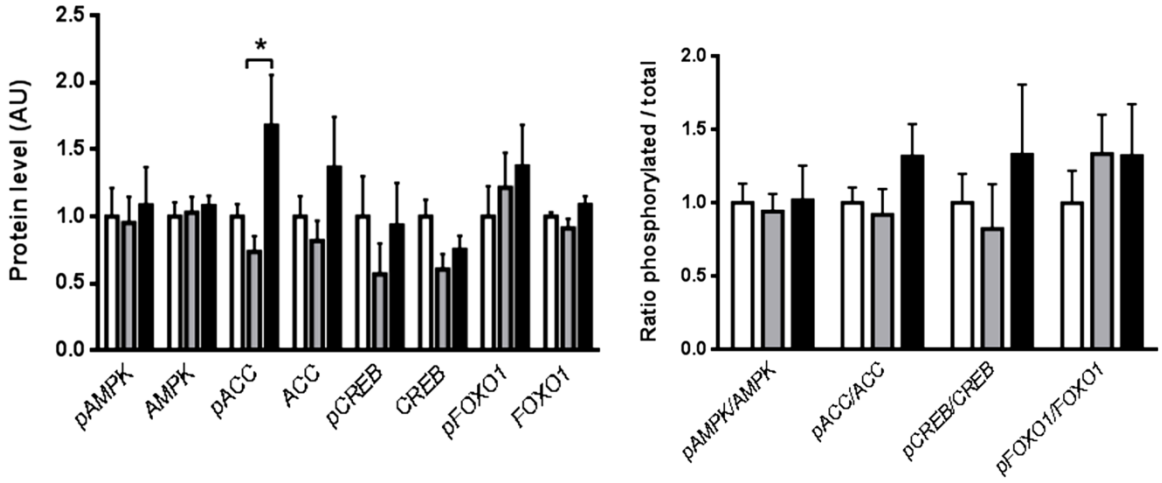


Figure 132. Left – Hypothalamic protein levels of AMPK, ACC, CREB, FOXO1 and their phosphorylated forms measured by Western blot (normalised to β-tubulin) in freely-fed mice (N=4-6/genotype). *P<0.05. Right – ratios of phosphorylated to total protein.

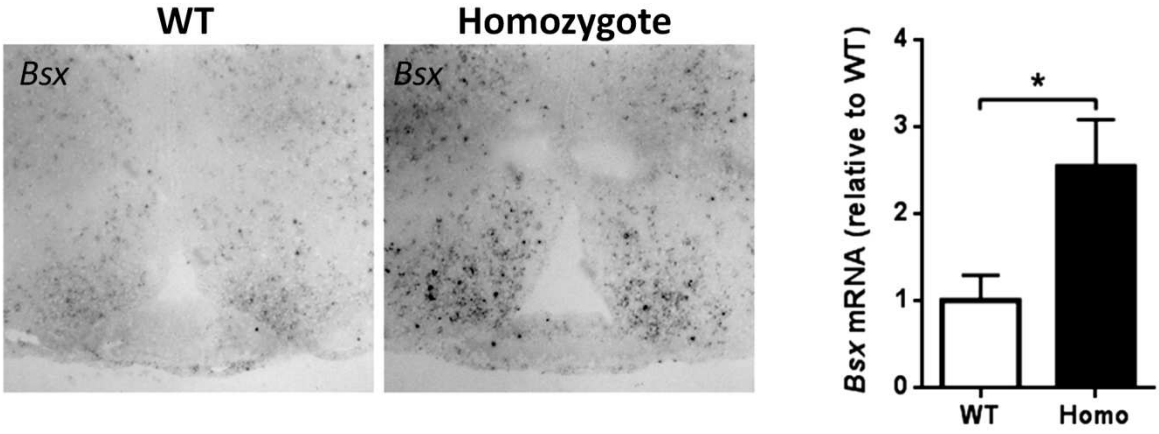


Figure 133. Hypothalamic *Bsx* transcript expression by *in situ* hybridisation and quantification (N=4/genotype). *P<0.05

In addition to pCREB and FOXO1, a further transcription factor described to mediate ghrelin's transcriptional effects downstream of GHSR-1a activation is the brain-specific homeobox factor (BSX)[349]. BSX is near-exclusively expressed in the ARC and is able to interact with other transcription factors (pCREB and FOXO1), to bind to *Npy* and *Agrp* regulatory sequence elements *in vivo*, enhancing their expression[349]. Given the lack of a definitive result implicating altered pCREB and FOXO1 in the enhanced feeding response to ghrelin (and likely exaggerated fast-

refeed response as well), the possibility that upregulated BSX expression might account for this was next investigated. Attempts made at measuring relative *Bsx* expression by qRT-PCR from whole mediobasal hypothalamic tissues were hindered by low transcript levels resulting in unreliable amplification. Thus, a different approach utilising *in situ* hybridisation was applied (Figure 133), revealing a significant increase in ARC *Bsx* expression in homozygous mutant mice.

7.5.8 Hyperphagic rescue

The preceding data suggested that the hyperphagia of R299Q γ2 mutant mice was driven by heightened central ghrelin-AgRP axis tone. To further substantiate the role of ghrelin signalling in R299Q γ2 mutant hyperphagia, the feeding response following a fast was assessed in mice that were treated with a single dose of the selective ghrelin receptor antagonist, [D-Lys-3]-GHRP-6, or an equivalent volume of saline (Figure 134).

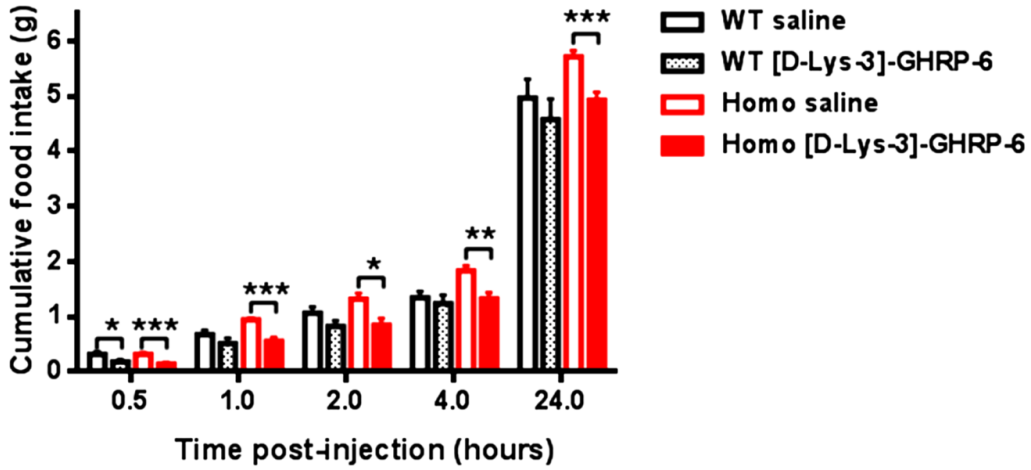


Figure 134. Effect of acute GHSR-1a antagonism with 200 nmol i.p. [D-Lys-3]-GHRP-6 on cumulative FI in 6 week old mice following a 16 hour fast (N=8-12/treatment group). ****P*<0.05, *****P*<0.01, ******P*<0.001

WT mice treated with a single dose of 200 nmol [D-Lys-3]-GHRP-6 displayed a significant reduction in FI compared to WT saline-treated animals at 30 minutes post-injection only. In contrast, R299Q γ2 homozygous mutant mice treated with the ghrelin receptor antagonist exhibited a significant reduction in FI compared to saline-treated homozygous animals at all time points assessed up to 24 hours post-injection.

These findings indicated a greater sensitivity to acute ghrelin receptor inhibition in homozygous

mutant mice at the dose selected, in keeping with a role for enhanced post-GHSR-1a signalling in the hyperphagia of mutant mice. In order to test whether *chronic* inhibition of the ghrelin receptor could restore homozygote FI to that of WT mice, [D-Lys-3]-GHRP-6 was administered at a dose of 100 nmol twice daily for just under 30 days (Figure 135). At this dose, chronic ghrelin receptor antagonism with [D-Lys-3]-GHRP-6 normalised the FI of homozygous mutant mice to that of WT saline-treated controls, but had no significant effect on WT FI.

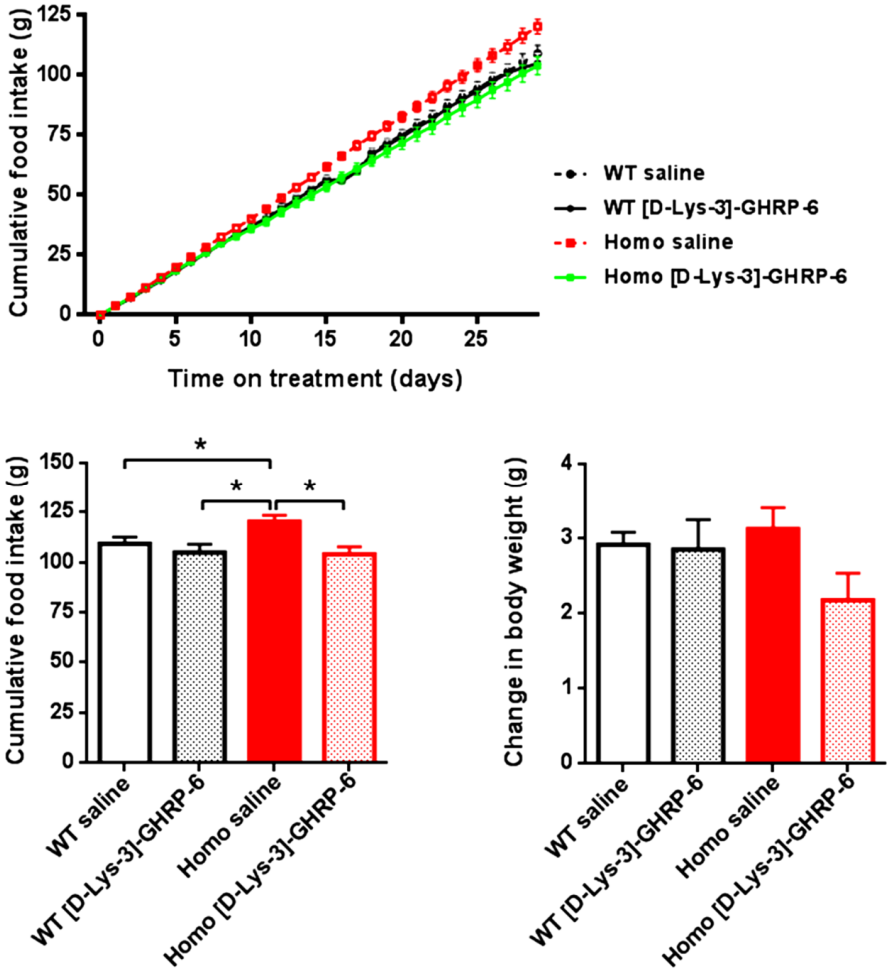


Figure 135. Top – Effect of ghrelin receptor antagonism with 100 nmol i.p. [D-Lys-3]-GHRP-6 twice daily on cumulative FI in WT and R299Q γ2 homozygous mutant mice over 29 days (N=9-10/treatment group). Significant (*P*<0.05 or greater) differences emerge between: homo saline and homo [D-Lys-3]-GHRP-6 groups by 21 days of treatment; homo saline and WT saline or WT [D-Lys-3]-GHRP-6 by 29 days.

Lower panels – Cumulative FI (left) and body weight change (right) after 29 days treatment with 100 nmol i.p. [D-Lys-3]-GHRP-6 or saline twice daily. **P*<0.05

7.6 Discussion

7.6.1 Summary of principal chapter findings

Following on from the experimental leads obtained in the preceding chapter, this chapter has sought to elucidate the central mechanistic pathways underlying the main driver of progressive weight gain and eventual obesity of R299Q γ2 mutant mice, namely hyperphagia. By investigating hypothalamic signalling and whole-animal feeding responses, both basally and in response to physiological or pharmacological challenges in pre-obese mice, the work presented in this chapter has identified the following:

i) Use of a pair-feeding paradigm confirms hyperphagia to be the principal factor underlying progressive weight gain in homozygous mutant mice, at least at a young age.

ii) Homozygous mutant mice manifest a pro-orexigenic signalling profile, with a near 2.5-fold elevation in ARC *Agrp* mRNA expression compared to WT mice in the freely-fed state.

iii) *Prkag2* transcript is expressed in murine hypothalamus, notably including the arcuate nucleus. As a corollary of this, R299Q mutant γ2 transcript is detectable in the hypothalamus of R299Q γ2 mutant mice, with broadly comparable levels of *Prkag2* expression between genotypes.

iv) The normal satiety response to leptin is not blunted by the R299Q γ2 mutation; indeed, evidence was identified to indicate a heightened response to leptin in mutant mice.

v) Mutant mice display a grossly intact satiety response to the melanocortin agonist MT-II.

vi) Mutant mice display a pronounced feeding and weight gain response following fast-refeeding.

vii) Homozygous mutant mice exhibit greater sensitivity to exogenous ghrelin administration in terms of FI, with chronic antagonism of ghrelin receptor signalling acting to normalise their hyperphagia.

7.6.2 Hyperphagia - the main driver of weight gain in R299Q γ2 homozygous mutants

Obesity is recognised to result from a fundamental, long-term imbalance between energy intake and expenditure. A key question to be addressed early on with regard to the systemic phenotype of mice bearing the R299Q γ2 KI mutation was the relative balance between the two and whether reduced EE played a significant role in the greater whole body, lean and fat mass gain of mutant mice. Findings from EE measures presented in the preceding chapter suggested that EE was not reduced in mutant mice but was, in fact, potentially increased. Differences in body composition, even at a young age, complicated this ready interpretation, however. Accordingly, in order to more definitively determine whether hyperphagia or altered EE was the primary defect underlying the progressive weight gain and eventual obesity of R299Q γ2 homozygous mutant mice, pair-feeding (PF) experiments were undertaken in young, pre-obese mice. Matching homozygote FI to that of age-matched WT mice resulted in a normalisation of mutant mice body weight and lean mass to that of WT levels. Notably, by the end of the experiment both absolute and % fat mass were significantly lower in PF homozygote mice than WT and freely-fed homozygote mice. This finding reinforces the view that homozygous mutant mice do indeed have greater EE than WT mice at the same body weight and that PF induced significant catabolism in homozygous mutant mice. Whether this greater EE reflected increased foraging for food in PF homozygotes experiencing a 'starvation-like' cue is uncertain.

7.6.3 The effect of the R299Q γ2 mutation on hypothalamic pathways regulating food intake and body weight

The hypothalamus has a pre-eminent role in the regulation of appetite and body weight. Within this, the arcuate nucleus acts as a primary locus for integrating peripheral endocrine and metabolic signals influencing FI, with the circulating hormones leptin and ghrelin – antagonistic in their effects on FI – converging on melanocortinergic neurocircuitry. Accordingly, the integrity of these pathways was investigated in their proper *in vivo* setting using a combination of drug and physiological challenges.

7.6.3.a Hypothalamic leptin signalling

Leptin plays an integral role in the regulation of appetite and energy homoeostasis, with perturbations in leptin signalling leading to morbid obesity syndromes such as that of the *ob/ob* mouse. Accordingly, the satiety response to exogenous leptin was examined in young, pre-obese R299Q γ2 mutant mice. On the assumption that the R299Q γ2 mutation behaved broadly as an 'activating' mutation in the hypothalamus, it was anticipated that R299Q γ2 mutant mice would demonstrate a blunted or absent FI inhibitory response to leptin. Surprisingly, not only did mutant mice exhibit a clear reduction in FI in response to leptin, there were features suggestive of an *enhanced* leptin sensitivity response, with a trend to greater reduction in FI following repeated leptin administration and significantly greater hypothalamic STAT3 phosphorylation after a single dose of leptin. Notable in this regard is the observation[322] that leptin has no satiety-inducing effect on the hyperphagia induced by hypothalamic expression of CA-AMPK, suggesting that the R299Q γ2 mutation does not induce constitutive activation of mutant γ2-containing AMPK complexes, but leaves them receptive to hormonal signals.

The interpretation of the true effect of the mutation on leptin sensitivity *in vivo* is complicated by the finding of significantly lower circulating leptin levels in young, pre-obese homozygous mutant mice, consistent with their lower total body fat % at this time point. Thus, experimental findings suggestive of heightened LEPR signalling could simply be mediated by low leptin levels. In support of this interpretation were subtle trends to upregulation of LEPR expression and lower *Socs3* mRNA expression, a feedback inhibitor of LEPR signalling.

7.6.3.b Melanocortin receptor signalling

Disruption of the melanocortinergic system in both mice[291, 313] and humans[315] results in an obesity syndrome characterised by a phenotype of hyperphagia, increased linear growth and lean mass, features bearing strong resemblance to the emergent obesity phenotype of R299Q γ2 mutant mice. Moreover, R299Q γ2 homozygous mutant mice had a ~2.5-fold degree of upregulation in hypothalamic expression of AgRP, the endogenous antagonist of the melanocortinergic system, which acts as the native counter-regulator to the satiety promoting peptide α-MSH at the MC4-R.

Whilst the intact satiety response to leptin suggested that the melanocortinergic system was grossly intact, the aforementioned considerations mandated direct investigation of this pathway. The FI of R299Q γ2 homozygous mutant mice was equally responsive to the satiety-inducing effects of 10 mg/kg of the MC3/4-R agonist, melanotan II (MT-II), consistent with the findings from indirect challenge provided by leptin, whose effects on FI and EE are thought to be mediated in large part by the melanocortinergic system. Use of MT-II at a dose an order of magnitude lower did provide some evidence to support subtle melanocortinergic dysfunction, however, with a greater duration of MT-II-induced satiety in homozygous mutant compared to WT mice. Whether this subtle finding is simply a reflection of greater synaptic AgRP to out-compete MT-II for binding to the MC4-R is unclear but, together with the findings from the leptin sensitivity experiments, this indicates that a primary disturbance of melanocortinergic signalling at or beyond the level of the MC4-R is unlikely to account for the hyperphagia of mutant mice.

7.6.3.c Hypothalamic ghrelin signalling pathway

AMPK has been implicated as a key mediator of ghrelin's transcriptional[229] and electrophysiological[64] effects on the AgRP and pre-synaptic AgRP neural circuitry governing FI. Accordingly, in view of the fact that critical defects in core anorexigenic signalling pathways did not seem to account for mutant hyperphagia, the pathway downstream of a key driver of orexigenic signalling – ghrelin – was investigated.

As an initial step, the effects of fasting on FI were assessed as a physiological stressor and stimulator of the central orexigenic response. Young, pre-obese R299Q γ2 homozygous mutant mice displayed an exaggerated response to fasting followed by refeeding, with greater cumulative FI and body weight gain than WT mice. Importantly, this response is not simply a general feature of hyperphagic murine models of obesity – heterozygous pre-obese A^y mice display re-feeding responses comparable to that of WT post-fast, whilst obese A^y mice actually manifest *impaired* refeeding responses compared to age-matched WT mice[342].

The response to fasting suggested that a primary 'gain' in central ghrelin signalling underpinned the hyperphagia of the R299Q γ2 KI. To test this, the feeding response to exogenous ghrelin was

investigated. Homozygous mutant mice were seen to display a greater hyperphagic response to peripheral ghrelin administration than WT mice. Probing of components of the signalling pathway downstream of ghrelin receptor (GHSR-1a) activation did not yield the expected clear differential expression profile between mutant and WT mice. Initial attempts at interrogating these downstream mediators[229] (including *Cpt1*, *Ucp2*, *Bsx* and *Nrf1*) using qRT-PCR from mediobasal hypothalamic wedges (data not presented) was hindered by low signal or high variability in expression, even in WT samples. Therefore, a different approach based on investigating the phosphorylation of key proteins implicated in the hypothalamic transcriptional response to ghrelin, was undertaken, both in the baseline state and in response to fasting. These included the transcription factors CREB and FOXO1, in addition to the direct target of AMPK, ACC. Western blotting of medial hypothalamic protein extracts revealed trends in favour of differential levels of phosphorylation of these proteins, but only reaching significance for pACC (homozygote versus heterozygote) and pFOXO1. These findings highlight the subtle effect of the R299Q γ2 mutation, potential competing effects of normal γ1-containing AMPK heterotrimers, as well as the limitations of sampling over multiple hypothalamic nuclei which may obscure distinct effects in one nucleus (as has been identified for AMPK in the VMH[327]). Notably, the only published report demonstrating altered phosphorylation of these proteins in response to exogenous ghrelin utilised ICV injections in rats[350].

These considerations notwithstanding, in view of the proposed key role played by hypothalamic malonyl-CoA as a signal of nutrient abundance[328], the finding of signals suggesting altered hypothalamic fatty acid metabolism in mutant mice is intriguing. Increased hypothalamic pACC would suggest greater AMPK activity and lead to a reduction in the malonyl-CoA pool, acting to increase FI by effectively generating a food deprivation cue. The identification of marked elevation in pFOXO1 in mutant mice in response to exogenous ghrelin is perhaps less straightforward to interpret. The transcription factor FOXO1 is a well-recognised downstream effector of insulin signalling which, via AKT, phosphorylates FOXO1, leading to its shuttling from nucleus to cytoplasm, rendering it inactive[351]. Hypothalamic expression of CA-FOXO1 in rats results in weight gain and inhibits leptin's effect on FI[352]. FOXO1 and STAT3 bind to adjacent sequences of the AgRP and POMC promoter, with both transcription factors exerting opposing actions on gene

expression of these neuropeptides[352]. Thus, the enhanced basal leptin sensitivity in young, pre-obese R299Q γ2 homozygous mutant mice would be expected to antagonise the action of FOXO1 by STAT3-induced competition for binding to the AGRP promoter. Moreover, insulin signalling has been shown to prevent FOXO1 binding and promote FOXO1 nuclear exclusion *in vitro*[352]. Thus, although not formally tested in young, pre-obese R299Q γ2 mutant mice, elevated pFOXO1 would be in keeping with intact or elevated hypothalamic insulin signalling which, together with enhanced leptin sensitivity, would imply that the central signalling of the two major afferent hormones indicating nutrient abundance to the hypothalamus are neither adversely affected by the R299Q γ2 mutation nor sufficient to account for the hyperphagic phenotype.

Leptin and insulin are not the only hormones shown to exert effects on hypothalamic FOXO1 phosphorylation and expression. Central administration of ghrelin to rats has been demonstrated to increase FOXO1 and pCREB – transcription factors promoting AgRP and NPY expression, respectively – and hence stimulate FI[350]. However, in contrast to leptin or insulin, central ghrelin administration increases *both* FOXO1 and pFOXO1 to a comparable extent[350]. The precise physiological relevance of the latter is uncertain but has also been identified in the pancreatic β-cell, where elevated levels of pFOXO1 are thought to elicit a protective effect against lipotoxicity-induced apoptosis and endoplasmic reticulum (ER) stress[348]. This protective effect of ghrelin may be particularly pertinent in the hypothalamus where ghrelin promotes fatty acid oxidation and ROS production, a recognised ER stress inducer[350].

What then is the transcription factor driving increased expression of AgRP to promote hyperphagia? The transcription factor BSX, which is expressed in both the ARC and DMH nuclei, has been conceptualised as a master regulator for hypothalamic orexigenic neuropeptide expression[353]. Both fasting and exogenous ghrelin upregulate *Bsx* mRNA expression in the ARC nucleus (but not DMH). However, the observation that mice which are deficient in the GHSR-1a still upregulate *Bsx* mRNA in response to 24 hour fasting indicates that, whilst ghrelin signalling can modulate *Bsx* expression, it is not essential for its regulation[353]. Whilst BSX KO mice do not manifest altered basal body weight or FI, they do exhibit marked downregulation (<20% of WT) of

ARC *Agrp* and *Npy* mRNA expression and blunted feeding response post-fast, with loss of BSX also attenuating the hyperphagia and severe obesity of the *ob*/*ob* mouse[349]. A further notable aspect of the phenotype of BSX KO mice is their severe reduction in locomotory behaviour, both at baseline and in response to food deprivation, indicating its essential role in the hypothalamic regulation of locomotion[349]. Against this background, the finding of increased spontaneous activity and 2.5-fold elevation in basal state ARC *Bsx* expression in AMPK R299Q γ2 homozygous mutant mice is consistent with a key role for BSX in their systemic phenotype. In combination with the exaggerated hyperphagia post-fasting, increased FI in response to ghrelin and normalisation of hyperphagia using a ghrelin receptor antagonist, the data lend support to the concept that a primary increase in central ghrelin signalling, converging on BSX, underlies the hyperphagia and increased locomotor activity of the R299Q γ2 KI.

Whether altered ghrelin signalling underlies other aspects of the systemic phenotype is uncertain, but its implication in the regulation of pancreatic glucose metabolism suggests that it may play a role in the impaired GSIS of R299Q γ2 mutant mice. Ghrelin is expressed in the pancreas and is secreted by a unique islet population of ε-cells, whilst ghrelin receptors have been identified on both α- and β-cells of the pancreatic islets[354]. Ghrelin exerts an insulinostatic effect on insulin secretion in isolated islets, whilst *in vivo* ghrelin administration attenuates the insulin response to an exogenous glucose load[354]. Intriguingly, a β-cell mechanism involving ghrelin-induced activation of AMPK and increased *Ucp2* expression, leading to reduction in insulin secretion, has been identified *in vitro*[355]. This is highly reminiscent of the pathway operating in the hypothalamus to regulate FI[229]. A model integrating these insights and the findings from investigation of the systemic phenotype of the R299Q γ2 KI is illustrated overleaf.

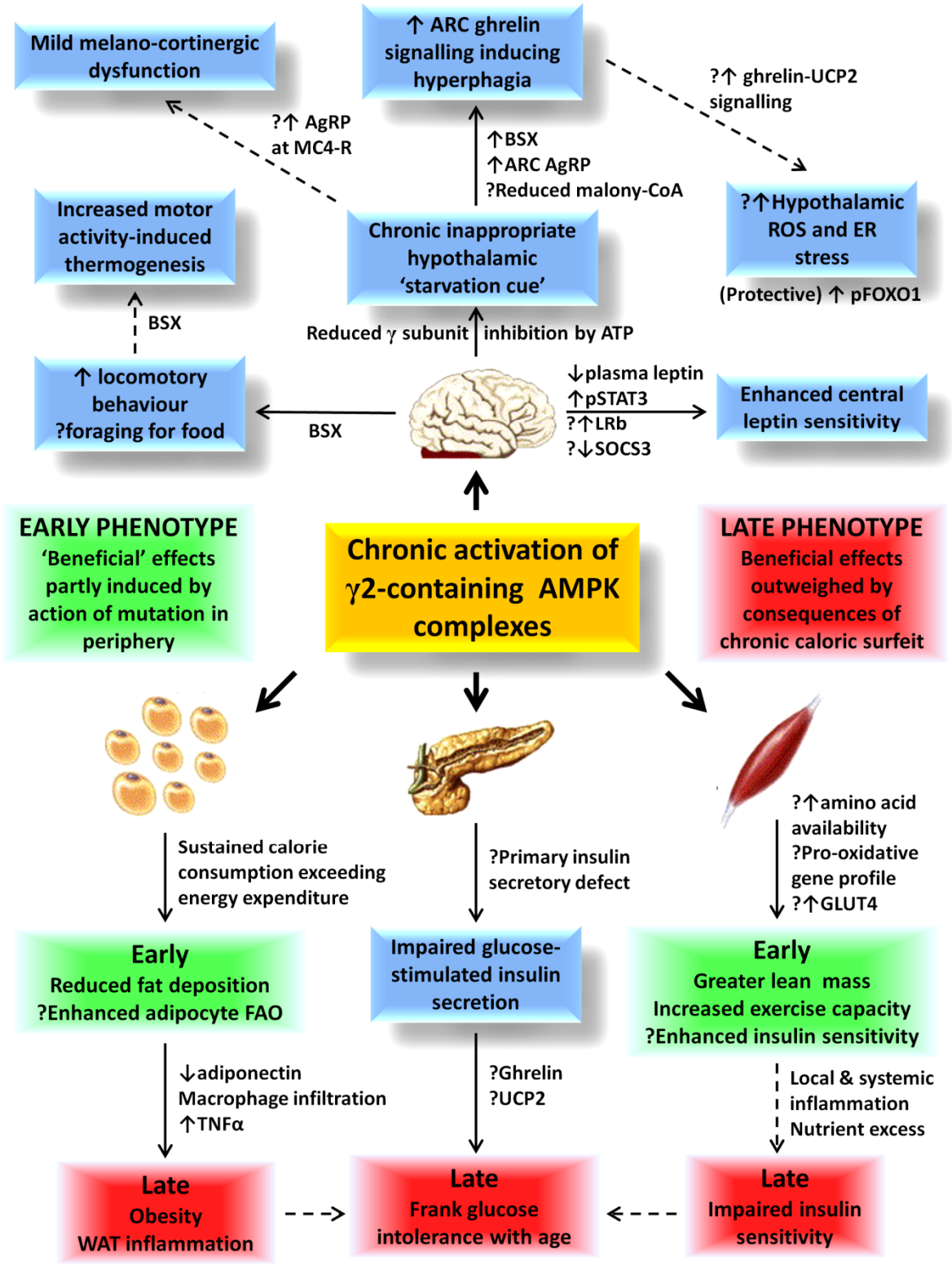


Figure 136. Model for the principal mechanisms underlying the systemic phenotype of the R299Q γ2 KI. Question marks highlight areas of uncertainty or hypotheses to be tested.

Chapter 8. Conclusions

8.1 Major results and significance of research

The experiments presented in this thesis are based on a novel mouse model bearing an R299Q mutation in *Prkag2*. Using this genetic platform, this thesis has sought to characterise its cardiac and systemic phenotype, to identify novel pathophysiological mechanisms underlying the cardiomyopathy associated with γ2 mutations and to begin to explore the potential physiological role(s) of γ2, both within (using a γ2 KO generated from the KI) and outside the heart. Using a combination of genetic, biochemical, cellular and *in vivo* techniques, the work presented in this thesis: provides novel insights for the pathophysiology of PRKAG2 cardiomyopathy, highlighting the need to consider both direct and glycogen-mediated consequences of the mutation in the pathogenesis of the cardiomyopathy; uncovers a novel physiological role for γ2 in the regulation of mammalian heart rate; and identifies significant negative metabolic sequelae ensuing from chronic (genetic) manipulation of γ2, insights that may be of particular relevance for evaluating the long-term risk-benefit profile of chronic pharmacological AMPK activation.

8.1.1 Principal cardiac findings and insights provided by the R299Q γ2 KI

i) The R299Q γ2 mutation is likely to exert a complex effect on AMPK activity dictated by ambient adenine nucleotide status. Evidence was obtained for the mutation abrogating allosteric activation of AMPK by AMP *in vitro*, in addition to significantly reducing γ2-specific AMPK activation under conditions of ATP depletion. In line with recent findings[124], indirect evidence was acquired from both the systemic and cardiac experiments to support the concept that the predominant and primary effect of γ2 mutations *in vivo* is to basally activate AMPK.

ii) By using a molecularly more faithful approach to model the disease, the R299Q γ2 KI is seen to exhibit a strikingly mild cardiac phenotype in comparison to all current transgenic models[119-122] for PRKAG2 disease. Whilst this may seem disadvantageous and limits the potential for certain lines of enquiry – notably an exploration of the mechanisms underlying the development of LVH – the absence of gross glycogen accumulation in the KI model provides a unique opportunity to

dissociate primary changes consequent to the γ2 mutation from secondary changes induced either directly by glycogen, or resulting from the effect of the latter on AMPK activity.

iii) Whilst it is the most frequently described *PRKAG2* mutation[82, 103, 110, 113], the choice of modelling the human R302Q mutation and its location in CBS1 may in large part explain the subtlety of the observed cardiac phenotype. Despite the rarity of PRKAG2 disease, some genotype-phenotype correlations can be drawn, with mutations affecting the second Bateman domain – such as R531Q (resulting in the most profound effects on AMPK activity) or E506Q – appearing to induce the most florid phenotypes and earliest onset of clinical presentation[106, 116]. Whilst gene-targeting murine ES cells with one of these mutations *may* have resulted in a more profound phenotype, permitting investigation of other aspects of the cardiomyopathy such as LVH and AV nodal disease, their likely systemic effects may have significantly confounded interpretation of cardiac findings. Moreover, detailed descriptions of families bearing the analogous human mutation to the R299Q mouse model and exhibiting a syndrome of sinus bradycardia, right bundle branch block (i.e. prolonged QRS), but no ventricular pre-excitation and low incidence of LVH (10%) have been published[113], highlighting the clinical relevance of the current KI model.

iv) The finding of altered cardiac function, electrophysiology and transcriptome at an early age in the R299Q γ2 KI points to a more complex view of the disease than that afforded by the current paradigm of a glycogen storage disorder. Novel disease mechanisms may potentially involve: modulation of ion channel expression and/or function, dysregulation of conduction system-enriched cell adhesion molecules (e.g. contactin-2) and, given the signal for marked upregulation of *Abhd1*, altered redox stress. In line with data from a genetic reversibility study[112], these findings suggest that a therapeutic strategy targeted solely at cardiac glycogen reduction is unlikely to be effective in all patients[110, 116], nor ameliorate the full breadth of cardiac disease features.

v) Taken in conjunction with findings from mutant *PRKAG2* transgenic models[119, 125], the combination of minimal glycogen excess with no overt pre-excitation in the R299Q γ2 KI strongly support a central role for profound glycogen accumulation in the pathogenesis of pre-excitation.

vi) A novel mechanism was identified for one of the most notable features of the cardiomyopathy evinced by R299Q γ2 KI mice, namely sinus bradycardia. In human PRKAG2 cardiomyopathy, sinus node abnormalities are a major indication for permanent pacemaker implantation and, arguably, more consistently present than either pre-excitation or LVH. Whilst there are undoubtedly limitations to extrapolating electrophysiological findings from murine models to humans[356] – including species differences in action potential duration, heart rate, ionic currents (in particular those determining repolarisation) and critical cardiac mass present to sustain arrhythmia – the findings from the R299Q γ2 KI strongly suggest that the sinus bradycardia and chronotropic incompetence of patients with PRKAG2 cardiomyopathy reflect an intrinsic reduction in sinus node automaticity and chronotropic modulation by adrenergic signalling consequent upon sinoatrial f-channel downregulation and reduced I_f current density.

vii) Given: the robust identification of HCN1 and HCN4 expression at both mRNA[196, 357] and protein[358] level in mammalian AV node; the progressive AV nodal block evidenced by a cardiac-inducible HCN4 KO model[197]; together with the findings of downregulation of cardiac *Hcn1* and *Hcn4* expression in R299Q γ2 mutant mice described here, one inference that can be made is that the high prevalence of progressive AV nodal conduction disease associated with *PRKAG2* mutations may reflect loss of f-channel function and progressive attrition in AV nodal I_f.

viii) In line with recent findings[358], the present work provides support for the concept that HCN1 – markedly downregulated at mRNA level in the hearts of R299Q γ2 homozygous mutant mice – plays a more prominent role in sinus node pacemaking than is currently widely considered. Indeed, it has been argued[358] that the identical pattern of expression of HCN1 and HCN4 denotes a combined contribution of the two isoforms to native sinoatrial I_f.

ix) Taking advantage of the *loxP* sequences flanking exon 7 of *Prkag2* in the KI, an attempt was made to generate the first-described global *Prkag2* KO. This mouse was viable, bred normally and appeared grossly normal until at least young adulthood. AMPK activity data suggested that the targeted deletion approach likely resulted in the presence of partially active peptides in some organs, notably the heart. Whilst its systemic phenotype was not the subject of this thesis, focused

cardiac phenotyping identified electrophysiological abnormalities, including alterations in intrinsic heart rate and upregulation in cardiac *Hcn1* and *Hcn4* expression opposite to that identified in the R299Q γ2 KI, supporting the contention that the R299Q γ2 KI broadly behaves as an activating mutation in the heart and indicating that γ2 is likely to be a novel physiological regulator of intrinsic sinoatrial cellular automaticity and, thus, mammalian heart rate *in vivo*. Furthermore, in view of the ongoing controversy regarding the precise contribution of I_f to pacemaking[359], the present work using both γ2 KI and KO models adds to the body of literature supporting a key role for sinoatrial HCN channels and their attendant I_f in the setting of intrinsic heart rate.

x) The observation that *Prkag2* is enriched in WT sinoatrial node (SAN) over ventricle, coupled with the finding of a (likely) basally activating γ2 mutation to coordinately repress multiple ion channel targets regulating the diastolic depolarisation phase of SAN myocytes – a fundamental property that permits them to function as pacemakers – raises the intriguing possibility that γ2 may have evolved to defend myocardial energy homeostasis by reducing overall cardiac oxygen consumption and metabolic demand via negative regulation of heart rate.

8.1.2 Principal systemic findings and insights provided by the R299Q γ2 KI

i) Gene-targeting *Prkag2* with the R299Q mutation induces profound systemic changes that alter with age. The net consequences of the mutation are broadly metabolically beneficial in young mice and include greater lean muscle mass, reduced fat mass and hypoleptinaemia, lower fasting insulin levels, a signal for greater spontaneous activity and enhanced voluntary exercise capacity.

ii) Over time, however, the progressive hyperphagia and sustained positive energy balance of R299Q γ2 mutant mice leads to frank obesity, systemic and white adipose tissue inflammation and impaired glucose tolerance.

iii) In contrast to rodent high-fat diet-induced models of the metabolic syndrome or diabetes, R299Q γ2 KI mice do not develop glucose intolerance associated with hyperinsulinaemia; rather, they display impaired glucose-stimulated insulin secretion (GSIS) and *lower* insulin levels than WT mice. Whilst not formally tested with isolated islet insulin secretion studies, the identification of

normal electrical glucose sensing in R299Q γ2 KI mice, coupled with existing observations on the regulation of pancreatic insulin secretion by AMPK[252, 290], is in keeping with an intrinsic pancreatic insulin secretory defect consequent to sustained, basal activation of γ2-containing heterotrimers.

iv) Hyperphagia, rather than reduced energy expenditure (EE), is the main driver of progressive weight gain and eventual obesity in KI mice. Indeed, signals were identified suggesting greater EE in KI mice, likely reflecting increases in lean mass and motor activity-induced thermogenesis.

v) R299Q γ2 homozygous mutant mice display an altered hypothalamic signalling substrate favouring hyperphagia, with ~2.5-fold upregulation in AgRP, a key pro-orexigenic neuropeptide whose expression is restricted to the ARC – the major hypothalamic locus for integration of peripheral nutritional and hormonal cues governing food intake and energy homeostasis.

vi) Probing the response of a fundamental satiety pathway downstream of the ARC – namely the melanocortinergic system – both directly with a melanocortin receptor agonist and indirectly with leptin, suggested that a major defect in anorexigenic signalling was unlikely to subserve KI hyperphagia. Indeed, evidence was found to suggest that the satiety response to leptin was fully intact or even enhanced in pre-obese mutant mice, likely in keeping with their hypoleptinaemia.

vii) Despite intact leptin sensitivity in R299Q γ2 KI mice, the manifest failure of endogenous lipostat signals to restrain their hyperphagia points to the likely relative ancestral importance of these two opposing systems, whereby signals driving food intake and food-seeking behaviour can override peripheral satiety signals to ensure survival of the organism. Seen in this light, R299Q γ2 KI mice can be conceptualised as experiencing an inappropriate, chronic starvation-like cue that drives food-seeking behaviour, hyperphagia and progressive weight gain.

viii) The identification of an exaggerated feeding response post-fasting and enhanced hyperphagic effect of exogenous ghrelin in R299Q γ2 KI mice points to a fundamental remodelling of hypothalamic signalling favouring enhanced receptivity and response to this key peripheral signal of negative energy balance. Evidence was found to support alterations in components of the hypothalamic ghrelin signalling pathway, most notably upregulation of BSX – a central

transcription factor regulating hypothalamic orexigenic neuropeptide expression in the ARC – in addition to signals suggestive of altered fatty acid metabolism, the latter an integral component of the post-GHSR pathway activated by ghrelin to promote AgRP transcription.

ix) The hypothesis of a primary 'gain' in the hypothalamic ghrelin-GHSR-AMPK-BSX-AgRP pathway as the predominant cause of hyperphagia in R299Q γ2 KI mice is supported by the finding that GHSR antagonism rescues their hyperphagia. Further, the findings from this thesis add to the growing body of literature highlighting the key role of AgRP neurons[303], AMPK, ghrelin and their interaction[64, 229] in driving mammalian food intake. They also allude to the potential potency of the pre- and post-synaptic AgRP neuron AMPK mechanism such that a modest but chronic elevation in basal AMPK activity can exert profound effects on cumulative food intake, thereby disrupting energy balance and leading to obesity. Given the emerging role of ghrelin in the regulation of pancreatic islet insulin secretion[354], activation of a β-cell ghrelin-AMPK-UCP2 pathway[355] may also account for the impaired GSIS of R299Q γ2 mutant mice.

x) Given the lack of cellular specificity of the gene-targeted model and the recognised ability of elevated hypothalamic AMPK activity to enhance orexigenic signals to increase food intake[321, 322], the particular utility of the R299Q γ2 KI may lie in its ability to model the effects of chronic AMPK activation over multiple organ systems *in vivo*. In the current setting of intense academic and pharmaceutical interest in the development of novel AMPK activators to more effectively treat the emerging global obesity epidemic and its attendant complication of type 2 diabetes, one of the key messages of the work in this thesis is to highlight that chronic systemic activation of (γ2) AMPK may come at significant metabolic cost – impaired GSIS and an excessive drive to eat – ultimately outweighing (at least in mice) beneficial peripheral effects and paradoxically actually contributing to glucose intolerance and increased adiposity.

xi) The specific biological role of γ2 in the regulation of mammalian appetite is arguably best dissected using mouse models bearing targeted deletions of *Prkag2* in discrete hypothalamic neuronal populations (e.g. AgRP or pre-AgRP neurons) and/or assessing the effects of bidirectional manipulation of *Prkag2* in the ARC on food intake using adeno-associated virus-mediated gene

transfer. Notwithstanding the limitations of the R299Q γ2 KI as a model with which to delineate the physiological role of γ2 in the regulation of food intake, the striking systemic phenotype associated with a subtle alteration in AMPK activity does raise the possibility that *PRKAG2* could be considered as a novel human obesity gene. However, the extrapolation of findings from monogenic obesity syndromes in mice to the situation in humans is not straightforward, with the current obesity epidemic – over 50% of adults and 30% of children in the US predicted to become clinically obese by 2030 – largely ascribed to complex interactions between a polygenic, non-syndromic substrate and adverse environmental/lifestyle/psychological factors, including (but not limited to) ready access to calorie-dense foodstuffs, reduced physical activity and disordered feeding behaviour[360]. Seen in this light, the investigation of mechanisms at work in rare rodent obesity models with simple Mendelian inheritance in order to shed light on human, non-syndromic common obesity may seem ambitious at best. Recent studies harnessing the power of genomics to elucidate the genetic architecture of common obesity have, however, raised support for the notion that common variants in *PRKAG2* may indeed play a role in influencing human metabolic traits, such as diabetes mellitus[361, 362].

8.2 Future directions

Whilst much indirect evidence has been obtained to indicate that the R299Q γ2 mutation is basally activating, definitive confirmation will likely require use of a fluorescent-based AMPK activity reporter[184] in live primary cells in addition to conventional SAMS assay readouts. Future cardiac work will include: a focused, direct interrogation of SAN ion channel expression in both KI and KO; assessment of SAN automaticity and I_f in the Sox2cre γ2 KO; determining whether acute loss of the R299Q γ2 mutant allele can restore a normal heart rate; and exploring the hypothesis that γ2 plays a key role in the intrinsic bradycardia of exercise. Systemic lines of enquiry will include: an assessment of skeletal muscle insulin sensitivity; measurement of pancreatic islet insulin secretion; testing whether direct islet GHSR or UCP2 antagonism can ameliorate the phenotype of impaired GSIS; and an exploration of the hypothalamic electrophysiological consequences of the R299Q γ2 mutation in mice co-expressing an NPY-hrGFP reporter[64].

REFERENCES

1. Gevers W, Krebs HA. The effects of adenine nucleotides on carbohydrate metabolism in pigeon-liver homogenates. Biochem J 1966;98:720-35.
2. Ramaiah A, Hathaway JA, Atkinson DE. Adenylate as a Metabolic Regulator. Effect on Yeast Phosphofructokinase Kinetics. J Biol Chem 1964;239:3619-22.
3. Atkinson DE. The energy charge of the adenylate pool as a regulatory parameter. Interaction with feedback modifiers. Biochemistry 1968;7:4030-4.
4. Krebs H. The Croonian Lecture, 1963. Gluconeogenesis. Proc R Soc Lond B Biol Sci 1964;159:545-64.
5. Hardie DG, Hawley SA. AMP-activated protein kinase: the energy charge hypothesis revisited. Bioessays 2001;23:1112-9.
6. Carling D, Zammit VA, Hardie DG. A common bicyclic protein kinase cascade inactivates the regulatory enzymes of fatty acid and cholesterol biosynthesis. FEBS Lett 1987;223:217-22.
7. Carlson CA, Kim KH. Regulation of hepatic acetyl coenzyme A carboxylase by phosphorylation and dephosphorylation. J Biol Chem 1973;248:378-80.
8. Yeh LA, Lee KH, Kim KH. Regulation of rat liver acetyl-CoA carboxylase. Regulation of phosphorylation and inactivation of acetyl-CoA carboxylase by the adenylate energy charge. J Biol Chem 1980;255:2308-14.
9. Beg ZH, Allmann DW, Gibson DM. Modulation of 3-hydroxy-3-methylglutaryl coenzyme A reductase activity with cAMP and wth protein fractions of rat liver cytosol. Biochem Biophys Res Commun 1973;54:1362-9.
10. Ferrer A, Caelles C, Massot N, Hegardt FG. Activation of rat liver cytosolic 3-hydroxy-3-methylglutaryl coenzyme A reductase kinase by adenosine 5'-monophosphate. Biochem Biophys Res Commun 1985;132:497-504.
11. Grahame Hardie D, Carling D, T.R. Sim A. The AMP-activated protein kinase: a multisubstrate regulator of lipid metabolism. Trends in biochemical sciences 1989;14:20-3.
12. Hardie DG, Ross FA, Hawley SA. AMPK: a nutrient and energy sensor that maintains energy homeostasis. Nat Rev Mol Cell Biol 2012;13:251-62.
13. Bungard D, Fuerth BJ, Zeng PY, et al. Signaling Kinase AMPK Activates Stress-Promoted Transcription via Histone H2B Phosphorylation. Science 2010.
14. Carling D, Aguan K, Woods A, et al. Mammalian AMP-activated protein kinase is homologous to yeast and plant protein kinases involved in the regulation of carbon metabolism. J Biol Chem 1994;269:11442-8.
15. Mitchelhill KI, Stapleton D, Gao G, et al. Mammalian AMP-activated protein kinase shares structural and functional homology with the catalytic domain of yeast Snf1 protein kinase. J Biol Chem 1994;269:2361-4.
16. Galdieri L, Mehrotra S, Yu S, Vancura A. Transcriptional regulation in yeast during diauxic shift and stationary phase. OMICS 2010;14:629-38.
17. Polge C, Thomas M. SNF1/AMPK/SnRK1 kinases, global regulators at the heart of energy control? Trends Plant Sci 2007;12:20-8.
18. Hong SP, Leiper FC, Woods A, Carling D, Carlson M. Activation of yeast Snf1 and mammalian AMP-activated protein kinase by upstream kinases. Proc Natl Acad Sci U S A 2003;100:8839-43.
19. Thelander M, Olsson T, Ronne H. Snf1-related protein kinase 1 is needed for growth in a normal day-night light cycle. EMBO J 2004;23:1900-10.
20. Hardie DG, Carling D, Gamblin SJ. AMP-activated protein kinase: also regulated by ADP? Trends Biochem Sci 2011;36:470-7.
21. Narbonne P, Roy R. Caenorhabditis elegans dauers need LKB1/AMPK to ration lipid reserves and ensure long-term survival. Nature 2009;457:210-4.
22. Hardie DG. AMP-activated protein kinase: an energy sensor that regulates all aspects of cell function. Genes Dev 2011;25:1895-908.
23. Xiao B, Heath R, Saiu P, et al. Structural basis for AMP binding to mammalian AMP-activated protein kinase. Nature 2007;449:496-500.
24. Steinberg GR, Kemp BE. AMPK in Health and Disease. Physiol Rev 2009;89:1025-78.
25. Dyck JR, Gao G, Widmer J, et al. Regulation of 5'-AMP-activated protein kinase activity by the noncatalytic beta and gamma subunits. J Biol Chem 1996;271:17798-803.
26. Xiao B, Sanders MJ, Underwood E, et al. Structure of mammalian AMPK and its regulation by ADP. Nature 2011;472:230-3.
27. Townley R, Shapiro L. Crystal structures of the adenylate sensor from fission yeast AMP-activated protein kinase. Science 2007;315:1726-9.

28. Amodeo GA, Rudolph MJ, Tong L. Crystal structure of the heterotrimer core of Saccharomyces cerevisiae AMPK homologue SNF1. Nature 2007;449:492-5.
29. Oakhill JS, Scott JW, Kemp BE. AMPK functions as an adenylate charge-regulated protein kinase. Trends Endocrinol Metab 2012;23:125-32.
30. Hardie DG. AMPK: a key regulator of energy balance in the single cell and the whole organism. Int J Obes (Lond) 2008;32 Suppl 4:S7-12.
31. Hardie DG. Signal transduction: How cells sense energy. Nature 2011;472:176-7.
32. Carling D, Thornton C, Woods A, Sanders MJ. AMP-activated protein kinase: new regulation, new roles? Biochem J 2012;445:11-27.
33. Polekhina G, Gupta A, Michell BJ, et al. AMPK beta subunit targets metabolic stress sensing to glycogen. Curr Biol 2003;13:867-71.
34. Hudson ER, Pan DA, James J, et al. A novel domain in AMP-activated protein kinase causes glycogen storage bodies similar to those seen in hereditary cardiac arrhythmias. Curr Biol 2003;13:861-6.
35. Martin DD, Beauchamp E, Berthiaume LG. Post-translational myristoylation: Fat matters in cellular life and death. Biochimie 2011;93:18-31.
36. Oakhill JS, Chen ZP, Scott JW, et al. beta-Subunit myristoylation is the gatekeeper for initiating metabolic stress sensing by AMP-activated protein kinase (AMPK). Proc Natl Acad Sci U S A 2010;107:19237-41.
37. Carling D, Mayer FV, Sanders MJ, Gamblin SJ. AMP-activated protein kinase: nature's energy sensor. Nat Chem Biol 2011;7:512-8.
38. Scott JW, Hawley SA, Green KA, et al. CBS domains form energy-sensing modules whose binding of adenosine ligands is disrupted by disease mutations. J Clin Invest 2004;113:274-84.
39. Kemp BE, Oakhill JS, Scott JW. AMPK structure and regulation from three angles. Structure 2007;15:1161-3.
40. Shirwany NA, Zou MH. AMPK in cardiovascular health and disease. Acta Pharmacol Sin 2010;31:1075-84.
41. Cheung PC, Salt IP, Davies SP, Hardie DG, Carling D. Characterization of AMP-activated protein kinase gamma-subunit isoforms and their role in AMP binding. Biochem J 2000;346 Pt 3:659-69.
42. Stapleton D, Mitchelhill KI, Gao G, et al. Mammalian AMP-activated protein kinase subfamily. J Biol Chem 1996;271:611-4.
43. Li J, Coven DL, Miller EJ, et al. Activation of AMPK alpha- and gamma-isoform complexes in the intact ischemic rat heart. Am J Physiol Heart Circ Physiol 2006;291:H1927-34.
44. Salt I, Celler JW, Hawley SA, et al. AMP-activated protein kinase: greater AMP dependence, and preferential nuclear localization, of complexes containing the alpha2 isoform. Biochem J 1998;334 (Pt 1):177-87.
45. McGee SL, Howlett KF, Starkie RL, Cameron-Smith D, Kemp BE, Hargreaves M. Exercise increases nuclear AMPK alpha2 in human skeletal muscle. Diabetes 2003;52:926-8.
46. McGee SL, Hargreaves M. AMPK-mediated regulation of transcription in skeletal muscle. Clin Sci (Lond) 2010;118:507-18.
47. Thornton C, Snowden MA, Carling D. Identification of a novel AMP-activated protein kinase beta subunit isoform that is highly expressed in skeletal muscle. J Biol Chem 1998;273:12443-50.
48. Lang T, Yu L, Tu Q, et al. Molecular cloning, genomic organization, and mapping of PRKAG2, a heart abundant gamma2 subunit of 5'-AMP-activated protein kinase, to human chromosome 7q36. Genomics 2000;70:258-63.
49. Pinter K, Grignani RT, Czibik G, Farza H, Watkins H, Redwood C. Embryonic expression of AMPK gamma subunits and the identification of a novel gamma2 transcript variant in adult heart. J Mol Cell Cardiol 2012;53:342-9.
50. Kim M, Shen M, Ngoy S, Karamanlidis G, Liao R, Tian R. AMPK isoform expression in the normal and failing hearts. J Mol Cell Cardiol 2012;52:1066-73.
51. Mahlapuu M, Johansson C, Lindgren K, et al. Expression profiling of the gamma-subunit isoforms of AMP-activated protein kinase suggests a major role for gamma3 in white skeletal muscle. Am J Physiol Endocrinol Metab 2004;286:E194-200.
52. Barnes BR, Marklund S, Steiler TL, et al. The 5'-AMP-activated protein kinase gamma3 isoform has a key role in carbohydrate and lipid metabolism in glycolytic skeletal muscle. J Biol Chem 2004;279:38441-7.
53. Kim M, Tian R. Transcript variant dictates Prkag2 cardiomyopathy? J Mol Cell Cardiol 2012.
54. Davies SP, Carling D, Hardie DG. Tissue distribution of the AMP-activated protein kinase, and lack of activation by cyclic-AMP-dependent protein kinase, studied using a specific and sensitive peptide assay. Eur J Biochem 1989;186:123-8.

55. Dale S, Wilson WA, Edelman AM, Hardie DG. Similar substrate recognition motifs for mammalian AMP-activated protein kinase, higher plant HMG-CoA reductase kinase-A, yeast SNF1, and mammalian calmodulin-dependent protein kinase I. FEBS Lett 1995;361:191-5.
56. Carling D, Sanders MJ, Woods A. The regulation of AMP-activated protein kinase by upstream kinases. Int J Obes (Lond) 2008;32 Suppl 4:S55-9.
57. Hardie DG. AMP-activated protein kinase as a drug target. Annu Rev Pharmacol Toxicol 2007;47:185-210.
58. Hawley SA, Boudeau J, Reid JL, et al. Complexes between the LKB1 tumor suppressor, STRAD alpha/beta and MO25 alpha/beta are upstream kinases in the AMP-activated protein kinase cascade. J Biol 2003;2:28.
59. Woods A, Dickerson K, Heath R, et al. Ca2+/calmodulin-dependent protein kinase kinase-beta acts upstream of AMP-activated protein kinase in mammalian cells. Cell Metab 2005;2:21-33.
60. Hawley SA, Pan DA, Mustard KJ, et al. Calmodulin-dependent protein kinase kinase-beta is an alternative upstream kinase for AMP-activated protein kinase. Cell Metab 2005;2:9-19.
61. Hurley RL, Anderson KA, Franzone JM, Kemp BE, Means AR, Witters LA. The Ca2+/calmodulin-dependent protein kinase kinases are AMP-activated protein kinase kinases. J Biol Chem 2005;280:29060-6.
62. Fogarty S, Hawley SA, Green KA, Saner N, Mustard KJ, Hardie DG. Calmodulin-dependent protein kinase kinase-beta activates AMPK without forming a stable complex: synergistic effects of Ca2+ and AMP. Biochem J 2010;426:109-18.
63. Anderson KA, Ribar TJ, Lin F, et al. Hypothalamic CaMKK2 contributes to the regulation of energy balance. Cell Metab 2008;7:377-88.
64. Yang Y, Atasoy D, Su HH, Sternson SM. Hunger states switch a flip-flop memory circuit via a synaptic AMPK-dependent positive feedback loop. Cell 2011;146:992-1003.
65. Momcilovic M, Hong SP, Carlson M. Mammalian TAK1 activates Snf1 protein kinase in yeast and phosphorylates AMP-activated protein kinase in vitro. J Biol Chem 2006;281:25336-43.
66. Herrero-Martin G, Hoyer-Hansen M, Garcia-Garcia C, et al. TAK1 activates AMPK-dependent cytoprotective autophagy in TRAIL-treated epithelial cells. EMBO J 2009;28:677-85.
67. Xie M, Zhang D, Dyck JR, et al. A pivotal role for endogenous TGF-beta-activated kinase-1 in the LKB1/AMP-activated protein kinase energy-sensor pathway. Proc Natl Acad Sci U S A 2006;103:17378-83.
68. Oakhill JS, Steel R, Chen ZP, et al. AMPK is a direct adenylate charge-regulated protein kinase. Science 2011;332:1433-5.
69. Oakhill JS, Scott JW, Kemp BE. Structure and function of AMP-activated protein kinase. Acta Physiol (Oxf) 2009;196:3-14.
70. Carling D, Clarke PR, Zammit VA, Hardie DG. Purification and characterization of the AMP-activated protein kinase. Copurification of acetyl-CoA carboxylase kinase and 3-hydroxy-3-methylglutaryl-CoA reductase kinase activities. Eur J Biochem 1989;186:129-36.
71. Bland ML, Birnbaum MJ. Cell biology. ADaPting to energetic stress. Science 2011;332:1387-8.
72. Mayer FV, Heath R, Underwood E, et al. ADP regulates SNF1, the Saccharomyces cerevisiae homolog of AMP-activated protein kinase. Cell Metab 2011;14:707-14.
73. Roach PJ, Depaoli-Roach AA, Hurley TD, Tagliabracci VS. Glycogen and its metabolism: some new developments and old themes. Biochem J 2012;441:763-87.
74. Bendayan M, Londono I, Kemp BE, Hardie GD, Ruderman N, Prentki M. Association of AMP-activated protein kinase subunits with glycogen particles as revealed in situ by immunoelectron microscopy. J Histochem Cytochem 2009;57:963-71.
75. McBride A, Hardie DG. AMP-activated protein kinase--a sensor of glycogen as well as AMP and ATP? Acta Physiol (Oxf) 2009;196:99-113.
76. Carling D, Hardie DG. The substrate and sequence specificity of the AMP-activated protein kinase. Phosphorylation of glycogen synthase and phosphorylase kinase. Biochim Biophys Acta 1989;1012:81-6.
77. Jorgensen SB, Nielsen JN, Birk JB, et al. The alpha2-5'AMP-activated protein kinase is a site 2 glycogen synthase kinase in skeletal muscle and is responsive to glucose loading. Diabetes 2004;53:3074-81.
78. Vernia S, Solaz-Fuster MC, Gimeno-Alcaniz JV, et al. AMP-activated protein kinase phosphorylates R5/PTG, the glycogen targeting subunit of the R5/PTG-protein phosphatase 1 holoenzyme, and accelerates its down-regulation by the laforin-malin complex. J Biol Chem 2009;284:8247-55.
79. Roma-Mateo C, Solaz-Fuster Mdel C, Gimeno-Alcaniz JV, et al. Laforin, a dual-specificity phosphatase involved in Lafora disease, is phosphorylated at Ser25 by AMP-activated protein kinase. Biochem J 2011;439:265-75.
80. McBride A, Ghilagaber S, Nikolaev A, Hardie DG. The glycogen-binding domain on the AMPK beta subunit allows the kinase to act as a glycogen sensor. Cell Metab 2009;9:23-34.
81. Milan D, Jeon JT, Looft C, et al. A mutation in PRKAG3 associated with excess glycogen content in pig skeletal muscle. Science 2000;288:1248-51.

82. Arad M, Benson DW, Perez-Atayde AR, et al. Constitutively active AMP kinase mutations cause glycogen storage disease mimicking hypertrophic cardiomyopathy. J Clin Invest 2002;109:357-62.
83. Davies SP, Helps NR, Cohen PT, Hardie DG. 5'-AMP inhibits dephosphorylation, as well as promoting phosphorylation, of the AMP-activated protein kinase. Studies using bacterially expressed human protein phosphatase-2C alpha and native bovine protein phosphatase-2AC. FEBS Lett 1995;377:421-5.
84. Moore F, Weekes J, Hardie DG. Evidence that AMP triggers phosphorylation as well as direct allosteric activation of rat liver AMP-activated protein kinase. A sensitive mechanism to protect the cell against ATP depletion. Eur J Biochem 1991;199:691-7.
85. Voss M, Paterson J, Kelsall IR, et al. Ppm1E is an in cellulo AMP-activated protein kinase phosphatase. Cell Signal 2011;23:114-24.
86. Garcia-Haro L, Garcia-Gimeno MA, Neumann D, Beullens M, Bollen M, Sanz P. The PP1-R6 protein phosphatase holoenzyme is involved in the glucose-induced dephosphorylation and inactivation of AMP-activated protein kinase, a key regulator of insulin secretion, in MIN6 beta cells. FASEB J 2010;24:5080-91.
87. Enfalt AC, Lundstrom K, Karlsson A, Hansson I. Estimated frequency of the RN- allele in Swedish Hampshire pigs and comparison of glycolytic potential, carcass composition, and technological meat quality among Swedish Hampshire, Landrace, and Yorkshire pigs. J Anim Sci 1997;75:2924-35.
88. Hamilton SR, Stapleton D, O'Donnell JB, Jr., et al. An activating mutation in the gamma1 subunit of the AMP-activated protein kinase. FEBS Lett 2001;500:163-8.
89. Costford SR, Kavaslar N, Ahituv N, et al. Gain-of-function R225W mutation in human AMPKgamma(3) causing increased glycogen and decreased triglyceride in skeletal muscle. PLoS One 2007;2:e903.
90. Crawford SA, Costford SR, Aguer C, et al. Naturally occurring R225W mutation of the gene encoding AMP-activated protein kinase (AMPK)gamma(3) results in increased oxidative capacity and glucose uptake in human primary myotubes. Diabetologia 2010;53:1986-97.
91. Blair E, Redwood C, Ashrafian H, et al. Mutations in the gamma(2) subunit of AMP-activated protein kinase cause familial hypertrophic cardiomyopathy: evidence for the central role of energy compromise in disease pathogenesis. Hum Mol Genet 2001;10:1215-20.
92. Gollob MH, Seger JJ, Gollob TN, et al. Novel PRKAG2 mutation responsible for the genetic syndrome of ventricular preexcitation and conduction system disease with childhood onset and absence of cardiac hypertrophy. Circulation 2001;104:3030-3.
93. Yavari A, Ashrafian H. Inherited cardiac disease. Medicine 2010;38:496-501.
94. Watkins H, Ashrafian H, Redwood C. Inherited cardiomyopathies. N Engl J Med 2011;364:1643-56.
95. Ashrafian H, Watkins H. Reviews of translational medicine and genomics in cardiovascular disease: new disease taxonomy and therapeutic implications cardiomyopathies: therapeutics based on molecular phenotype. J Am Coll Cardiol 2007;49:1251-64.
96. Redwood CS, Moolman-Smook JC, Watkins H. Properties of mutant contractile proteins that cause hypertrophic cardiomyopathy. Cardiovasc Res 1999;44:20-36.
97. Moore JR, Leinwand L, Warshaw DM. Understanding cardiomyopathy phenotypes based on the functional impact of mutations in the Myosin motor. Circ Res 2012;111:375-85.
98. Ashrafian H, Redwood C, Blair E, Watkins H. Hypertrophic cardiomyopathy:a paradigm for myocardial energy depletion. Trends Genet 2003;19:263-8.
99. Spindler M, Saupe KW, Christe ME, et al. Diastolic dysfunction and altered energetics in the alphaMHC403/+ mouse model of familial hypertrophic cardiomyopathy. J Clin Invest 1998;101:1775-83.
100. Neubauer S. The failing heart--an engine out of fuel. N Engl J Med 2007;356:1140-51.
101. Crilley JG, Boehm EA, Blair E, et al. Hypertrophic cardiomyopathy due to sarcomeric gene mutations is characterized by impaired energy metabolism irrespective of the degree of hypertrophy. J Am Coll Cardiol 2003;41:1776-82.
102. MacRae CA, Ghaisas N, Kass S, et al. Familial Hypertrophic cardiomyopathy with Wolff-Parkinson-White syndrome maps to a locus on chromosome 7q3. J Clin Invest 1995;96:1216-20.
103. Gollob MH, Green MS, Tang AS, et al. Identification of a gene responsible for familial Wolff-Parkinson-White syndrome. N Engl J Med 2001;344:1823-31.
104. Willems JL, Robles de Medina EO, Bernard R, et al. Criteria for intraventricular conduction disturbances and pre-excitation. World Health Organizational/International Society and Federation for Cardiology Task Force Ad Hoc. J Am Coll Cardiol 1985;5:1261-75.
105. J.Podrid P. Preexcitation syndromes. In: Basow DS, ed. Waltham, MA: UpToDate; 2012.
106. Burwinkel B, Scott JW, Buhrer C, et al. Fatal congenital heart glycogenosis caused by a recurrent activating R531Q mutation in the gamma 2-subunit of AMP-activated protein kinase (PRKAG2), not by phosphorylase kinase deficiency. Am J Hum Genet 2005;76:1034-49.

107. Murphy RT, Mogensen J, McGarry K, et al. Adenosine monophosphate-activated protein kinase disease mimicks hypertrophic cardiomyopathy and Wolff-Parkinson-White syndrome: natural history. J Am Coll Cardiol 2005;45:922-30.
108. Genge A, Massie R. Mitochondrial myopathies: Clinical features and diagnosis. In: Basow DS, ed. Waltham, MA: UpToDate 2012.
109. Gollob MH, Green MS, Tang AS, Roberts R. PRKAG2 cardiac syndrome: familial ventricular preexcitation, conduction system disease, and cardiac hypertrophy. Curr Opin Cardiol 2002;17:229-34.
110. Tan HL, van der Wal AC, Campian ME, et al. Nodoventricular accessory pathways in PRKAG2-dependent familial preexcitation syndrome reveal a disorder in cardiac development. Circ Arrhythm Electrophysiol 2008;1:276-81.
111. Govindan M, Ward D, Behr E. A rare connection: fasciculoventricular pathway in PRKAG2 disease. J Cardiovasc Electrophysiol 2010;21:329-32.
112. Wolf CM, Arad M, Ahmad F, et al. Reversibility of PRKAG2 glycogen-storage cardiomyopathy and electrophysiological manifestations. Circulation 2008;117:144-54.
113. Sternick EB, Oliva A, Magalhaes LP, et al. Familial pseudo-Wolff-Parkinson-White syndrome. J Cardiovasc Electrophysiol 2006;17:724-32.
114. Akman HO, Sampayo JN, Ross FA, et al. Fatal infantile cardiac glycogenosis with phosphorylase kinase deficiency and a mutation in the gamma2-subunit of AMP-activated protein kinase. Pediatr Res 2007;62:499-504.
115. Arad M, Maron BJ, Gorham JM, et al. Glycogen storage diseases presenting as hypertrophic cardiomyopathy. N Engl J Med 2005;352:362-72.
116. Kelly BP, Russell MW, Hennessy JR, Ensing GJ. Severe hypertrophic cardiomyopathy in an infant with a novel PRKAG2 gene mutation: potential differences between infantile and adult onset presentation. Pediatr Cardiol 2009;30:1176-9.
117. Bayrak F, Komurcu-Bayrak E, Mutlu B, Kahveci G, Basaran Y, Erginel-Unaltuna N. Ventricular pre-excitation and cardiac hypertrophy mimicking hypertrophic cardiomyopathy in a Turkish family with a novel PRKAG2 mutation. Eur J Heart Fail 2006;8:712-5.
118. Laforet P, Richard P, Said MA, et al. A new mutation in PRKAG2 gene causing hypertrophic cardiomyopathy with conduction system disease and muscular glycogenosis. Neuromuscul Disord 2006;16:178-82.
119. Arad M, Moskowitz IP, Patel VV, et al. Transgenic mice overexpressing mutant PRKAG2 define the cause of Wolff-Parkinson-White syndrome in glycogen storage cardiomyopathy. Circulation 2003;107:2850-6.
120. Sidhu JS, Rajawat YS, Rami TG, et al. Transgenic mouse model of ventricular preexcitation and atrioventricular reentrant tachycardia induced by an AMP-activated protein kinase loss-of-function mutation responsible for Wolff-Parkinson-White syndrome. Circulation 2005;111:21-9.
121. Davies JK, Wells DJ, Liu K, et al. Characterization of the role of gamma2 R531G mutation in AMP-activated protein kinase in cardiac hypertrophy and Wolff-Parkinson-White syndrome. Am J Physiol Heart Circ Physiol 2006;290:H1942-51.
122. Banerjee SK, Ramani R, Saba S, et al. A PRKAG2 mutation causes biphasic changes in myocardial AMPK activity and does not protect against ischemia. Biochem Biophys Res Commun 2007;360:381-7.
123. Ng WA, Grupp IL, Subramaniam A, Robbins J. Cardiac myosin heavy chain mRNA expression and myocardial function in the mouse heart. Circ Res 1991;68:1742-50.
124. Folmes KD, Chan AY, Koonen DP, et al. Distinct early signaling events resulting from the expression of the PRKAG2 R302Q mutant of AMPK contribute to increased myocardial glycogen. Circ Cardiovasc Genet 2009;2:457-66.
125. Patel VV, Arad M, Moskowitz IP, et al. Electrophysiologic characterization and postnatal development of ventricular pre-excitation in a mouse model of cardiac hypertrophy and Wolff-Parkinson-White syndrome. J Am Coll Cardiol 2003;42:942-51.
126. Gollob MH. Glycogen storage disease as a unifying mechanism of disease in the PRKAG2 cardiac syndrome. Biochem Soc Trans 2003;31:228-31.
127. Luptak I, Shen M, He H, et al. Aberrant activation of AMP-activated protein kinase remodels metabolic network in favor of cardiac glycogen storage. J Clin Invest 2007;117:1432-9.
128. Gollob MH. Modulating phenotypic expression of the PRKAG2 cardiac syndrome. Circulation 2008;117:134-5.
129. Bulkley BH, Hutchins GM. Pompe's disease presenting as hypertrophic myocardiopathy with Wolff-Parkinson-White syndrome. Am Heart J 1978;96:246-52.
130. Cheng Z, Fang Q. Danon disease: focusing on heart. J Hum Genet 2012;57:407-10.
131. Doetschman T, Azhar M. Cardiac-specific inducible and conditional gene targeting in mice. Circ Res 2012;110:1498-512.

132. Banerjee SK, Wang DW, Alzamora R, et al. SGLT1, a novel cardiac glucose transporter, mediates increased glucose uptake in PRKAG2 cardiomyopathy. J Mol Cell Cardiol 2010;49:683-92.
133. Hunter RW, Treebak JT, Wojtaszewski JF, Sakamoto K. Molecular mechanism by which AMP-activated protein kinase activation promotes glycogen accumulation in muscle. Diabetes 2011;60:766-74.
134. Hue L, Taegtmeyer H. The Randle cycle revisited: a new head for an old hat. Am J Physiol Endocrinol Metab 2009;297:E578-91.
135. Banerjee SK, Wang DW, Alzamora R, et al. SGLT1, a novel cardiac glucose transporter, mediates increased glucose uptake in PRKAG2 cardiomyopathy. J Mol Cell Cardiol 2010.
136. Ha AC, Renaud JM, Dekemp RA, et al. In vivo assessment of myocardial glucose uptake by positron emission tomography in adults with the PRKAG2 cardiac syndrome. Circ Cardiovasc Imaging 2009;2:485-91.
137. Watkins H, Ashrafian H, McKenna WJ. The genetics of hypertrophic cardiomyopathy: Teare redux. Heart 2008;94:1264-8.
138. Banerjee SK, McGaffin KR, Huang XN, Ahmad F. Activation of cardiac hypertrophic signaling pathways in a transgenic mouse with the human PRKAG2 Thr400Asn mutation. Biochim Biophys Acta 2010;1802:284-91.
139. Hallows KR, Raghuram V, Kemp BE, Witters LA, Foskett JK. Inhibition of cystic fibrosis transmembrane conductance regulator by novel interaction with the metabolic sensor AMP-activated protein kinase. J Clin Invest 2000;105:1711-21.
140. Wyatt CN, Mustard KJ, Pearson SA, et al. AMP-activated protein kinase mediates carotid body excitation by hypoxia. J Biol Chem 2007;282:8092-8.
141. Light PE, Wallace CH, Dyck JR. Constitutively active adenosine monophosphate-activated protein kinase regulates voltage-gated sodium channels in ventricular myocytes. Circulation 2003;107:1962-5.
142. Light PE. Familial Wolff-Parkinson-White Syndrome: a disease of glycogen storage or ion channel dysfunction? J Cardiovasc Electrophysiol 2006;17 Suppl 1:S158-S61.
143. Yoshida H, Bao L, Kefaloyianni E, et al. AMP-activated protein kinase connects cellular energy metabolism to KATP channel function. J Mol Cell Cardiol 2012;52:410-8.
144. Hardie DG. AMPK and SNF1: Snuffing Out Stress. Cell Metab 2007;6:339-40.
145. Ignoul S, Eggermont J. CBS domains: structure, function, and pathology in human proteins. Am J Physiol Cell Physiol 2005;289:C1369-78.
146. Arad M, Seidman CE, Seidman JG. AMP-activated protein kinase in the heart: role during health and disease. Circ Res 2007;100:474-88.
147. Daniel T, Carling D. Functional analysis of mutations in the gamma 2 subunit of AMP-activated protein kinase associated with cardiac hypertrophy and Wolff-Parkinson-White syndrome. J Biol Chem 2002;277:51017-24.
148. Ahmad F, Arad M, Musi N, et al. Increased alpha2 subunit-associated AMPK activity and PRKAG2 cardiomyopathy. Circulation 2005;112:3140-8.
149. Zou L, Shen M, Arad M, et al. N488I mutation of the gamma2-subunit results in bidirectional changes in AMP-activated protein kinase activity. Circ Res 2005;97:323-8.
150. Gordon JW, Scangos GA, Plotkin DJ, Barbosa JA, Ruddle FH. Genetic transformation of mouse embryos by microinjection of purified DNA. Proc Natl Acad Sci U S A 1980;77:7380-4.
151. Yutzey KE, Robbins J. Principles of genetic murine models for cardiac disease. Circulation 2007;115:792-9.
152. Doyle A, McGarry MP, Lee NA, Lee JJ. The construction of transgenic and gene knockout/knockin mouse models of human disease. Transgenic Res 2012;21:327-49.
153. Haruyama N, Cho A, Kulkarni AB. Overview: engineering transgenic constructs and mice. Curr Protoc Cell Biol 2009;Chapter 19:Unit 19 0.
154. Moga MA, Nakamura T, Robbins J. Genetic approaches for changing the heart and dissecting complex syndromes. J Mol Cell Cardiol 2008;45:148-55.
155. Moroy T, Heyd F. The impact of alternative splicing in vivo: mouse models show the way. RNA 2007;13:1155-71.
156. Picciotto MR, Wickman K. Using knockout and transgenic mice to study neurophysiology and behavior. Physiol Rev 1998;78:1131-63.
157. Branda CS, Dymecki SM. Talking about a revolution: The impact of site-specific recombinases on genetic analyses in mice. Dev Cell 2004;6:7-28.
158. Rance KA, Hambly C, Dalgleish G, Fustin JM, Bunger L, Speakman JR. Quantitative trait Loci for regional adiposity in mouse lines divergently selected for food intake. Obesity (Silver Spring) 2007;15:2994-3004.
159. Schmittgen TD, Livak KJ. Analyzing real-time PCR data by the comparative C(T) method. Nat Protoc 2008;3:1101-8.

160. Livak KJ. Allelic discrimination using fluorogenic probes and the 5' nuclease assay. Genet Anal 1999;14:143-9.
161. Hastie CJ, McLauchlan HJ, Cohen P. Assay of protein kinases using radiolabeled ATP: a protocol. Nat Protoc 2006;1:968-71.
162. Schneider CA, Rasband WS, Eliceiri KW. NIH Image to ImageJ: 25 years of image analysis. Nat Meth 2012;9:671-5.
163. Mark M, Teletin M, Antal C, et al. Histopathology in mouse metabolic investigations. Curr Protoc Mol Biol 2007;Chapter 29:Unit 29B 4.
164. Ashrafian H, Czibik G, Bellahcene M, et al. Fumarate Is Cardioprotective via Activation of the Nrf2 Antioxidant Pathway. Cell Metab 2012;15:361-71.
165. Lang RM, Bierig M, Devereux RB, et al. Recommendations for chamber quantification: a report from the American Society of Echocardiography's Guidelines and Standards Committee and the Chamber Quantification Writing Group, developed in conjunction with the European Association of Echocardiography, a branch of the European Society of Cardiology. J Am Soc Echocardiogr 2005;18:1440-63.
166. Collins KA, Korcarz CE, Lang RM. Use of echocardiography for the phenotypic assessment of genetically altered mice. Physiol Genomics 2003;13:227-39.
167. Stypmann J, Engelen MA, Troatz C, Rothenburger M, Eckardt L, Tiemann K. Echocardiographic assessment of global left ventricular function in mice. Lab Anim 2009;43:127-37.
168. Fayssoil A. Tissue Doppler characterization of cardiac phenotype in mouse. Eur J Radiol 2009;72:82-4.
169. Claycomb WC, Lanson NA, Jr., Stallworth BS, et al. HL-1 cells: a cardiac muscle cell line that contracts and retains phenotypic characteristics of the adult cardiomyocyte. Proc Natl Acad Sci U S A 1998;95:2979-84.
170. White SM, Constantin PE, Claycomb WC. Cardiac physiology at the cellular level: use of cultured HL-1 cardiomyocytes for studies of cardiac muscle cell structure and function. Am J Physiol Heart Circ Physiol 2004;286:H823-9.
171. Schneider JE, Wiesmann F, Lygate CA, Neubauer S. How to perform an accurate assessment of cardiac function in mice using high-resolution magnetic resonance imaging. J Cardiovasc Magn Reson 2006;8:693-701.
172. Schneider JE, Stork LA, Bell JT, et al. Cardiac structure and function during ageing in energetically compromised Guanidinoacetate N-methyltransferase (GAMT)-knockout mice - a one year longitudinal MRI study. J Cardiovasc Magn Reson 2008;10:9.
173. Phillips D, Ten Hove M, Schneider JE, et al. Mice over-expressing the myocardial creatine transporter develop progressive heart failure and show decreased glycolytic capacity. J Mol Cell Cardiol 2010;48:582-90.
174. Wiesmann F, Ruff J, Hiller KH, Rommel E, Haase A, Neubauer S. Developmental changes of cardiac function and mass assessed with MRI in neonatal, juvenile, and adult mice. Am J Physiol Heart Circ Physiol 2000;278:H652-7.
175. Taksir TV, Griffiths D, Johnson J, Ryan S, Shihabuddin LS, Thurberg BL. Optimized preservation of CNS morphology for the identification of glycogen in the Pompe mouse model. J Histochem Cytochem 2007;55:991-8.
176. Raben N, Nagaraju K, Lee E, et al. Targeted disruption of the acid alpha-glucosidase gene in mice causes an illness with critical features of both infantile and adult human glycogen storage disease type II. J Biol Chem 1998;273:19086-92.
177. James JF, Hewett TE, Robbins J. Cardiac physiology in transgenic mice. Circ Res 1998;82:407-15.
178. Hoit BD. New approaches to phenotypic analysis in adult mice. J Mol Cell Cardiol 2001;33:27-35.
179. Tan LB. Cardiac pumping capability and prognosis in heart failure. Lancet 1986;2:1360-3.
180. Francis GS, Desai MY. Contractile reserve: are we beginning to understand it? JACC Cardiovasc Imaging 2008;1:727-8.
181. Fewell JG, Osinska H, Klevitsky R, et al. A treadmill exercise regimen for identifying cardiovascular phenotypes in transgenic mice. Am J Physiol 1997;273:H1595-605.
182. Yin FC, Spurgeon HA, Rakusan K, Weisfeldt ML, Lakatta EG. Use of tibial length to quantify cardiac hypertrophy: application in the aging rat. Am J Physiol 1982;243:H941-7.
183. Taegtmeyer H, Sen S, Vela D. Return to the fetal gene program: a suggested metabolic link to gene expression in the heart. Ann N Y Acad Sci 2010;1188:191-8.
184. Tsou P, Zheng B, Hsu CH, Sasaki AT, Cantley LC. A fluorescent reporter of AMPK activity and cellular energy stress. Cell Metab 2011;13:476-86.
185. Dipple KM, McCabe ER. Phenotypes of patients with "simple" Mendelian disorders are complex traits: thresholds, modifiers, and systems dynamics. Am J Hum Genet 2000;66:1729-35.

186. Dipple KM, McCabe ER. Modifier genes convert "simple" Mendelian disorders to complex traits. Mol Genet Metab 2000;71:43-50.
187. Hughes ED, Qu YY, Genik SJ, et al. Genetic variation in C57BL/6 ES cell lines and genetic instability in the Bruce4 C57BL/6 ES cell line. Mamm Genome 2007;18:549-58.
188. Seong E, Saunders TL, Stewart CL, Burmeister M. To knockout in 129 or in C57BL/6: that is the question. Trends Genet 2004;20:59-62.
189. Suzuki M, Carlson KM, Marchuk DA, Rockman HA. Genetic modifier loci affecting survival and cardiac function in murine dilated cardiomyopathy. Circulation 2002;105:1824-9.
190. Barnabei MS, Palpant NJ, Metzger JM. Influence of genetic background on ex vivo and in vivo cardiac function in several commonly used inbred mouse strains. Physiol Genomics 2010;42A:103-13.
191. Linder CC. Genetic variables that influence phenotype. ILAR J 2006;47:132-40.
192. Morton DB, Hawkins P, Bevan R, et al. Refinements in telemetry procedures. Seventh report of the BVAAWF/FRAME/RSPCA/UFAW Joint Working Group on Refinement, Part A. Lab Anim 2003;37:261-99.
193. Berul CI, Aronovitz MJ, Wang PJ, Mendelsohn ME. In vivo cardiac electrophysiology studies in the mouse. Circulation 1996;94:2641-8.
194. Gomes J, Finlay M, Ahmed AK, et al. Electrophysiological abnormalities precede overt structural changes in arrhythmogenic right ventricular cardiomyopathy due to mutations in desmoplakin-A combined murine and human study. Eur Heart J 2012.
195. Brazma A, Hingamp P, Quackenbush J, et al. Minimum information about a microarray experiment (MIAME)-toward standards for microarray data. Nat Genet 2001;29:365-71.
196. Marionneau C, Couette B, Liu J, et al. Specific pattern of ionic channel gene expression associated with pacemaker activity in the mouse heart. J Physiol 2005;562:223-34.
197. Baruscotti M, Bucchi A, Viscomi C, et al. Deep bradycardia and heart block caused by inducible cardiac-specific knockout of the pacemaker channel gene Hcn4. Proc Natl Acad Sci U S A 2011;108:1705-10.
198. Spodick DH. Reduction of QT-interval imprecision and variance by measuring the JT interval. Am J Cardiol 1992;70:103.
199. Aanhaanen WT, Boukens BJ, Sizarov A, et al. Defective Tbx2-dependent patterning of the atrioventricular canal myocardium causes accessory pathway formation in mice. J Clin Invest 2011;121:534-44.
200. Allison DB, Cui X, Page GP, Sabripour M. Microarray data analysis: from disarray to consolidation and consensus. Nat Rev Genet 2006;7:55-65.
201. Butte A. The use and analysis of microarray data. Nat Rev Drug Discov 2002;1:951-60.
202. Downey T. Analysis of a multifactor microarray study using Partek genomics solution. Methods Enzymol 2006;411:256-70.
203. Verdugo RA, Deschepper CF, Munoz G, Pomp D, Churchill GA. Importance of randomization in microarray experimental designs with Illumina platforms. Nucleic Acids Res 2009;37:5610-8.
204. Chuaqui RF, Bonner RF, Best CJ, et al. Post-analysis follow-up and validation of microarray experiments. Nat Genet 2002;32 Suppl:509-14.
205. Moroni A, Gorza L, Beltrame M, et al. Hyperpolarization-activated cyclic nucleotide-gated channel 1 is a molecular determinant of the cardiac pacemaker current I(f). J Biol Chem 2001;276:29233-41.
206. Yusuf S, Camm AJ. The sinus tachycardias. Nat Clin Pract Cardiovasc Med 2005;2:44-52.
207. Grant AO, Carboni M. Cardiac arrhythmia: mechanisms, diagnosis and management. In: Podrid PJ, Kowey PR, eds. Basic electrophysiology: generation of the cardiac action potential. 2 ed. US: Lippincott, Williams & Wilkins; 2001.
208. Hoogaars WM, Engel A, Brons JF, et al. Tbx3 controls the sinoatrial node gene program and imposes pacemaker function on the atria. Genes Dev 2007;21:1098-112.
209. Espinoza-Lewis RA, Yu L, He F, et al. Shox2 is essential for the differentiation of cardiac pacemaker cells by repressing Nkx2-5. Dev Biol 2009;327:376-85.
210. Espinoza-Lewis RA, Liu H, Sun C, Chen C, Jiao K, Chen Y. Ectopic expression of Nkx2.5 suppresses the formation of the sinoatrial node in mice. Dev Biol 2011;356:359-69.
211. Mangoni ME, Traboulsie A, Leoni AL, et al. Bradycardia and slowing of the atrioventricular conduction in mice lacking CaV3.1/alpha1G T-type calcium channels. Circ Res 2006;98:1422-30.
212. Kuratomi S, Ohmori Y, Ito M, et al. The cardiac pacemaker-specific channel Hcn4 is a direct transcriptional target of MEF2. Cardiovasc Res 2009;83:682-7.
213. Park DS, Fishman GI. The cardiac conduction system. Circulation 2011;123:904-15.
214. Monfredi O, Dobrzynski H, Mondal T, Boyett MR, Morris GM. The anatomy and physiology of the sinoatrial node--a contemporary review. Pacing Clin Electrophysiol 2010;33:1392-406.
215. Lipsius SL, Bers DM. Cardiac pacemaking: I(f) vs. Ca(2+), is it really that simple? J Mol Cell Cardiol 2003;35:891-3.

216. Chandler NJ, Greener ID, Tellez JO, et al. Molecular architecture of the human sinus node: insights into the function of the cardiac pacemaker. Circulation 2009;119:1562-75.
217. DiFrancesco D. The role of the funny current in pacemaker activity. Circ Res 2010;106:434-46.
218. DiFrancesco JC, Barbuti A, Milanesi R, et al. Recessive loss-of-function mutation in the pacemaker HCN2 channel causing increased neuronal excitability in a patient with idiopathic generalized epilepsy. J Neurosci 2011;31:17327-37.
219. Obenauer JC, Cantley LC, Yaffe MB. Scansite 2.0: Proteome-wide prediction of cell signaling interactions using short sequence motifs. Nucleic Acids Res 2003;31:3635-41.
220. Safaei J, Manuch J, Gupta A, Stacho L, Pelech S. Prediction of 492 human protein kinase substrate specificities. Proteome Sci 2011;9 Suppl 1:S6.
221. Altschul SF, Gish W, Miller W, Myers EW, Lipman DJ. Basic local alignment search tool. J Mol Biol 1990;215:403-10.
222. Frank DU, Carter KL, Thomas KR, et al. Lethal arrhythmias in Tbx3-deficient mice reveal extreme dosage sensitivity of cardiac conduction system function and homeostasis. Proc Natl Acad Sci U S A 2012;109:E154-63.
223. Sohal DS, Nghiem M, Crackower MA, et al. Temporally regulated and tissue-specific gene manipulations in the adult and embryonic heart using a tamoxifen-inducible Cre protein. Circ Res 2001;89:20-5.
224. Shimoda Y, Watanabe K. Contactins: emerging key roles in the development and function of the nervous system. Cell Adh Migr 2009;3:64-70.
225. Pallante BA, Giovannone S, Fang-Yu L, et al. Contactin-2 expression in the cardiac Purkinje fiber network. Circ Arrhythm Electrophysiol 2010;3:186-94.
226. Zhang W, Wang J, Wang H, et al. Acadesine inhibits tissue factor induction and thrombus formation by activating the phosphoinositide 3-kinase/Akt signaling pathway. Arterioscler Thromb Vasc Biol 2010;30:1000-6.
227. Wang S, Dale GL, Song P, Viollet B, Zou MH. AMPKalpha1 deletion shortens erythrocyte life span in mice: role of oxidative stress. J Biol Chem 2010;285:19976-85.
228. Schuhmacher S, Foretz M, Knorr M, et al. alpha1AMP-activated protein kinase preserves endothelial function during chronic angiotensin II treatment by limiting Nox2 upregulation. Arterioscler Thromb Vasc Biol 2011;31:560-6.
229. Andrews ZB, Liu ZW, Walllingford N, et al. UCP2 mediates ghrelin's action on NPY/AgRP neurons by lowering free radicals. Nature 2008;454:846-51.
230. Li XN, Song J, Zhang L, et al. Activation of the AMPK-FOXO3 pathway reduces fatty acid-induced increase in intracellular reactive oxygen species by upregulating thioredoxin. Diabetes 2009;58:2246-57.
231. Swaminathan PD, Purohit A, Soni S, et al. Oxidized CaMKII causes cardiac sinus node dysfunction in mice. J Clin Invest 2011;121:3277-88.
232. Kim YM, Guzik TJ, Zhang YH, et al. A myocardial Nox2 containing NAD(P)H oxidase contributes to oxidative stress in human atrial fibrillation. Circ Res 2005;97:629-36.
233. Edgar AJ, Polak JM. Cloning and tissue distribution of three murine alpha/beta hydrolase fold protein cDNAs. Biochem Biophys Res Commun 2002;292:617-25.
234. Stoelting M, Geyer M, Reuter S, Reichelt R, Bek MJ, Pavenstadt H. Alpha/beta hydrolase 1 is upregulated in D5 dopamine receptor knockout mice and reduces O2- production of NADPH oxidase. Biochem Biophys Res Commun 2009;379:81-5.
235. Hayashi S, Lewis P, Pevny L, McMahon AP. Efficient gene modulation in mouse epiblast using a Sox2Cre transgenic mouse strain. Mech Dev 2002;119 Suppl 1:S97-S101.
236. Vincent SD, Robertson EJ. Highly efficient transgene-independent recombination directed by a maternally derived SOX2CRE transgene. Genesis (New York, N Y : 2000) 2003;37:54-6.
237. Foretz M, Hebrard S, Guihard S, et al. The AMPKgamma1 subunit plays an essential role in erythrocyte membrane elasticity, and its genetic inactivation induces splenomegaly and anemia. FASEB J 2011;25:337-47.
238. Hayashi S, Tenzen T, McMahon AP. Maternal inheritance of Cre activity in a Sox2Cre deleter strain. Genesis 2003;37:51-3.
239. Cochrane RL, Clark SH, Harris A, Kream BE. Rearrangement of a conditional allele regardless of inheritance of a Cre recombinase transgene. Genesis 2007;45:17-20.
240. Sartiani L, Bochet P, Cerbai E, Mugelli A, Fischmeister R. Functional expression of the hyperpolarization-activated, non-selective cation current I(f) in immortalized HL-1 cardiomyocytes. J Physiol 2002;545:81-92.
241. Viana R, Towler MC, Pan DA, et al. A conserved sequence immediately N-terminal to the Bateman domains in AMP-activated protein kinase gamma subunits is required for the interaction with the beta subunits. J Biol Chem 2007;282:16117-25.

242. Bhuvanagiri M, Schlitter AM, Hentze MW, Kulozik AE. NMD: RNA biology meets human genetic medicine. Biochem J 2010;430:365-77.
243. Ferrari R, Censi S, Mastrorilli F, Boraso A. Prognostic benefits of heart rate reduction in cardiovascular disease. European Heart Journal Supplements 2003;5:G10-G4.
244. Hardie DG. Energy sensing by the AMP-activated protein kinase and its effects on muscle metabolism. Proc Nutr Soc 2011;70:92-9.
245. Nylander E, Sigvardsson K, Kilbom A. Training-induced bradycardia and intrinsic heart rate in rats. Eur J Appl Physiol Occup Physiol 1982;48:189-99.
246. Katona PG, McLean M, Dighton DH, Guz A. Sympathetic and parasympathetic cardiac control in athletes and nonathletes at rest. J Appl Physiol 1982;52:1652-7.
247. Scott AS, Eberhard A, Ofir D, et al. Enhanced cardiac vagal efferent activity does not explain training-induced bradycardia. Auton Neurosci 2004;112:60-8.
248. Danson EJ, Paterson DJ. Enhanced neuronal nitric oxide synthase expression is central to cardiac vagal phenotype in exercise-trained mice. J Physiol 2003;546:225-32.
249. Kahn BB, Alquier T, Carling D, Hardie DG. AMP-activated protein kinase: ancient energy gauge provides clues to modern understanding of metabolism. Cell Metab 2005;1:15-25.
250. Lage R, Dieguez C, Vidal-Puig A, Lopez M. AMPK: a metabolic gauge regulating whole-body energy homeostasis. Trends Mol Med 2008;14:539-49.
251. Viollet B, Guigas B, Leclerc J, et al. AMP-activated protein kinase in the regulation of hepatic energy metabolism: from physiology to therapeutic perspectives. Acta Physiol (Oxf) 2009;196:81-98.
252. da Silva Xavier G, Leclerc I, Varadi A, Tsuboi T, Moule SK, Rutter GA. Role for AMP-activated protein kinase in glucose-stimulated insulin secretion and preproinsulin gene expression. Biochem J 2003;371:761-74.
253. Beall C, Piipari K, Al-Qassab H, et al. Loss of AMP-activated protein kinase alpha2 subunit in mouse beta-cells impairs glucose-stimulated insulin secretion and inhibits their sensitivity to hypoglycaemia. Biochem J 2010;429:323-33.
254. Dzamko NL, Steinberg GR. AMPK-dependent hormonal regulation of whole-body energy metabolism. Acta Physiol (Oxf) 2009;196:115-27.
255. Shaw RJ, Lamia KA, Vasquez D, et al. The kinase LKB1 mediates glucose homeostasis in liver and therapeutic effects of metformin. Science 2005;310:1642-6.
256. Leto D, Saltiel AR. Regulation of glucose transport by insulin: traffic control of GLUT4. Nat Rev Mol Cell Biol 2012;13:383-96.
257. Huang S, Czech MP. The GLUT4 glucose transporter. Cell Metab 2007;5:237-52.
258. Lim CT, Kola B, Korbonits M. AMPK as a mediator of hormonal signalling. J Mol Endocrinol 2010;44:87-97.
259. Kola B, Hubina E, Tucci SA, et al. Cannabinoids and ghrelin have both central and peripheral metabolic and cardiac effects via AMP-activated protein kinase. J Biol Chem 2005;280:25196-201.
260. Lopez M, Varela L, Vazquez MJ, et al. Hypothalamic AMPK and fatty acid metabolism mediate thyroid regulation of energy balance. Nat Med 2010;16:1001-8.
261. Christ-Crain M, Kola B, Lolli F, et al. AMP-activated protein kinase mediates glucocorticoid-induced metabolic changes: a novel mechanism in Cushing's syndrome. FASEB J 2008;22:1672-83.
262. Luquet S, Perez FA, Hnasko TS, Palmiter RD. NPY/AgRP neurons are essential for feeding in adult mice but can be ablated in neonates. Science 2005;310:683-5.
263. Flier JS. AgRP in energy balance: Will the real AgRP please stand up? Cell Metab 2006;3:83-5.
264. Lathe R. Mice, gene targeting and behaviour: more than just genetic background. Trends Neurosci 1996;19:183-6; discussion 8-9.
265. Dzamko N, van Denderen BJ, Hevener AL, et al. AMPK beta1 deletion reduces appetite, preventing obesity and hepatic insulin resistance. J Biol Chem 2010;285:115-22.
266. Jorgensen SB, Viollet B, Andreelli F, et al. Knockout of the alpha2 but not alpha1 5'-AMP-activated protein kinase isoform abolishes 5-aminoimidazole-4-carboxamide-1-beta-4-ribofuranosidebut not contraction-induced glucose uptake in skeletal muscle. J Biol Chem 2004;279:1070-9.
267. Nielsen JN, Jorgensen SB, Frosig C, et al. A possible role for AMP-activated protein kinase in exercise-induced glucose utilization: insights from humans and transgenic animals. Biochem Soc Trans 2003;31:186-90.
268. Villena JA, Viollet B, Andreelli F, Kahn A, Vaulont S, Sul HS. Induced adiposity and adipocyte hypertrophy in mice lacking the AMP-activated protein kinase-alpha2 subunit. Diabetes 2004;53:2242-9.
269. Claret M, Smith MA, Batterham RL, et al. AMPK is essential for energy homeostasis regulation and glucose sensing by POMC and AgRP neurons. J Clin Invest 2007;117:2325-36.
270. Steinberg GR, O'Neill HM, Dzamko NL, et al. Whole body deletion of AMP-activated protein kinase {beta}2 reduces muscle AMPK activity and exercise capacity. J Biol Chem 2010;285:37198-209.

271. De Bono JP, Adlam D, Paterson DJ, Channon KM. Novel quantitative phenotypes of exercise training in mouse models. Am J Physiol Regul Integr Comp Physiol 2006;290:R926-34.
272. Arch JR, Hislop D, Wang SJ, Speakman JR. Some mathematical and technical issues in the measurement and interpretation of open-circuit indirect calorimetry in small animals. Int J Obes (Lond) 2006;30:1322-31.
273. Tschop MH, Speakman JR, Arch JR, et al. A guide to analysis of mouse energy metabolism. Nat Methods 2012;9:57-63.
274. Ning K, Miller LC, Laidlaw HA, et al. A novel leptin signalling pathway via PTEN inhibition in hypothalamic cell lines and pancreatic beta-cells. EMBO J 2006;25:2377-87.
275. Nagy TR, Krzywanski D, Li J, Meleth S, Desmond R. Effect of group vs. single housing on phenotypic variance in C57BL/6J mice. Obes Res 2002;10:412-5.
276. Tinsley FC, Taicher GZ, Heiman ML. Evaluation of a quantitative magnetic resonance method for mouse whole body composition analysis. Obes Res 2004;12:150-60.
277. Fantuzzi G. Adipose tissue, adipokines, and inflammation. J Allergy Clin Immunol 2005;115:911-9; quiz 20.
278. Heikkinen S, Argmann CA, Champy MF, Auwerx J. Evaluation of glucose homeostasis. Curr Protoc Mol Biol 2007;Chapter 29:Unit 29B 3.
279. Ashcroft FM, Rorsman P. Diabetes mellitus and the beta cell: the last ten years. Cell 2012;148:1160-71.
280. Voss-Andreae A, Murphy JG, Ellacott KL, et al. Role of the central melanocortin circuitry in adaptive thermogenesis of brown adipose tissue. Endocrinology 2007;148:1550-60.
281. Cannon B, Nedergaard J. Brown adipose tissue: function and physiological significance. Physiol Rev 2004;84:277-359.
282. Viollet B, Andreelli F, Jorgensen SB, et al. The AMP-activated protein kinase alpha2 catalytic subunit controls whole-body insulin sensitivity. J Clin Invest 2003;111:91-8.
283. Buhl ES, Jessen N, Pold R, et al. Long-term AICAR administration reduces metabolic disturbances and lowers blood pressure in rats displaying features of the insulin resistance syndrome. Diabetes 2002;51:2199-206.
284. Cool B, Zinker B, Chiou W, et al. Identification and characterization of a small molecule AMPK activator that treats key components of type 2 diabetes and the metabolic syndrome. Cell Metab 2006;3:403-16.
285. Halseth AE, Ensor NJ, White TA, Ross SA, Gulve EA. Acute and chronic treatment of ob/ob and db/db mice with AICAR decreases blood glucose concentrations. Biochem Biophys Res Commun 2002;294:798-805.
286. Narkar VA, Downes M, Yu RT, et al. AMPK and PPARdelta agonists are exercise mimetics. Cell 2008;134:405-15.
287. Davis TA, Suryawan A, Orellana RA, Nguyen HV, Fiorotto ML. Postnatal ontogeny of skeletal muscle protein synthesis in pigs. J Anim Sci 2008;86:E13-8.
288. Miyazaki M, Esser KA. Cellular mechanisms regulating protein synthesis and skeletal muscle hypertrophy in animals. J Appl Physiol 2009;106:1367-73.
289. Shaw RJ. LKB1 and AMP-activated protein kinase control of mTOR signalling and growth. Acta Physiol (Oxf) 2009;196:65-80.
290. Tsuboi T, da Silva Xavier G, Leclerc I, Rutter GA. 5'-AMP-activated protein kinase controls insulin-containing secretory vesicle dynamics. J Biol Chem 2003;278:52042-51.
291. Ellacott KL, Cone RD. The role of the central melanocortin system in the regulation of food intake and energy homeostasis: lessons from mouse models. Philos Trans R Soc Lond B Biol Sci 2006;361:1265-74.
292. Minor RK, Chang JW, de Cabo R. Hungry for life: How the arcuate nucleus and neuropeptide Y may play a critical role in mediating the benefits of calorie restriction. Mol Cell Endocrinol 2009;299:79-88.
293. Stark R, Ashley SE, Andrews ZB. AMPK and the neuroendocrine regulation of appetite and energy expenditure. Mol Cell Endocrinol 2012.
294. Elmquist JK, Elias CF, Saper CB. From lesions to leptin: hypothalamic control of food intake and body weight. Neuron 1999;22:221-32.
295. Morton GJ, Cummings DE, Baskin DG, Barsh GS, Schwartz MW. Central nervous system control of food intake and body weight. Nature 2006;443:289-95.
296. Zhang Y, Proenca R, Maffei M, Barone M, Leopold L, Friedman JM. Positional cloning of the mouse obese gene and its human homologue. Nature 1994;372:425-32.
297. Rink TJ. Genetics. In search of a satiety factor. Nature 1994;372:406-7.
298. Friedman JM. A tale of two hormones. Nat Med 2010;16:1100-6.
299. Dhillo WS. Appetite regulation: an overview. Thyroid 2007;17:433-45.

300. Magni P, Dozio E, Ruscica M, et al. Feeding behavior in mammals including humans. Ann N Y Acad Sci 2009;1163:221-32.
301. Blanco Martinez de Morentin P, Gonzalez CR, Saha AK, et al. Hypothalamic AMP-activated protein kinase as a mediator of whole body energy balance. Rev Endocr Metab Disord 2011;12:127-40.
302. Morton GJ, Schwartz MW. The NPY/AgRP neuron and energy homeostasis. Int J Obes Relat Metab Disord 2001;25 Suppl 5:S56-62.
303. Aponte Y, Atasoy D, Sternson SM. AGRP neurons are sufficient to orchestrate feeding behavior rapidly and without training. Nat Neurosci 2011;14:351-5.
304. Garofalo RS. Genetic analysis of insulin signaling in Drosophila. Trends Endocrinol Metab 2002;13:156-62.
305. Schwartz MW, Woods SC, Porte D, Jr., Seeley RJ, Baskin DG. Central nervous system control of food intake. Nature 2000;404:661-71.
306. Kojima M, Hosoda H, Date Y, Nakazato M, Matsuo H, Kangawa K. Ghrelin is a growth-hormone-releasing acylated peptide from stomach. Nature 1999;402:656-60.
307. Patterson M, Bloom SR, Gardiner JV. Ghrelin and appetite control in humans--potential application in the treatment of obesity. Peptides 2011;32:2290-4.
308. Nakazato M, Murakami N, Date Y, et al. A role for ghrelin in the central regulation of feeding. Nature 2001;409:194-8.
309. Shan X, Yeo GS. Central leptin and ghrelin signalling: comparing and contrasting their mechanisms of action in the brain. Rev Endocr Metab Disord 2011;12:197-209.
310. Tschop M, Smiley DL, Heiman ML. Ghrelin induces adiposity in rodents. Nature 2000;407:908-13.
311. van den Top M, Lee K, Whyment AD, Blanks AM, Spanswick D. Orexigen-sensitive NPY/AgRP pacemaker neurons in the hypothalamic arcuate nucleus. Nat Neurosci 2004;7:493-4.
312. Qian S, Chen H, Weingarth D, et al. Neither agouti-related protein nor neuropeptide Y is critically required for the regulation of energy homeostasis in mice. Mol Cell Biol 2002;22:5027-35.
313. Huszar D, Lynch CA, Fairchild-Huntress V, et al. Targeted disruption of the melanocortin-4 receptor results in obesity in mice. Cell 1997;88:131-41.
314. Ste Marie L, Miura GI, Marsh DJ, Yagaloff K, Palmiter RD. A metabolic defect promotes obesity in mice lacking melanocortin-4 receptors. Proc Natl Acad Sci U S A 2000;97:12339-44.
315. Yeo GS, Farooqi IS, Aminian S, Halsall DJ, Stanhope RG, O'Rahilly S. A frameshift mutation in MC4R associated with dominantly inherited human obesity. Nat Genet 1998;20:111-2.
316. Myers MG, Jr., Munzberg H, Leinninger GM, Leshan RL. The geometry of leptin action in the brain: more complicated than a simple ARC. Cell Metab 2009;9:117-23.
317. Robertson SA, Leinninger GM, Myers MG, Jr. Molecular and neural mediators of leptin action. Physiol Behav 2008;94:637-42.
318. Pinto S, Roseberry AG, Liu H, et al. Rapid rewiring of arcuate nucleus feeding circuits by leptin. Science 2004;304:110-5.
319. Briggs DI, Andrews ZB. Metabolic status regulates ghrelin function on energy homeostasis. Neuroendocrinology 2011;93:48-57.
320. Yaswen L, Diehl N, Brennan MB, Hochgeschwender U. Obesity in the mouse model of pro-opiomelanocortin deficiency responds to peripheral melanocortin. Nat Med 1999;5:1066-70.
321. Andersson U, Filipsson K, Abbott CR, et al. AMP-activated protein kinase plays a role in the control of food intake. J Biol Chem 2004;279:12005-8.
322. Minokoshi Y, Alquier T, Furukawa N, et al. AMP-kinase regulates food intake by responding to hormonal and nutrient signals in the hypothalamus. Nature 2004;428:569-74.
323. Minokoshi Y, Shiuchi T, Lee S, Suzuki A, Okamoto S. Role of hypothalamic AMP-kinase in food intake regulation. Nutrition 2008;24:786-90.
324. Minokoshi Y, Kim YB, Peroni OD, et al. Leptin stimulates fatty-acid oxidation by activating AMP-activated protein kinase. Nature 2002;415:339-43.
325. Dagon Y, Hur E, Zheng B, Wellenstein K, Cantley LC, Kahn BB. p70S6 Kinase Phosphorylates AMPK on Serine 491 to Mediate Leptin's Effect on Food Intake. Cell Metab 2012;16:104-12.
326. Hill JW, Williams KW, Ye C, et al. Acute effects of leptin require PI3K signaling in hypothalamic proopiomelanocortin neurons in mice. J Clin Invest 2008;118:1796-805.
327. Lopez M, Lage R, Saha AK, et al. Hypothalamic fatty acid metabolism mediates the orexigenic action of ghrelin. Cell Metab 2008;7:389-99.
328. Folmes CD, Lopaschuk GD. Role of malonyl-CoA in heart disease and the hypothalamic control of obesity. Cardiovasc Res 2007;73:278-87.
329. He W, Lam TK, Obici S, Rossetti L. Molecular disruption of hypothalamic nutrient sensing induces obesity. Nat Neurosci 2006;9:227-33.
330. Kahn BB, Myers MG, Jr. mTOR tells the brain that the body is hungry. Nat Med 2006;12:615-7.

331. Cota D, Proulx K, Smith KA, et al. Hypothalamic mTOR signaling regulates food intake. Science 2006;312:927-30.
332. Andrews ZB, Diano S, Horvath TL. Mitochondrial uncoupling proteins in the CNS: in support of function and survival. Nat Rev Neurosci 2005;6:829-40.
333. Kohno D, Sone H, Minokoshi Y, Yada T. Ghrelin raises [Ca2+]i via AMPK in hypothalamic arcuate nucleus NPY neurons. Biochem Biophys Res Commun 2008;366:388-92.
334. Sleeman MW, Latres E. The CAMplexities of central ghrelin. Cell Metab 2008;7:361-2.
335. Dietrich MO, Horvath TL. Synaptic plasticity of feeding circuits: hormones and hysteresis. Cell 2011;146:863-5.
336. Elmquist JK, Flier JS. Neuroscience. The fat-brain axis enters a new dimension. Science 2004;304:63-4.
337. Zapala MA, Hovatta I, Ellison JA, et al. Adult mouse brain gene expression patterns bear an embryologic imprint. Proc Natl Acad Sci U S A 2005;102:10357-62.
338. Wilkinson DG. Whole mount in situ hybridisation of vertebrate embryos. In: Wilkinson DG, ed. In situ hybridisation: a practical approach. Oxford, UK: IRL; 1992.
339. Chen AS, Metzger JM, Trumbauer ME, et al. Role of the melanocortin-4 receptor in metabolic rate and food intake in mice. Transgenic Res 2000;9:145-54.
340. Czyzyk TA, Sikorski MA, Yang L, McKnight GS. Disruption of the RIIbeta subunit of PKA reverses the obesity syndrome of Agouti lethal yellow mice. Proc Natl Acad Sci U S A 2008;105:276-81.
341. Wang L, Saint-Pierre DH, Tache Y. Peripheral ghrelin selectively increases Fos expression in neuropeptide Y - synthesizing neurons in mouse hypothalamic arcuate nucleus. Neurosci Lett 2002;325:47-51.
342. Martin NM, Small CJ, Sajedi A, Patterson M, Ghatei MA, Bloom SR. Pre-obese and obese agouti mice are sensitive to the anorectic effects of peptide YY(3-36) but resistant to ghrelin. Int J Obes Relat Metab Disord 2004;28:886-93.
343. Doi A, Shono T, Nishi M, Furuta H, Sasaki H, Nanjo K. IA-2beta, but not IA-2, is induced by ghrelin and inhibits glucose-stimulated insulin secretion. Proc Natl Acad Sci U S A 2006;103:885-90.
344. Asakawa A, Inui A, Kaga T, et al. Antagonism of ghrelin receptor reduces food intake and body weight gain in mice. Gut 2003;52:947-52.
345. Dong J, Peeters TL, De Smet B, et al. Role of endogenous ghrelin in the hyperphagia of mice with streptozotocin-induced diabetes. Endocrinology 2006;147:2634-42.
346. Maletinska L, Matyskova R, Maixnerova J, et al. The Peptidic GHS-R antagonist [D-Lys(3)]GHRP-6 markedly improves adiposity and related metabolic abnormalities in a mouse model of postmenopausal obesity. Mol Cell Endocrinol 2011;343:55-62.
347. Myers MG, Jr. Leptin receptor signaling and the regulation of mammalian physiology. Recent Prog Horm Res 2004;59:287-304.
348. Varela L, Vazquez MJ, Cordido F, et al. Ghrelin and lipid metabolism: key partners in energy balance. J Mol Endocrinol 2011;46:R43-63.
349. Sakkou M, Wiedmer P, Anlag K, et al. A role for brain-specific homeobox factor Bsx in the control of hyperphagia and locomotory behavior. Cell Metab 2007;5:450-63.
350. Lage R, Vazquez MJ, Varela L, et al. Ghrelin effects on neuropeptides in the rat hypothalamus depend on fatty acid metabolism actions on BSX but not on gender. FASEB J 2010;24:2670-9.
351. Sasaki T, Kitamura T. Roles of FoxO1 and Sirt1 in the central regulation of food intake. Endocr J 2010;57:939-46.
352. Kitamura T, Feng Y, Kitamura YI, et al. Forkhead protein FoxO1 mediates Agrp-dependent effects of leptin on food intake. Nat Med 2006;12:534-40.
353. Nogueiras R, Lopez M, Lage R, et al. Bsx, a novel hypothalamic factor linking feeding with locomotor activity, is regulated by energy availability. Endocrinology 2008;149:3009-15.
354. Verhulst PJ, Depoortere I. Ghrelin's second life: from appetite stimulator to glucose regulator. World J Gastroenterol 2012;18:3183-95.
355. Wang Y, Nishi M, Doi A, et al. Ghrelin inhibits insulin secretion through the AMPK-UCP2 pathway in beta cells. FEBS Lett 2010;584:1503-8.
356. Berul CI. Electrophysiological phenotyping in genetically engineered mice. Physiol Genomics 2003;13:207-16.
357. Greener ID, Monfredi O, Inada S, et al. Molecular architecture of the human specialised atrioventricular conduction axis. J Mol Cell Cardiol 2011;50:642-51.
358. Herrmann S, Layh B, Ludwig A. Novel insights into the distribution of cardiac HCN channels: an expression study in the mouse heart. J Mol Cell Cardiol 2011;51:997-1006.
359. Lakatta EG, DiFrancesco D. What keeps us ticking: a funny current, a calcium clock, or both? J Mol Cell Cardiol 2009;47:157-70.

360. Walley AJ, Asher JE, Froguel P. The genetic contribution to non-syndromic human obesity. Nat Rev Genet 2009;10:431-42.
361. Nouira S, Arfa I, Kammoun I, et al. Identification of two novel variants in PRKAG2 gene in Tunisian type 2 diabetic patients with family history of cardiovascular disease. Diabetes Res Clin Pract 2010;87:e7-10.
362. Jablonski KA, McAteer JB, de Bakker PI, et al. Common Variants in 40 Genes Assessed for Diabetes Incidence and Response to Metformin and Lifestyle Interventions in the Diabetes Prevention Program. Diabetes 2010.

Appendix 1. ABI TaqMan inventoried murine gene expression assays used in real-time PCR

Gene symbol (alias)	Gene name (synonym)	ABI ID
Abhd1	Abhydrolase domain containing 1	Mm00502360_m1
Acta1	Actin, alpha 1, skeletal muscle	Mm00808218_g1
Actb	Actin, beta	Mm00607939_s1
Adipoq	Adiponectin, C1Q and collagen domain containing	Mm00456425_m1
Adrb3	Adrenergic receptor, beta 3	Mm02601819_g1
Agrp	Agouti related protein	Mm00475829_g1
Bdh1	3-hydroxybutyrate dehydrogenase, type 1	Mm00558330_m1
Bsx	Brain specific homeobox	Mm00626440_m1
Cacna1g	Calcium channel, voltage-dependent, T type, alpha 1G subunit	Mm00486572_m1
Cartpt	CART prepropeptide	Mm00489086_m1
Cav3	Caveolin 3	Mm01182632_m1
Ccl2 (MCP-1)	Chemokine (C-C motif) ligand 2	Mm00441242_m1
Cdc42ep1	CDC42 effector protein (Rho GTPase binding) 1	Mm00840486_m1
Cntn2 (TAG-1)	Contactin 2	Mm00516138_m1
Cpt1a	Carnitine palmitoyltransferase 1a, liver	Mm00550438_m1
Dio2	Deiodinase, iodothyronine, type II	Mm00515664_m1
Emr1 (F4/80)	EGF-like module containing, mucin-like, hormone receptor-like sequence 1	Mm00802529_m1
Foxo1	Forkhead box O1	Mm00490672_m1
Gbe1	Glucan (1,4-alpha-), branching enzyme 1	Mm00472347_m1
Gja5 (Cx40)	Gap junction protein, alpha 5	Mm01265686_m1
Gjc1 (Cx45)	Gap junction protein, gamma 1	Mm01253027_m1
Gjd3 (cx30.2)	Gap junction protein, delta 3 (connexion 30.2)	Mm00731344_s1
Gys1	Glycogen synthase 1, muscle	Mm00472712_m1
Hcn1	Hyperpolarisation-activated, cyclic nucleotide-gated K+ 1	Mm00468832_m1
Hcn2	Hyperpolarisation-activated, cyclic nucleotide-gated K+ 2	Mm00468538_m1
Hcn3	Hyperpolarisation-activated, cyclic nucleotide-gated K+ 3	Mm01212852_m1
Hcn4	Hyperpolarisation-activated, cyclic nucleotide-gated K+ 4	Mm01176086_m1
Hprt	Hypoxanthine guanine phosphoribosyl transferase	Mm01545399_m1
Il6	Interleukin 6	Mm00446190_m1
Kcna1 (Kv1.1)	Potassium voltage-gated channel, shaker-related subfamily, member 1	Mm00439977_s1
Lbh	Limb-bud and heart	Mm00522505_m1
Myh7b	Myosin, heavy chain 7B, cardiac muscle, beta	Mm01249977_m1

Gene symbol (alias)	Gene name (synonym)	ABI ID
Nkx2-5	NK2 transcription factor related, locus 5, Drosophila	Mm00657783_m1
Nppa (ANP)	Natriuretic peptide type A	Mm01255747_g1
Npy	Neuropeptide Y	Mm00445771_m1
Pomc	Pro-opiomelanocortin-alpha	Mm00435874_m1
Ppia	Peptidylprolyl isomerase A (cyclophilin A)	Mm02342430_g1
Ppib	Peptidylprolyl isomerase B (cyclophilin B)	Mm00478295_m1
Prdm16	PR domain containing 16	Mm00712556_m1
Prkag1	Protein kinase, AMP-activated, gamma 1 non-catalytic subunit	Mm00450298_g1
Prkag2	Protein kinase, AMP-activated, gamma 2 non-catalytic subunit	Mm00513977_m1
Prkag3	Protein kinase, AMP-activated, gamma 3 non-catalytic subunit	Mm00463997_m1
Pygm	Muscle glycogen phosphorylase	Mm00478582_m1
Scgb1c1	Secretoglobin, family 1C, member 1	Mm01165525_g1
Scn3b	Sodium channel, voltage-gated, type III, beta	Mm00463369_m1
Shox2	Short stature homeobox 2	Mm00443183_m1
Slc27a1 (Fatp)	Solute carrier family 27 (fatty acid transporter), member 1	Mm00449511_m1
Slc5a1 (Sglt1)	Solute carrier family 5 (sodium/glucose cotransporter), member 1	Mm00451203_m1
Socs3	Suppressor of cytokine signaling 3	Mm00545913_s1
Tbx3	T-box 3	Mm01195726_m1
Tmem116	Transmembrane protein 116	Mm01196748_m1
Tnf (TNFalpha)	Tumour necrosis factor	Mm00443258_m1
Ugp2	UDP-glucose pyrophosphorylase 2	Mm00454826_m1

Appendix 2. Antibodies used in Western blotting and immunoprecipitation

Antibody (epitope)	Source	Type	MW (kDa)	Manufacturer	Ref. No.
Primary antibodies used					
Acetyl-CoA carboxylase	Rabbit	Monoclonal	280	Cell Signaling	3676
AMPK pan-α	Rabbit	Polyclonal	62	Cell Signaling	2532
AMPK α1	Goat	Polyclonal	63	Santa Cruz	19128
AMPK α2	Goat	Polyclonal	62	Santa Cruz	19131
AMPK β1	Rabbit	Polyclonal	38	Cell Signaling	4182
AMPK β2	Rabbit	Polyclonal	30	Cell Signaling	4148
AMPK γ1	Rabbit	Monoclonal	38	Abcam	ab32508
AMPK γ1 (used for immunoprecipitation only)	Rabbit	Polyclonal	38	Kind gift of Professor Carling	-
AMPK γ2 (C-terminal epitope)	Rabbit	Polyclonal	63	Kind gift of Professor Carling	-
AMPK γ2 (N-terminal epitope)	Goat	Polyclonal	63	Santa Cruz	19141 (N-20)
AMPK γ3	Rabbit	Polyclonal	54	Cell Signaling	2550
Contactin-2	Rabbit	Monoclonal	135	Epitomics	3870-1
CREB	Rabbit	Monoclonal	43	Cell Signaling	9197
FLAG (M2)	Mouse	Monoclonal	-	Sigma	F3165
FoxO1	Rabbit	Monoclonal	80	Cell Signaling	2880
Phospho-Acetyl-CoA carboxylase (Ser 79)	Rabbit	Polyclonal	280	Cell Signaling	3661
Phospho-AMPK α (Thr172)	Rabbit	Monoclonal	62	Cell Signaling	2535
Phospho-CREB (Ser133)	Rabbit	Monoclonal	43	Cell Signaling	9198
Phospho-Stat3 (Tyr705)	Rabbit	Polyclonal	79,86	Cell Signaling	9131
sip2 (pan-β) (used for immunoprecipitation only)	Rabbit	Polyclonal	30	Kind gift of Professor Carling	-
Stat3	Rabbit	Polyclonal	79,86	Cell Signaling	9132
Antibodies used for loading controls					
α-actinin	Rabbit	Polyclonal	95	Abcam	ab11007
β-tubulin	Rabbit	Polyclonal	50	Abcam	ab6046
HRP-conjugated secondary antibodies used					
Goat IgG	Rabbit	Polyclonal	-	Abcam	ab6741
Mouse IgG	Sheep	Polyclonal	-	GE Healthcare	NA931
Rabbit IgG	Donkey	Polyclonal	-	GE Healthcare	NA934

Appendix 3. Cardiac function of γ2 WT and R299Q γ2 knock-in mutant mice

	WT γ2	R299Q γ2 heterozygote	R299Q γ2 Homozygote
Cardiac MRI (2 months)	N=8	N=19	N=11
LV EDVI (μL/g)	2.43±0.20 (2.10-2.80)	2.46±0.28 (2.12-3.10)	2.67±0.31 (2.20-3.10)
LV ESVI (μL/g)	0.73±0.09 (0.60-0.86)	0.89±0.16 (0.62-1.21)	0.96±0.21 (0.65-1.28)
LV EF(%)	70.1±3.8 (64.3-74.9)	63.9±4.5 (55.9-72.2)	64.5±4.73 (58.2-73.1)
CI (mL/min/g body weight)	0.64±0.12 (0.49-0.86)	0.58±0.09 (0.46-0.79)	0.59±0.08 (0.49-0.77)
LV mass indexed to body weight at time of scan (mg/g)	3.35±0.32 (2.93-3.76)	3.28±0.32 (2.78-4.06)	3.47±0.32 (3.04-4.10)
Heart rate (bpm)	374±41 (313-432)	369±29 (317-428)	341±24 (295-375)
Cardiac MRI (10 months)	N=7	N=17	N=11
LV EDVI (μL/g)	1.55±0.21 (1.26-1.80)	1.66±0.28 (1.12-2.11)	1.74±0.36 (1.26-2.23)
LV ESVI (μL/g)	0.51±0.10 (0.37-0.66)	0.59±0.15 (0.32-0.85)	0.68±0.25 (0.41-1.19)
LV EF(%)	67.9±4.5 (62.4-72.5)	64.9±5.5 (58.1-75.4)	61.7±7.5 (43.4-68.0)
CI (mL/min/g body weight)	0.49±0.08 (0.35-0.62)	0.47±0.07 (0.38-0.63)	0.47±0.07 (0.35-0.62)
LV mass indexed to tibial length (mg/mm)	5.77±1.28 (4.26-7.64)	5.76±1.02 (3.43-7.60)	5.68±1.71 (4.39-10.32)
Heart rate (bpm)	470±22 (431-493)	444±39 (397-552)	451±29 (407-491)
Baseline LV haemodynamics (12 months)	N=15	N=18	N=10
LVESP (mmHg)	102.7±18.7 (77.5-153.4)	102.5±12.4 (76.5-119.8)	91.2±14.8 (72.8-125.3)
LVEDP (mmHg)	7.7±3.2 (1.2-11.1)	7.9±4.7 (1.4-15.9)	5.1±3.9 (1.3-11.7)
dP/dt max (mmHg/s)	8275±1338 (6139-10612)	7711±2643 (3887-15686)	6545±1607 (4126-9307)
dP/dt min (mmHg/s)	-10154±2459 (-5426– -14389)	-8822±3003 (-5696– -13099)	-7303±2333 (-3076– -10025)
τ (ms)	8.6±1.9 (6.4-10.6)	11.2±4.1 (5.9-21.6)	12.3±5.6 (6.1-26.4)
Heart rate (bpm)	507±52 (451-572)	493±73 (412-572)	428±46 (383-501)

All data are presented as mean ± SD (range)

Appendix 4a. Differentially expressed gene list: R299Q γ2 homozygote vs WT comparison

Illumina ID	Gene Symbol*	Gene Title	R299Q γ2 Homozygote vs. WT	
			Fold change	Raw *P* value
ILMN_2672772	Abhd1	Abhydrolase domain containing 1	19.7366	1.54E-09
ILMN_2672778	Abhd1	Abhydrolase domain containing 1	18.2495	1.87E-09
ILMN_1245678	Abhd1	Abhydrolase domain containing 1	13.4256	1.09E-08
ILMN_2595299	A830021M18Rik	RIKEN cDNA A830021M18 gene	4.57678	5.04E-06
ILMN_1250030	Cdc42ep1	CDC42 effector protein (Rho GTPase binding) 1 (Cdc42ep1)	2.75369	2.13E-05
ILMN_2609421	Scgb1c1 (Ryd5)	Secretoglobin, family 1C, member 1	2.37899	9.27E-08
ILMN_2624031	Tmem116	Transmembrane protein 116	1.5955	1.81E-06
ILMN_1221373	Slc9a2	Solute carrier family 9 (sodium/hydrogen exchanger), member 2	1.52598	4.25E-05
ILMN_2700400	Galnt11	UDP-N-acetyl-alpha-D-galactosamine:polypeptide N-acetylgalactosaminyltransferase 11	1.51412	8.52E-10
ILMN_1228109	Tmem116	Transmembrane protein 116	1.50873	7.15E-06
ILMN_2731035	Dhrs7c	Dehydrogenase/reductase (SDR family) member 7C	1.42672	3.50E-05
ILMN_1231948	Grm1	Glutamate receptor, metabotropic 1	1.42645	2.81E-05
ILMN_2488846	Tmod4	Tropomodulin 4	1.40556	1.38E-05
ILMN_2592815	Gnai1	Guanine nucleotide binding protein (G protein), alpha inhibiting 1	1.37443	2.92E-06
ILMN_2726055	Shmt1	Serine hydroxymethyltransferase 1 (soluble)	1.24458	3.17E-05
ILMN_1234082	Srebf2	Sterol regulatory element binding factor 2	1.23944	2.74E-05
ILMN_2751854	Ndrg4	N-myc downstream regulated gene 4	-1.15718	1.76E-05
ILMN_1230777	0610007C21Rik	RIKEN cDNA 0610007C21 gene	-1.23181	3.49E-05
ILMN_2771360	Guk1	Guanylate kinase 1	-1.25713	1.28E-05
ILMN_2710455	Hebp2	Heme binding protein 2	-1.29273	3.87E-05
ILMN_2676481	Mir16	Membrane interacting protein of RGS16	-1.33096	3.85E-05
ILMN_2986315	Mir16	Membrane interacting protein of RGS16	-1.34411	1.62E-06
ILMN_1230048	Fxr2h	Fragile X mental retardation, autosomal homolog 2	-1.37123	8.61E-07
ILMN_1255776	BC017643	cDNA sequence BC017643 (BC017643)	-1.37188	2.00E-05
ILMN_2799351	Acot11	Acyl-CoA thioesterase 11	-1.37538	2.52E-05
ILMN_1232849	Cd99	CD99 antigen	-1.38857	6.44E-06
ILMN_1252621	Itfg2	Integrin alpha FG-GAP repeat containing 2 (Itfg2)	-1.42768	4.47E-07
ILMN_2638121	Nucb2	Nucleobindin 2 (Nucb2)	-1.43026	6.32E-07
ILMN_2618526	Mbldc1	Mus musculus cDNA sequence AB112350 (AB112350)	-1.47015	4.74E-05
ILMN_1250116	Masp1	Mannan-binding lectin serine peptidase 1	-1.47964	6.19E-06
ILMN_2774572	Crygn	Crystallin, gamma N	-1.51786	4.60E-05
ILMN_1231851	Enpp1	Ectonucleotide pyrophosphatase/phosphodiesterase 1	-1.51946	1.74E-05
ILMN_2581762	Galnt11	UDP-N-acetyl-alpha-D-galactosamine:polypeptide N-acetylgalactosaminyltransferase 11	-1.52208	1.27E-05
ILMN_2704184	Gpr177	G protein-coupled receptor 177	-1.52534	3.81E-05
ILMN_1221149	Mycn	Mycn v-myc myelocytomatosis viral related oncogene, neuroblastoma derived (avian)	-1.6071	1.06E-07
ILMN_1250760	Masp1	Mannan-binding lectin serine peptidase 1	-1.73781	4.39E-05
ILMN_2483748	Xrcc2	X-ray repair complementing defective repair in Chinese hamster cell	-1.79615	1.80E-07
ILMN_2454325	Rbm33	RNA binding motif protein 33	-1.83621	7.35E-08
ILMN_2895630	Xrcc2	X-ray repair complementing defective repair in Chinese hamster cell	-1.85518	1.76E-07
ILMN_2722488	Thumpd1	THUMP domain containing 1	-1.8812	2.57E-06
ILMN_1232800	Cyfip2	Cytoplasmic FMR1 interacting protein 2	-1.88636	1.01E-05
ILMN_1220131	Hcn1	Hyperpolarization-activated, cyclic nucleotide-gated K+ 1	-2.32216	3.51E-06
ILMN_2672943	Cntn2	Contactin 2	-2.46758	2.96E-05
ILMN_1231553	Bdh	3-hydroxybutyrate dehydrogenase, type 1	-3.80073	1.64E-05
ILMN_3161626	Prkag2	Protein kinase, AMP-activated, gamma 2 non-catalytic subunit	-6.07003	1.39E-11

Appendix 4b. Differentially expressed gene list: R299Q γ2 heterozygote vs WT comparison

Illumina ID	Gene Symbol*	Gene Title	R299Q γ2 Heterozygote vs WT	
			Fold change	Raw *P* value
ILMN_2672772	Abhd1	Abhydrolase domain containing 1	8.98591	6.24E-08
ILMN_2672778	Abhd1	Abhydrolase domain containing 1	8.74919	6.36E-08
ILMN_1245678	Abhd1	Abhydrolase domain containing 1	7.0432	3.18E-07
ILMN_2700400	Galnt11	UDP-N-acetyl-alpha-D-galactosamine:polypeptide N-acetylgalactosaminyltransferase 11	1.31386	1.33E-07
ILMN_1230048	Fxr2h	Fragile X mental retardation, autosomal homolog 2	-1.31051	4.71E-06
ILMN_3161626	Prkag2	Protein kinase, AMP-activated, gamma 2 non-catalytic subunit	-1.86019	4.81E-06

Appendix 4c. Differentially expressed gene list: R299Q γ2 homozygote vs heterozygote comparison

Illumina ID	Gene Symbol*	Gene Title	R299Q γ2 Homozygote vs Heterozygote	
			Fold change	Raw *P* value
ILMN_3161626	Prkag2	Protein kinase, AMP-activated, gamma 2 non-catalytic subunit	-3.26312	2.70E-09

*** All genes significant at FDR 5%**

Gene symbols and titles identified with Illumina's annotation file, supplemented by searches of: Mouse Genome Database (MGD, Mouse Genome Informatics, The Jackson Laboratory, Bar Harbor, Maine); the Database for Annotation, Visualization and Integrated Discovery (DAVID Bioinformatics Resources 6.7; NIAID, NIH); Entrez Gene (NCBI); Reannotation and Mapping of Oligonucleotide Arrays Technology (ReMOAT ver 1.0, University of Cambridge).

Appendix 5. Baseline cardiac function of Sox2cre γ2 line by transthoracic echocardiography

	WT Sox2cre	**Het fl Sox2cre+**	**Homofl Sox2cre+**
Echocardiography	N=11	N=9	N=12
Age (days)	43±1	44±3	44±3
Body weight (g)	20.6±1.5 (18.1-22.8)	23.3±1.1 (21.5-24.8)***	22.3±1.4 (19.9-24.2)*
Heart rate (bpm)	463±33 (407-515)	478±50 (411-581)	469±19 (447-504)
LV EF(%)	56.7±7.8 (46.6-70)	49.31±12.6 (35.5-74.8)	53.6±7.9 (40.3-62.6)
FS (%)	29.5±5.2 (23.0-38.9)	25.2±8.3 (16.8-42.9)	27.4±4.9 (19.4-33.1)
LV EDD (mm)	3.93±0.3 (3.36-4.26)	4.1±0.2 (3.77-4.49)	3.8±0.3 (3.57-4.30)
LV ESD (mm)	2.78±0.33 (2.18-3.22)	3.10±0.49 (2.16-3.63)	2.80±0.36 (2.41-3.46)
LVAWt (mm)	0.78±0.11 (0.66-1.00)	0.83±0.14 (0.69-1.10)	0.70±0.09 (0.59-0.88)
LVPWt (mm)	0.75±0.06 (0.65-0.81)	0.69±0.14 (0.48-0.88)	0.69±0.08 (0.58-0.84)
LV EDV (µL)	67.8±12.3 (46.1-81.3)	75.8±10.1 (60.9-92.0)	64.3±10.5 (53.3-82.9)
LV ESV (µL)	29.6±8.2 (15.8-41.4)	39.4±13.6 (15.4-55.6)	30.4±9.7 (20.4-49.3)
Peak Syst Vel (mm/s)	21.2±3.0 (16.2-25.9)	19.4±3.3 (15.3-24.5)	21.7±2.5 (17.3-24.9)

All data are presented as mean ± SD (range)

*P<0.05 vs WT Cre+, ***P<0.001 vs WT Cre+